Combinatorial surface-based electronic tongue development : Analytical applications and conception of 2D and 3D biomimetic surfaces

Maria Genua

To cite this version:

Maria Genua. Combinatorial surface-based electronic tongue development : Analytical applications and conception of 2D and 3D biomimetic surfaces. Other. Université de Grenoble, 2013. English. NNT : 2013GRENI044 . tel-00965649

HAL Id: tel-00965649
https://theses.hal.science/tel-00965649v1

Submitted on 25 Mar 2014

UNIVERSITÉ DE GRENOBLE

THÈSE

Pour obtenir le grade de

DOCTEUR DE L'UNIVERSITÉ DE GRENOBLE

Spécialité : Matériaux, mécanique, génie civil, électrochimie

Arrêté ministériel : 7 août 2006

Présentée par

Maria GENUA

Thèse dirigée par **Martial BILLON** et
codirigée par **Yanxia HOU-BROUTIN**

préparée au sein du **CEA Grenoble**
Institut Nanosciences et Cryogénie (INAC)
Service : Structures et Propriétés d'Architectures Moléculaires (SPrAM UMR 5819)
Groupe : Chimie pour la Reconnaissance et l'Etude des Assemblages Biologiques (CREAB)
dans **l'École Doctorale I-(MEP)2**

Développement d'une langue électronique sur des surfaces combinatoires :

Applications analytiques et conception de surfaces biomimétiques 2D et 3D

Thèse soutenue publiquement le **24 Octobre 2013**, devant le jury composé de :

M. Franz BRUCKERT
Professeur (INP-Grenoble), President
Mme. Edith PAJOT
Directrice de recherche INRA (INRA Jouy en Josas), Rapporteur
M. Yann CHEVOLOT
Chargé de recherche CNRS (Institut des nanotechnologies de Lyon), Rapporteur
M. Ralf RICHTER
Chargé de Recherche (CIC-Biomagune, San Sebastián), Membre
Mme. Yanxia HOU-BROUTIN
Chargée de recherche CNRS (CEA Grenoble), Membre
M. Martial BILLON
Maître de Conferences (Université de Grenoble), Membre

UNIVERSITÉ DE GRENOBLE

Combinatorial surface-based electronic tongue development:

Analytical applications and conception of 2D and 3D biomimetic surfaces.

PhD Thesis by

Maria GENUA

Grenoble 2013

Remerciements

Une thèse est un projet scientifique que, durant trois ans, le thésard doit développer. Commencer avec un projet, découvrir les techniques nécessaires à cette étude, discuter avec des experts en la matière pour que ce projet devienne finalement ton projet, c'est à la fois un chemin extrêmement intéressant et enrichissant mais également un chemin plein de défis et de doutes. Si parcourir ce chemin a été, non seulement possible, mais aussi un grand plaisir pour moi, c'est grâce à toutes ces personnes que j'ai pu côtoyer pendant cette période, qui ont contribué dans ma vie scientifique ainsi que dans ma vie personnelle, et que je tiens à remercier en quelques mots (bien que ces quelques mots ne sembleront jamais assez pour certains cas).

Tout d'abord, je voudrais remercier les membres du jury qui ont accepté de juger mon travail et moi-même en ma qualité de chercheuse. Merci à madame Edith Pajot et à monsieur Yann Chevolot pour le temps qu'ils ont consacré à la lecture et correction détaillée de mon manuscrit de thèse et à leur appréciation pour ce travail. Merci au professeur Franz Bruckert d'avoir présidé le jury de soutenance ainsi qu'à monsieur Ralf Richter pour ses corrections et pour avoir participé activement dans la discussion scientifique lors des questions.

Dans un deuxième temps, je voudrais remercier tous les collaborateurs qui ont rendu ce travail possible. A Hugues Lortat-Jacob et aux membres de son laboratoire à l'IBS, pour nous avoir donné l'opportunité de travailler avec leurs produits, et pour m'avoir accueillie dans leur labo à l'occasion de mes manips ELISA. A David Bonnaffé et Christine Le Narvor, ainsi qu'à Maryline Macé et tout le reste de l'équipe ICMMO de l'Université de Paris Sud, pour la synthèse des sucres utilisés tout au long de ce travail et pour leur excellent accueil lors de ma semaine de manipulations RMN dans leur laboratoire. A Arnaud De Geyer, du laboratoire SGX à l'INAC, pour son expertise et ses explications extrêmement pédagogiques lors des expériences avec la technique SAXS, et à Arnaud Buhot, du GT, pour son important rôle dans ce projet, pour les analyses mathématiques des résultats et pour sa patience lors de l'explication des analyses faites.

Ensuite, je voudrais exprimer mon énorme reconnaissance à mes directeurs de thèse. A Martial Billon, pour sa patience, sa perpétuelle bonne humeur et pour avoir toujours trouvé une petite place dans son agenda pour moi. Et à Yanxia Hou-Broutin, bon, à Yanxia je la remercie pour tout. D'abord, de m'avoir donné l'opportunité de faire un stage de master avec elle, de m'avoir fait confiance pour continuer en thèse sur un projet très apprécié par elle-même, de m'avoir appris tellement de choses, et d'être toujours disponible pour discuter. Discuter non seulement du projet, mais de tout en général, car j'ai fini par apprécier Yanxia autant scientifiquement que personnellement.

A ces deux directeurs de thèse, on peut rajouter mon « troisième directeur de thèse » et accessoirement, directeur du laboratoire, Thierry Livache. Thierry n'était pas obligé de suivre mon travail de près, il l'a fait, et en plus il a apporté de précieuses idées et conseils. Il m'a de même appris des choses encore plus importantes, comme l'application du sens commun dans la vie quotidienne d'un laboratoire. C'est grâce à sa façon particulière de gérer le laboratoire et à son grand sens de l'humour que Thierry a réussi à avoir un laboratoire comme le CREAB.

Le CREAB est un laboratoire spécial. Tous les matins, à 10h, au CREAB on prend le café. Tous les midis, au CREAB on va manger (après 13h, car le dessert ne coûte que 1 point !) Quand quelqu'un arrive ou s'en va du CREAB, on mange des croissants. Quand c'est l'anniversaire de quelqu'un, on mange des croissants. Bref, au CREAB, on fait tout ensemble (surtout manger). La petite famille du CREAB se maintient unie grâce à un groupe de permanents qui, en plus de donner de l'importance à la qualité scientifique de leurs travaux, donnent de l'importance aux personnes. Merci Yoann, André, Aurélie, Elodie, Loïc (aussi pour ton aide avec les manips electrochimiques), Yanxia, Arnaud, Thierry, Martial, Seb, Roberto, Raph, José et Pascal de m'avoir fait découvir que science et vie peuvent (et devraient) aller toujours ensemble. Spéciale mention pour Roberto, qui a beaucoup collaboré sur ce projet, et pour André et Aurélie, qui m'ont beaucoup aidée lors des corrections de la présentation de la soutenance. Aux secretaires du SPrAM, Catherine, Céline et specialement à Charlie, merci d'avoir fait les demarches administratives un peu plus faciles pour moi et de votre bonne humeur.

Merci aussi aux non-permanents que j'ai croisés au labo. Ceux qui ont travaillé avec moi : Damien, Laurie, Violette, Hillary, Benji, pour avoir contribué au projet et m'avoir supportée comme « chef d'esclaves » pendant un temps. Et les autres non-permanents, qui souvent ont aussi aidé avec mes manips, et parmi lesquels il y en a que je considère comme de vrais amis que j'espère conserver longtemps. Jie et Sami, les deux meilleurs co-bureaux du monde, les « frères » Laurent et Florian, les meilleurs conseillers, Loïc Leprince, toujours avec une idée plus bizarre que celle d'avant en tête mais que nous aimons tel qu'il est ☺, Feriel, la seule qui frappe à la porte avant d'entrer et reine des boureks, Laurie, toujours dispo pour faire une faveur et bonne personne pathologique, Laure et Sandrine, les filles des soirées cocktail/potains, Cyril, grand curieux de la science, Radek, le polaco tropical, Radé, qui un jour racontera sa vie dans un livre, Seb, José et Raph, les McGuivers du laboratoire, Timothée et Isabel qui même s'ils ne sont pas du CREAB, le sont presque, et les filles que j'ai un peu moins croisées mais qui semblent être très aptes a garder l'esprit du labo, Vanessa, Yulia, Emilie, Diane et Stacie. Bien sûr, une ligne à part pour Camille, mon âme sœur longtemps ignorée. Elle sait bien tout ce qu'elle a fait pour moi ; Dieu le payera avec un bon mari.

Et hors du laboratoire j'ai aussi quelques personnes à remercier, surtout d'avoir fait que j'aie une vie hors du laboratoire. Aux amis, comme Olivier pour ses cours de russe et les diners chez lui où on n'est pas obligé de ramener quelque chose à manger, à Morgane, pour la « Morganisation » des visites à Grenoble et son super accueil chez elle à Paris, à Joni qui est parti en aventure, mais avec lequel j'ai bien rigolé avec ses petites histoires, à Dipankar et Priya, les indiens, à Marc, Florian, Tiphaine, Esther et Miguel, Fabien, Marcello etc. du CIRE, avec lesquels j'ai partagé un bon nombre de bières. Aux colocs de Camille, Paolo pour son accueil à Turin et pour nous avoir fait découvrir la bataille des oranges (et le poulet à l'orange), Max, et Nadège pour me laisser toujours rentrer chez eux.

Ensuite je remercie ma « famille » grenobloise pour lesquels je ne peux écrire qu'un énorme MERCI. Ma déjà présentée sœur, Camille (et a Guillaume le gladiator, mon… frère ?), ma maman, Christoph (et Carina !) et la tante qui est partie en Italie, Radek. A mes trois autres colocs Lucie Fer (et Aurélien), Nico Lamentable et Remy Nicerveau : ça a été compliqué de supporter votre connerie, mais vous allez vraiment, vraiment me manquer. Je n'aurais jamais pu imaginer une coloc plus agréable et amusante qu'avec vous. A Diego, mon copain d'aventures, avec lequel on a tout fait ensemble et sans lequel je n'aurais fait rien de tout ça. Merci Diego pour avoir été toujours là.

Et finalement, je voudrais remercier ma vrai famille et les amis que j'ai abandonés pour m'embarquer dans cette aventure, cette fois en espagnol/basque: Me gustaría gradecer a los aitas, a Ander y a las dos Idoias, por su apoyo, sus animos cuando han hecho falta y por venir a buscarme al aeropuerto de Biarritz siempre que he vuelto a casa (y por las altas dosis de pescado). Al resto de la familia, aitonas, primos, tios, amigos de los aitas, eskerrik asko por hacerme sentir que hago algo importante y por vuestro amor incondicional. A las amigas de la uni, Ainoha, Ane, Vero y Pauli (y a Oscar y Borjita). A la cuadrilla (Ander, Zuito, Imanol el Grande, Iñaki, Lierni, Leyre, Eli, Cris, Izas, Naitxu y la Esnaola), por hacerme sentir que aunque haga 6 meses que no nos veamos, parezca que nos hayamos visto el sábado pasado. Por vuestros ánimos y vuestra amistad que no tiene precio. Especialmente a Cristina, la tesis no me ha permitido estar contigo en un doloroso momento de tu vida y tú lo has comprendido, perdonado y además me has apoyado. Eres la mejor. Mila esker guztioi.

Contents

Abbreviations

2D	Two-Dimensional
3D	Three-Dimensional
ATIII	Antithrombin III
Au NP	Gold Nanoparticle
BB	Building Block
CCD	Charge-Coupled Device
CEL	Continuous Evolution Landscape
CEP	Continuous Evolution Profile
ChemFET	Chemical Field-effect Transistor
CoCRR	Combinatorial Cross-Reactive Receptor
ConA	Concanavalin A
CRR	Cross-Reactive Receptor
Da	Dalton
DLS	Dynamic light scattering
DMF	Dimethylformamide
DNA	Deoxyribonucleic acid
e-Nose	Electronic Nose
e-Tongue	Electronic Tongue
ECL	Erythrina Cristagalli Lectin
EPR	Enhanced Permeability and Retention
FBS	Fetal Bovine Serum
FET	Field-effect Transistor
FGF	Fibroblast Growth Factor
G-Protein	Guanosine nucleotide binding Protein
GAG	Glycosaminoglycan
GFP	Green Fluorescent Protein
HATU	O-(7-azabenzotriazol-1-yl)-N,N,N’,N?-tetramethyluronium hexafluorophosphate
HEPES	4-(2-hydroxyethyl)-1-piperazineethanesulfonic acid
HIV	Human immunodeficiency virus
HP	Heparin
HS	Heparan Sulphate

HSA	Human Serum Albumin
HSbp	Heparan Sulphate Binding Protein
IBS	Institut de Biologie Structurale
IFN	Interferon
IgG	Immunoglobulin G
ISE	Ion-selective Electrode
KD	Dissociation constant
MEMS	Microelectromechanical System
MIP	Molecularly Imprinted Polymer
MOS	Metal Oxide Semiconductor
MOSFET	Metal Oxide Semiconductor Field-effect Transistor
MW	Molecular Weight
NEMS	Nanoelectromechanical System
NMR	Nuclear Magnetic Resonance
NP	Nanoparticle
OR	Odorant Receptor
PCA	Principal Component Analysis
PEG	Polyethylenglycol
PG	Proteoglycan
pI	Isoelectric Point
PolFET	Polymer Field-effect Transistor
PPE	Poly(p-phenyleneethynylene)
QCM	Quartz Crystal Microbalance
R%	Reflectivity percentage
RNA	Ribonucleic acid
RSV	Respiratory Syncytial virus
RT-PCR	Reverse Transcription Polymerase Chain Reaction
SAM	Self-Assembled Monolayer
SAW	Surface Acoustic Wave
SAXS	Small Angle X-Ray Scattering
SDF	Stromal-Derived Factor
SDS	Sodium Dodecyl Sulfate
SPR	Surface Plasmon Resonance
SPRi	Surface Plasmon Resonance imaging
UHT	Ultra High Temperature
UV	Ultraviolet
WT	Wild Type

CHAPTER 1.

Project Background and State of the Art

Résumé en français du chapitre 1

Contexte du projet et état de l’art

Les travaux menés au cours de cette thèse trouvent leur fil conducteur dans le développement et l’exploration des applications d’une langue électronique innovante et performante. Il est donc pertinent de commencer par introduire les concepts de base liés à ce type de système d’analyse, ainsi que l’état de l’art actuel du domaine.

Basés sur le puissant système olfactif des vertébrés, les langues et nez électroniques sont des capteurs chimiques qui ne reposent pas sur le principe classique de reconnaissance spécifique sonde-cible, mais sur le concept d’utilisation des capteurs à réactivité croisée. Dans cette approche, la réponse individuelle de chaque récepteur n’est pas suffisante pour la reconnaissance d’un analyte, et c’est la réponse globale d’une collection de récepteurs proprement traitée qui permet d’identifier le, ou les, échantillons.

Avec cette approche, les propriétés de base que doivent respecter les récepteurs se simplifient énormément par rapport aux capteurs spécifiques, qui ont besoin d’être spécifiques et sélectifs de façon individuelle. En effet, les trois caractéristiques principales des récepteurs à réactivité croisée sont :

1- Chaque récepteur peut reconnaitre plusieurs analytes

2- Chaque analyte peut être détecté par plusieurs récepteurs

3- Différents analytes sont reconnus par différentes combinaisons de récepteurs

Ce design permet d’obtenir des motifs de reconnaissance pour des analytes contenant un ou plusieurs composants, y compris pour des analytes pour lesquels le système n’a pas été conçu initialement. Les échantillons peuvent être en phase gazeuse ou en phase liquide, ce qui fait la différence entre les nez électroniques et les langues électroniques.

Une infinité d’applications peuvent être trouvées pour ce type de système notamment dans les milieux où l’analyse en routine d’échantillons est nécessaire. Cela a suscité un intérêt croissant envers les langues et nez électroniques, de la part des chercheurs et des industries, durant les 20 dernières années. Cet intérêt a permis de faire progresser rapidement le développement de ces systèmes, auparavant mis de coté par rapport aux systèmes mimétiques d’autres sens comme la vision, l’audition ou le toucher.

Les différentes approches de fabrication de ce type de système sont détaillées dans la section 1.3 de ce chapitre. Elles varient principalement selon le système de transduction employé, ainsi que selon les matériaux sensibles utilisés pour l'obtention des récepteurs à réactivité croisée.

On prêtera un intérêt particulier aux langues et nez électroniques dédiés à la détection de protéines. Ces systèmes sont souvent limités par l'irréversibilité des réponses, les longs temps de récupération du système, dus à des interactions trop fortes entre analyte et récepteur, et la courte durée de vie de certaines puces, causée par le photoblanchiment des fluorophores employés.

Dans ce contexte, l'objectif de cette thèse est ainsi le développement et l'exploration des applications d'une langue électronique qui comporte des améliorations par rapport aux systèmes existants, et notamment, qui simplifie la création et l'obtention des récepteurs à réactivité croisée.

Il est en effet possible de réduire les efforts dédiés à la création d'une librairie de matériaux sensibles en mélangeant un nombre restreint de briques de base (BBs). Les briques de base sont définies comme des petites molécules, faciles à obtenir, ayant différentes propriétés physicochimiques. En mélangeant ces briques de base selon différents ratios et en les laissant s'auto-assembler, il est possible d'obtenir une collection de surfaces combinatoires appelées récepteurs combinatoires à réactivité croisée (CoCRRs). Les propriétés physicochimiques de ces récepteurs combinatoires dépendent bien sûr des propriétés physicochimiques des briques de base, ainsi que du ratio des mélanges à partir desquels ils sont réalisés. Cette approche permet l'obtention facile et rapide d'un grand nombre de CoCRRs, en ajoutant par exemple de nouvelles briques de base, ou en augmentant le nombre de ratios de mélange effectués. De plus, même si les CoCRRs ont des compositions variables, la différence entre deux CoCRRs successifs peut être très faible, aboutissant à une représentation continue des données obtenues sur chaque CoCRR, ce qui permet l'identification rapide des artefacts et données incohérentes. Cette dernière caractéristique établit une différence avantageuse par rapport aux langues électroniques actuelles, qui présentent leurs résultats de façon discrète et non corrélée.

La langue électronique « modèle » fabriquée était initialement conçue pour la différentiation de protéines interagissant avec les héparanes sulfates. Néanmoins, au cours de ces travaux, sa capacité de discrimination a été évaluée non seulement pour l'analyse de protéines pures ou des mélanges de protéines, mais également pour l'analyse de mélanges complexes. La langue électronique développée offre également d'autres fonctionnalités. D'un coté, elle peut mimer les capacités de reconnaissance des l'héparanes sulfates. Ceci peut être utile pour une meilleure compréhension de la nature des interactions héparane sulfate-protéine. D'un autre coté, elle peut être utilisée en tant qu'outil de criblage de surfaces combinatoires possédant des propriétés bioactives, utiles à la fabrication de nanovecteurs biomimétiques qui ciblent de manière spécifique des protéines d'intérêt thérapeutique.

Project Background and State of the Art

Sensory systems of living organisms are responsible for generating an internal representation of the outside world. They are capable of perceiving and analyzing stimuli, and hence, they can induce consequent reactions towards them. Taste and smell, the two chemical senses of the human being, enable people to interact with the chemistry around and contribute critically to their experience of the environment, from the pleasure of eating food to the formation of childhood memories. Despite this, research into chemical sensing historically took a back seat to vision, audition and touch, challenged by the complexities of indefinable stimuli that are often not even consciously processed, and by difficulties in understanding even basic mechanisms of transduction and representation. It was not before 1991, when Buck and Axel [1] identified the genes of odorant receptors (ORs), throwing some light on the issue and launching chemical sensing research to the forefront.

Nature has always been the principal source of inspiration for human technological research and development. Therefore, intelligent sensing machines acquire and process signals in a very similar way as living organisms (Figure 1.1). For this reason, understanding the mechanisms through which humans and other animals interact with the chemistry of the environment is highly interesting for the development of new generations of chemical sensors.

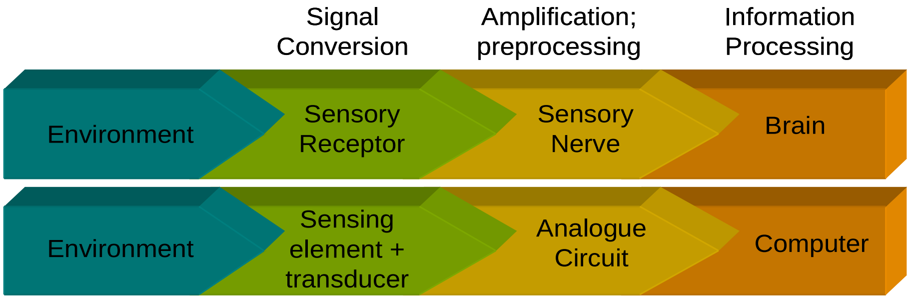

Figure 1.1. Similarities between signal processing in living organisms and intelligent machines.

Human taste is made up just of a handful type of sensations that researchers have agreed on at least five: sweet, umami, bitter, salt and sour tastes [2]. Although this repertoire may seem modest, it has satisfactorily covered the evolutionary need for an effective and reliable platform to help recognize and distinguish key dietary components [3].

In the case of smell, odors are made up of mixtures of baic odorants. However, the olfactory system shows a much more impressive discrimination power than the gustatory. It is not only able to detect thousands of different odorants, but also participates in a large part of what we call flavour [4]. The sense of taste detects if the eaten substance is sweet, sour, bitter, umami or salty, but it is thanks to the complexity of the sense of smell that we are able to identify the combination of sensations that leads to flavour.

This introduction will reveal the way the sense of smell works in humans and what are the important features that have inspired the development of alternatives to classical sensing approaches. Afterwards, the work will be focused on smell sense-based sensors applied to liquid and gaseous sample analysis, making a special focus on their application to the analysis of proteins.

1.1. Human sense of smell: a source of inspiration

The sense of smell is mediated by the olfactory system, a system that is characterized by exquisite sensitivity and discriminatory power. It is estimated that the humans can sense as many as 10.000 to 100.000 chemicals as having distinct odors. All of these odorants are small, volatile molecules. However, they have diverse structures and somehow those different structures are perceived as having different odors.

Odorants are initially detected by olfactory sensory neurons, which are located in the olfactory epithelium lining the nasal cavity (Figure 1.2). These neurons transmit signals to the olfactory bulb of the brain, which then relays those signals to the olfactory cortex. From there, olfactory information is sent to a number of other brain areas [5]. These include higher cortical areas, thought to be involved in odor discrimination, as well as deep limbic areas of the brain which are thought to mediate emotional and physiological effects of odors.

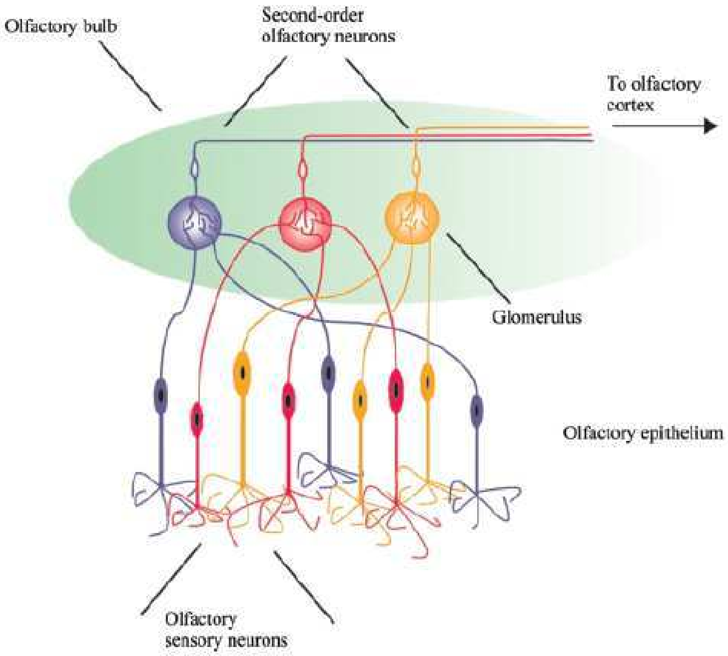

Figure 1.2. Vertebrate olfactory system. Odorants reach the olfactory epithelium in the nasal cavity and interact with odorant receptors (ORs) in the fine cilia of olfactory sensory neurons. The axons of the olfactory sensory neurons project to the olfactory bulb, where they synapse with the dendrites of the second-order neurons, which in turn project to the olfactory cortex. A schematic representation of 3 populations of olfactory sensory neurons, each expressing 1 different type of OR, is shown in different colors. The axons in the olfactory sensory neurons expressing the same type of OR converge to the same glomerulus in the olfactory bulb [6].

1.1.1. Odorant Receptors

In 2004, the Nobel Prize in Physiology or Medicine was awarded jointly to Richard Axel and Linda B. Buck (Figure 1.3) "for their discoveries of odorant receptors and the organization of the olfactory system". An overview of their work is reported in Linda Buck's Nobel Lecture [5] whose reading I highly recommend. The objective of the present work not being to enter into details of history and chronology of the discoveries made in this field, I will just take advantage of the efforts to unravel the sense of smell made by these two, as well as many other scientists, to make a small recapitulation of the present knowledge in the field. Understanding the key features of olfaction mechanisms is essential for understanding the principle of bioinspired sensors developed in the last few decades.

Figure 1.3. The Nobel Prize laureates in Physiology or Medicine 2004: Richard Axel and Linda B. Buck for their discoveries on ORs and the organization of the olfactory system.

ORs are located at the membrane of cilia of olfactory sensory neurons. They belong to the superfamily of G protein-coupled receptors and have the same general structure with seven hydrophobic membrane-spanning regions. They differ in their amino acid sequence, especially in the third, fourth and fifth transmembrane regions, which may form the ligand-binding pocket of odorant molecules (Figure 1.4) [7, 8]. Studies indicate that humans have about 350 different ORs and mice have about 1000 [5].

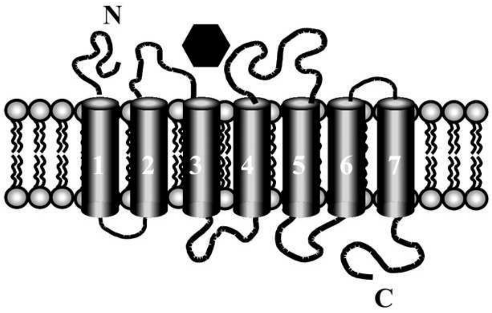

Figure 1.4. General structure corresponding to the superfamily of G protein-coupled receptors. [6]

The binding of odorants to ORs in the cilia causes, via G protein activation of adenyl cyclase, the production of a cyclic nucleotide, cAMP, which directly opens ionic channels in the plasma membrane (Figure 1.5) [6]. An inward transduction current is carried by Na^+ and Ca^{2+} ions. Olfactory sensory neurons maintain an unusually high intracellular concentration of Cl^- ions, and the increase in the internal concentration of Ca^{2+} causes the opening of Ca^{2+}-activated Cl^- channels that produce an efflux of Cl^- from the cilia, contributing to the olfactory neuron depolarization. The depolarization spreads passively to the dendrite and soma of the olfactory neuron, triggering action potentials that propagate along the axon to the olfactory bulb [9].

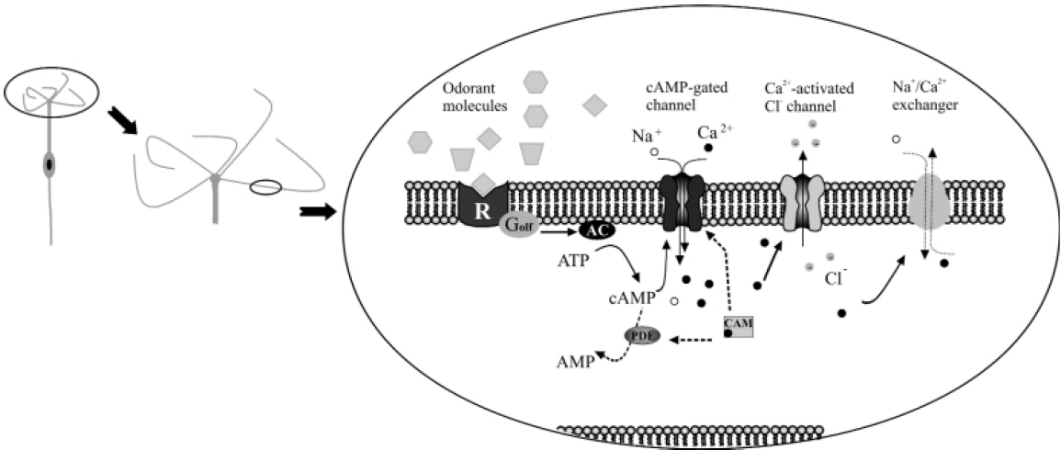

Figure 1.5. Olfactory transduction takes place in the cilia of the olfactory sensory neurons. Odorant molecules bind to ORs and trigger the transduction of the signal. [6]

The discovery of ORs not only explains how the olfactory system detects a vast array of chemicals in the external world, but also provides a set of molecular tools to explore how the nervous system translates chemical structures into odor perception. The first thing studied was how information from different ORs is organized in the olfactory epithelium. The studies provided two important findings:

- First, input from one type of OR is highly distributed in the epithelium. Therefore, neurons with receptors for one odorant are interspersed with neurons that have receptors for another odorant.
- Second, each neuron expresses only one OR gene, thus, the information that each neuron transmits to the brain is derived from a single receptor type.

1.1.2. Combinatorial Receptor Codes for Odors

Later studies were devoted to understanding how the OR family encodes the identities of different odorants [10]. This was made by exposing mouse olfactory neurons to four different classes of linear aliphatic odorants (19 in total) with different functional groups and carbon chains ranging in length from four to nine carbon atoms. Each neuron was imaged as it was exposed sequentially to different odorants. In response to odorants; olfactory neurons exhibited transient increase in intracellular calcium that could be detected by calcium imaging. If a response was seen, the neuron was retested with a lower concentration of the same odorant. Figure 1.6 shows the response profiles of 14 neurons, and therefore the recognition properties of the ORs expressed in those neurons.

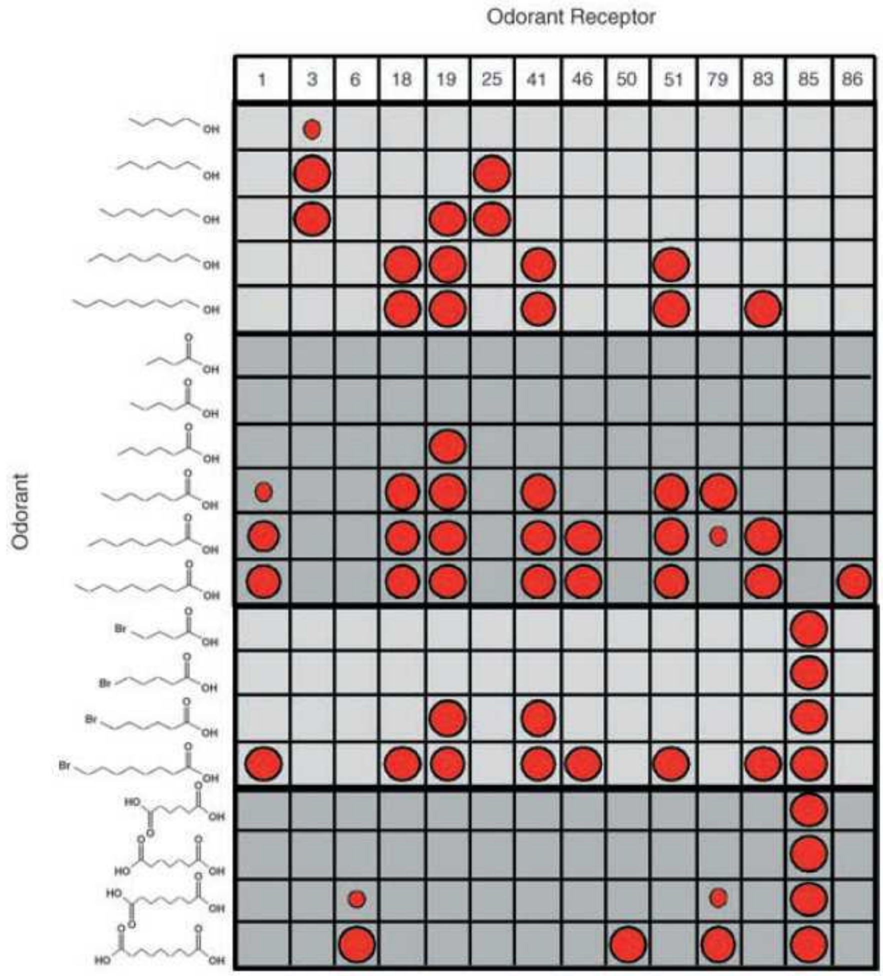

Figure 1.6. ORs were used combinatorially to detect odorants and encode their identities. The recognition profiles of individual ORs to a series of odorants were determined by calcium imaging and single-cell RT-PCR. The size of the circles reflects response intensity [5].

Based on the obtained data, three key conclusions were made:

1- Each OR can recognize multiple odorants.

2- Each odorant can be detected by multiple different ORs.

3- Different odorants are recognized by different combinations of ORs.

ORs are thus used combinatorially to encode odor identities. Different odors are detected and thereby encoded by different combinations of ORs, as illustrated in Figure 1.7. Given the number of combinations of 1000 different ORs, this combinatorial coding scheme should allow the discrimination of an almost unlimited number of odorants. Studies also showed that a change in the concentration of an odorant can also change its receptor code. This may explain why changing the concentration of an odorant can alter its perceived odor.

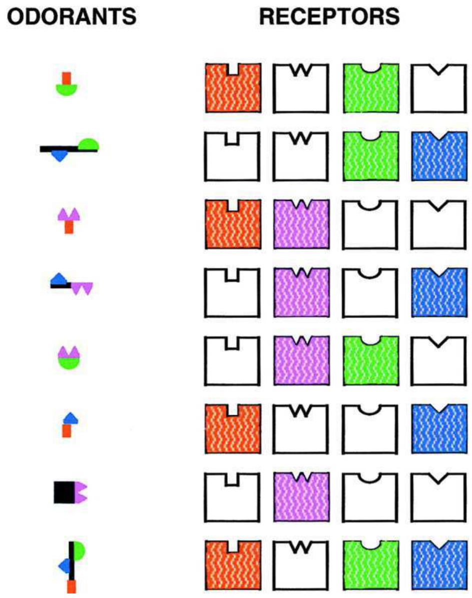

Figure 1.7. Combinatorial receptor codes for odorants. In this model proposed by Linda Buck [10], the receptors shown in color are those that recognize the odorant on the left. The identities of different odorants are encoded by different combinations of receptors. However, each receptor can serve as one component of the combinatorial receptor code for many odorants.

1.2. Bioinspired arrays of sensors

1.2.1. Electronic noses and electronic tongues

The superb performance of biological olfactory systems in odor detection, identification, tracking, and location tasks has inspired an alternative to traditional selective chemosensing techniques: the use of cross-reactive or differential sensor arrays. Named after their source of inspiration, these alternative systems are commonly designated as artificial or electronic noses (e-noses) and tongues (e-tongues), but can also be found under the appellation mechanical noses, odor sensors, cross-reactive sensor arrays, differential sensor arrays or pattern-based sensors.

In this alternative sensor architecture, the strict “lock-and-key” design criterion of traditional sensing devices is abandoned. Instead, an array of differential receptors is used. In an analogue way to the previously described ORs (the source of inspiration of this approach) cross reactive sensors possess three key features:

1- Each receptor can recognize multiple analytes.
2- Each analyte can be detected by multiple different receptors.
3- Different analytes are recognized by different combinations of receptors.

As the elements of such an array do not need to be individually specific and highly selective toward any given analyte, sensor design becomes an easier task. Instead, sensors for e-noses/tongues should possess stable analytical behavior, the collection of sensors should contain as much chemical diversity as possible in order to target the largest possible cross-section of analytes, and sensors should have high cross-reactivity, which is considered as the reactivity towards several components of the solution analyzed at the time. There are many terms describing the very same effect as cross-reactivity that are used as synonyms, like unselectivity, cross-sensitivity, low selectivity, partial specificity and even global selectivity. [11].

In this design, as it happens for the olfactory system, identification of an analyte cannot be accomplished from the response of a single sensor element. Instead, the distinct pattern of responses produced over the collection of cross-reactive receptors (also called differential receptors) in the array allows classification and identification of the analyte, which is called pattern recognition. This can be applied both when the sample contains a single analyte and when it contains multiple analytes, see Figure 1.8. One of the main advantages of this approach is that it can yield responses to a variety of different analytes, including those for which the array was not necessarily originally designed to detect [12, 13].

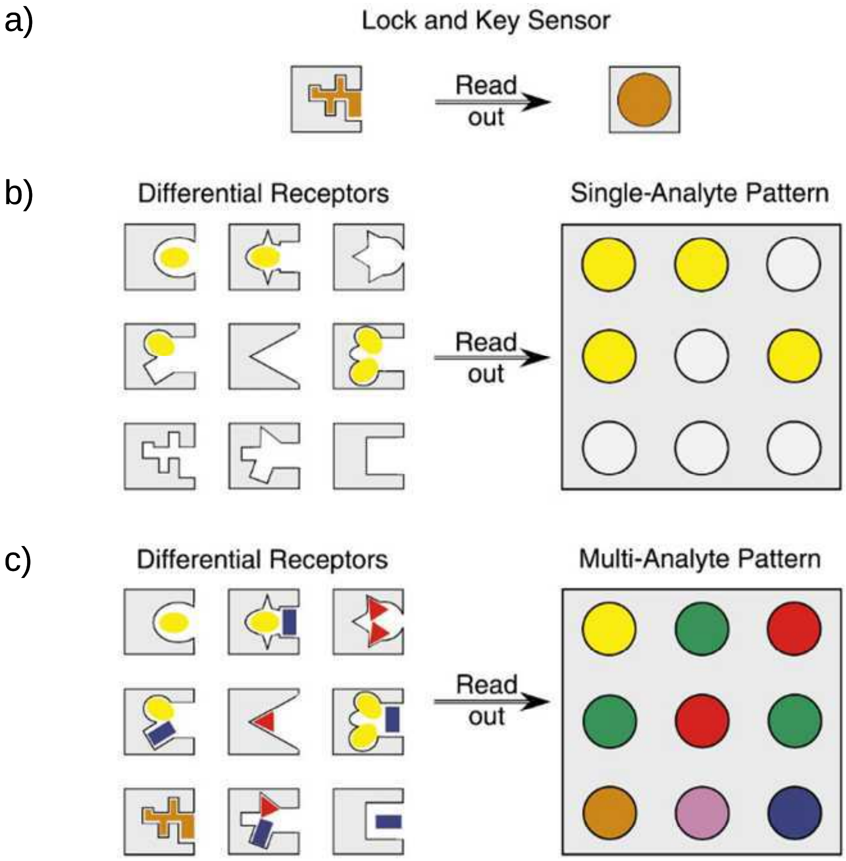

Figure 1.8. Schematic representation of host-guest interactions. a) A specific binding event (lock-to-key paradigm) which exhibits a large degree of complementarity between the host and the guest. b) An array of cross-reactive/differential receptors interacting with one analyte. The identification results from the pattern of responses obtained from the entire array. c) An array of cross-reactive/differential receptors interacting with a complex sample. The identification results from the pattern of responses obtained from the entire array [13].

The difference between electronic noses and electronic tongues

Although mainly inspired by the sense of smell, this approach can be applied both to the analysis of gaseous samples and liquid samples, differentiated by the terms “electronic nose” in the case of gaseous media analysis and “electronic tongue” in the case of liquid media analysis.

The e-tongue system can thus, be defined as an analytical device comprising an array/set of chemical sensors with not very high selectivities, exhibiting reactivity towards several components of the analyzed solution simultaneously (cross-reactivity), in which the appropriate multivariate methods are used for processing of the data [14].

The e-nose, similarly, is defined as an instrument which comprises an array of chemical sensors with partial specificity and an appropriate pattern recognition system for processing the data [15].

Such systems, often associated with an adequate calibration/learning method are suitable for recognition (identification, classification) of various liquid and gaseous media and multicomponent quantitative analysis of organic and inorganic compounds.

The difference between electronic tongues and taste sensors

Sometimes in the literature the reader can find ambiguities with respect to the differences between an e-tongue and a taste sensor. The origin of this ambiguity is the existence of devices which are not clearly classified in one or the other class and the similarity of the samples studied with both devices. However, the fundamental concepts of the taste sensor and the e-tongue are different.

The taste sensor, also called taste system or taste chip, is designed in such a way that it responds to taste chemical substances and can be used to quantify the taste of foods on the basis of the five basic tastes of the tongue (see Figure 1.9). Toko's group, for instance, works on the development of lipid/polymer membranes that respond specifically to sodium chloride (salty), hydrochloric acid (sour), monosodium glutamate (umami), and quinine hydrochloride (bitter) molecules to assess the taste of analyzed substances [16]. Taste sensors find, thus, applications in the cosmetic, perfume, pharmaceutical and food industries for instance, to quantify bitterness of drinks or dissolved compounds, or to quantify taste masking efficiency of formulations in the pharmacological domain.

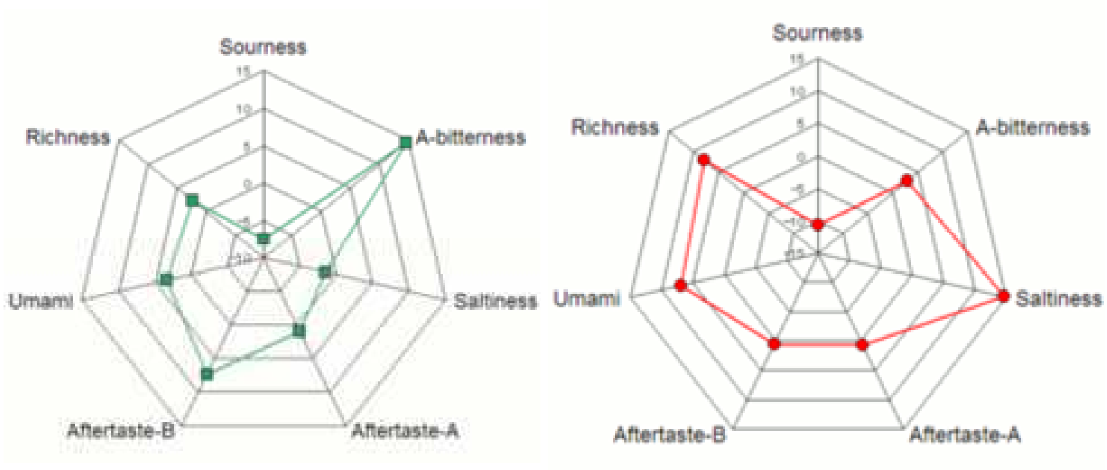

Figure 1.9. Results issue of a taste sensor. The shape of the displayed data gives the user an idea of the taste of beer (in green) and soy sauce (in red). From reference [17]

On the other hand, e-tongues aim to discriminate and analyze samples using sensor arrays with different specificity properties coupled to a statistical analysis. The application domains of e-tongues are much broader than taste quantification based on the five basic tastes. They can be used for analysis of some other quality property of the sample, not necessarily applicable to the taste sensation of humans [18].

1.2.2. Potential applications of electronic noses and tongues

E-noses and e-tongues find potential applications in all the areas where routine analysis are needed and, thus, they attract the interest of experts in many fields; from biomedical and pharmaceutical industries, environment monitoring, food industry, and energy engineering, to artificial intelligence.

Monitoring industrial processes, for instance, controlling the quality of industrial waste water is one of the applications found for these devices. Gutes *et al*. employed a voltammetric e-tongue to the characterization of wastewater coming from the paper mill industry [19]. Kranz-Ruckler *et al*. were able to monitor the process of a drinking water production plant, see Figure 1.10 [20]. Concretely, they were able to differentiate the water at the different stages of the cleaning process.

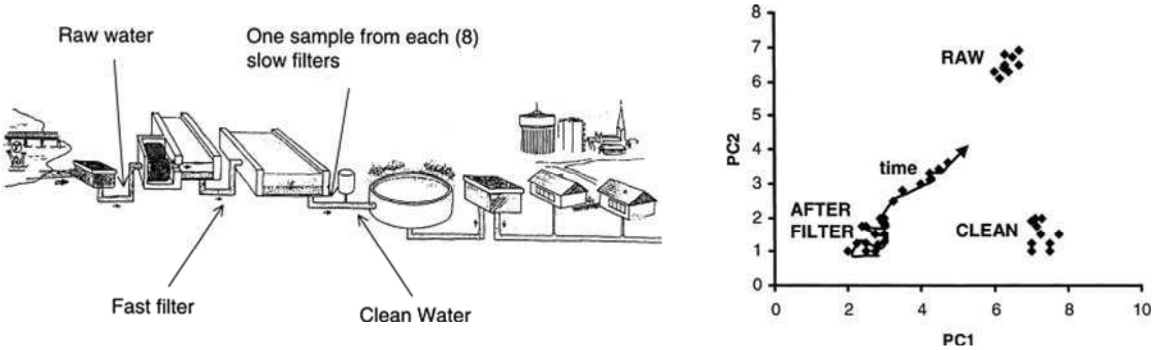

Figure 1.10. Schematic of a drinking water production plant (arrows indicate sampling points) and principal component analysis showing different clusters for samples taken at different stages of the cleaning process. The raw, untreated water was cleaned and transported to a filter where all the firm particles were removed. After, there was a slow filter, where the water was cleaned biologically from germs and flavors. Finally, chloride and sodium hydroxide were added to the water to kill germs and to adjust the pH value. The cleaned water was stored in a reservoir before transported out to the distribution net for fresh water. From reference [20].

Along the same lines, several applications of e-noses and tongues are related to environmental protection, concretely to toxic and pollutant monitoring and air quality control [21]. Some companies propose commercial devices for air quality and odor control. Odowatch for instance, is a patented e-nose from Odotech, an American environmental company specialized in the measurement and monitoring of odors at waste water treatment plants, composting sites, landfills, rendering plants and industrial odor producing plants. The Odowatch devices are positioned near the odor sources on a site and they communicate with each other over a wireless network. The analysis of the obtained data and other parameters generates a map of the real-time odor plume, overlaid on a map of the site and the surrounding area (see Figure 1.11).

Figure 1.11. Odor map generated by the Odowatch device.

Due to their capacity to monitor air contaminants and control air quality, e-noses are also currently studied by the NASA as a way to ensure the health and safety of the astronauts, as well as equipment integrity inside the International Space Station (see Figure 1.12) [22, 23].

Figure 1.12. Illustration of the electronic nose (e-nose) device that was integrated in the International Space Station.

The use of e-nose/tongue devices for the systematic quality control of liquids could serve as a way to check batch to batch consistency, to detect contamination, spoilage or adulteration of products and to monitor storage conditions. This is interesting for biomedical applications such as haemodialysis control [24], and also for an enormous variety of applications in food processing and quality control. These include process monitoring (fermentation monitoring [25]), authenticity assessment, foodstuff recognition, quantitative analysis, or freshness evaluation and shelf-life investigation. [26-28]. For illustration, El Babri *et al.* employed a portable e-nose system to classify the states of freshness of Moroccan sardine samples stored at 4 °C, as it can be seen in the PCA score plot in Figure 1.13[29] .

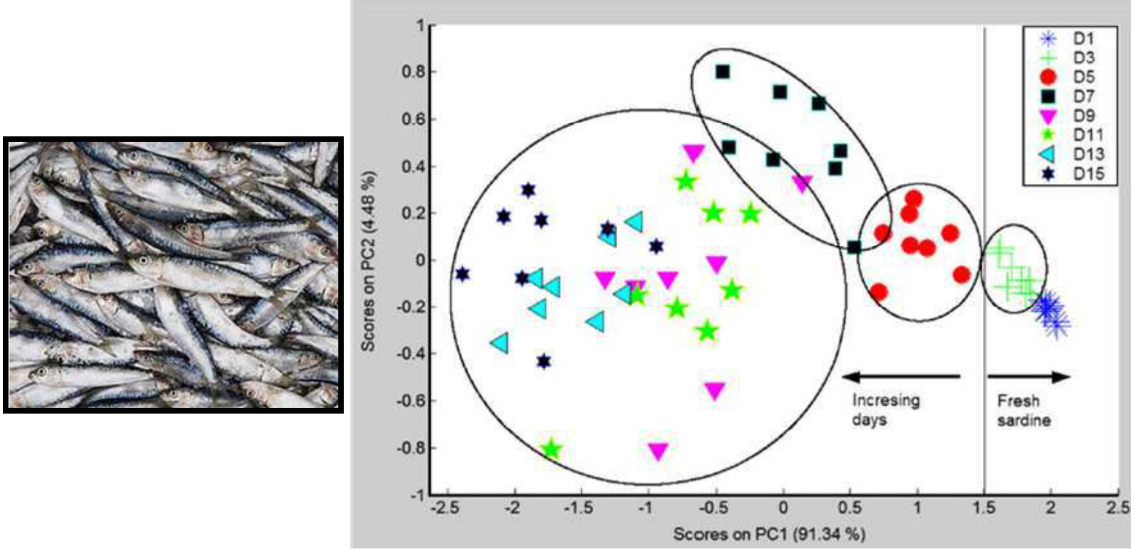

Figure 1.13. Sardines from Morocco and PCA score plot on sardine data using a 6-element gas sensor array.

The ability of the e-noses to detect not only odors but also odorless chemicals makes them ideal for use for crime prevention and security purposes, such as drug odor detection despite of the presence of other masking odors capable of confusing police dogs. It may also be used as a bomb detection method in airports. Through careful placement of several e-noses and effective computer systems, it is expected to locate bombs within a few meters of their position in less than a few seconds. Woodka *et al*. developed an e-tongue system consisting on a fluorescent polymer sensor array which showed an excellent ability to discriminate between explosives and explosive related compounds in aqueous solution with a low false alarm rate [30].

More recently, it has been demonstrated that the e-noses/tongues can be applied for medical diagnosis [31, 32]. Human exhaled breath consists of numerous volatile compounds, which can provide information on a patient’s physical condition, such as infections, intoxications, or metabolic diseases and can be used as biomarkers. Professor Haick has developed an e-nose by analyzing exhaled air of patients, which has been successfully used to diagnose different cancers including lung cancer at a very early stage with 95% reliability. In the future they expect to assess the exact stage of the disease during treatment and to adjust the treatment [33].

1.2.3. Development perspectives for electronic noses and tongues

The outlook for the development of e-nose and tongue devices is highly positive and promising. Important research centers like IBM have expert scientists working in computer development who predict that in five years, computers and smart phones will integrate the senses of smell and taste [34]. This, together with the interest that e-noses and e-tongues present for other multiple applications, has made these devices a subject of increasing interest in the scientific community, as it is reflected by the increasing number of publications in this area over the past 20 years (see Figure 1.14 and Figure 1.15) as well as by different important international conferences like ISOEN

(International Symposium on Olfaction and Electronic Nose) dedicated to the development of e-nose and tongue systems and ISOT (The International Symposium on Olfaction and Taste).

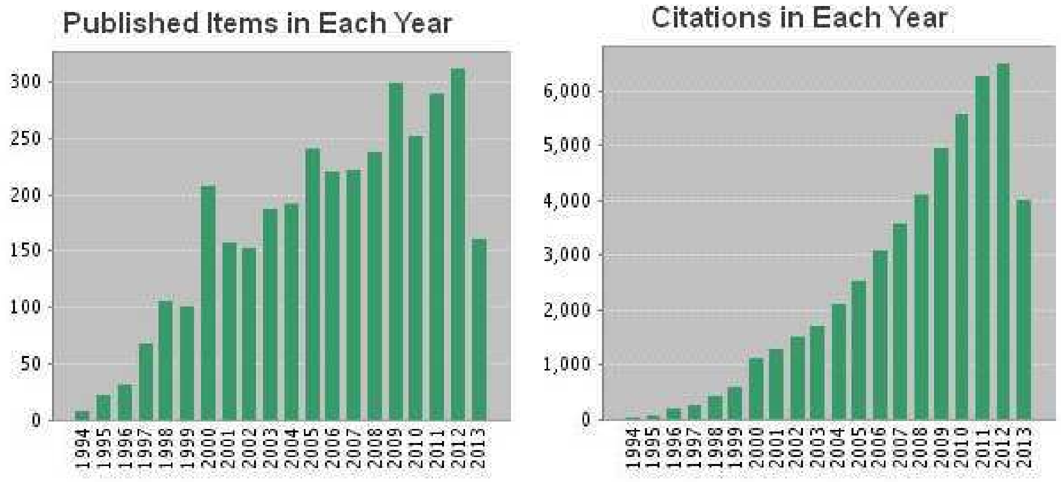

Figure 1.14. Publications found using the key word “electronic nose”. On the left, published items in each year since 1994 and on the right, citations in each year. Source: Web of Science ®, July 2013.

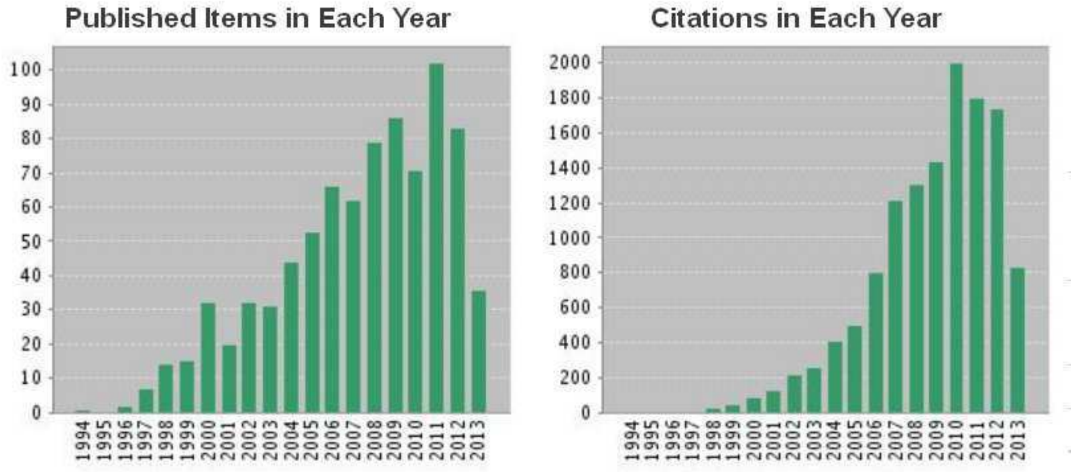

Figure 1.15. Publications found using the key word “electronic tongue”. On the left, published items in each year since 1994 and on the right, citations in each year. Source: Web of Science ®, July 2013.

1.3. State of the art on electronic noses and tongues

In general, biosensors and chemical sensors are composed of three parts: a sensing element that interacts with the analyte, a transducer that is able to convert the interaction into a measurable signal, and a signal processing system; see Figure 1.16. In a similar way, e-noses and e-tongues are also composed of these three parts.

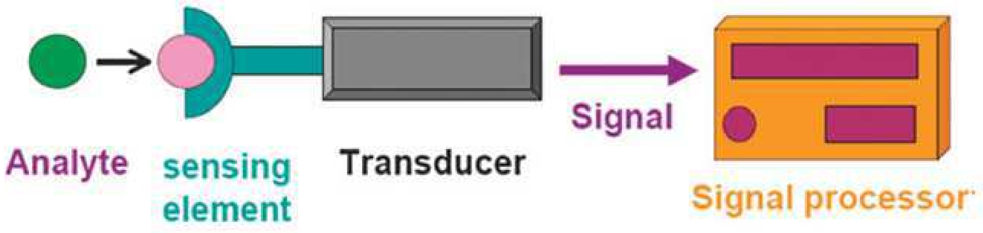

Figure 1.16. Main components of a biosensor and chemical sensor.

Herein we present a review of the literature on the principal research carried out in the domain of e-noses and e-tongues, classified by the transduction method employed. Some transduction methods have been mostly developed for e-nose applications while some others have been found more interesting for e-tongue applications.

1.3.1. Electronic noses and tongues based on electrochemical transduction

Electrochemical is definitely the most developed transduction system both for e-noses and tongues. Most examples of e-noses classified in this section are based on conducting polymers and metal oxide semiconductors (MOS), as well as the small MOSFET devices. E-tongues, on the other hand, have been classically based on potentiometric sensor electrodes and find their miniaturized version in ChemFET devices.

a) Chemoresisitive/conductivity sensors

Chemoresistive/conductivity sensor-based devices have been developed mainly in the frame of gaseous analysis. They work on the principle that a change in some property of the material resulting from interaction with a gas/odor leads to a change in resistance in the sensor. The mechanisms that lead to resistance changes are different for each material type; however, the structure and layout of conductivity sensors prepared using these materials are essentially the same. A scheme of a typical conductivity sensor design is shown in Figure 1.17. Two types of materials have been mainly developed for such devices: conducting polymers and metal oxide semiconductors.

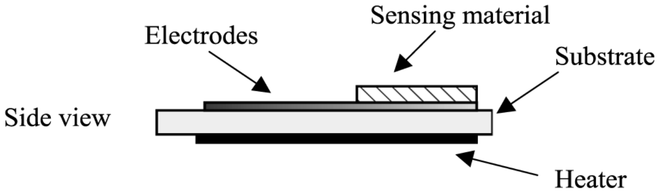

Figure 1.17. Typical structure of a chemoresistive/conductivity sensor. [35]

Conducting polymers are widely used for odor sensing in the form of arrays. The interaction with volatile compounds affects several properties of conducting polymers such as conductivity, work function, optical absorption spectra and others. Among these, conductivity variations, which can be easily detected, are a linear function of the analyte concentration and are therefore often used as actual signals in conducting polymer-based e-noses. Since all these changes are largely reversible, interactions between the polymer and the volatile chemical are supposed to be weak [36]. Main drawbacks of these sensors are their sensitivity to temperature changes, that result in expansion/contraction and thus in resistance changes and their chemical instability face to strong oxidizers such as chlorine and ozone.

Wilson *et al*. developed an e-nose which was able to characterize the aroma profiles of volatiles released from excised woody samples. The instrument measured electrical-resistance changes generated by adsorption of volatiles to the surface of electroactive, polymer-coated sensors. Unique digital electronic fingerprints of wood aromas, derived from multisensor-responses to distinct mixtures of wood volatiles, were obtained from woods of individual tree species. A reference library containing aroma signature patterns for 23 tree species was constructed for identifications of unknown samples using pattern-recognition algorithms [37].

Another basic choice of sensors is metal-oxide semiconductor sensors (illustrated in Figure 1.18), which are the most commercially extended ones. Certain metal-oxides behave as semiconductors at high temperatures. MOS sensors are designed as having a heater element and a sensor element (sintered metal-oxide with or without catalyst). Both elements are separated by a very thin isolating membrane. Redox-reactions occurring at the sensor surface result in changes in resistance which can be measured. These redox-reactions depend on the nature of the metal-oxide/catalyst, the reacting gases, and the temperature.

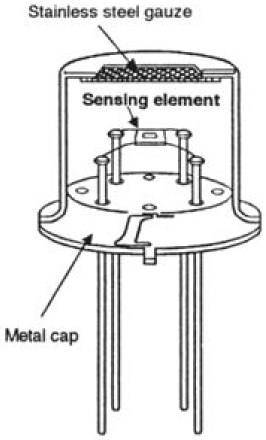

Figure 1.18. Illustration of a MOS sensor.

The Odowatch commercial e-nose mentioned previously is based on the use of MOS. The gas sensors used in the gas detection chamber are differently doped SnO_2-type sensors. Large number of sensors (15 for example) enable the device to sense given classes of odorant gases that are perceived by the human nose: alcohols, aldehydes and ketones (*e.g.* acetaldehyde), carboxylic acids and fatty acids (*e.g.* butyric acid), amines (including NH_3, $R\bullet NH_2$, indole, methylamine, *etc*), sulfurous-compounds (including H_2S, DMS, DMDS, Mercaptans, *etc*.), aromatics (BTEX, terpenes, *etc*.) [17].

b) Potentiometric sensors

In 1985, the first system for liquid analysis based on a cross reactive receptor array, the first e-tongue, was presented by Otto and Thomas [38] and it was based on potentiometric sensors. Potentiometric sensors, and especially ion-selective electrodes (ISEs), see Figure 1.19, are the most commonly employed sensors for the development of e-tongues. The principle of operation of ion-selective electrodes is based on the measurement of their potential changes against a reference electrode in zero-current conditions. The potential of the ISE is a function of the activity of the ionic species in a sample solution and is formed in the ion-sensitive membrane, where the selective complexation (ion recognition) of the analyte molecule occurs. ISEs are considered good sensors for e-tongues since they can be considered broadly selective sensors; able to respond in varying degrees to other ions rather than specifically to a single ion. The main advantages of potentiometric sensors are a well-know working principle, the possibility of obtaining sensors selective to many various species, and the relative low cost. Nonetheless, they present some disadvantages like the temperature dependence and big size.

Most research in the field is devoted to the development of suitable electrodes. Semi-permeable membranes of various types have demonstrated varying degrees of selectivity and specificity suitable to be combined with pattern recognition techniques and have found an infinity of applications particularly in food analysis [39-41]. Solid-state potentiometric sensors have been reported for heavy metal ions [42], while chalcogenide glass membranes have been reported for food and environmental analysis [21, 43-45].

Figure 1.19. Photography of a potentiometric electronic tongue (e-tongue) composed of an array of ISEs. From reference [17].

c) Voltammetric Sensors

In contrast with potentiometric methods, voltammetric measurements are performed when equilibrium is not reached, and the signal obtained is the measure of the current as the potential is varied. The simplest measurement set-up employs three electrodes: reference, working and auxiliary electrodes, see Figure 1.20. The potential of the reference electrode is assumed to be constant and between the working and auxiliary electrodes the current flows. However, although very robust, as it happens for potentiometric electrodes, electrodes must be calibrated and cleaned regularly. Since 1997 [46], voltammetric e-tongues have been developed for several applications in industrial applications and in the food industry [47].

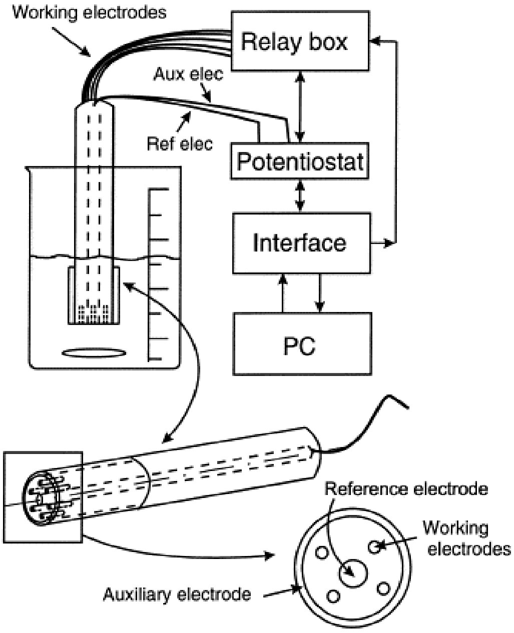

Figure 1.20. Common configuration of a voltammetric e-tongue with four working electrodes. From reference [47].

d) Field-effect transistors (FET)

Metal Oxide Semiconductor Field Effect Transistors (MOSFET) are also employed as sensors for e-noses. These transistors comprise three layers, a silicon semiconductor, a silicon oxide insulator and a catalytic metal (Pd, Pt, Ir, Rh) called the gate. This kind of transistors operates by means of three contacts, two of them allow the current in (source) and out (drain), and the third one acts as the gate and regulates the current through the transistor. The structure of a MOSFET sensor is given in Figure 1.21. Molecules interacting with the metal gate produce a change in the MOSFET signal that can then be interpreted by pattern recognition computer systems. Polymers have also been used as gate material for MOSFET devices, and are usually called PolFETs.

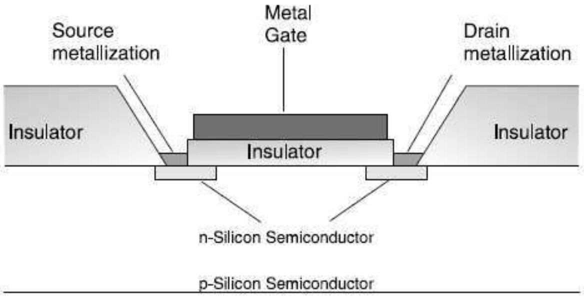

Figure 1.21. Schematic illustration of a MOSFET transistor.

The current leader in the area of MOSFET e-noses is the French company Alpha Mos, which develops e-noses like FOX or GEMINI, both based on MOSFET technology. They have also developed an e-tongue, called ASTREE. This e-tongue uses sensors based on the ChemFET (chemical field effect transistor) technology for liquid sample analysis; see Figure 1.22. ChemFET is a structural analogue of a MOSFET transistor, where the change on the gate electrode is produced by a chemical process. In this case, each sensor's gate has a specific organic membrane, which interacts with ionic and neutral chemical compounds present in the liquid sample in a specific manner. Any interaction at the membrane interface is detected by the sensor and converted into an electronic signal.

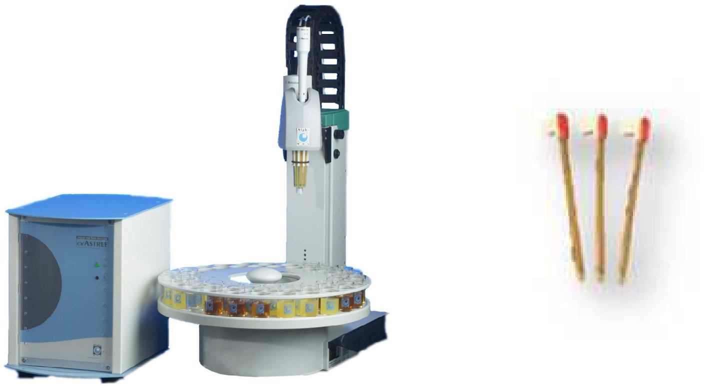

Figure 1.22. The ASTREE e--tongue system fabricated by Alpha Mos and the ChemFET employed for the measurements.

More recently, nanomaterials have been used in combination with FET to fabricate more sensitive e-nose devices. Goldsmith *et al*. immobilized mouse ORs on carbon nanotubes and succeeded in detecting a number of odorants based on FET, as shown in Figure 1.23 [48]. The idea of immobilizing ORs as sensing materials is not new and has already been widely studied by Pajot *et al* [49-52]. Park's group has integrated conducting polymer nanotubes, on which ORs were immobilized, into a FET platform and the field induced sensitivity derived from odorant recognition was observed even at a 10 fM concentration. [53, 54].

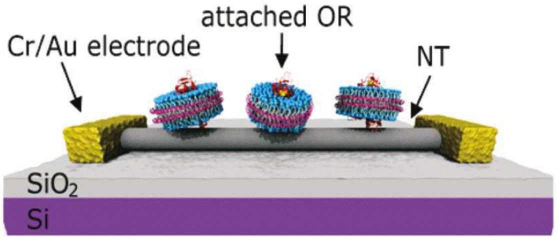

Figure 1.23. Scheme of a carbon nanotubes transistor functionalized with mouse ORs. From reference [48].

1.3.2. Electronic noses and tongues based on gravimetric transduction

In 1880, Jacques and Pierre Curie discovered that certain crystals generate an electrical potential proportional to an applied mechanical stress, termed the piezoelectric effect. Inversely, the converse piezoelectric effect, which is the basis of piezoelectric sensors, is a phenomenon in which when a voltage is applied across the piezoelectric quartz crystal the material oscillates at its resonance frequency [31]. There are two principal types of piezoelectric sensors: the surface acoustic wave (SAW) device and the quartz crystal microbalance (QCM). The main difference between them is that SAW device produces a surface wave that travels along the surface of the sensor, while the QCM produces a wave that travels through the bulk of the sensor. Both types of devices work on the principle that a change in the mass of the piezoelectric sensor coating due to analyte absorption results in a change in the resonant frequency.

a) Quartz Crystal Microbalance (QCM) Sensors

In a QCM, an increase on the mass of the sensitive material deposited on the surface of the crystal alters the resonant frequency of the quartz crystal and, this change in the resonant frequency, is therefore used for the detection of the analyte. The sensitive materials or chemically active surfaces employed for e-nose applications are usually polymers or modified polymers, see Figure 1.24. Micromachining is used to fabricate the QCM devices, which makes the fabrication of small sensor structures possible. [35] Arrays of this type of sensors can be used for both e-noses and tongues [55].

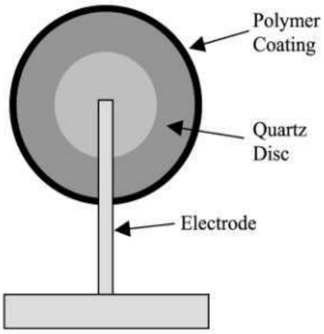

Figure 1.24. QCM sensor is composed of a quartz disc coated with the absorbing polymer layer and a set of gold electrodes evaporated onto either side of the polymer/quartz structure.

Di Natale *et al*. analyzed body odors by an e-nose composed of an array of seven quartz microbalance sensors, in which quartz was coated with different kinds of metalloporphyrins, used as sensing materials. To do that, they collected human body odors from a population of patients affected by different mental disorders and from a population of healthy people as reference controls. The response of the e-nose was detected in Hz when the surface of the sensor was exposed to body odors. The result of this experiment showed that body odor changes are so complex that none of the compounds could be regarded as a specific chemical marker of disease. Rather, a disease like schizophrenia could be diagnosed by analyzing their combination [56].

b) Surface Acoustic Wave Sensors

A SAW sensor also works on the principle of frequency shifts. The SAW device is composed of a piezoelectric substrate with an input (transmitting) and an output (receiving) transducer deposited on top of a substrate. The sensitive membrane is placed between the transducers (see Figure 1.25), and an electrical signal is applied across the input transducer creating an acoustic two-dimensional wave that propagates along the surface of the crystal. SAW e-noses and tongues have been applied in fields like food industry [57] or household appliance industry [58], amongst others.

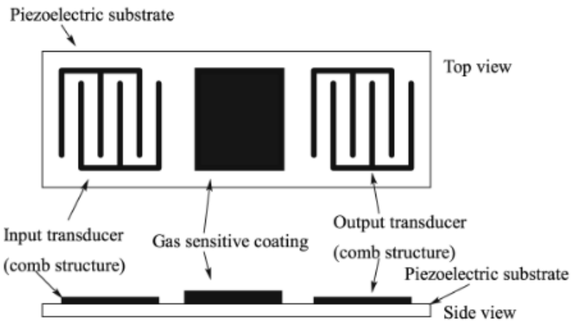

Figure 1.25. Structure of a SAW sensor [35].

c) Micromecanical Sensors

Alternative devices proposed for e-nose/tongue applications are microelectromechanical systems (MEMS) and nanoelectromechanical systems (NEMS) which find their application mainly in e-nose applications [59-61] although some examples of e-tongue applications can be found [62]. The classical design for these applications is the use of an array of cantilever sensors [63], see Figure 1.26a [59]. The cantilevers are individually coated, and transform the physical and chemical reactions of the analyte with the sensor layers to a mechanical response. The cantilevers are optically read out by recording the position of an incident light spot reflected off the cantilever's apex by using a position-sensitive detector, as shown in Figure 1.26b.

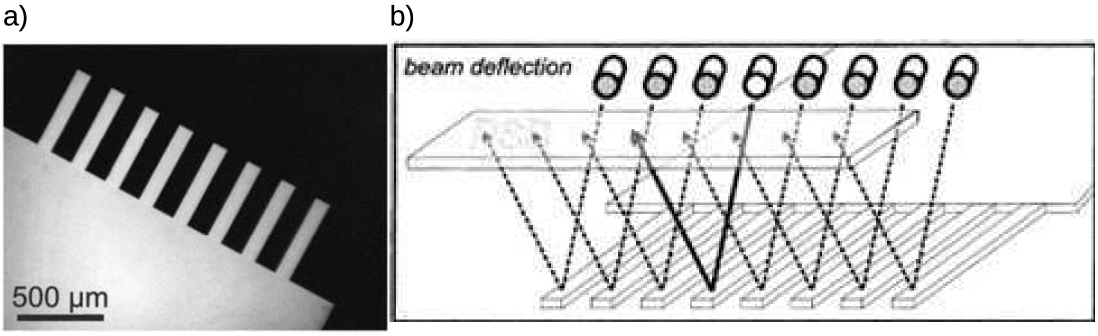

Figure 1.26. E-nose developed by Lang *et al*. a) The cantilever sensor array. b) Beam deflection technique to read out the cantilever bending using a position-sensitive detector. [59]

Apix Technology, a start-up founded by Leti and Caltech in 2011, is developing multi-gas emissions analyzers based on combination of miniaturization of gas-phase chromatography and NEMS sensors. Targeted applications include gas analysis for industrial processing in the petrochemical and natural gas distribution industries, analysis of ambient air quality, as well as medical diagnosis through the analysis of biomarkers in a patient's breath.

1.3.3. Electronic "noses" and "tongues" based on optical transduction

Despite optical transduction is not very extended in the case of gas sensing, some examples can be found, for instance, the use of optical fiber sensors [35]. In contrast, optical transduction for e-tongue-type applications is quite extended and diverse. Even if these type of systems, also known as cross-reactive sensor arrays, have not still been explored as much as electrochemical ones, they appear to be specially popular for biological sample analysis applications [64].

The most popular optical detection method is the colorimetry/fluorimetry. Professor Eric V. Anslyn is a pioneer in the field of cross-reactive receptor array development for molecular recognition coupled with optical transduction systems. In 1998, his group developed an e-tongue taking advantage of the advances in micromachining techniques at the time and efficient charge-coupled devices (CCDs) [65]. Poly-(ethylene glycol)-polystyrene resin beads derivatized with a variety of indicators were deposited in micromachined wells (see Figure 1.27) and the absorption property changes upon analyte exposure were measured with a CCD camera. A further improvement of this system was the addition of temporal dimension to the measurements to follow the kinetics of the binding [66]. They developed several resin-bound synthetic receptors with functionalities targeted toward certain analyte classes, leading to customizable differential sensor arrays. Studies made by this system include recognition and discrimination of nucleotide phosphates, tripeptides, tripeptide mixtures, proteins and glycoproteins. A variation of this system was the derivatization of the core of the beads with a colorimetric indicator and the periphery with metal ligands. This variation was used for making pattern responses of various metallic cations [67].

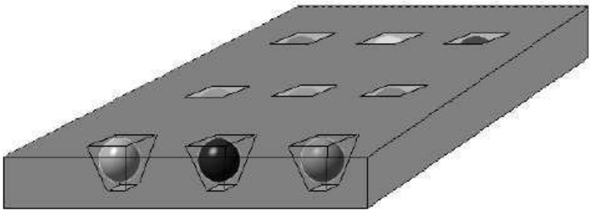

Figure 1.27. Multicomponent sensor array on a silicon chip used for e-tongue system by Anslyn's group. [13]

Also for metal ion determination, arrays of unselective indicators arranged in a micro titer plate [68], and fluorescent self-assembled monolayers [69] have been used.

The response of a molecularly imprinted polymer (MIP) array can also be coupled to an optical, colorimetric response, using a dye displacement strategy. MIPs are highly crosslinked polymer matrices developed in the presence of a template analyte molecule. After templating, the analyte molecule is removed leaving a binding cavity functionally suitable to the target analyte [70, 71].

Moreover, porphyrins and metalloporphyrins can be used in both fluorescent and colorimetric signaling arrays by measuring fluorescence quenching of the receptors upon interaction with the analytes. Both are readily modifiable, stable and have large surface areas for binding. Kenneth S. Suslick has exploited these molecules, as well as other dyes, for making patterns of organic molecules in water, as well as common drinks [72-74]. In Figure 1.28, we show the results obtained by this group for beer discrimination. These sensing molecules were also employed by Hamilton *et al.* for the differentiation of proteins, as it will be described later [75, 76].

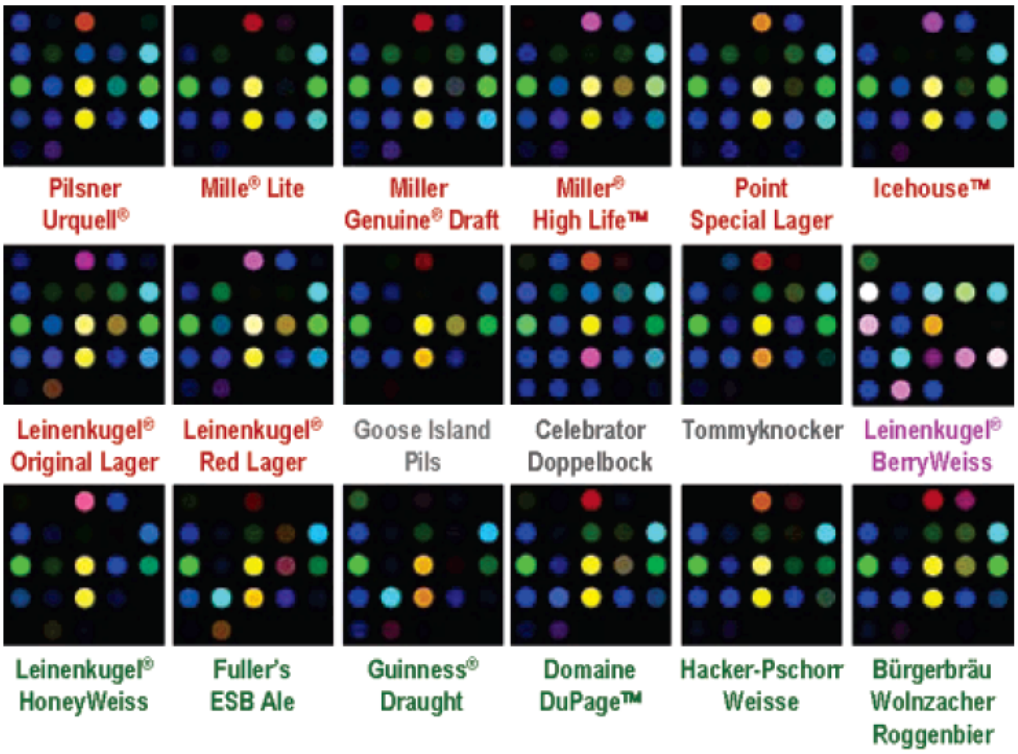

Figure 1.28. Patterns of 18 commercial beers for their discrimination obtained with the system developed by Suslick. [74]

Other tailored biomolecules that have also been used as cross-reactive receptors in colorimetric/fluorescence devices include three-way junctions [77], gold nanoparticle-fluorophore complexes [78], aptamers [79, 80], metal-dye complexes [81, 82] and fluorescent dyes embedded in a hydrogel matrix [83]. One example is given here. By using a hydrogel-based fluorescent micro array containing different combinations of eight dyes, researchers succeeded in the differentiation of common alcoholic beverages like white wine, German and Indian beer, dry wine or vodka. The remarkable advantage of this design is the use of combination of dyes for obtaining a wider diversity of cross-reactive receptors in an easy way (see Figure 1.29).

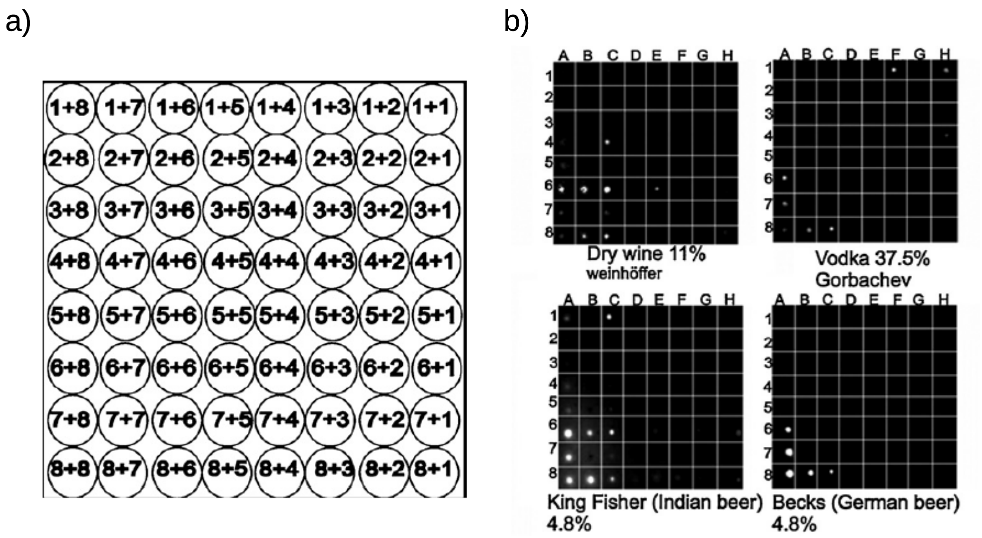

1+8	1+7	1+6	1+5	1+4	1+3	1+2	1+1
2+8	2+7	2+6	2+5	2+4	2+3	2+2	2+1
3+8	3+7	3+6	3+5	3+4	3+3	3+2	3+1
4+8	4+7	4+6	4+5	4+4	4+3	4+2	4+1
5+8	5+7	5+6	5+5	5+4	5+3	5+2	5+1
6+8	6+7	6+6	6+5	6+4	6+3	6+2	6+1
7+8	7+7	7+6	7+5	7+4	7+3	7+2	7+1
8+8	8+7	8+6	8+5	8+4	8+3	8+2	8+1

Figure 1.29. a) Map of the 64 micro spots produced from eight different dyes, by binary combination. b) Array responses for some alcoholic beverages. Reference mage subtraction was used to visualize the spot pattern differences [83].

1.4. Electronic noses and tongues based on optical detection for protein recognition

The identification of protein species and quantification of their concentrations are important processes and have many applications in proteomics, medical diagnosis and pathophysiological studies, including the detection of toxic pathogens. Traditional methods for the identification and quantification of proteins include generally protein separation in a first step and then identification and quantification, for example, using combination of electrophoresis/mass spectroscopy or liquid chromatography/mass spectroscopy. These procedures are often tedious and time-consuming. Besides, protein-detecting arrays remain under-developed due to the lack of highly selective and specific binding agents that interact with proteins through complementary interactions (aptamers, antibodies, mimetics...). Currently, antibodies are the most used type of such ligands, but their application is limited by difficult preparation procedures and by their instability.

These are the reasons why enormous effort has been made in searching for alternative protein binders that, similar to antibodies, could recognize protein surfaces. In this context, about ten years ago the e-tongue approach revolutionized protein recognition methods. With the conviction that this alternative approach to antibody mimetics could circumvent difficulties associated with the design of potent and selective protein binders, many groups have developed methods for protein surface recognition that, when combined with pattern-based detection arrays, result in a novel class of diagnostic devices capable of high throughput protein identification and analysis. [84]. The most popular transduction method for this purpose is the optical one, permitting direct, simultaneous and real-time detection.

In optical protein sensing arrays, non-specific interactions between the receptors and proteins induce a change in the intensity of the signal generated by the receptors, leading to a unique optical fingerprint for each protein. Although visualization of the results is sometimes sufficient for differentiating between the proteins, in the case of classification of all the samples with a large set of data, some mathematical methods are usually applied, such as principal component analysis (PCA), as illustrated in Figure 1.30.

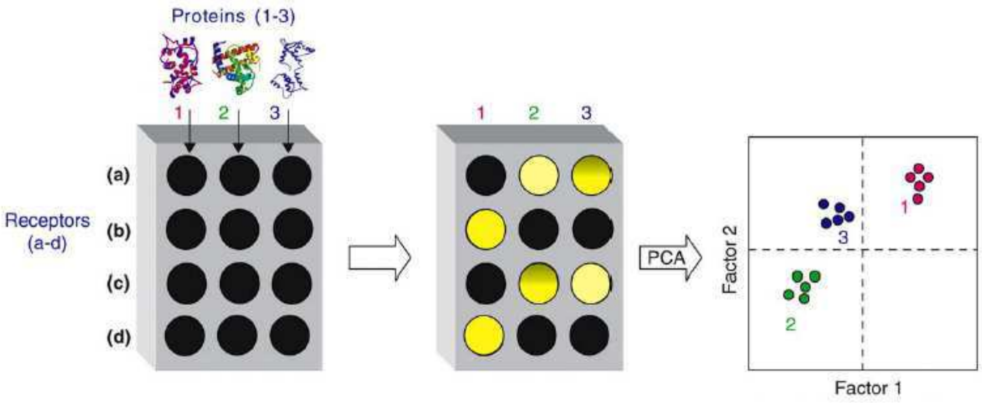

Figure 1.30. Simplified scheme for a protein sensing array in which each of the proteins (1-3) is incubated with each of the receptors (a-d). Non-specific interactions between the receptors and proteins induce a change in the receptors' signaling, resulting in unique optical fingerprints. PCA is used for classification purpose. [84]

There is a variety of systems that have been developed in the past few years proposing different approaches to protein sensing by varying sensing materials and optical detection methods. Herein, we describe the most relevant ones.

As mentioned in section 1.3.3., porphyrin and porphyrin derivatives are popular alternative to build differential receptors. Hamilton's group [75, 76] modified porphyrins with amino acids. The hydrophobic core of the porphyrin primarily contributes to binding affinity, and the periphery can be modified with a mixture of hydrophobic and hydrophilic groups to enhance selectivity towards different proteins. Labeling of sample proteins was not required since the recognition patterns were made thanks to the changes in fluorescence of the porphyrin receptors (Figure 1.31). This system was able to discriminate up to 10 proteins.

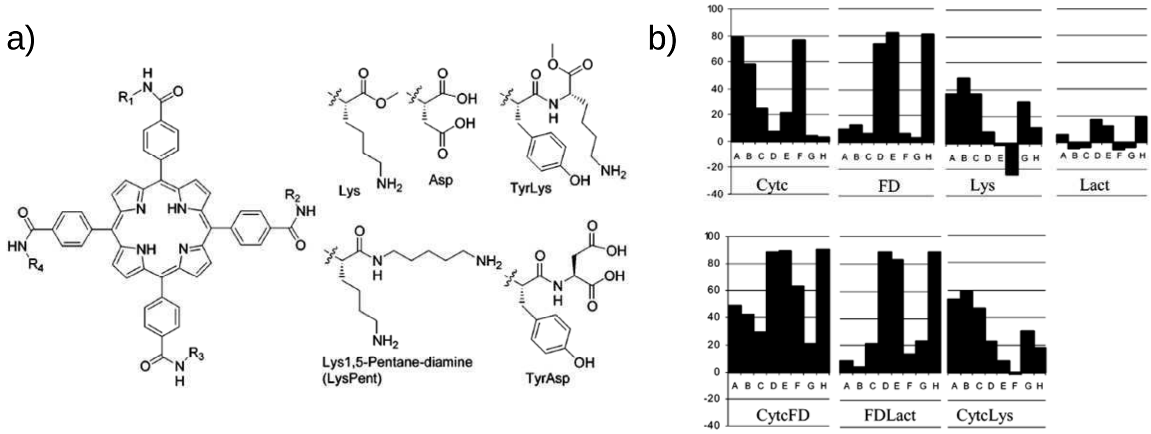

Figure 1.31. a) Synthetic tetra-meso-carboxylphenylporphyrin conjugated with amino acids or amino acid derivatives. b) Fingerprints obtained for protein samples by an 8-porphyrin array. [75]

Following with their previously mentioned work in e-tongues, Anslyn's group designed and synthesized a library with 6859 unique members of receptors using combinatorial chemistry (Figure 1.32). In this model, resin-bound peptide arms provided sites for molecular recognition of proteins by means of ion pairing, hydrogen bonding, and the hydrophobic effect. The patterns created by the array of receptors were obtained by measuring the intensity of transmitted red, blue and green light for each bead using a charge-coupled device attached to a customized reader. This system was conceived to be able to differentiate proteins from glycoproteins. [85, 86].

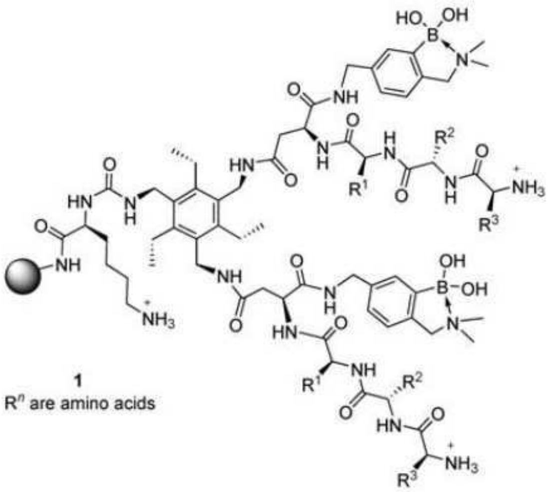

1

R^n are amino acids

Figure 1.32. The structure of the resin-bound receptor collection synthesized by Anslyn's group. [85]

A great synthetic effort was also done by Thomas Kodadek's group. [87] They constructed a Small Molecule Microarray (SMM) consisting on an array of 7680 peptoids that bind fluorescently labeled proteins. The results were displayed in form of fingerprints that permitted an easy identification of the proteins (Figure 1.33).

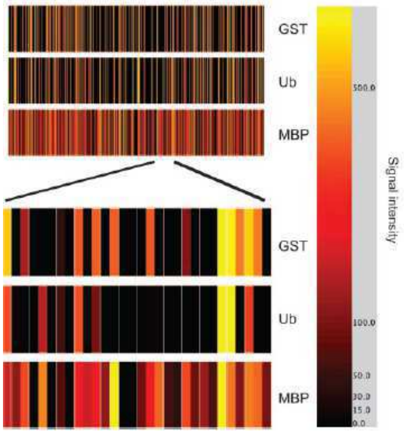

Figure 1.33. Protein fingerprints generated with the system developed by Kodadek's group. [87]

These approaches described above are very promising, although limited by the relatively high analyte concentrations needed for efficient sensing (above ten µM).

Thayumanavan et al. introduced a new method in which they played with the assembly and disassembly of supramolecular polymers (a complex between a polyelectrolyte and a surfactant) caused by the interaction with the protein analyte. The disassembly of the complex could be quantified for fluorescent reporting when a non-covalently sequestered fluorescent guest molecule was released. By varying the structure and charge of the surfactant and the polyelectrolyte structures they were able to generate analyte-specific patterns for proteins. This method appeared to be more sensitive for the detection of metalloproteins (limit of detection 80 nM) than for non-metalloproteins (limit of detection 80 µM) (Figure 1.34). [88, 89]

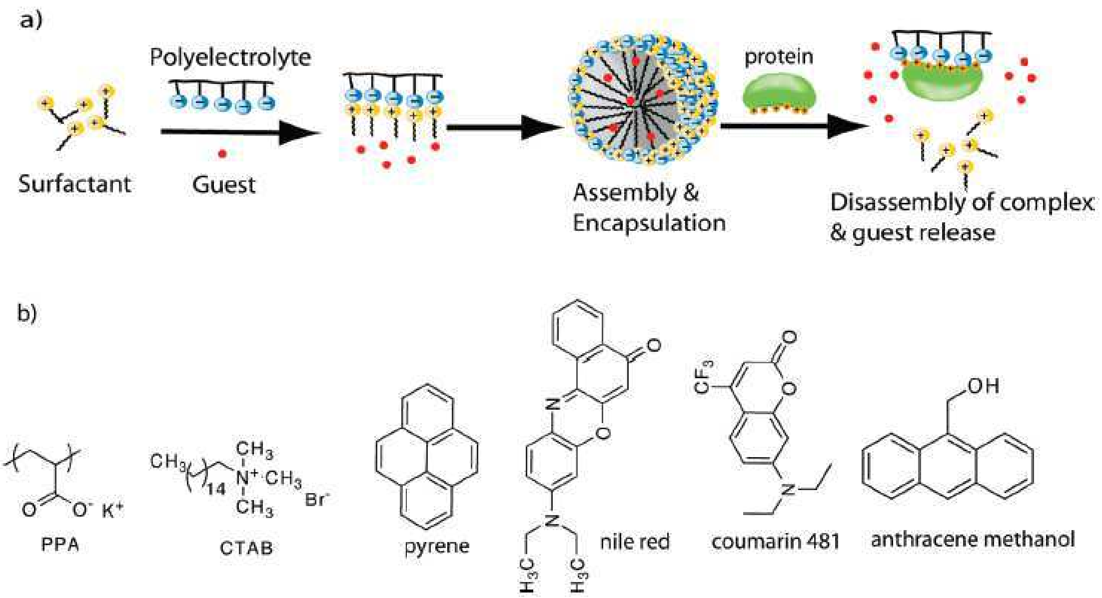

Figure 1.34. a) The principle based on polymer-surfactant complex assembly and protein-induced disassembly. b) Structures of the polymer, surfactant and dye molecules used in this system. [89]

A major improvement for this kind of device was achieved by Rotello's group. In their earlier study, they used highly fluorescent polymers as cross-reactive receptors. These materials can bind protein surfaces through multivalent interactions. Moreover, their optical properties are sensitive to minor conformational or environmental changes, enabling efficient signal transduction of binding events. Using six functionalized poly(p-phenyleneethynylene)s (PPEs), which possessed various charge characteristics and molecular scales with important binding diversity upon interaction with protein analytes, an array was constructed and generated distinct patterns for proteins (Figure 1.35). The array was able to discriminate at least 17 protein analytes in the nanomolar range. [90]

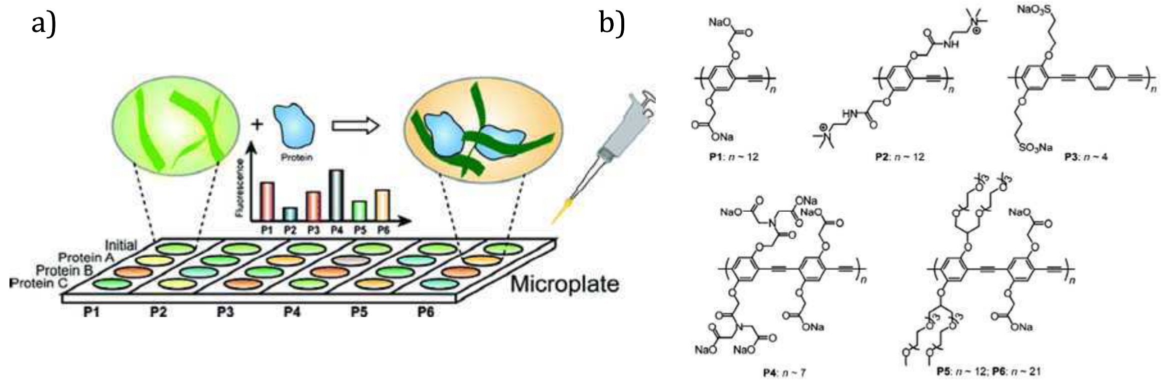

Figure 1.35. a) PPE-based protein sensor array. b) Chemical structures of PPE polymers used in the study. [90]

Later on, to increase the sensitivity of the system, they conjugated an anionic fluorescent polymer to different cationic functionalized gold nanoparticles. As illustrated in Figure 1.36, electrostatic complexation of Au NPs and polymer results in fluorescence quenching of the polymer (fluorescence "OFF") through energy transfer. Addition of protein analytes then disrupts the quenched polymer/Au NPs complexes via competitive binding, causing fluorescence recovery of the polymer (fluorescence "ON"). The protein-nanoparticle interactions are differential thanks to different physicochemical properties of terminal groups of the functionalized nanoparticles, hydrophobic, hydrophilic, or aromatic [91]. This system was not only able to detect and identify proteins in the low nanomolar range, but also to differentiate normal cells from their cancerous and metastatic counterparts [92], as well as to detect and identify bacteria [93].

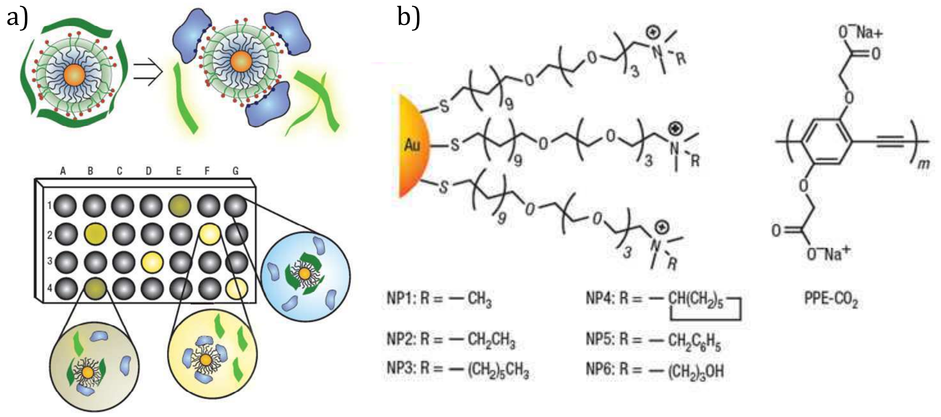

Figure 1.36. Schematic illustration of the sensor array based on Au NP-fluorescent polymer conjugates. a) The competitive binding between the protein and quenched polymer-Au NP complexes leads to the restoration of fluorescence. b) Structural features of cationic gold nanoparticles and the anionic PPE. [91]

Based on the same principle, by replacing the fluorescent polymer with biocompatible green fluorescent protein (GFP), the sensor array was able to discriminate different concentrations of the same protein, as well as a mixture of proteins in human serum at physiologically relevant concentrations, see Figure 1.37. This last result illustrates the potential of e-Tongues in profiling real samples for diagnosing disease states. [94]

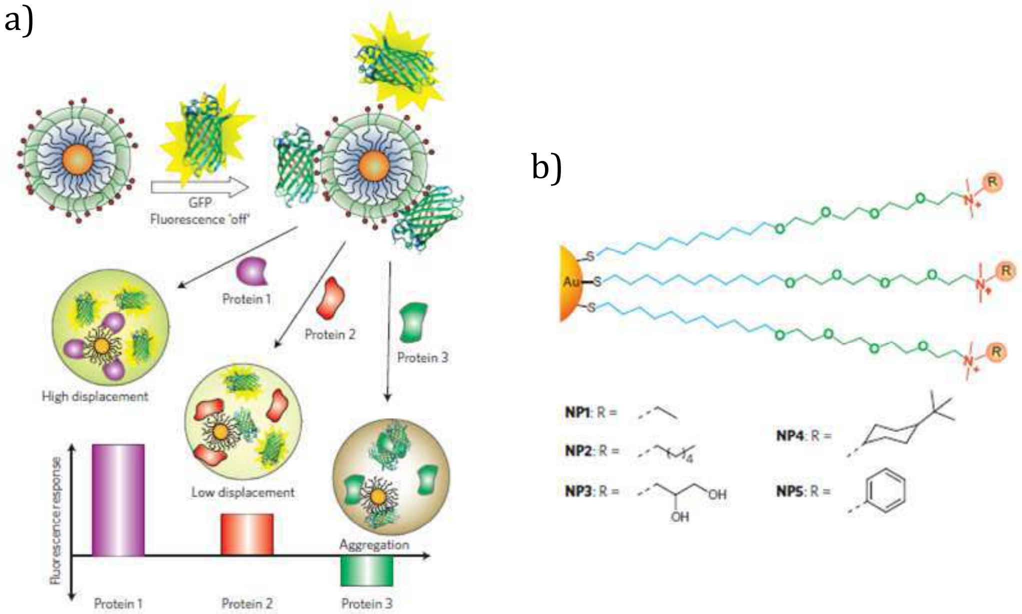

Figure 1.37. a) Schematic illustration showing that the competition binding between proteins and quenched Au NP-GFP complexes, whose aggregation leads to fluorescence ‘turn on’ or further quenching using a library of cationic nanoparticles. b) Structural features of cationic gold nanoparticles used in the study. [94]

More recently, they further improved their system in order to overcome the restrictions caused by the inherent emissivity of the used fluorophores. They developed an enzyme-amplified array sensor approach, which was able to sense and identify a range of biomedically relevant proteins at 1 nM in both buffer and desalted human urine (Figure 1.38). [95, 96]

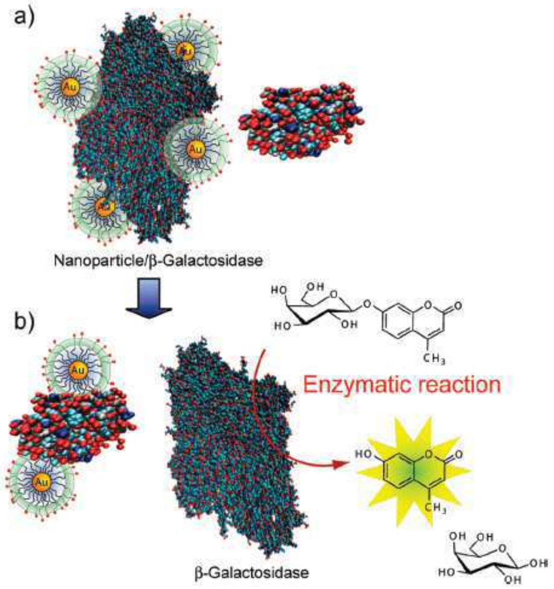

Figure 1.38. Enzyme-amplified sensing array. a) Functionalized cationic AuNPs electrostatically bind to the anionic β-Galactosidase (β-Gal), reversibly inhibiting the enzyme. b) Displacement of the particles by the analyte restores β-Gal activity toward a fluorogenic substrate, generating a readout signal that is amplified through enzymatic catalysis. [95]

In summary, the results obtained with the e-nose and e-tongue systems described above for protein recognition are very promising. However, these approaches may be limited by irreversible responses or long recovery times due to the strong interaction between analytes and receptors or short lifetimes of some dye-arrays due to fluorescence bleaching. In addition, the array preparation usually requires the design and synthesis of a set of differential receptors whose structures are often complex. There is thus an identified and current need for the development of new strategies and sensing materials to promote a more widespread use of eN/eT systems.

1.5. Presentation of the PhD project

The main objective of this thesis is to develop a novel approach that greatly simplifies the design and production of sensing materials for the construction of electronic tongues.

In this regard, we reasoned that the design and synthetic efforts could be drastically reduced if the cross-reactive receptors are prepared by self-assembly of a restricted set of building blocks (BBs), ideally small and easily accessible molecules displaying different physicochemical properties. Upon combination of such BBs in varying and controlled proportions, a collection of combinatorial cross-reactive receptors (CoCRRs) with evolutive properties could be obtained. A major advantage of this approach is to allow a very quick growth of the diversity: eleven CoCRRs can be prepared by mixing only two BBs with concentration varying from 0 to 100% in 10 % increment, while 66 can theoretically be accessed by adding a third BB. Such growth can be generalized to n BBs and i % concentration increment, leading to an impressive number of [(100/i)+n-1]!/(n-1)!(100/i)! potential different CoCRRs.

In order to assure both a good match between the CoCRRs precursor mix and their reproducible assembly, we further reasoned that the BBs should be designed to allow self-assembly on a surface. In addition, such chemistry should allow arraying the BB mixtures on a surface with spatial encoding of their composition. In this new e-tongue approach, surface plasmon resonance imaging (SPRi) seems to be the ideal tool for protein sensing on the CoCRR array. Indeed, the gold surface of the SPRi prism should allow easy formation of SAMs through thiol or disulfide chemistry, while recording the changes in reflectivity of all the spots upon infusion of protein solutions, should provide label free, synchronous, parallel and real-time observation of binding events on the CoCRRs array.

In this thesis, a model e-tongue, initially designed for differentiation of heparan sulfates binding proteins, was constructed using only two small modified disaccharides as BBs. Its discrimination capacities as an e-tongue were evaluated by analyzing not only pure protein analytes but also complex mixtures (beverages). More interestingly, the developed e-tongue offers other innovative features. On one hand, it was capable of mimicking the recognition properties of heparan sulfate (HS), being useful for understanding the nature of HS/protein interactions, On the other hand, it offered a medium throughput screening capacity for bioactive 2D combinatorial surfaces to fabricate 3D biomimetic nanovectors that are able to target specifically proteins of therapeutic interest.

CHAPTER 2.

Construction of an Electronic Tongue Using Combinatorial Cross-Reactive Receptors

Résumé en français du chapitre 2

Construction d'une langue électronique avec des récepteurs combinatoires à réactivité croisée.

Ce chapitre est dédié à l'explication détaillée de la construction d'une langue électronique basée sur l'exploitation d'une collection de CoCRRs comme matériaux sensibles (récepteurs) couplée à un système de transduction en temps réel et sans marquage : l'imagerie par résonance des plasmons de surface (SPRi).

Les CoCRRs sont préparés à partir de deux BBs dérivées du lactose que nous appelons lactose (BB1) et lactose sulfatée (BB2). Ces deux molécules ont un groupe dithiol permettant leur auto-assemblage sur des surfaces d'or. Elles sont toutes les deux hydrophiles ; néanmoins, BB1 possède une charge neutre tandis que BB2 est négativement chargée. Pour la préparation des CoCRRs, les BBs sont mélangées selon 11 proportions contrôlées où BB1% varie de 0 à 100% par incréments de 10%. Une fois les mélanges effectués, les solutions sont déposées sous forme de plots circulaires sur un prisme de verre recouvert d'une fine couche d'or d'environ 45 nm, à l'aide d'un appareil piézoélectrique d'éjection de nanovolumes. L'auto-assemblage des BBs se déroule au cours d'une nuit entière, après laquelle la puce ainsi réalisée est prête à être utilisée.

L'instrument SPRi nous permet de suivre en temps réel tout changement d'indice de réfraction ayant lieu près de la surface d'or. Cela veut dire qu'une perturbation provoquée par l'attachement de molécules sur l'un des plots CoCRR est détectable en temps réel et sans besoin de marquage, ce qui est extrêmement intéressant pour le fonctionnement de notre langue électronique.

Le montage expérimental est constitué d'un système optique permettant la détection des événements de reconnaissance ayant lieu entre la surface du prisme et l'échantillon, et d'un système microfluidique qui permet le transport et la mise en contact des échantillons avec les CoCRRs situés à la surface du prisme.

Grâce a une caméra CCD, il est possible de suivre l'augmentation locale de masse à la surface due aux interactions entre l'analyte et les CoCRRs *via* l'augmentation de l'intensité lumineuse réfléchie qu'elle provoque ; de telle manière que l'image globale du prisme permet de voir quels CoCRRs sont très réactifs face à l'analyte et lesquels ne le sont pas. On obtient pour chaque plot l'évolution du changement de réflectivité en fonction du temps, alors appelée «sensogramme».

Le fait que les CoCRRs aient des compositions différentes mais quue la différence entre deux CoCRRs successives soit très faible permet une répresentation continue des données ; un axe représentant l’incrément de BB1%, un autre représentant le temps, et l´axe vertical correspondant à la réflectivité mesurée par plot. Ce type de représentation 3D est appelé image d’évolution continue (CEL – *Continuous Evolution Landscape*) et est caractéristique de l’échantillon analysé. Une coupe de ce graphe à un temps donné permet d’obtenir un profil d’évolution continue (CEP - *Continuous Evolution Profile*) 2D, qui reste caractéristique de l’échantillon analysé. L’ensemble des données obtenues peut être traité par une analyse statistique en composantes principales (ACP) afin de regrouper et éventuellement d’identifier les analytes ainsi détectés.

En conclusion, une méthode simplifiée d’obtention de récepteurs à réactivité croisée à été mise au point et couplée à une méthode optique de transduction pour obtenir une langue électronique innovante et performante. Ce procédé permet l’enregistrement en temps réel des événements de reconnaissance qui ont lieu sur les surfaces sensibles. Les données obtenues peuvent ensuite être représentées de façon simplifiée par rapport aux langues ou nez électroniques existants grâce aux CEP et CEL. La différentiation des échantillons peut également être obtenue par une méthode statistique telle que l’ACP.

Construction of an Electronic Tongue Using Combinatorial Cross-Reactive Receptors

For proof of concept, we designed a model array inspired by the way cell surface heparan sulfates recognize HS binding proteins (HSbps), an important group of extracellular mediators involved in many physiological and pathological processes. HS are negatively charged polysaccharides displaying a high degree of molecular diversity arising from the regulated generation of various epimerization and sulfation patterns during biosynthesis. According to cell type and activation state, HS chains with different negative charge topologies are expressed, with the presumed aim of promoting selective interactions with HSbps. We hypothesized that a cross-reactive receptor array able to differentiate HSbps could be prepared from modified lactose (BB1), neutral, and sulfated lactose (BB2), negatively charged. We anticipated that variation of the BB2 to BB1 ratio in the spotted solutions should provide, after self-assembly, CoCRRs displaying different charge densities and thus susceptible to promote the differential binding of HSbps.

In this chapter, we present the construction of the electronic tongue based on the CoCRR array and SPRi detection.

2.1. Preparation of the CoCRR array

2.1.1. Building blocks

The choice of the building blocks was a critical step in the design of sensing materials. In this thesis, modified lactose (BB1) and sulfated lactose (BB2) were used as building blocks. They were derived from lactose (a disaccharide obtained from the condensation of galactose and glucose by the formation of a β-1 4 glycosidic linkage, see Figure 2.1).

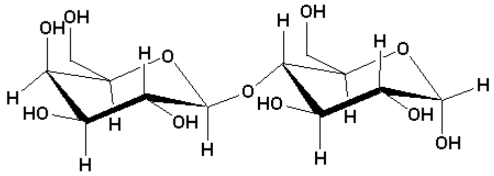

Figure 2.1. Chemical structure of lactose molecule.

The building blocks were synthesized following the process described here: the β-lactoside 1(1 in Figure 2.2) was first converted to the lactosylated disulfide, used as BB1 using HATU mediated amide bond formation between amine 1 and acid 2. Further sulfatation in standard conditions lead to incomplete sulfation, as evidenced by ^{1}H and ^{13}C NMR. Gratifyingly, further treatment of this mixture with sulfurtrioxyde•pyridine complex in DMF at 60 °C allowed to complete the sulfation leading to the fully sulfated disulfide, used as BB2. In order to increase solubility in organic solvent compound BB2 was conditioned as tetrabutylammonium salt. These two molecules were provided by Professor David Bonnaffé, Université Paris-Sud, Orsay, France.

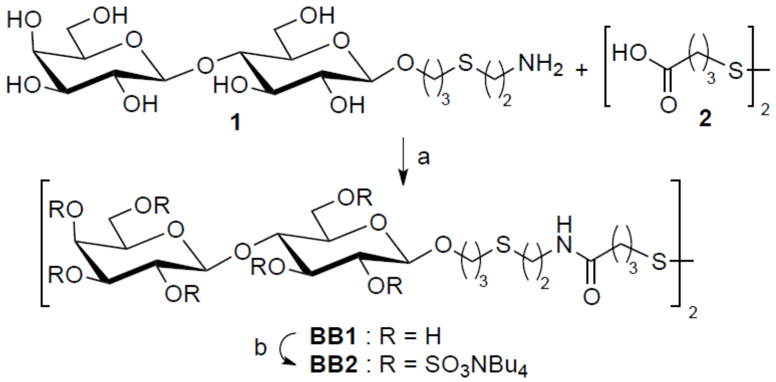

Figure 2.2. Synthetic pathway to prepare the two building blocks BB1 and BB2.

The structure of the obtained BBs is shown in Figure 2.3 and their ^{1}H and ^{13}C NMR spectra in the Appendix B. They are composed of three main parts: the functional terminal group lactose and sulfated lactose, for BB1 and BB2, respectively, the spacer chain, and the head group which consists of a disulfide moiety for self-assembly of BBs on a gold surface. Both molecules are hydrophilic, but BB1 is neutral while BB2 is highly negatively charged.

BB1:

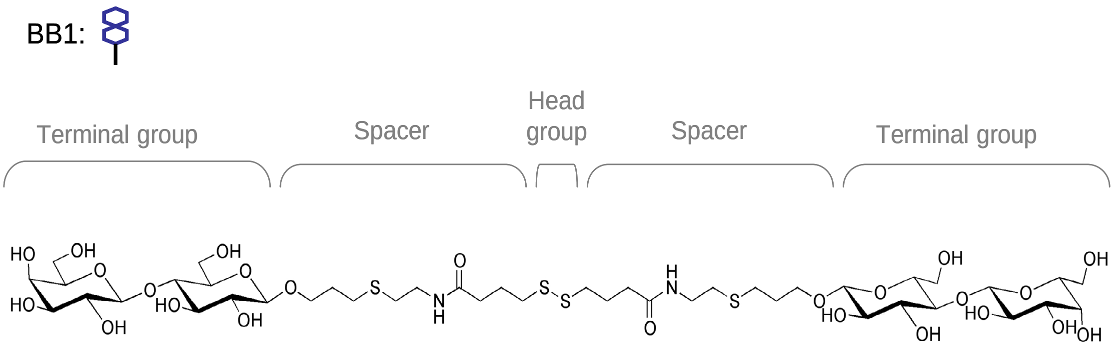

Chemical Formula: $C_{42}H_{76}N_2O_{24}S_4$
Exact Mass: 1120,37
Molecular Weight: 1121,31

BB2:

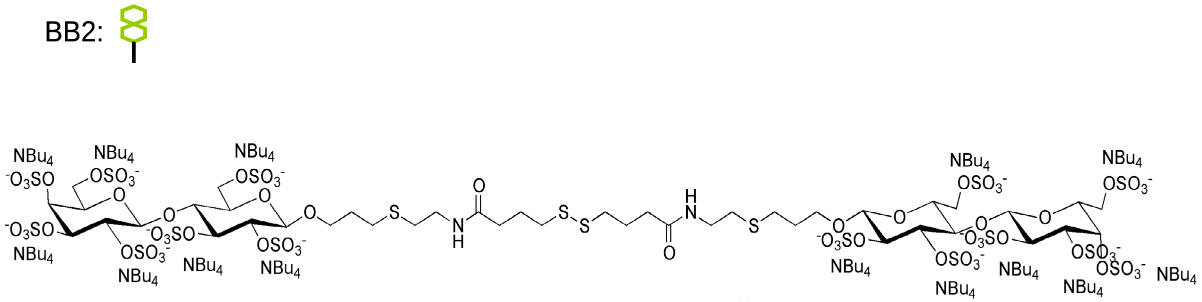

Chemical Formula: $C_{266}H_{566}N_{16}O_{66}S_{18}^{14-}$
Exact Mass: 5617,65
Molecular Weight: 5622,59

Figure 2.3. Chemical structures of BB1 and BB2. In this thesis, schematic representations of the BBs will be colored in blue for BB1 and in green for BB2.

2.1.2. Preparation of the CoCRR array

For the preparation of the CoCRR array, the two building blocks were mixed in 11 controlled proportions with [BB1]/([BB1]+[BB2]) ratios of 0, 10, 20, 30, 40, 50, 60, 70, 80, 90 and 100%. In the table below (Table 2.1), the detailed composition of each mixed solution is given. The standard volume prepared for each ratio was 50 µL. The total final concentration of BBs was 0.1 mM. These mixed solutions were deposited on the gold surface of a prism in the following step. 5% of glycerol was added in order to prevent solvent evaporation and consecutive evolution of BB concentrations in the drops after deposition on the prism.

	100% BB1	90% BB1	80% BB1	70% BB1	60% BB1	50% BB1	40% BB1	30% BB1	20% BB1	10% BB1	0% BB1
BB1 0.2mM in HEPES (µL)	25	22.5	20	17.5	15	12.5	10	7.5	5	2.5	0
BB2 0.2mM in HEPES (µL)	0	2.5	5	7.5	10	12.5	15	17.5	20	22.5	25
H_2O+10% Glycerol (µL)	25	25	25	25	25	25	25	25	25	25	25

Table 2.1. The composition of the 11 mixed solutions needed for the preparation of the CoCRR array.

The prisms used as support were provided by GenOptics (Horiba-Scientific-GenOptics, Orsay, France). They are made of high refractive index glass coated with a thin gold film (45 nM). 48h before use, they were cleaned by plasma treatment (0,6mBar, 75% Oxygen, 25% Argon, power 40 W, 3 min) using a Femto plasma cleaner (Diener Electronic, Germany). Cleaning was made 48h before spotting in order to obtain more reproducible self-assembly of the CoCRRs.

Droplets of 8 nL of the 11 mixed solutions were deposited on the prism surface using a non-contact piezoelectric spotter (Siliflow, France) with four duplicates for each ratio. This automatic spotter permits the non-contact deposition of drops of a minimum volume of 4 nL in the desired configuration thanks to a piezoelectric mechanism, see Figure 2.4. This spotting design, containing four randomly distributed replicates of each CoCRR is given in the Appendix C.

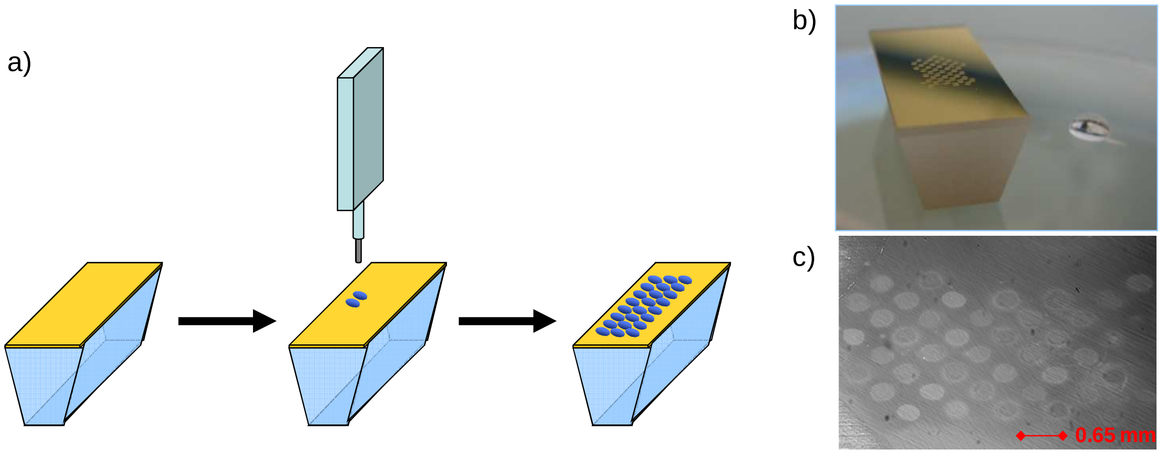

Figure 2.4. a) Schematic representation of the spotting process. b) Photography of the prism after spotting. c) SPRi differential image of a prism surface after self-assembly of the BBs.

Afterwards, the prism was placed inside a Petri dish containing 1 mL of water to ensure a humid ambient and it was left overnight (18h) at room temperature for self-assembly of BBs. Then, the prism was washed thoroughly with ultrapure water and dried under a flow of argon. In each spot, the ratio of the two BBs anchored on the gold surface was assumed to be equal to the molar ratio in the parent solution [97]. A schematic illustration of the array containing 11 CoCRRs is shown in Figure 2.5.

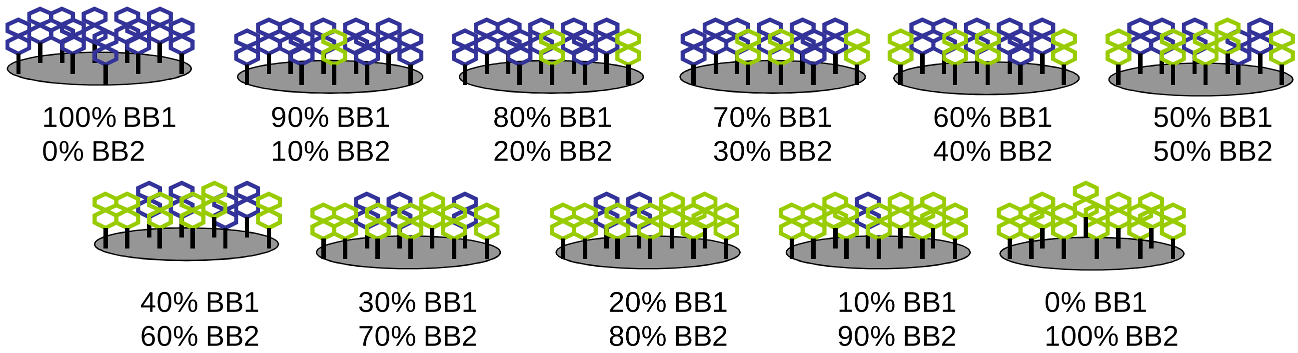

Figure 2.5. The array consisting of eleven CoCRRs made by mixing and self-assembly of two BBs at different ratios and at a constant total concentration.

Finally, the prism was fixed on a metallic support (see Figure 2.6) and placed together with the flow cell for sample analysis using SPRi. To avoid leakage, the prism was pressed against the flow cell using a clamping handle.

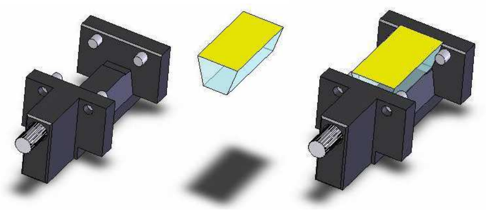

Figure 2.6. Positioning the prism on the support for sample analysis using SPRi.

2.2. Detection method: surface plasmon resonance imaging

The detection of the binding events occurring on the CoCRRs was performed using SPRi, which allows label-free and real time monitoring of molecular binding events at a metal/dielectric interface [98-104].

2.2.1. Surface plasmon resonance phenomenon

According to Snell-Descartes law, when light arrives to an interface between two media, 1 and 2, with refracting indexes of n1 and n2 respectively, n1 being bigger than n2, if the incident angle of light is superior to the critical angle, the incident light is totally reflected and no light is refracted in medium 2. This phenomenon is called total internal reflection (see Figure 2.7). When this occurs, a non-propagating evanescent wave is created in the interface. The intensity of the evanescent wave decays exponentially with the distance to the interface (see Figure 2.7)

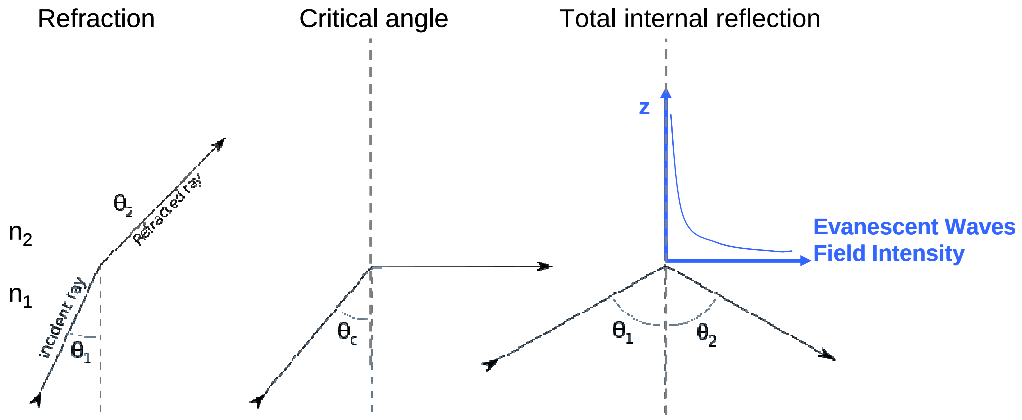

Figure 2.7. When a light ray passes from a highly refractive media to lower one, three phenomena can occur depending on the incident angle and the refraction indexes of the media. Incident light is refracted until it arrives to a critical angle where it is not refracted nor reflected. After the critical angle light suffers total internal reflection, a phenomenon causes evanescent waves. In blue, plot of the evanescent waves field intensity *vs.* the distance from the interfacial surface. Figure adapted from reference [105].

Because the evanescent wave remains confined to the interface between the two media, it is only sensitive to perturbations occurring at the vicinity of the interface. [106]

If a golden surface is between a glass and a liquid, surface plasmons of the metal, which are collective oscillations of conduction electrons, can interact strongly with light to produce a surface plasmon wave. In a total internal reflection situation, surface plasmons can couple with the evanescent wave and resonate. The conditions to reach the resonance of the surface plasmons depend not only on the wavelength, polarization and incident angle of the incoming light, but also on the properties of the metallic layer and the medium above the surface.

The intensity of the reflected light after a biochip at a total reflection configuration can be measured with a CCD camera for different incident angles. The resulting curve is called a plasmon curve and goes through a minimum of intensity called resonance angle. It corresponds to the resonance of surface plasmons of the gold layer, which is traduced as a complete attenuation of the reflected light. The position of the resonance angle is characteristic of the metal surface and the medium above. For example, changes of refractive indexes of the medium above the biochip will induce changes of the position of the resonance angle (see Figure 2.8).

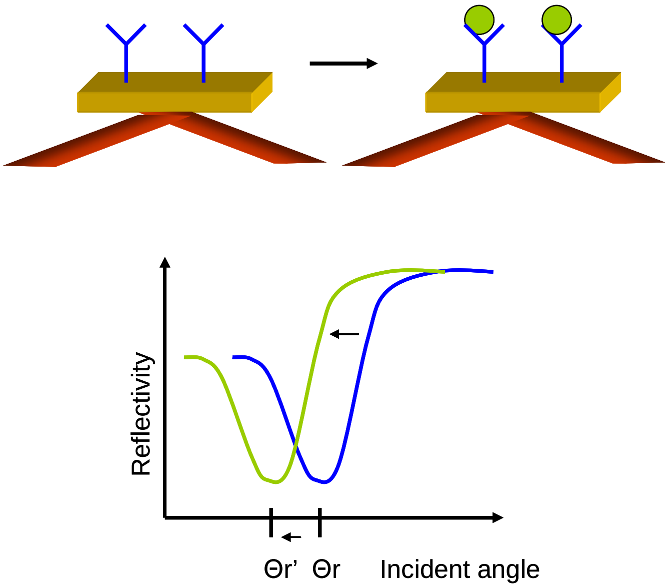

Figure 2.8. Effect of a binding event (or mass accumulation) between ligands immobilized on a gold surface and analytes flowing on the surface. The binding event induces a change of refractive index and, thus, a change of the position of the resonance angle. This shift can be measured in real time.

2.2.2. Surface Plasmon Resonance Imaging

The instrumental formats used in SPR experiments can be globally categorized into three types of measurements: scanning angle SPR, scanning wavelength SPR and SPR imaging [107]. For all SPR formats, the reflectivity of incident light on the metal/dielectric interface is monitored and correlated to changes on the local index of refraction of the dielectric adjacent to the metal film. The most widely used format for an SPR experiment is the scanning angle technique, in which the reflectivity of monochromatic incident light on a metal film is monitored as a function of the incident angle. The popularity of the scanning angle technique can be partially attributed to the existence of commercially available instrumentation from Biacore [108], which has made it possible to use SPR as a detection method for many applications.

However, both scanning angle and scanning wavelength measurements typically provide only one or a few data points at a time. In contrast, SPR imaging, sometimes called SPR microscopy, adds an imaging capacity to SPR. It combines the strength of SPR to monitor label-free biomolecular interactions with the high throughput of microarrays. It is thus possible to measure several dozens to several hundreds of interactions in parallel (multiplexing).

Imaging allows monitoring simultaneously the resonance conditions on the whole surface of the array. If the array contains different immobilized molecules (array of spots), potential interactions on those different molecules can be monitored in parallel. In addition, the real time image of the array surface is also retrieved. The “difference image” shows interacting spots when the analyte solution is injected. The spots light up at different grey level according to different affinity between the receptors and samples. Meanwhile, these images are registered and treated by imaging software. In this way, SPR images are converted into variations of reflectivity (expressed as R%) versus time for each spot, which generate a series of kinetic binding curves called sensorgrams.

In Figure 2.9 a classical sensorgram is presented. On the first stage, the ligands or receptors are immobilized on the gold surface and running buffer flows through the system, giving the baseline which is stable upon time. When the sample solution enters the flow cell, molecular binding can occur. This induces a shift of the plasmon curves and an augmentation of reflectivity, see association phase. After the sample injection is completed, the ligand-analyte complex dissociates. This induces a diminution of the reflectivity versus time, see dissociation phase. Afterwards, the surface of the array is usually regenerated using an appropriate regeneration solution for re-use.

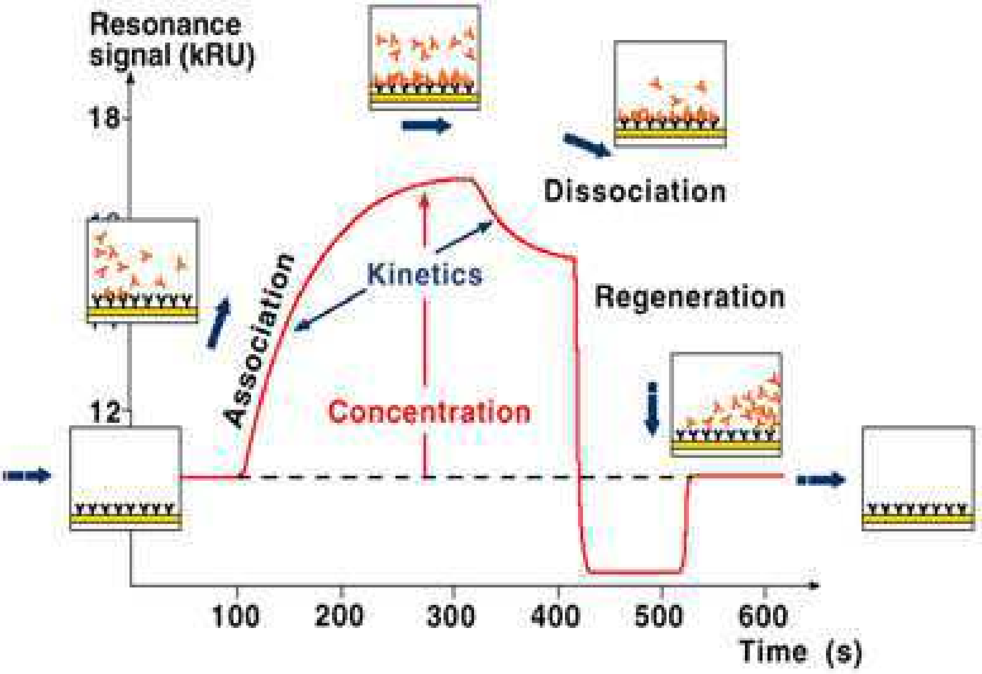

Figure 2.9. Scheme of a classical sensorgram showing the variation of reflectivity during an analysis cycle: 1; buffer is in contact with the array (baseline); 2 sample injection (association step); 3, injection of buffer (dissociation step); 4, regeneration step. (www.biacore.com)

2.2.3. SPR imaging instrumental set-up

The used SPRi instrument was provided by Horiba-Scientific-GenOptics. It consists of two main parts that will be exhaustively described in the following two sections: the optical system and the microfluidic system (see Figure 2.10).

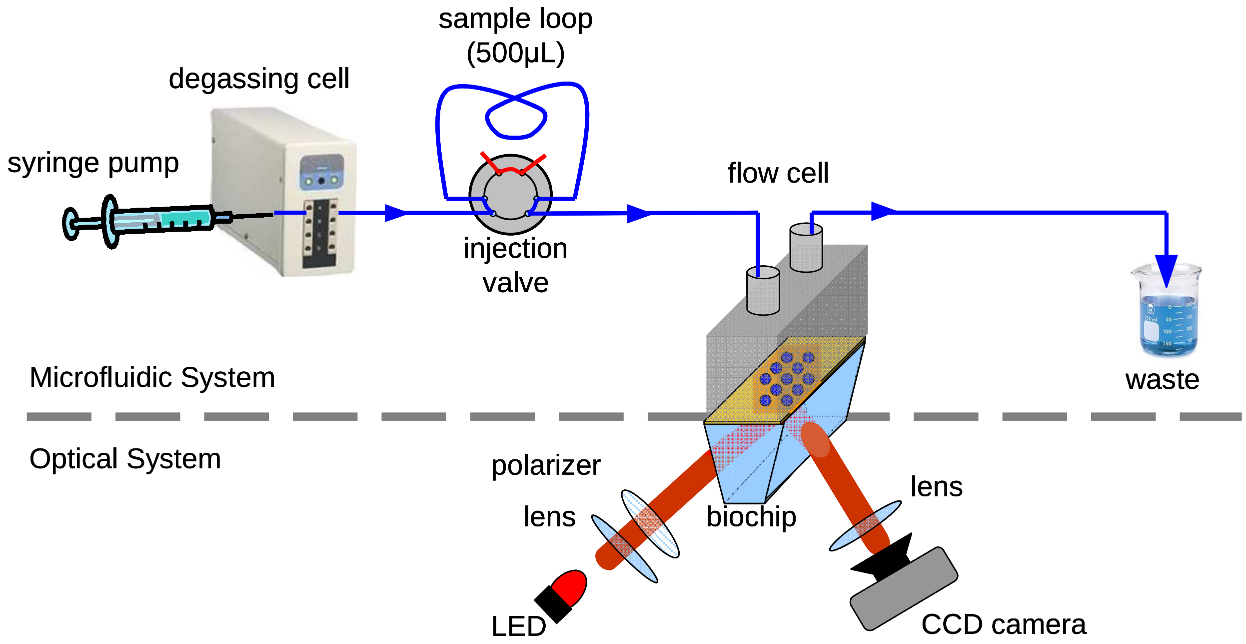

Figure 2.10. SPRi set-up, consisting of two main parts: optical system and microfluidic system.

The optical system

In Figure 2.11 a photography of the optical system is included. The incident light wave (660 nm) was generated by a light-emitting diode (LED) and collimated by a biconvex lens. Further optical pathway was equipped with a rotating polarizer providing TM (SPR detection) and TE (total reflection used as reference) polarization modes. The incident light was reflected on the biochip surface and the resulting light was detected by an 8-bit CCD camera connected to a computer provided with adapted software for signal treatment.

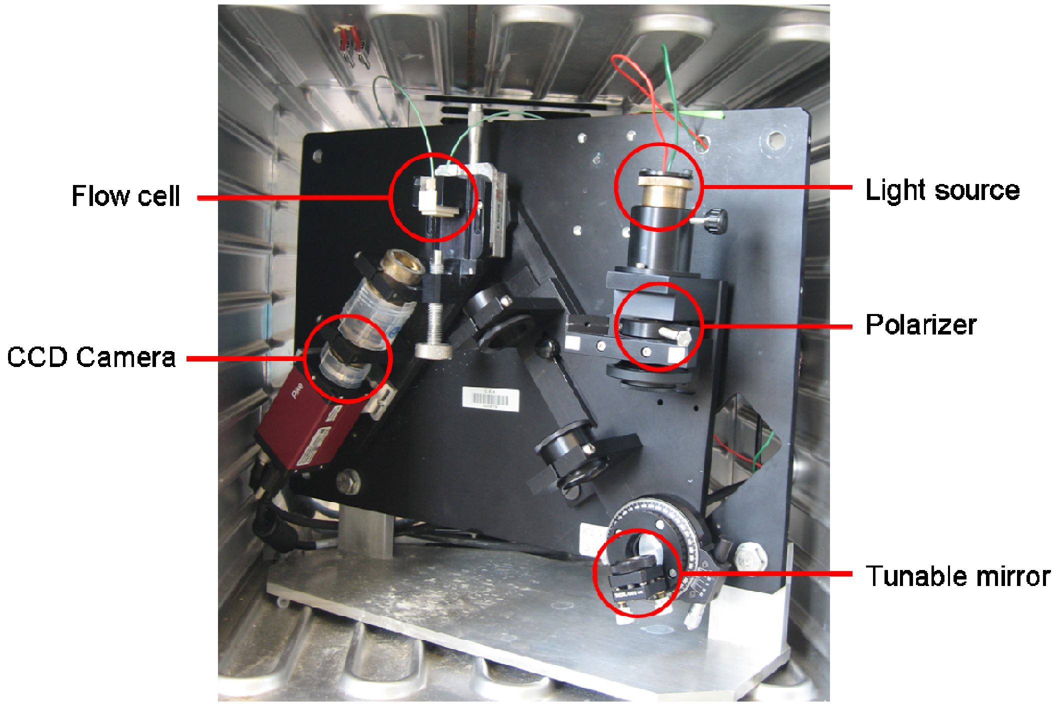

Figure 2.11. Photography of the optical SPRi system. Main components are highlighted.

The microfluidic system

The microfluidic system allows the samples to get in contact with the CoCRR array on the prism surface. As depicted in Figure 2.10, the buffer solution is constantly injected by a remotely controlled 5 mL syringe pump (Cavro XLP 6000, Cavro scientific instruments, USA) and degassed with a degassing system (Alltech, France). Samples (500 µL) were injected using a 6-channel medium pressure injection valve (Upchurch Scientific, USA) at a 100 µL/min flow rate and transported to the flow cell. The sample charge and injection positions of the valve are depicted in Figure 2.12.

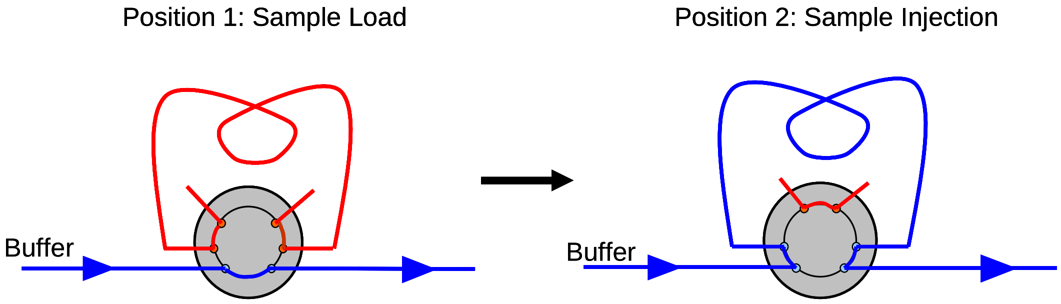

Figure 2.12. Schematic illustration of the two positions of the injection valve. Position 1: The running buffer flows through the valve and enters directly the flow cell. The injection loop can be filled with the sample (in red) and the excess goes directly to the waste beaker. Position 2: The running buffer flows through the injection loop pushing the sample to the flow cell.

All the connections were done by PEEK tubes. The injection valve was connected to a 10 µL PEEK flow cell with hexagonal configuration (see Figure 2.13). Before use, the flow cell was cleaned by 10 min immersion in ethanol and 5 min immersion in ultrapure water in an ultrasonic bath. The flow cell's exit tube goes directly to a waste beaker.

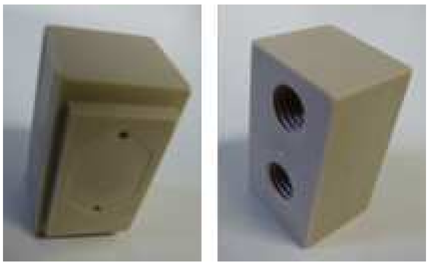

Figure 2.13. Photography of the two sides of the flow cell. On the left, the hexagonal reaction chamber with the entrance and exit holes. On the right, the upper side of the flow cell where the connection tubes are placed.

2.3. Electronic tongue

Based on the CoCRR array and SPRi, an electronic tongue was constructed, as illustrated in Figure 2.14.

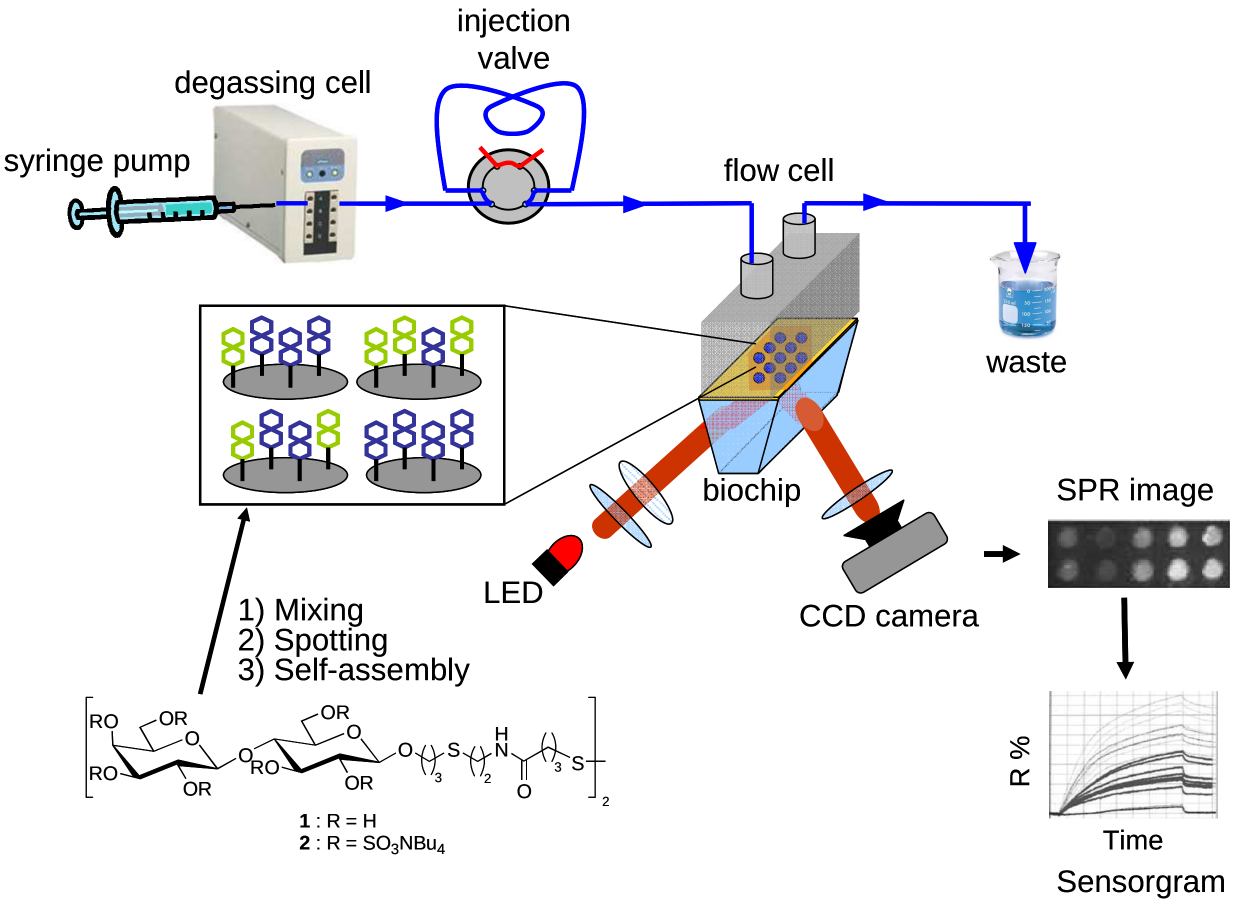

Figure 2.14.The schematic illustration of the e-Tongue based on the CoCRR array and SPRi.

Sample sensing was monitored at 25 °C with the SPRi apparatus placed in a temperature regulated incubator (Memmert, Germany) to avoid refractive index changes due to temperature oscillations. The working angle is selected within the highest slope range of the plasmon curves in order to have the best sensitivity. In this way, all the refractive index changes provoked by binding, dissociation or rinsing events occurring at the proximity of the prism surface result in a shift on the plasmon curve (and on the position of the resonance angle) that was recorded in form of SPR images at intervals of 0.05 minutes with the help of the CCD camera. Using Imaging software (Horiba Scientific-GenOptics, Orsay, France), all SPR images were analyzed and then converted to variations of reflectivity (expressed as R%) versus time, which generated a series of kinetic binding curves, sensorgrams.

Masks were defined in order to separate individual signals coming from each spot. These masks allow the user to define the areas occupied by the spots (CoCRRs) and to automatically calculate the average reflectivity of each spot upon the time. In all the experiments, in addition to the CoCRR spots, three spots on bare gold surface were also defined and used as control surfaces, see Figure 2.15.

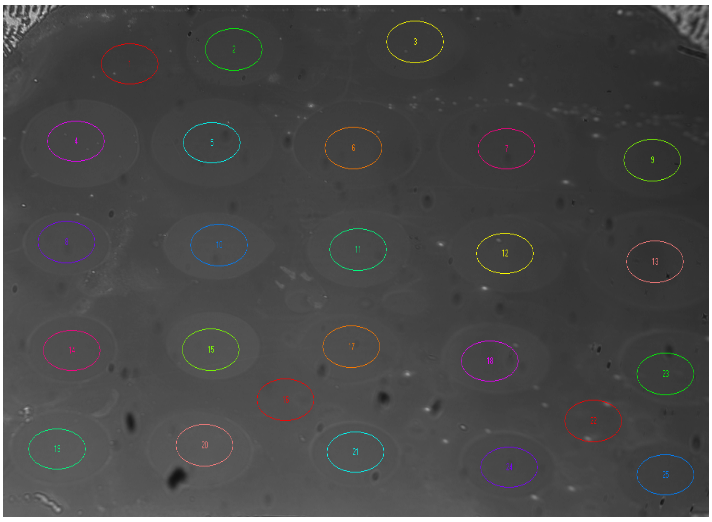

Figure 2.15. An example of defined masks on a CoCRR array surface using circles with same diameter.

2.3.1. Recognition patterns generated by the electronic tongue: CELs and CEPs

Based on SPR images and sensorgrams, a recognition pattern for each analyte can be generated. Interestingly, from the concept, the composition of each CoCRR is close to those of its neighbors, therefore, the signal obtained with each CoCRR is correlated and close in intensity to those of its neighbors. Consequently, the series of signals generated upon interaction between CoCRRs and analytes can be considered as continuous. As illustrated in Figure 2.16, the obtained standard sensorgrams can be advantageously combined in a 3D continuous evolution landscape (CEL) by adding an axis describing the BB1% evolution ([BB1]/[BB1]+[BB2]). The CEL offers an accurate representation of the time-dependent recognition patterns of the 11-CoCRR array. Moreover, from such a 3D CEL we can derive 2D continuous evolution profiles (CEPs), which are sections of CELs at a fixed time. The CEP offers a more direct way to evaluate the binding affinity between all the CoCRRs and each analyte.

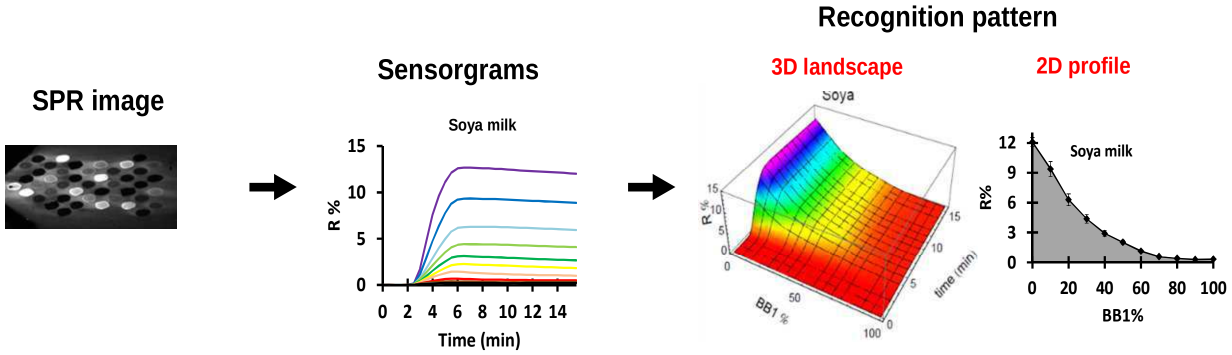

Figure 2.16. Data processing for analysis of samples using our electronic tongue: SPR images are converted into sensorgrams, based on which two types of recognition patterns were generated: 3D CEL and 2D CEP. 3D CEL was obtained by plotting the variation of reflectivity (R%) versus the ratio [BB1]/([BB1]+[BB2]) in BB1% and time. 2D CEP corresponds to the section of the CEL at a fixed time.

A major advantage of 3D CELs or 2D CEPs is that abnormal signals can be easily identified in a similar way as our brain is capable of reconstructing an image from a screen even when defective pixels are present. For example, the brain is still able to reconstruct and recognize the image of a tree even when 20% of defective pixels are present, as illustrated in Figure 2.17. Similarly, in a 2D CEP, a defective signal can be easily identified and corrected if necessary thanks to the continuity of the pattern. In addition, in case of doubt, more intermediate points could be added to the array to better define the profile. Such “auto-corrective” behavior contrasts favorably with the sets of uncorrelated discrete data obtained via traditional eN/eT approaches, providing an unprecedented reliability for our system.

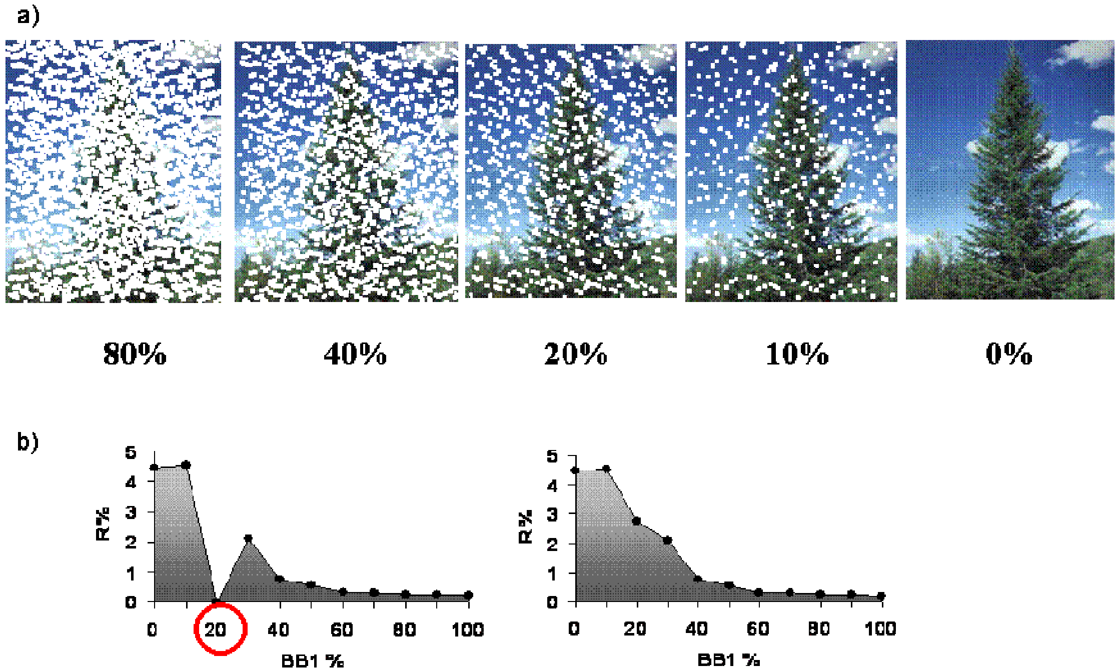

Figure 2.17. Illustration of the auto-corrective behavior of the continuous evolution profiles. a) Images of a tree presenting different percentages of defective pixels. b) 2D CEP corresponding to the injection of a protein. On the left, the 2D profile obtained with an array containing a defective CoCRR. On the right, normal 2D profile obtained with an array without any defect.

2.3.2. Classification of samples using principal component analysis

Data containing high dimensionality can be studied using several mathematical methods. One of the most popular ones is Principal Component Analysis (PCA). In this thesis, it was used for classification purposes. It takes data in n dimensions and reorients the axes along which the data are represented. The axes are chosen such that PC1 contains the majority of the response variance from the data; PC2 is orthogonal to PC1 and contains the second most response variance, etc. This mathematical approach is extremely useful for convenient visualization by re-expressing the original data along a truncated number of principal components, thus elucidating in two dimensions the natural response clustering of higher-dimensional data, see Figure 2.18 for illustration [109, 110]. In this work, PCA was performed using the appropriate package within Mathematica 8.0 software.

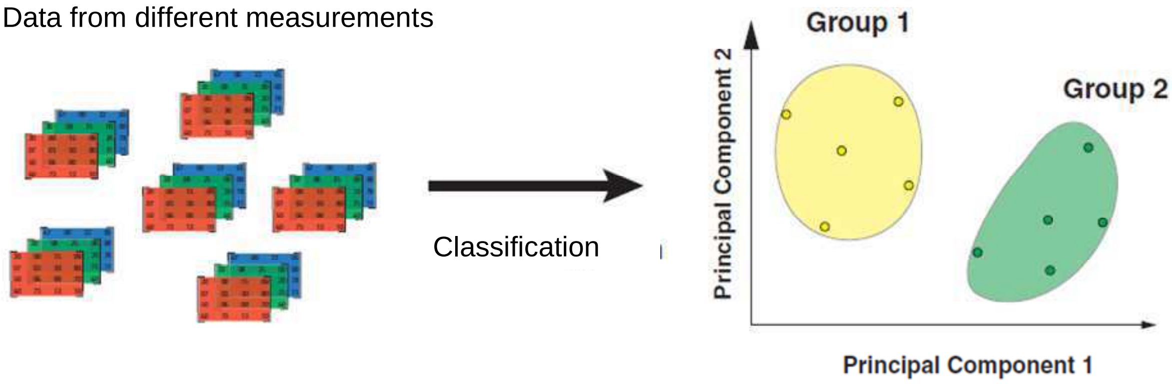

Figure 2.18. Classification of samples by PCA. Figure adapted from reference [26].

CHAPTER 3.

Differentiation and Identification of Pure Proteins and Complex Mixtures Using the Electronic Tongue

Résumé en français du chapitre 3

Différentiation et identification de protéines pures et de mélanges complexes avec la langue électronique

Le but principal du chapitre 3 est d'explorer les capacités de la langue électronique développée pour des tâches de différentiation et/ou d'identification d'échantillons par rapport à des références connues. La première étape de cette exploration consiste à calibrer le système ; pour cela des tests sont réalisés afin de vérifier que la réponse des plots est due à leur interaction avec l'analyte et non à des différences de sensibilité intrinsèque. La sensibilité globale du système est également vérifiée afin de s'assurer qu'il est utilisable en pratique pour l'analyse d'échantillons réels.

Une fois cette vérification réalisée, la langue électronique est utilisée pour la différentiation et l'identification de protéines pures. Pour cela, trois protéines sont sélectionnées : CXCL12α, CXCL12γ et ECL. Les deux premières protéines sont des isomères de la même protéine, connue pour son affinité envers l'héparane sulfate, un polysaccharide présent sur les surfaces cellulaires. La structure de l'héparane sulfate est très variable étant donné la quantité de variantes structurales des sucres qui le composent, ainsi que la diversité de répartitions de charge qu'il peut présenter. Nous estimons que la composition des BBs, en particulier leur nature disaccharidique chargée ou non, utilisées pour la fabrication de notre langue électronique peut donner lieu à des caractéristiques de surface mimant les différentes densités de charges de l'héparane sulfate. Les raisons du choix des protéines CXCL12α et CXCL12γ reposent ainsi sur notre volonté de vérifier, d'une part, qu'elles sont bien détectées par le système, et d'autre part, que le système est, en effet, capable de faire la différence entre deux protéines de structure proche. Enfin, le choix de l'ECL est dicté par son interaction bien connue avec le lactose.

Les trois protéines ont donc été successivement analysées avec la langue électronique. Les résultats obtenus, sous forme de profil CEP, montrent que le système est non seulement capable de détecter la présence des protéines en solution mais également que les profils obtenus pour les trois protéines sont différents. Le système s'est ainsi montré apte à différentier deux protéines dont l'une est affine à l'héparane sulfate et l'autre non, ainsi qu'à identifier deux isomères de la même protéine.

L'injection de mélanges de protéines a aussi été étudiée. Les résultats montrent que l'injection conjointe de deux protéines génère un CEP que l'on peut décomposer en deux CEPs correspondant aux deux protéines pures composant le mélange. Ces résultats sont très encourageants pour la suite et la complexification des échantillons à analyser.

Une grande quantité des systèmes de langues et nez électroniques qui ont été développés à ce jour ont trouvé leur application dans le domaine alimentaire. Nous avons donc ensuite voulu mettre à l'épreuve notre système avec des échantillons de ce domaine, tels que du vin, de la bière et du lait. Après l'injection de ces échantillons, l'analyse des résultats sous forme de CEP et CEL ainsi que l'analyse ACP nous ont montré que les trois types d'échantillons étaient différentiables. Dans le même esprit, des analyses d'échantillons de lait en cours de vieillissement ont été faits afin de distinguer l'état du lait après 48 et 72 heures de conservation à 25 ºC ou juste après ouverture.

Les bonnes performances de différentiation et d'identification d'échantillons nous ont conduits à considérer le point faible d'une grande quantité de systèmes de langues électroniques : la reproductibilité et la stabilité. Les résultats obtenus à ce sujet sont très satisfaisants. Suite à l'injection répétée d'une même protéine sur le même prisme, une corrélation supérieure à 98% entre deux profils est obtenue. Cette valeur diminue légèrement lorsque les injections comparées sont effectuées sur des prismes différents (>93%), ce qui indique qu'une meilleure fiabilité peut être obtenue lors d'une expérience réalisée entièrement sur un même prisme. La stabilité à long terme d'un prisme a par ailleurs été évaluée. La comparaison de profils obtenus lors d'injections d'une même protéine sur un même prisme au cours d'une période de 5 mois donne une corrélation supérieure à 95%, ce qui signifie une excellente stabilité à long terme du système développé de langue électronique.

En conclusion, l'approche choisie pour le développement d'une langue électronique se montre très prometteuse pour l'élaboration de systèmes d'analyse dans plusieurs domaines. D'une part, ce système est suffisamment sensible pour la détection de molécules biologiques et est même capable de différentier celles qui sont structurellement très proches. D'autre part, quand il est exposé à des mélanges complexes comprenant des centaines de composants, il est capable de donner une réponse qui permet, non seulement la classification selon la nature du mélange, mais aussi le suivi de l'état du vieillissement de l'échantillon. Ces résultats, accompagnés d'une bonne reproductibilité et stabilité du système, nous ont encouragés à poursuivre l'exploration des applications de ce système et en particulier à l'utiliser pour l'étude détaillée d'interactions sucre-protéine.

Differentiation and Identification of Pure Proteins and Complex Mixtures Using the Electronic Tongue

In this chapter, preliminary experiments were carried out in order to evaluate discrimination capacities of our system as an electronic tongue. For this, samples of varying complexities were analyzed, including single-component samples, such as pure proteins with both HSbps and non-HSbps, dual-component samples by mixing two pure proteins, as well as real-world complex samples, such as beer, wine and milk. The objective was to explore potential applications of the developed electronic tongue in different domains

3.1. Calibration of the electronic tongue

First of all, calibration procedures were performed on the array to see if there is intrinsic sensibility difference between spots. To do so, a classical procedure was used by injecting a NaCl solution (8.57 mM) on the array [98]. Under such a condition, the contribution of signal changes are dominated by changes in bulk solution’s refractive index and not by changes in any adsorbed film. As shown in Figure 3.1, the sensibility of the different BB% spots towards NaCl was very similar with a variance of <5%. This means that the change on each spot upon analyte injection is not related to CoCRR intrinsic sensibility differences but to the affinity of the CoCRRs for the analyte.

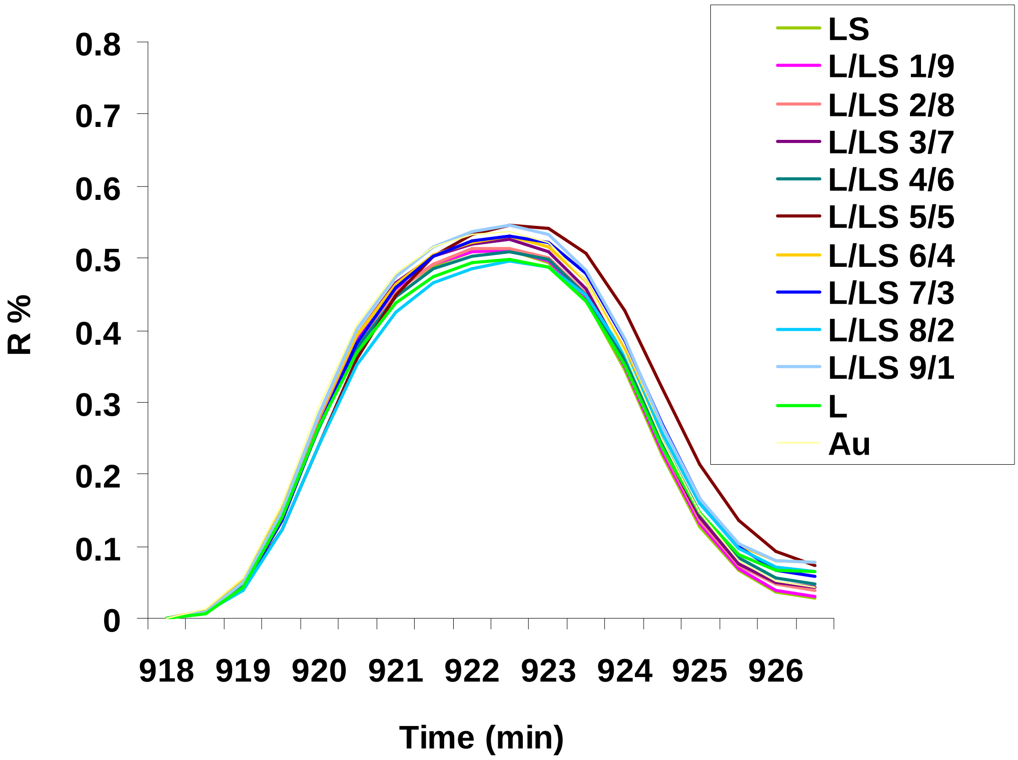

Figure 3.1. Reflectivity change induced by the injection of an aqueous solution of NaCl 8.57 mM on the CoCRR array.

Then, in order to verify if the CoCRR array functions correctly as sensing system, a calibration curve was established using a protein *Erythrina cristagalli lectin* (ECL), which is known to be a lactose-binding protein [111]. Injections of ECL were made at various concentrations, 200 nM, 400 nM, 800nM and 1.6µM.

The obtained reflectivity data of all the CoCRRs after the end of complete ECL injection (t = 8min) were averaged and plotted versus the injected protein concentration. This led to a curve (see Figure 3.2), that fits a Langmuir adsorption profile, from which a K_D with a value of 300 +/- 50 nM could be extrapolated [112]. This confirms the capacity of the e-tongue system to function as a detection array.

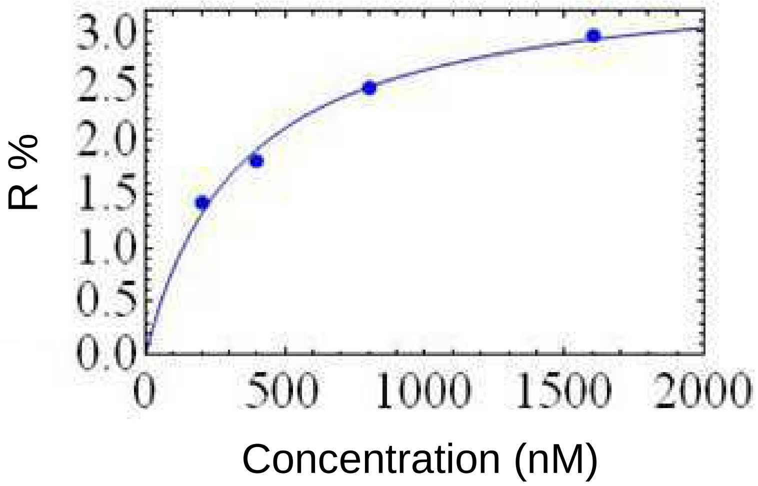

Figure 3.2. Calibration curve obtained with the electronic tongue (e-tongue) by plotting reflectivity signals for ECL injections at different concentrations.

3.2. Differentiation and identification of pure proteins

For preliminary tests, two HSbps, the α and γ isoforms of the chemokine CXCL12, were analyzed. They were provided by Dr. Hugues Lortat-Jacob (Groupe Structure et Activité des Glycosaminoglycanes, Institut de Biologie Structurale, Grenoble, France). ECL was also analyzed since it is a non-HSbps and should represent a negative control for binding onto CoCRRs containing a low BB1%. In addition, as it is a lactose-binding protein, ECL could be used as a positive reference for the CoCRRs rich in BB1. The structures of these three proteins are shown in the following part.

3.2.1. Characteristics of the tested proteins

CXCL12α and CXCL12γ

Chemokines represent a family of small proteins (8-12kDa) comprising over fifty members. These proteins bind to and trigger the activation of G-protein coupled receptors and ultimately promote the directional kinesis of a large array of cells [113]. Interestingly, most, if not all, chemokines bind to heparan sulfate, a glycosaminoglycan (GAG) present ubiquitously at the cell surface and in the extracellular matrix. HS is thought to affect the local concentration, compartmentalization, stability, structure or activity of its ligands. Chemokines are traditionally classified into four groups (CC, CXC, CX3C, and C) depending on their structure [114, 115]. They all have very similar tertiary structures, organized around a core domain with a triple stranded β-sheet overlaid by a C-terminal α-helix. Upstream of the β-sheet is the N-terminal region. The overall structure is stabilized by disulfide bonds involving N-terminal and core domain cysteines.

CXCL12, a chemokine highly conserved among mammalian species and also called SDFα, is constitutively expressed within tissues during organogenesis and adult life. Its biological activities are mainly mediated by the G-protein coupled receptor CXCR4, to which the chemokine binds. The CXCL12/CXCR4 signaling axis is critically involved in a wide variety of physiological functions. These include margination of neutrophils into the site of infection, embryonic development, mobilization and direct migration of stem cells, and neurological function [116, 117]. Most information on this chemokine has been obtained from two isoforms (CXCL12 α and β). Nevertheless, a novel isoform, CXCL12γ, was identified more recently [118], and is characterized by a distinctive 30 amino acids long C-terminal peptide. This peptide contains three HS-binding domains and is characterized by an important flexibility and high disorder in solution, while the first 68 residues of CXCL12γ have a very similar structure to that of CXCL12α with a typical chemokine fold. It has been demonstrated that the C-terminus extension is strongly involved in GAG recognition. This, in combination with the heparin (HP, a highly negatively charged GAG) binding site of the core domain, provides the chemokine with the highest affinity for HP ever observed: K_D =

0.9nM for CXCL12γ (93nM for CXCL12α) [113]. In Figure 3.3, structures of the α and γ isoforms of CXCL12 are presented.

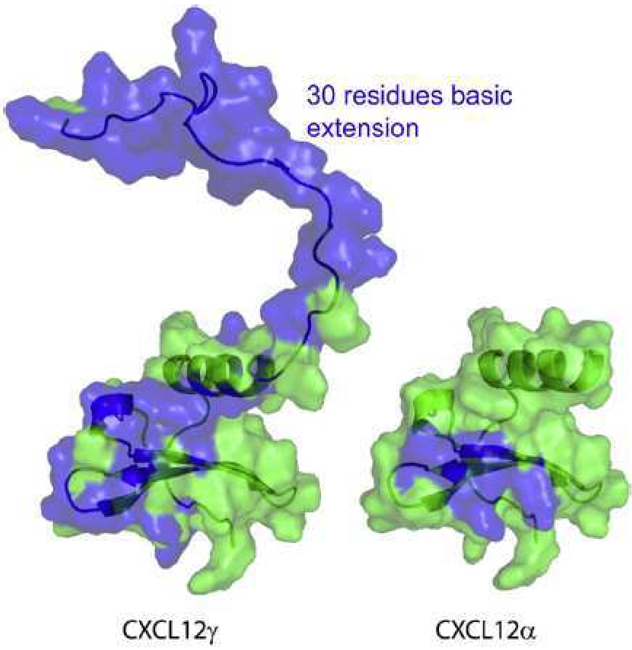

Figure 3.3. GAG Binding surfaces of the CXCL12 α and γ isoforms. The GAG binding sites on both CXCL12α and CXCL12γ are shown in blue. The γ isoform is characterized by an extended GAG binding surface that provides the chemokine an unprecedented high affinity for HS. [113]

Erythrina cristagalli lectin (ECL)

Erythrina cristagalli lectin (ECL) is a galactose-specific legume lectin. With a molecular weight of 54 kDa, ECL is biologically active as a dimer, where both of the subunits contain a functional carbohydrate binding site [119]. The crystal structure of native ECL has recently been determined in complex with lactose and frucosyllactose [120]. Protomers of ECL adopt a jelly-roll fold characteristic of legume lectins (Figure 3.4). The binding site is located in a shallow cleft on the surface of ECL and accommodates the galactose moiety of bound carbohydrates. ECL binds lactose through a set of structural water molecules, which mediate indirect hydrogen bonds between the lectin and the O2, O3 and O6 of galactose and the O2 of glucose. Hydrophobic stacking interactions are also observed between the lactose and lectin [119].

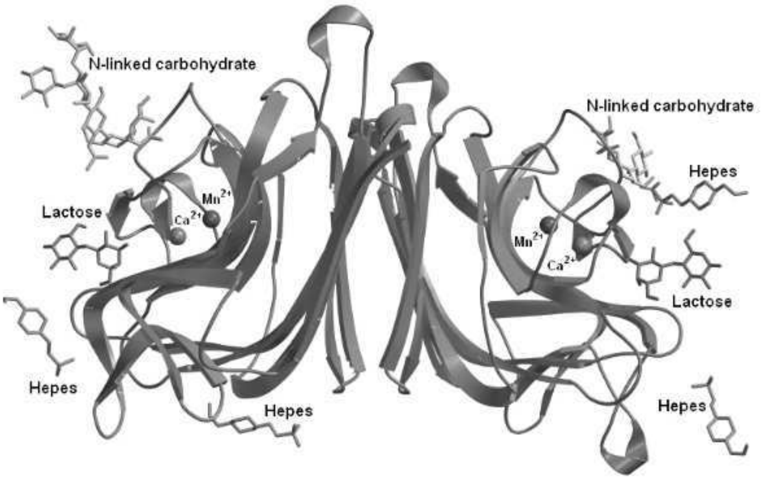

Figure 3.4. Structure of ECL dimer, which is stabilized by two hydrogen bonds and a series of contacts between side chains in four strands of the flat, six-stranded β-sheet. Each protomer adopts the conserved jelly-roll fold characteristic of legume lectins. The N-linked carbohydrates, lactoses bound at the binding site and HEPES molecules (from the crystallization medium) are shown. The manganese and calcium ions bound in the vicinity of the combined site are shown as small spheres. [119]

3.2.2. Analysis of pure proteins

The e-tongue was first used to analyze pure proteins, concretely to differentiate HSbps from non-HSbps by injecting sequentially solutions of CXCL12α, CXCL12γ (both 100 nM) and ECL (200 nM). For regeneration of the CoCRR array after each protein injection, different solutions were tested. The optimal conditions for complete regeneration of the array without any damage on the chip surface are: NaCl (1M) after CXCL12γ injection, SDS (1%) after CXCL12α injection and NaOH (0.02M) after ECL injection.

After protein injections, analysis of the sensorgrams revealed that the different CoCRRs displayed different reflectivities for a given protein. More importantly, the individual response of each protein on a given CoCRR is dependent on the composition of the parent BB mixture. In other words, for a given CoCRR composition, the intensity of the response is dependent on the protein injected, indicating that the CoCRRs array responds differently toward each protein. For easier visualization, a 2D continuous evolution profile was generated for each protein sample, as illustrated in Figure 3.5.

The resulting CEPs for the three proteins were clearly differentiable. We thus further explored whether the CEP obtained for each protein could be used for reliable identification. ECL, as expected, displays a higher affinity for CoCRRs rich in BB1, reaching a maximum for the CoCRR containing 70% of BB1. In contrast, the HSbps have higher affinity for CoCRRs with higher content in BB2, reaching a maximum for the CoCRR containing 90% of BB2.

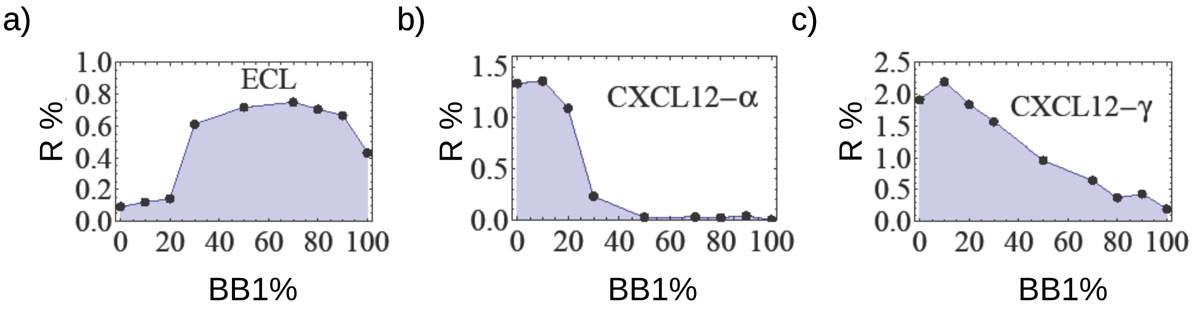

Figure 3.5. CEPs corresponding to a) ECL injection, b) CXCL12α injection, and c) CXCL12γ injection.

More importantly, it is noteworthy that the response obtained from a CoCRR for a given protein is not a simple linear addition of the responses obtained on the pure BB1 and BB2 spots. This non-linear behavior allows each combinatorial receptor to generate additional information relative to its neighbors, justifying a posteriori the use of a set of CoCRRs instead of spots of pure BB1 or BB2. It can be evidenced by the comparison of the CEPs obtained for the CXCL12α and γ. Indeed, even though they display similar behavior towards pure BB1 or BB2 receptors, they differ notably in their binding on receptors of mixed compositions: the reflectivity for CXCL12α is almost zero when BB1 content in the CoCRR is 50% or higher, whereas CXCL12γ still binds significantly on CoCRR containing up to 70 % BB1.

The difference in the CEPs of the two isoforms could be explained by their structural differences. As described previously, both CXCL12 isoforms share the same first 68 amino acids, which are similarly folded and display a typical HS binding site (K24-K27-R41) located in a highly structured domain. Moreover, the CXCL12γ contains additional HS binding sites in its unfolded C-terminal extension, which displays high conformational flexibility. This flexibility could maximize contact points with the ligands at low energetic cost through conformational fluctuations. In contrast, the single HS binding domain of CXCL12α is located in a rigid domain that may limit the adaption of the conformation of basic residues to low charge density CoCRRs.

These results proved that 2D CEPs generated by the e-tongue can be used as recognition patterns for both differentiation and identification of different pure proteins, even for the two isomers of the same protein. In addition, these results reveal that the designed CoCRR array is very sensitive to the charge topologies of HSbps and offers an unprecedented and simple tool to investigate the overall organization of the HS domains (charge density and distribution along the chain), independent of the fine structure found in the polymer. [121, 122] This will be discussed in more detail in chapter 4.

3.3. Analysis of protein mixtures

Beyond the differentiation and identification of pure samples, another goal of this work was to analyze complex samples. The preliminary study made in this direction was the injection of dual-component samples by mixing proteins ECL (200nM) and CXCL12α (100nM) (Mix1).

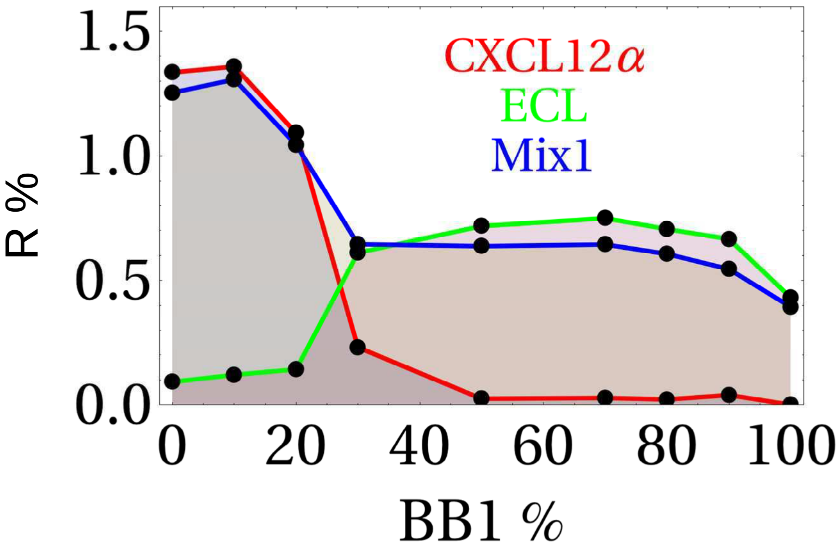

Figure 3.6. 2D CEPs of pure protein ECL (200 nM) in green, CXCL12α (100 nM) in red and their dual-component mixture (Mix1) in blue.

The CEP of the Mix1 is given together with those of ECL and CXCL12α in Figure 3.6. Gratifyingly, a simple visual examination of the three CEPs established that the CoCRR array was able to discriminate between Mix1 and the individual proteins. Moreover, the Mix1 CEP indicates additive behavior with respect to the signals obtained from the pure proteins. A simple linear decomposition of the CEP into pure analytes showed the potential of the system for identification of components in this kind of relatively simple mixtures.

In addition, 3D recognition patterns, continuous evolution landscapes, were generated for ECL, CXCL12α and Mix1, as given in Figure 3.7. Such CELs, where time evolution is added to the 2D CEP analysis, illustrate the added value of real-time SPRi interaction measurements. Simple visual examination reveals that desorption of ECL is much faster than that of CXCL12α. Such kinetic information is supplementary and could facilitate further differentiation and identification of analytes. The third CEL, corresponding to the infusion of Mix 1, shows that CEL follows the additive behavior found for CEP.

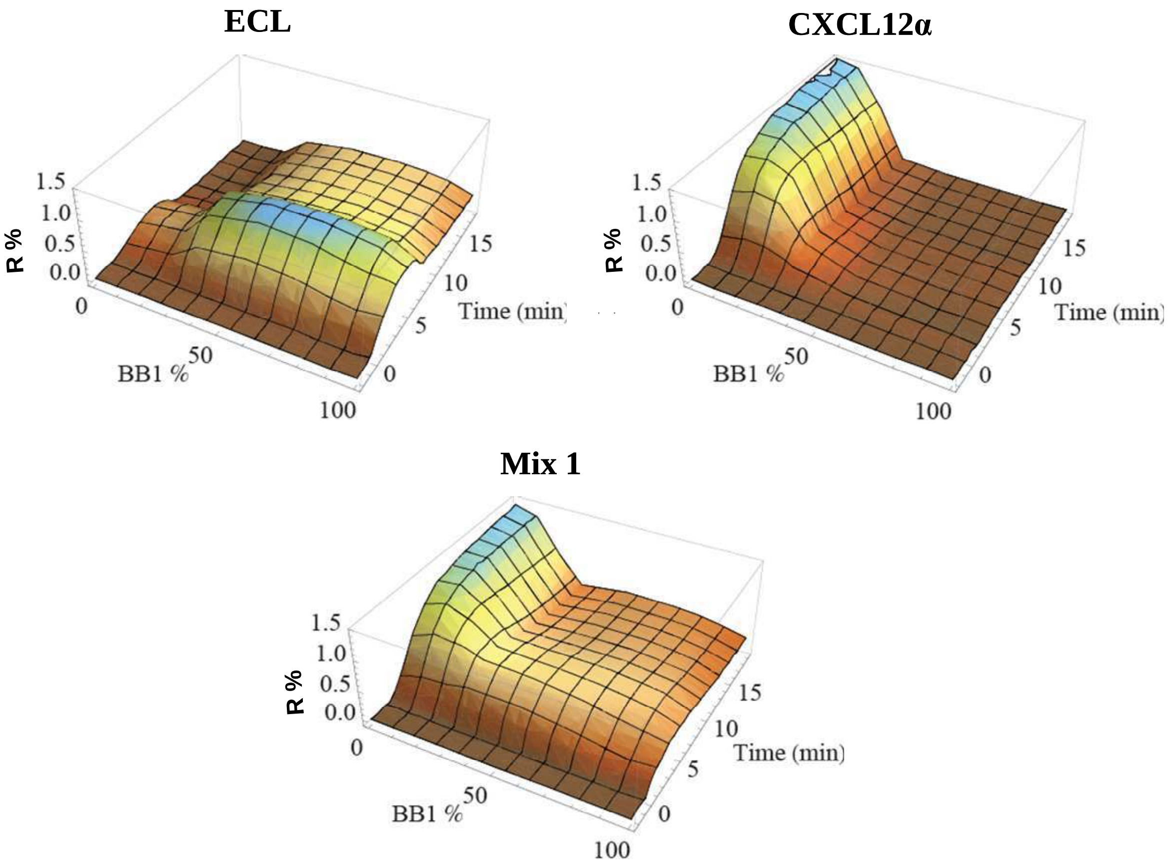
ECL

CXCL12α

Mix 1

Figure 3.7. 3D continuous evolution landscapes obtained with the electronic tongue for pure proteins ECL and CXCL12α, and their dual-component mixture (Mix1).

3.4. Analysis of complex mixtures

In the last decade, e-noses/tongues have emerged as promising alternatives for analysis of complex mixtures in the domain of food and beverages, particularly when a full component-by-component analysis is unnecessary, such as for comparisons against a standard, discrimination of subtle differences among mixtures, or detection of changes in the mixture as a function of time or conditions. [27, 123].

In this part, the feasibility of our e-tongue system for analysis of real-world complex samples and its potency for applications in the domain of food and beverages will be evaluated.

3.4.1. Differentiation and identification of complex samples

For this study three types of complex mixtures, wine, beer, and milk, were tested. In Table 3.1, all details about tested samples as well as their pre-treatment protocol are given.

Sample Type	Name	Origin	Sample Pre-treatment
Wine	Côtes du Rhône	France	Two filtrations through a 0.2 µm syringe filter and dilution to 1% (v/v) in
Wine	Bordeaux	France	

Wine	Bourgogne	France	HEPES buffer.
Beer	Stella Artois	Belgium	Degassing by filtration under vacuum through a 22 µm sintered glass filter, filtration through a 0.2 µm syringe filter and dilution to 10% (v/v) in HEPES buffer.
Beer	Leffe	Belgium	
Beer	Pelforth-dark	France	
Milk	Casino UHT	France	Dilution to 0.125% (v/v) without any other pre-treatment

Table 3.1. Tested complex samples and their corresponding pre-treatment protocol.

They were all bought in a local supermarket and freshly opened before treatment and injection on the system. At least three replicated injections and measurements were performed for each sample in a random order during the experiment. After each injection, the array was regenerated with 2% SDS (w/w) dissolved in ultrapure water, which permits complete regeneration of the system without any damage.

Upon the injection of the complex mixtures, the resulting sensorgrams revealed that the CoCRR array was sensitive to all these three kinds of complex samples. More importantly, it responded quite differently toward each beverage species. Figure 3.8 shows examples of the unique CEL and CEP recognition patterns generated by the CoCRR array for each species. The CEPs correspond to the section of the corresponding CELs at the 13th minute after sample injection, which is 6 minutes after the end of injection. This time was chosen to avoid the strong refractive index changes systematically induced by complex mediums. Our studies showed that, at the 13th minute after sample injection, the intensity of signal on the CoCRRs for each beverage species is more related to the binding affinity rather than to the changes of refractive index.

Clearly, the three CELs and CEPs were very different from each other. The CELs offered an accurate representation of the time-dependent recognition patterns of the CoCRR array, while the CEPs offered a more direct way to evaluate the binding affinity between all the CoCRRs and each beverage species. Gratifyingly, the CEP of red wine reached a maximum for the CoCRR containing 100% BB1 and was completely different from the ones obtained for beer and milk, which displayed maximal signals at 100% BB2. Moreover, the signal intensity upon injection of milk was much higher than those following injections of beer or wine, permitting its differentiation. Remarkably, for the milk sample the signal intensity on the CoCRRs rich in lactose BB1 was very low, probably due to the competition of lactose present in abundance in milk. In a word, their CELs and CEPs showed remarkable differences between each other and could thus behave both as “fingerprints” for rapid differentiation and identification of each species.

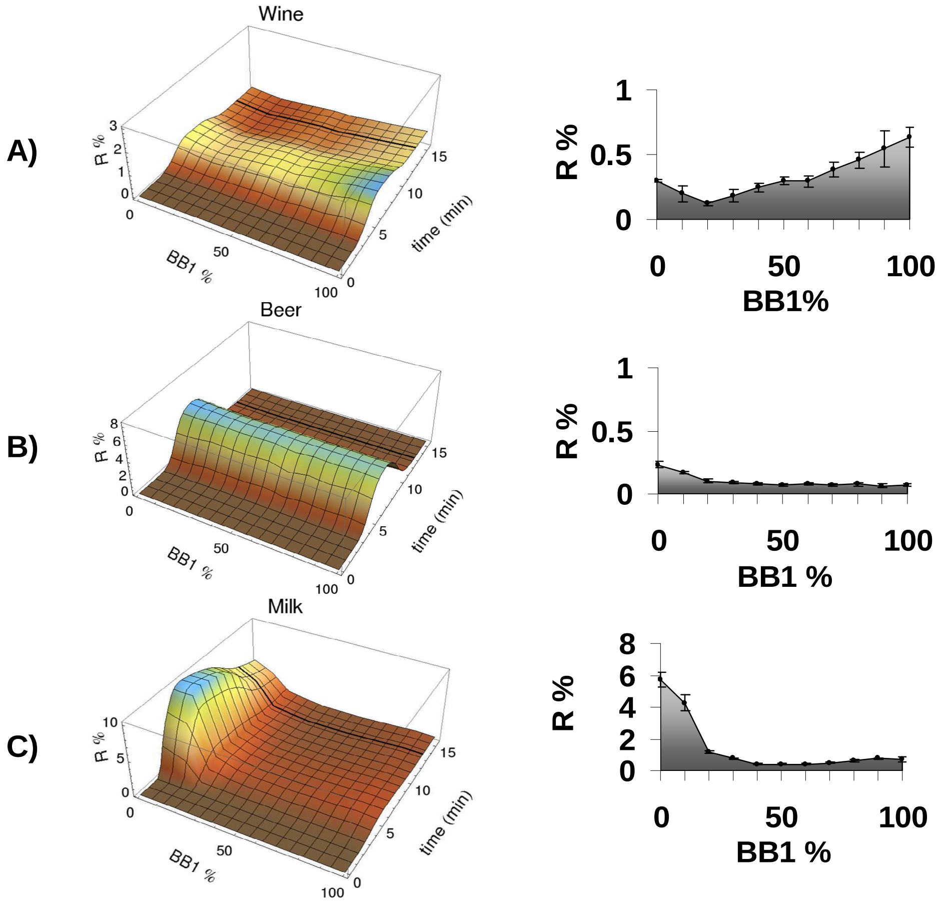

Figure 3.8. 3D CELs and 2D CEPs generated by the e-tongue for complex mixtures: A) Red wine (Bourgogne); B) beer (Leffe) and C) UHT milk. Each error bar represents the standard deviation of four duplicates of the CoCRRs on the same array.

3.4.2. Classification of complex samples

The capacity of the e-tongue for classification of complex mixtures was then studied using a larger number of samples, including three different brands of red wines (Côtes du Rhône, Bordeaux and Bourgogne) and beers (Stella Artois, Leffe and Pelforth-dark), as well as UHT milk. For easier visualization, the data based on CEPs were analyzed by PCA to classify these samples in a 2D single plot. PCA was performed using the experimental data of 33 complex mixture injections where the 11 ratios of the BB were considered as independent variables.

Triplicate measurements for each brand of wine and beer were plotted together with fifteen replicated measurements for the UHT milk sample, as shown in Figure 3.9. Excellent separation of the three species was obtained using the two principal component axes to present 97% of the variance in the original data set. This attested to the significant degree of success in the discrimination of these real-world complex mixtures using the model e-tongue system. However, there is no clear distinction between different brands of wines and beers. More building blocks with different physicochemical properties are needed to obtain more efficient discrimination between different brands of the same species.

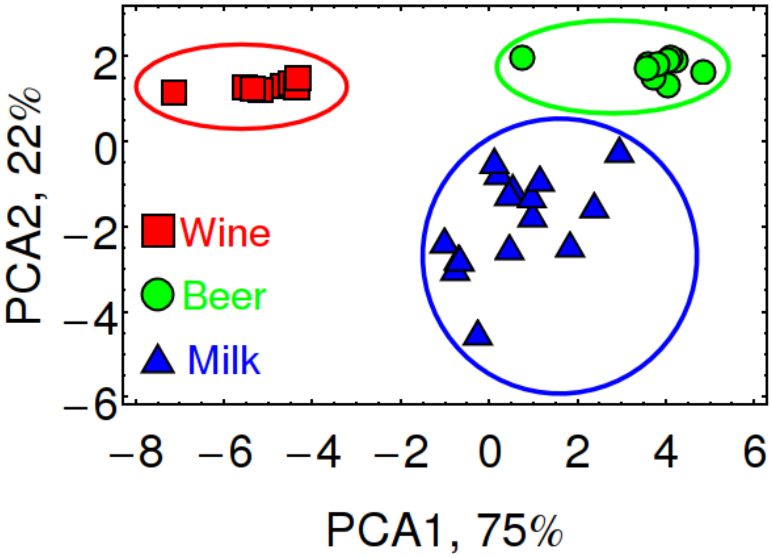

Figure 3.9. PCA score plot using two principal components representing 97% of the variance from the original data for the analysis of complex mixtures wine, beer, and milk.

3.4.3. Monitoring the spoilage of milk by the e-tongue

Food shelf life, especially that of diary products such as milk, varies with the age and the type of ingredients, the process, the packaging, the environmental conditions during distribution, and consumer holding. The control of the first three factors is carried out by manufacturers, which can ensure the initial quality of the product. However, the quality of beverage products depends not only on the manufacturers, but also on existing distribution, marketing systems and consumer food storage habit [124]. Thus, quality control of food and beverages is extremely important for both industrial and personal concerns. Traditional methodologies (e.g., gas or liquid chromatography), though accurate and reliable, are often time-consuming and laborious to perform. Consequently, there has been an increase in demand for new technologies able to provide reliable, inexpensive and rapid analysis. E-noses/tongues have emerged as promising alternatives in such contexts.

To demonstrate the potential of our e-tongue system for quality control in the food and beverage industry, a set of preliminary experiments were conducted to monitor the deterioration of UHT milk over time. Immediately upon opening, undiluted aliquots of milk samples were stored at 25°C in an open tube and measurements were taken 1, 24, 48, and 72 hours after exposing the sample to air. The resulting 3D landscapes are shown in Figure 3.10A.

The pattern of the milk after the 1st hour of storage was barely distinguishable from that obtained after 24 hours but easily distinguishable from those collected in the 48th and 72nd hours, which may be attributed to milk spoilage. Moreover, the array allowed imaging the changes in the complex milieu with increasing storage time. The signals of the CoCRRs rich in BB 2 increased for storage time up to 48 hours, then decreased: the CoCRR containing 100% of BB 2 displayed 4% reflectivity after 1 hour of aging, 5.5% after 24 hours and 11.8% after 48 hours. Then, the signal decreased to 1.5% after 72 hours of aging, which was even lower than that of fresh milk and was associated with casein precipitation in the spoiled milk. These preliminary results demonstrated that the CoCRRs-SPRi e-tongue system is quite sensitive to the changes associated with the deterioration of the milk.

The PCA derived from the data obtained using these milk samples, each with at least six replicates, is shown in Figure 3.10B. Two principal components accounted for 99.2% of the total variance and corroborate the visual examination of the CELs. The absence of clear separation between the clusters representing patterns of the milk samples after 1 hour and 24 hours storage may be attributed to a lack of major changes in the complex mixtures between the two stages. Importantly, excellent discrimination was achieved between these samples and those stored for 48 and 72 hours, illustrating that the e-tongue is able to discriminate between different aging phases of milk and thus confirming the potential of the CoCRRs-SPRi e-Tongue system for quality control of milk.

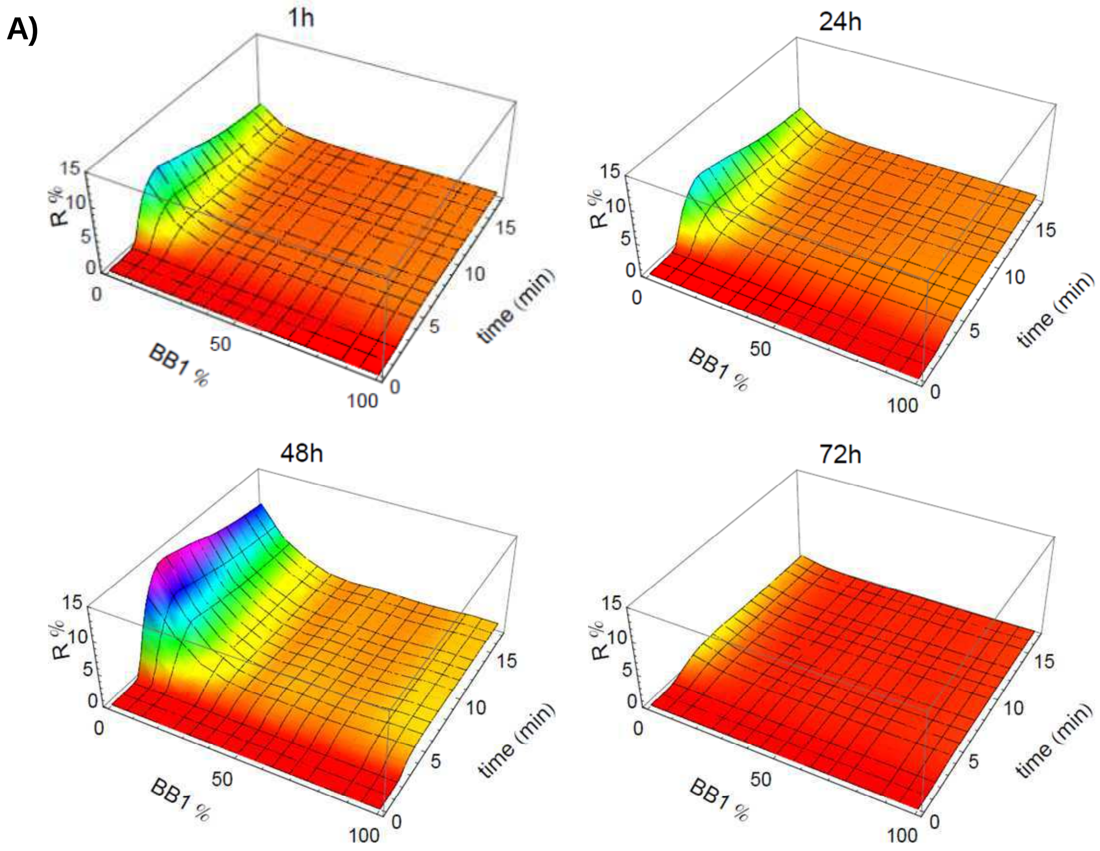

B)

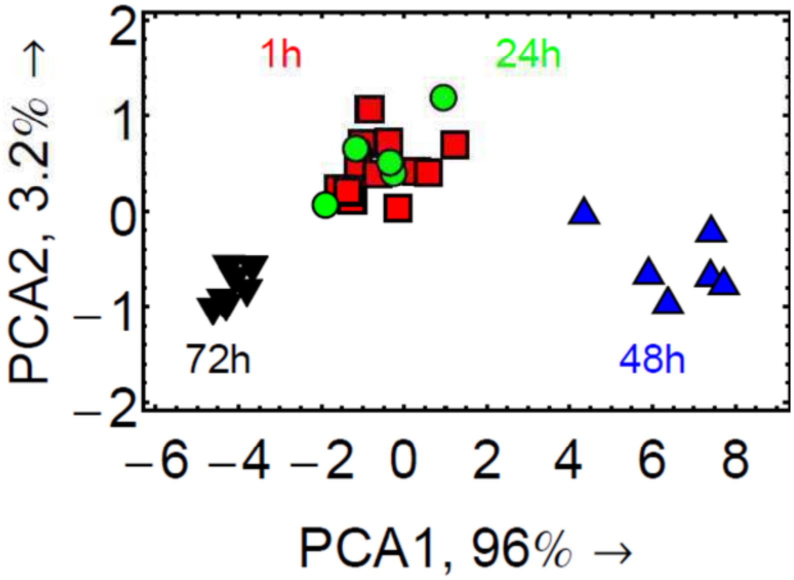

Figure 3.10. A) 3D CELs of the milk samples at the 1st, 24th, 48th and 72nd hour after opening. B) PCA score plot of the two most important principal components representing 99.2% of the variance from the original data for the milk samples at the 1st, 24th, 48th and 72nd hour after opening.

3.5. Repeatability and stability

For any e-nose/tongue system, there are two important features: repeatability and stability. Evaluating the repeatability and stability is much more complicated for systems incorporating multidimensional sensor arrays than for devices based on single sensors. In this thesis, the repeatability and stability of the CoCRR arrays was not evaluated for each cross-reactive receptor separately but for the correlation between the overall 2D CEP patterns obtained with replicated measurements. The continuous evolution profiles must be evaluated holistically to provide an accurate assessment of repeatability since the relationship between each ratio and neighboring points is crucial to understanding the agreement between two full patterns. The correlation coefficient C_{12} between two full patterns is defined as follows,

$$C_{12} = \frac{\sum_{BB1\%} R_1(BB1\%)R_2(BB1\%)}{\sqrt{\sum_{BB1\%} R_1^2(BB1\%) \sum_{BB1\%} R_2^2(BB1\%)}}$$

Equation 3.1. Calculation of the correlation coefficient C12 between two full patterns. R1 and R2 are the reflectivity values of the two CEPs to compare at a given BB1%.

3.5.1. Measurement to measurement and batch to batch repeatability

The repeatability of the e-tongue was evaluated both from measurement to measurement and from batch to batch with ECL (200 nM) as reference, due to its good stability and easy availability. ECL solutions were all freshly and identically prepared before injection. Systematically, for each round of measurements on a CoCRR array, ECL was injected at the very beginning, several times in the middle and at the end of the assay to evaluate the measurement to measurement repeatability. Generally speaking, a "round of measurements" consists of at least 20 analyte injection/regeneration cycles.

The results obtained upon different injections of ECL on the same CoCRR array during a period of 2-week in continuous use exhibited good repeatability between measurements. The correlation between two different full pattern profiles was >98% (not shown).

As for batch to batch repeatability, five different arrays were fabricated in the same way and tested with same sensing assay. The correlation between two different full pattern profiles was >93%, although at certain points, such as at the point of the 20% BB1, larger disparities between measurements may appear, as shown in Figure 3.11. This confirms that more reliable analysis can be obtained by such an e-tongue system based on patterns with continuous evolution profiles.

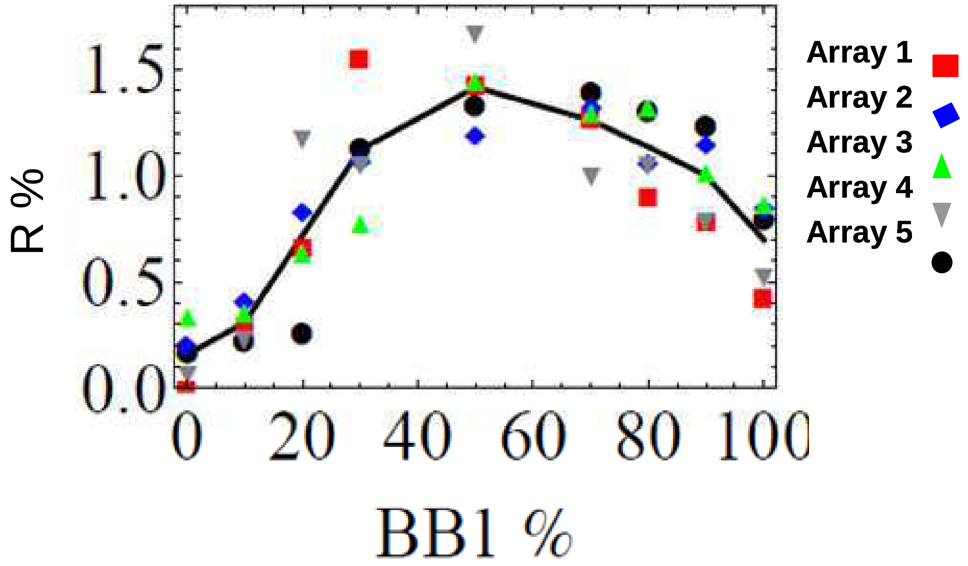

Figure 3.11. CEP of ECL (200nM) obtained with 5 different arrays for batch-to-batch repeatability evaluation.

3.5.2. Long-term stability

We have addressed the long-term stability of the CoCRR array upon storage at 4°C by performing regular injections of the ECL solution (200nM) over a period of 5 months (day 1, 3, 5, 9, 16, 23, 31, 50, 89, 116, and 157). After each measurement, the array was regenerated with 2% SDS, thoroughly cleaned with ultrapure water, dried carefully under an argon gas flow, and then stored in a small closed bottle at 4°C for reuse.

As shown in Figure 3.12, there is no significant variation for all patterns with respect to the signal intensity and profile. The coefficient C12 between any two different full patterns is >95%, which shows an excellent stability of the e-tongue upon prolonged storage.

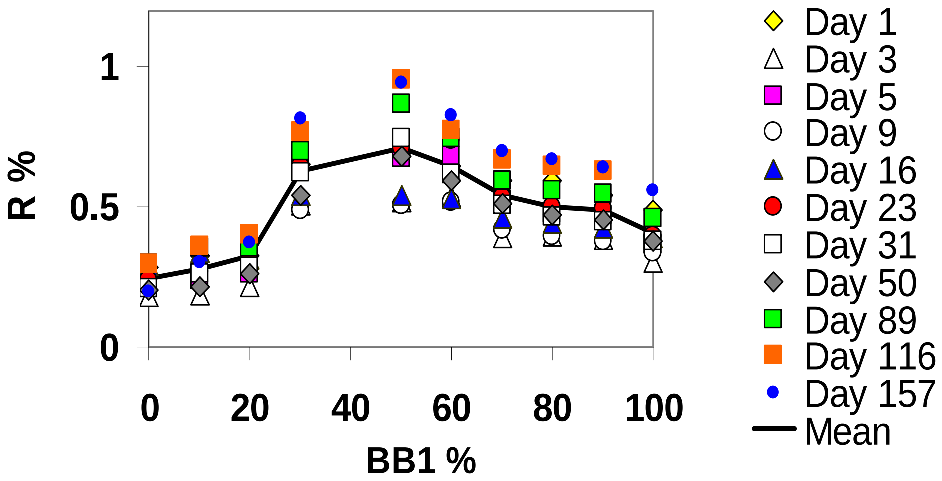

Figure 3.12. Long-term stability of the e-tongue, evaluated by injecting ECL (200 nM) on the same CoCRR array on different days. The profile of each color was obtained by averaging the signals of the four duplicates of each CoCRR. The black line is the average profile.

3.6. Main conclusions of the chapter

We have demonstrated that the CoCRRs-SPRi electronic tongue system is able to generate distinct 3D continuous evolution landscapes and 2D continuous evolution profiles behaving as “fingerprints” for differentiation and identification of various samples of different complexity, including pure proteins, protein mixtures, as well as complex mixtures. In addition to its ease of preparation, the identification of analytes is greatly simplified and secured with the continuous evolution profiles or landscapes. Furthermore, the electronic tongue exhibits very good repeatability and stability upon prolonged storage period up to 5 months. We thus believe strongly that this new methodology will contribute to the design of cheaper and more reliable e-noses/tongues and facilitate their implementation in even broader domains of application.

CHAPTER 4.

An Electronic Tongue With Biomimetic Properties

Résumé en français du chapitre 4

Une langue électronique avec des propriétés biomimétiques

Ce chapitre est dédié à l'exploration d'une idée née de l'observation de la forte interaction développée entre les protéines affines à l'héparane sulfate et notre langue électronique préalablement développée. Cette observation laisse penser que la langue électronique pourrait mimer la capacité de reconnaissance des protéines par l'héparane sulfate (HS).

Les chaînes HS sont des polysaccharides de structure très variable, qui font partie de la grande famille des glycosaminoglycanes (GAGs). Une propriété qui fait de l'HS une molécule intéressante est sa capacité d'interagir de façon spécifique avec certaines protéines. Il semblerait que cette spécificité dans la reconnaissance soit principalement due à deux propriétés structurales des chaînes HS. D'un côté, il existe des preuves qui indiquent que les micro-hétérogénéités provoquées par les différents motifs d'épimerisation et sulfatation des chaînes HS représentent un premier niveau de diversité moléculaire très importante pour la reconnaissance des protéines. D'un autre coté, il existe un deuxième niveau de diversité, donnée par la distribution des charges tout au long de la chaîne HS. En effet, les chaînes HS sont composées de domaines « A » où la charge globale est faible, de domaines « S » avec une forte charge négative, ainsi que de domaines « A/S » qui font la transition entre les domaines A et les domaines S. Tout cela forme des topologies SAS de charge le long de la chaîne.

De façon similaire, le système langue électronique développé contient à la fois une microstructuration, donnée par les caractéristiques structurales des mélanges de BB utilisées, mais également une distribution de domaines plus ou moins chargés, donnée par l'ensemble des CoCRRs sur la surface de prisme. Ce parallélisme rend possible le mime des propriétés de reconnaissance de l'HS par la langue électronique, et donc, son utilisation en tant qu'outil pour l'étude des interactions HS-protéine.

Les explorations menées sur ce sujet se sont basées sur l'interferon γ (IFNγ), une protéine de grand intérêt thérapeutique, qui contient une région C-terminale connue pour être le site d'interaction de l'IFNγ avec l'HS. Cette région contient deux domaines basiques, appelés D1 et D2, qui sont fortement impliqués dans la reconnaissance.

Les premiers résultats montrent que le système langue électronique est capable de donner un profil de réponse spécifique lors de l'injection de l'IFNγ, et que cette réponse est proportionnelle à la concentration de la protéine, ce qui peut être intéressant d'un point de vue quantitatif. L'affinité de l'interaction entre l'IFNγ et la langue électronique a pu être estimée sous forme de K_D. Le K_D calculé, de l'ordre de 0,5 µM, démontre une forte affinité qui n'est pas observée pour des protéines ne reconnaissant pas l'HS, ce qui prouve la capacité HS-mimétique de la langue électronique. Cette reconnaissance s'est révélée non seulement forte, mais aussi spécifique, car il fut possible de détecter de l'IFNγ dans un milieu riche en protéines, comme le sérum de veau fœtal.

Les caractéristiques de la reconnaissance de l'IFNγ nous ont encouragés à poursuivre l'exploration des interactions IFNγ-HS sur la langue électronique, en étudiant plusieurs types de mutants d'IFNγ fournis par notre collaborateur Hugues Lortat-Jacob (IBS, Grenoble). Les résultats obtenus lors de l'analyse par le système langue électronique sont très intéressants. Non seulement le système est capable de différentier certains des mutants d'une même protéine, mais il est également capable de fournir des informations concernant l'implication de certains domaines dans le processus de reconnaissance; informations qui sont totalement en accord avec les recherches faites à ce sujet par l'équipe du Dr. Hugues Lortat-Jacob.

Nous avons également montré que ce processus de reconnaissance avec la langue électronique est non seulement guidé par les interactions électrostatiques, mais que la structure moléculaire des BBs joue aussi un rôle important dans cette reconnaissance. Pour conclure, nous avons confirmé que les surfaces combinatoires ont des propriétés plus intéressantes que celles composées de BB1 ou BB2 pures, ce qui ouvre une nouvelle voie exploratoire de la langue électronique comme méthode de criblage de surfaces combinatoires d'intérêt thérapeutique pour la fabrication de nanovecteurs bioactifs.

An Electronic Tongue with Biomimetic Properties

In the previous chapter, it was demonstrated that the e-tongue, inspired by the way cell surface HS recognize HSbps, can generate distinct recognition patterns for two HSbps of the same family, CXCL12α and CXCL12γ, for their differentiation and identification. More interestingly, the capacity to bind, recognize and differentiate HSbps showed by our CoCRR-SPRi e-tongue suggests that, in some way, the e-tongue is able to mimic the recognition properties of HS and, thus, could be employed as a useful tool to study HS/protein interactions. In this chapter, a complete study will be carried out to explore biomimetic properties of the e-tongue.

4.1. Introduction to GAGs

Glycosaminoglycans (GAGs) are a family of linear, generally sulfated, polysaccharides present on all cell surfaces and in the extracellular matrix (see Figure 4.1). They are usually found attached covalently to core proteins forming the proteoglycan family. Two main types of cell surface-bound proteoglycan core proteins have been identified: the glypicans and the transmembrane syndecans. Both are thought to be expressed in high copy numbers (up to 10^6 per cell; [125]) [126].

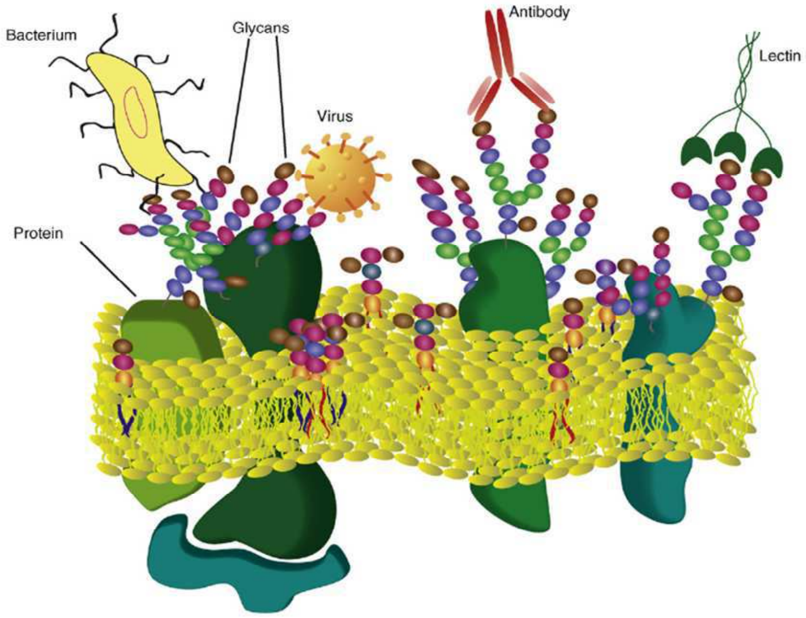

Figure 4.1. Illustration of cell surface glycans and their interactions with some biomolecules. From reference [127]

GAGs are also known as mucopolysaccharides because of their viscous, lubricating properties, as found in mucous secretions. This is why GAGs have been long thought to have the only function of water retention. However, more recently it has been discovered that some of them interact with a wide range of proteins including chemokines, cytokines, growth factors, morphogens, enzymes, extracellular matrix, or adhesion molecules involved in several physiological and pathological processes. These include cell growth, differentiation, morphogenesis, cell migration, inflammation, angiogenesis or viral/bacterial infections. [113, 128-130]

These long polysaccharides, all unbranched (with the exception of keratan sulfate), are composed of repeating disaccharide units; called disaccharide repeating regions. Each disaccharide is composed by a hexuronic acid and a hexosamine, except the keratan sulfate, which contains a galactose instead of the hexuronic acid. GAGs can be classified, thus, depending on the nature of the sugars on the basic disaccharide and their glycosidic bond, into two groups: the chondroitin/dermatan sulfate, containing a galactosamine as hexosamine, and the GAGs containing a glucosamine as hexosamine. This latter, at the same time, can be divided into three families: the hyaluronic acid, the heparan sulfate/heparin (HS/HP) and the keratan sulfate. All of them are schematized in Figure 4.2. However, this a priori simple structure leads to an extreme heterogeneity in GAGs due to the variations in length and different modifications that can take place (epimerization, sulfatation). [113, 129, 131] This structure variability seems to be the reason why GAGs are able to encode information to specifically interact with a number of important growth factors and functional proteins. These interactions are crucial to the biological functions of these proteins. For illustration, in Figure 4.3, we present a picture of the multiple roles of HS in cell physiology.

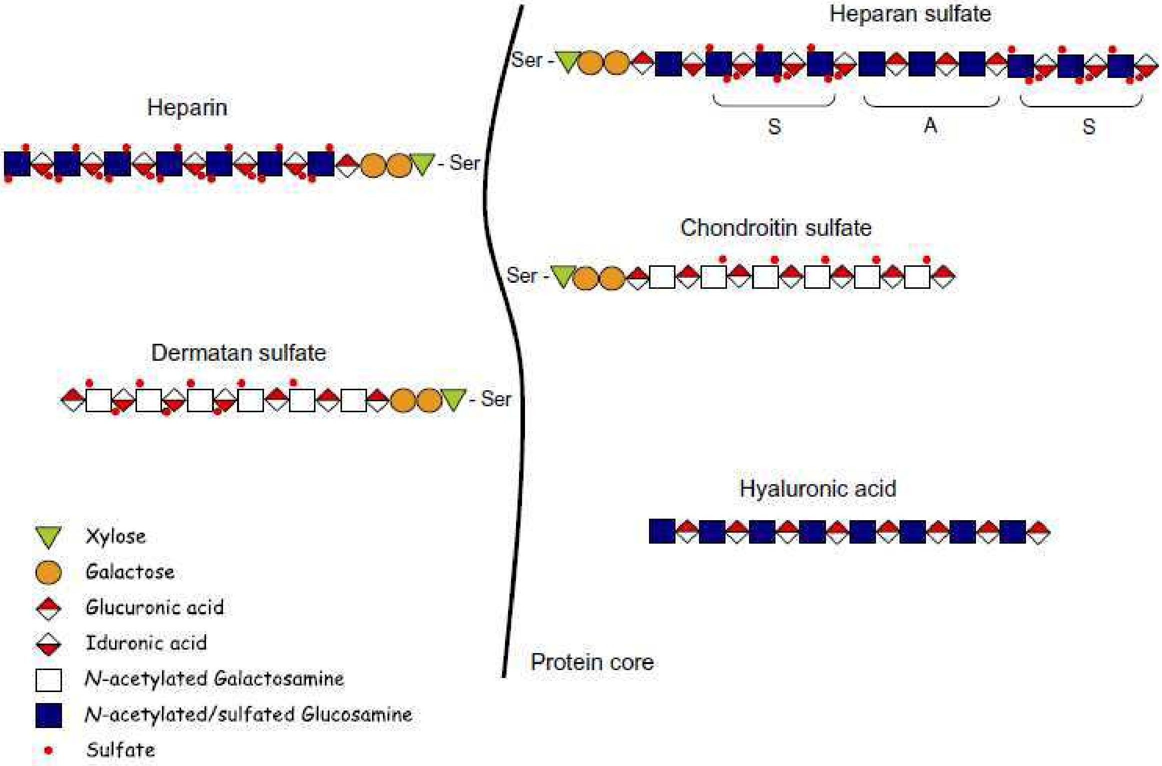

Figure 4.2. Schematic representation of the different GAGs. From reference [130].

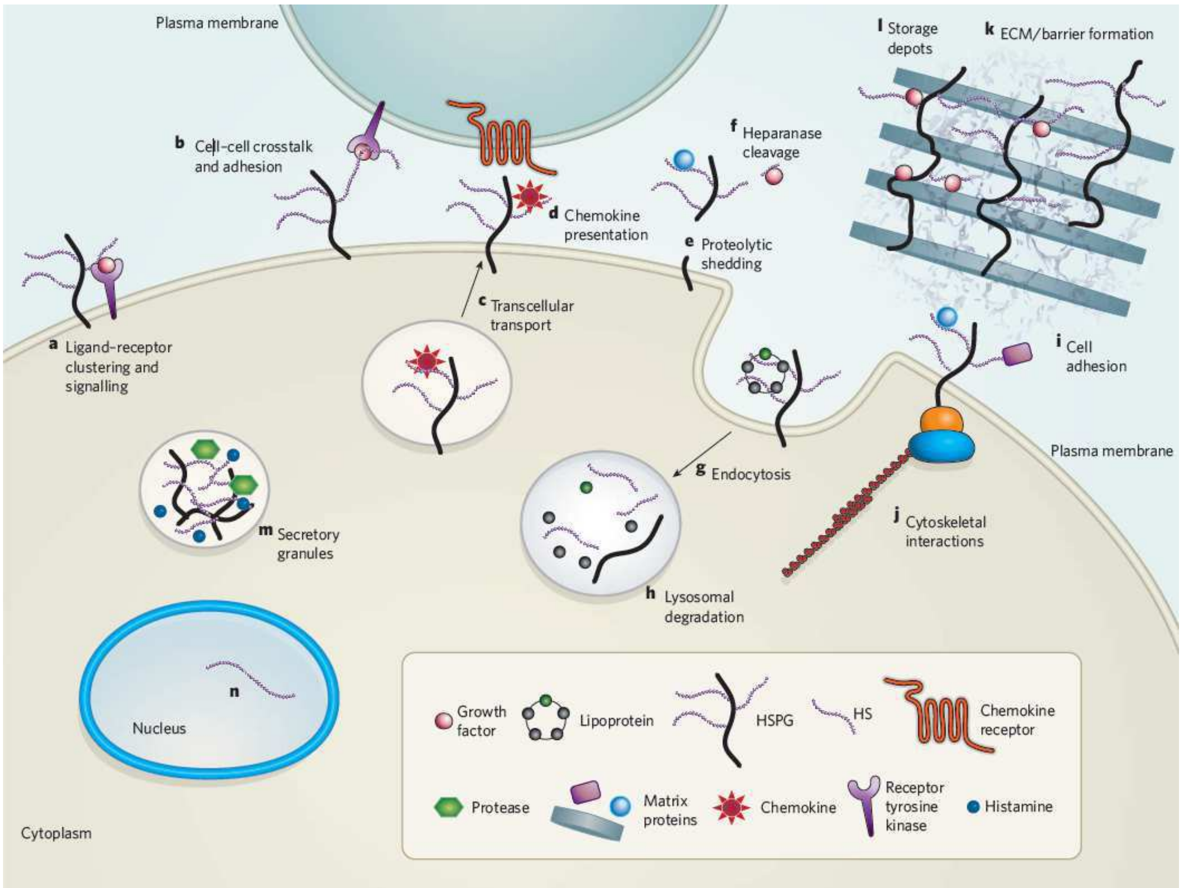

Figure 4.3. Illustration of the multiple roles of HS proteoglycans on cell physiology. HS proteoglycans function as co-receptors for growth factors and their receptor tyrosine kinases, which are present either on the

same cell (a) or on adjacent cells (b). They transport chemokines across cells (c) and present them at the cell surface (d). Proteolysis can liberate HS proteoglycans from the cell surface (e) and heparanase cleaves HS chains (f), liberating bound ligands (such as growth factors). Cell surface HS proteoglycans are actively taken up by endocytosis (g) and can recycle back to the surface or be degraded in lysosomes (h). HS also facilitate cell adhesion to the extracellular matrix (i) and form bridges to he cytoskeleton (j). Secreted HS proteoglycans are involved in the in the formation of organized extracellular matrices that form physiological barriers (k) an sequester growth factors and morphogens for later release (l). Serglycin carrying highly sulfated heparin chains is packaged into secretory granules of hematopoietic cells (m). Finally, some experiments suggest that HS chains are present in the nucleous (n), although their function in this location is unknown. From [132].

4.1.1. Heparin and heparan sulfate

The remarkable capacity of GAGs to specifically interact with functional proteins is particularly significant in HS and HP. The basic disaccharide unit of HS/HP consists in an uronic acid linked to a α-D-glycosaminyl moiety, linked itself to the next uronic acid residue. Structural distinction between HS and HP is difficult to establish and is generally performed on the basis of the polysaccharide sulfate content, since in HP a high proportion, generally over 80%, of the glucosaminyl residues is N-sulfated. The main difference between HP and HS is better established based on their localization in vertebrates: HP is essentially present in mast cells and is released in the extracellular matrix free from any core protein. HS is present linked to a core protein at the cell surface or in the extracellular matrix surrounding almost any type of cell [122].

HS is one of the most heterogeneous biopolymers. In addition to the possible configurations that can be adopted by the uronic acid, various sulfation patterns may occur along the chain. O-sulfation may occur on position 2 of the uronic acid and 3 and/or 6 of the aminosugar, while the glucosamine nitrogen may be sulfated, acetylated or, less frequently, unmodified, leading to 48 possible disaccharides, see Figure 4.4. The diversity grows exponentially with the polymer length, leading to 2304 possible tetrasaccharides 110592 hexasaccharides and more than $5x10^6$ octasaccharides.

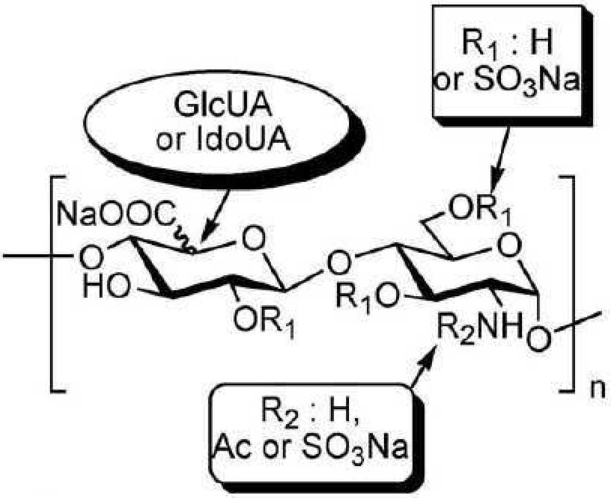

Figure 4.4. Theoretical molecular diversity found in HP/HS. Adapted from [122].

4.1.2. Heparan sulfate-protein interactions

Early evidence for specificity in HS-protein interactions was the ATIII-binding sequence, which is responsible for the clinically exploited blood anticoagulant activity of HP [133]. Each one of the sulfate substituents of this pentasaccharide structure is essential for high affinity interaction with ATIII, and, thus, for anticoagulant activity [126]. However, it was recently discovered that the existence of hypervariable domains in HS could not account for all the regulatory effects of this polysaccharide and that many interactions appear to depend more on the overall organization of the HS domains than on their fine structure [121]. Indeed, it seems that the microheterogeneities resulting from the variation in sulfation and epimerisation patterns represent only a first level of molecular diversity in HS. In fact, the polymer, typically composed of 50-200 disaccharide units, is not fully heterogeneous. Quite regular N-acetylated regions (A domains) with low global charge separate domains rich in L-iduronic acid and N-sulfated glucosamine (S domains) which are hypervariable and highly charged. In between, mixed A/S regions of variable length make the transition between A and S domains. Thus, in addition to the first level of molecular diversity, HS presents a second level of diversity due to the various combinations of S, A and A/S domains generating multiple SAS charge topologies along the polymer chain, as illustrated in Figure 4.5.

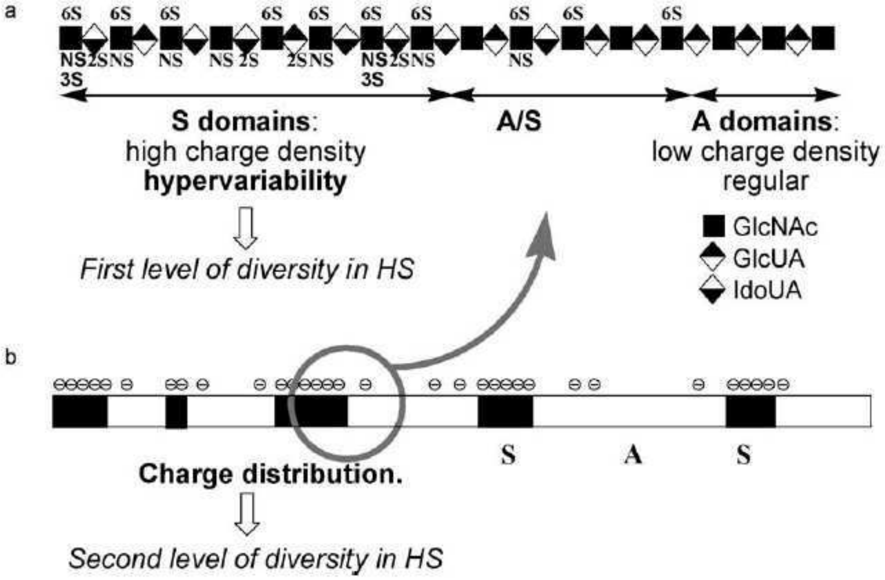

Figure 4.5. Dual molecular diversity in HS chains. a) Hypervariability resulting from various epimerisation and sulfation patterns generates a first level of molecular diversity. b) The charge distribution due to the alternation of S and A-A/S-domains of variable length, leads to different SAS charge topologies that generate a second level of molecular diversity. From reference [122].

The primary interaction between HS and a protein is an attraction between the highly negatively charged S-Domains and clusters of basic residues at the protein surface, mainly arginines and lysines. In some cases, a single S domain is sufficient to allow a high affinity interaction, whose specificity is linked to the uronic acid and sulfation pattern of the S-domain. However, with other proteins such as Interferon γ (IFNγ), a single S-domain is too short for high affinity binding, so a longer fragment, including an A-domain is needed for an efficient interaction. If the SAS domains whose charge topology is complementary to that of the basic clusters of the protein, a high affinity binding may occur. Instead, lower affinities are obtained if the polysaccharide and protein charge topologies do not match. Indeed, it has been proposed that the HS chain may adapt its conformation in order to meet the needs of recognition of a protein.

4.1.3. Heparan sulfate mimetics

Despite their enormous potential, very few GAG fragments have been developed for therapeutic use mostly because the synthesis of such fragments is difficult. The synthetic challenges associated with these oligosaccharides arise from the low availability of precursors from commercial or natural sources, the lack of efficient synthetic routes to make sufficient amounts of product, the difficulties due to several protection/deprotection steps needed, or the difficulty in stereo-selective and efficient formation of inter-glycosidic bonds of the carbohydrate backbone.

Certainly, the most successful example of GAG-based drug is the development of Arixtra® [134]. The structure of this drug is shown in Figure 4.6. The specific binding of this pentasaccharide sequence to Antithrombin III (ATIII) causes a conformational change within the protein allowing it to inhibit thrombin and other serine proteases within the coagulation cascade. This drug is employed as anticoagulant drug as a substitute of the traditional full-length HP (used in medicine since the 1930s) or low molecular weight HP.

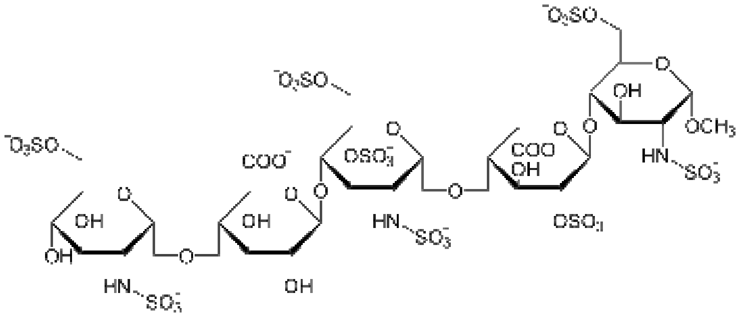

Figure 4.6. Structure of Fondaparinux (trade name Arixtra ®)

4.2. Structure and function of Interferon γ

IFNγ was discovered in 1957 by Isaacs Lindenmann when he observed that some virus-infected cells in culture produced a protein that made them resistant to the virus. Due to its “interfering” role during viral infection, this protein was named Interferon. Nowadays, we know that this homodimeric cytokine, predominantly produced by natural killer cells and some T-lymphocytes, is a known GAG-binding protein which coordinates a large array of cellular functions. In particular, IFNγ plays a central role in both adaptive and innate immune responses and it is important in early host defense against pathogens. [135]. IFNγ, is considered, thus, an attractive target for the treatment of a big number of diseases including autoimmune pathologies such as rheumatoid arthritis, systemic lupus erythematosus, multiple sclerosis, insulin-dependent diabetes mellitus, psoriasis, and alopecia areata [136] or chronic inflammatory bowel diseases such as Crohn disease and ulcerative colitis [137] [138].

The globular V-shaped dimer (MW = 16900), is composed by two monomers each of which are composed by six α-helixes, see structure in Figure 4.7. The global dimensions are 60 Å per 40 Å per 30 Å. The protein contains a highly hydrophilic and non-structured and flexible C-terminal part (residues 126 to 143). This makes this part non-visible in the crystallographic structure but is highly important for the biological activity of the cytokine.

The IFNγ transmits its signals by the interaction with its specific receptor present on its target cells. This receptor is composed of two proteins: IFNγRα and IFNγRβ The affinity between the IFNγ and its receptor is of about 1 to 10 nM [139].The crystallographic determination of the structure of the IFNγ:IFNγRα complex shows that the residues of IFNγ that take part in the interaction with its receptor are placed in the regions 1-42 and 108-124 [140-142].

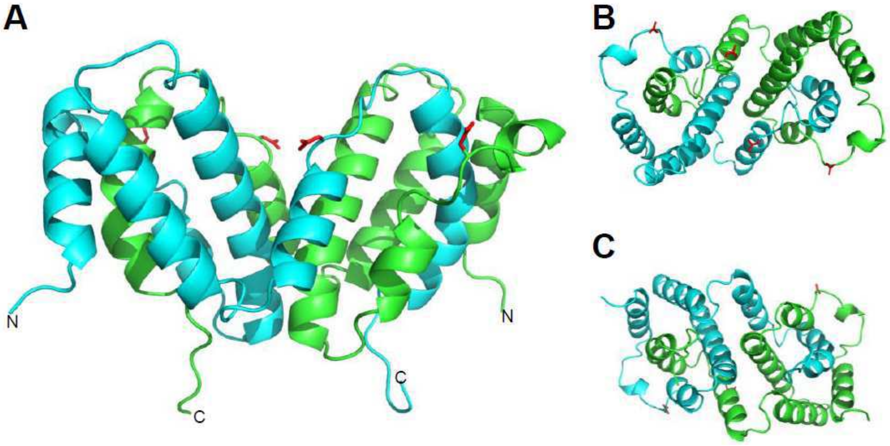

Figure 4.7. IFNγ structure issue from the structure of the complex of IFNγ with the soluble extracellular part of IFNγRα. Red and blue colors correspond to each monomer of the homodimeric structure of IFNγ and A, B and C correspond to different points of view. The C-terminal region is not visible. [140]

4.2.1. The C-terminal region of IFNγ

The C-terminal region of IFNγ comprises two adjacent clusters of basic residues: D1 (KTGKRKR), located between residues 125 and 131, and D2 (RGRR), located between residues 137 and 140 (see Figure 4.8). In addition to having a role in the interaction between the IFNγ and its receptor, the C-terminal region of IFNγ is known to be the site for interaction between IFNγ and HS [143, 144] IFNγ binding to HS determines its local concentration within tissues and controls its biological activity [145] [146]. This interaction was discovered in 1990, and was found to be very strong (K_D = 1.5 nM) [147], an affinity comparable to that of IFNγ towards its receptor [148]. The affinity of IFNγ for HS was found to be higher than the affinity of basic fibroblast growth factor (FGF), 610 nM, although FGF (pI = 9.8) is more basic than IFNγ (pI = 8.7). This suggests that the binding of IFNγ to HS is not only based on a simple electrostatic interaction [149].

Thanks to the work done by Dr. Lortat-Jacob and his team, nowadays we have much more information about the role of D1 and D2 domain in the interaction of IFNγ both with his receptor and with HS. They demonstrated that the binding to heparin of the D1 cluster is governed by favorable entropic and enthalpic contributions. The second cluster, D2, appeared to kinetically drive the interaction. They thus proposed that the heparin binding to IFNγ is a two-step process, in which close association is preceded by non-specific interactions that guide « diffusion to capture » of the protein. The D2 domain operates during the association phase but not in the formed complex.

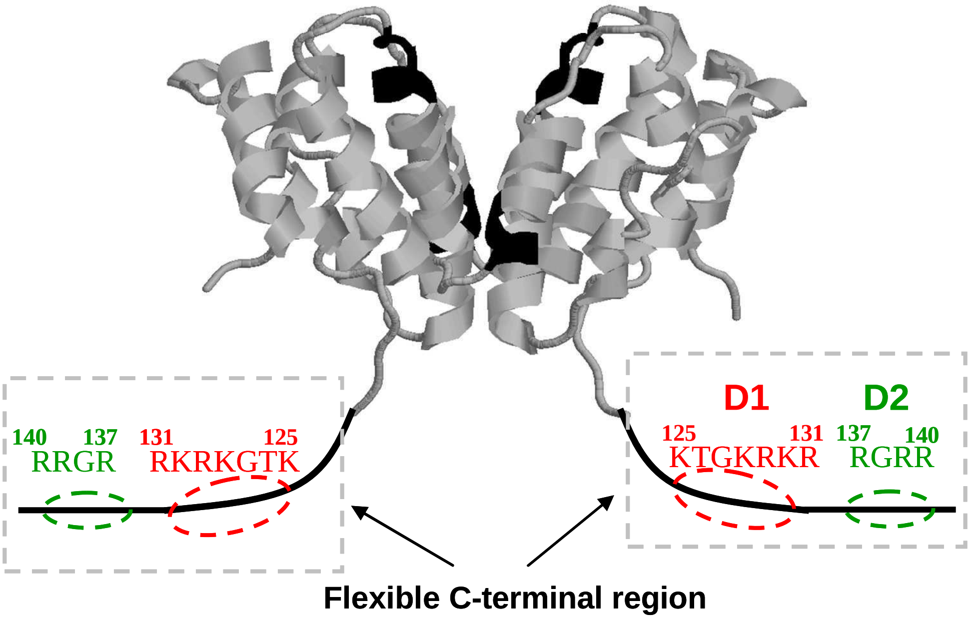

Figure 4.8. Representation of structure of IFNγ WT including the two basic domains D1 and D2 of the C-terminal region.

On the other hand, an impressive synthetic effort was done by Sarrazin *et al*. who targeted IFNγ by synthesizing different HS-mimetic oligosaccharides and linking them using molecular spacers of distinct lengths. Their objective was to validate the HS structural determinants for IFNγ recognition and to provide a new strategy to inhibit the cytokine. The presence of the spacer on the HS-mimetic was found to be indispensable for efficient binding. An optimal IFNγ inhibiting activity was found for the HS mimetic containing two octasaccharide units bound by a spacer of 50 Å length (see structure in Figure 4.9) [122, 138].

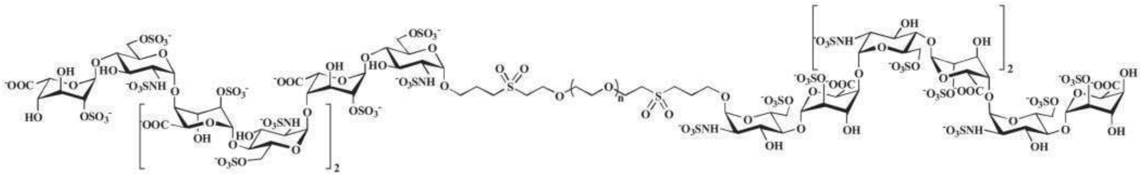

Figure 4.9. Molecular structure of the $2O_{10}$ molecule developed in reference [138].

4.3. Objective of the chapter

Finding easy ways, which avoid the complexity of GAG fragment synthesis, to understand and study GAG-protein interactions would be extremely helpful for future development of new GAG-mimetic drugs. In this context, the capacity to bind, recognize and differentiate HSbps showed by our CoCRR-SPRi e-tongue suggests the e-tongue is able to mimic the recognition properties of HS and, thus, could be employed as a useful tool to study HS/protein interactions.

We previously explained that there are two complexity levels that determine the recognition capacity of a HS molecule: First, the microheterogeneities resulting from the variation in sulfation and epimerization patterns of the disaccharide repeating regions. Second, the overall organization of the HS domains generating multiple SAS charge topologies along the polymer chain. The combination of these two levels of polymer complexity gives the HS the specificity in the recognition of the targeted protein.

Interestingly, we find two comparable levels of complexity in our e-tongue system, as illustrated in Figure 4.10. The first level of complexity is given by the microheterogeneities provided by the different charges and structures of the BBs on each CoCRR. At the same time, the whole array of CoCRRs presents different domains of charge, in a similar way as it happens in SAS charge topologies along HS chain. Obviously, the natural approach occurs at the molecular level while the e-tongue approach is macroscopic. However, the result of both approaches is the same: protein recognition.

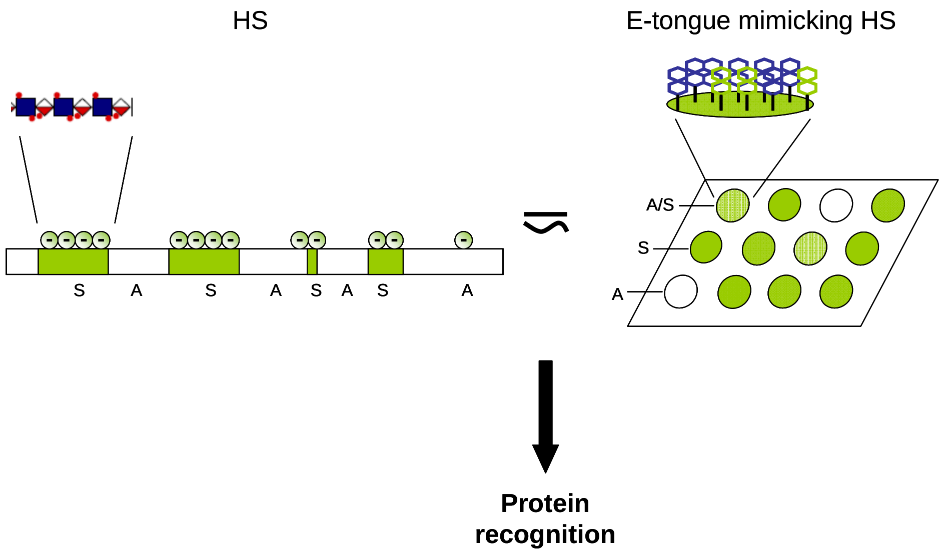

Figure 4.10. E-tongue mimics HS. The microheterogeneities in the disaccharide repeating regions are mimicked by each CoCRR, a combinatorial surface composed of different BBs ; the SAS charge topologies of HS are mimicked by the whole CoCRR array, which displays differently charged areas.

The objectives of this chapter were to demonstrate that the e-tongue is able to mimic the biological properties of HS, on one hand; and that it could be employed as a simple tool for better understanding of the nature of HS/protein interactions, on the other hand.

4.4. Study of the electronic tongue/interferon γ interactions

4.4.1. Electronic tongue/interferon γ interaction affinity

To study the recognition properties of the e-tongue, the chosen protein was IFNγ for several reasons: first, because of the well studied C-terminal region-HS interaction; second, because of the availability of IFNγ mutants if further studies are desired; and finally, because of the already presented therapeutic interest of this protein.

The study started with the injection of IFNγ on the CoCRR array at different concentrations and analysis of the obtained responses. The protein was injected at 10 nM, 30 nM, 50 nM, 100 nM, 200 nM, 400 nM and 800 nM. The obtained CEPs are shown in Figure 4.11. Although the intensity of the signals varied according to the concentration, the shape of the CEP remained unchanged. Therefore, in principle, the CEP shape could be used for identification and its intensity for quantification purposes.

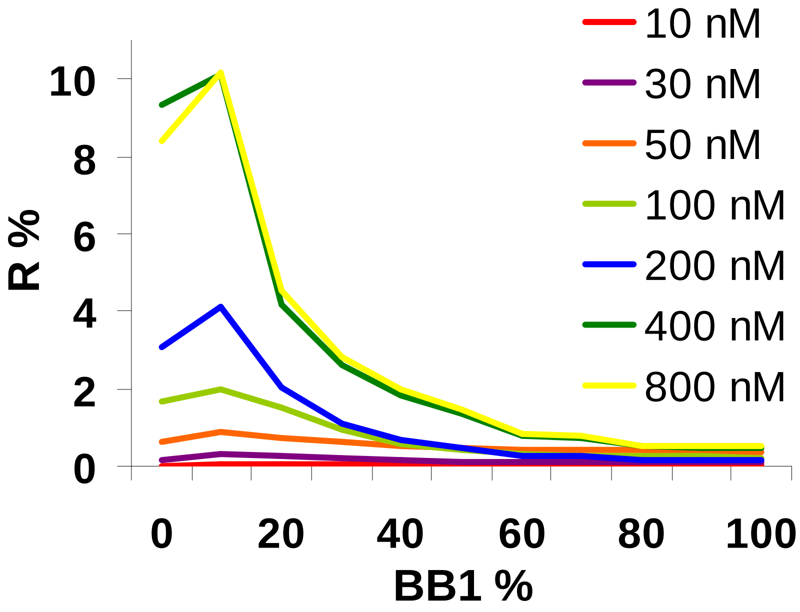

Figure 4.11. CEPs obtained for the injection of IFNγ at concentrations ranging from 10 nM to 800 nM.

In order to quantify the affinity between the IFNγ and the e-tongue, the dissociation constant (K_D) was calculated based on these results. The K_D is commonly used to describe the affinity between a ligand and a protein. It is defined in Equation 4.1, where [P] is the protein concentration, [L] is the ligand concentration; and [C] is the ligand-protein complex concentration in the equilibrium.

$$K_d = \frac{[P]\,[L]}{[C]}$$

Equation 4.1. Definition of dissociation constant.

In order to derive an affinity constant from the SPRi data a particular binding model must be used. The simplest (Langmuir) model (L+P↔PL) is applicable in the vast majority of cases. The Langmuir model, developed by Irving Langmuir in 1916 is a molecular model describing adsorption of molecules on surfaces. It describes the dependence of the surface coverage of an adsorbed inert gas on the pressure (or partial pressure) of the gas above the surface at a fixed temperature. Although developed for non-interacting simple gases, it is extensively employed to analyze macromolecular adsorption processes in biology. It assumes that the analyte (P) is both monovalent and homogenous, that the ligand (L) is homogeneous, and that all binding events are independent. Under these conditions data should conform to the Langmuir binding isotherm (Equation 4.2).

$$Bound = \frac{C \cdot Max}{K_D + C}$$

Equation 4.2. Langmuir equation, where “bound” is the measured R %, "Max" is the maximum response at the equilibrium (R %). C is the concentration of injected analyte and K_D is the dissociation constant. K_D has the same units as C (normally M)

The K_D and Max values were obtained by non-linear curve fitting of the equation to the data using Origin software. The analyzed data were issue from the mean of all the R % values of each CEP divided by the number of values (11 CoCRRs). This leads to a single reflectivity value for each IFNγ concentration. The obtained curve is shown in Figure 4.12.

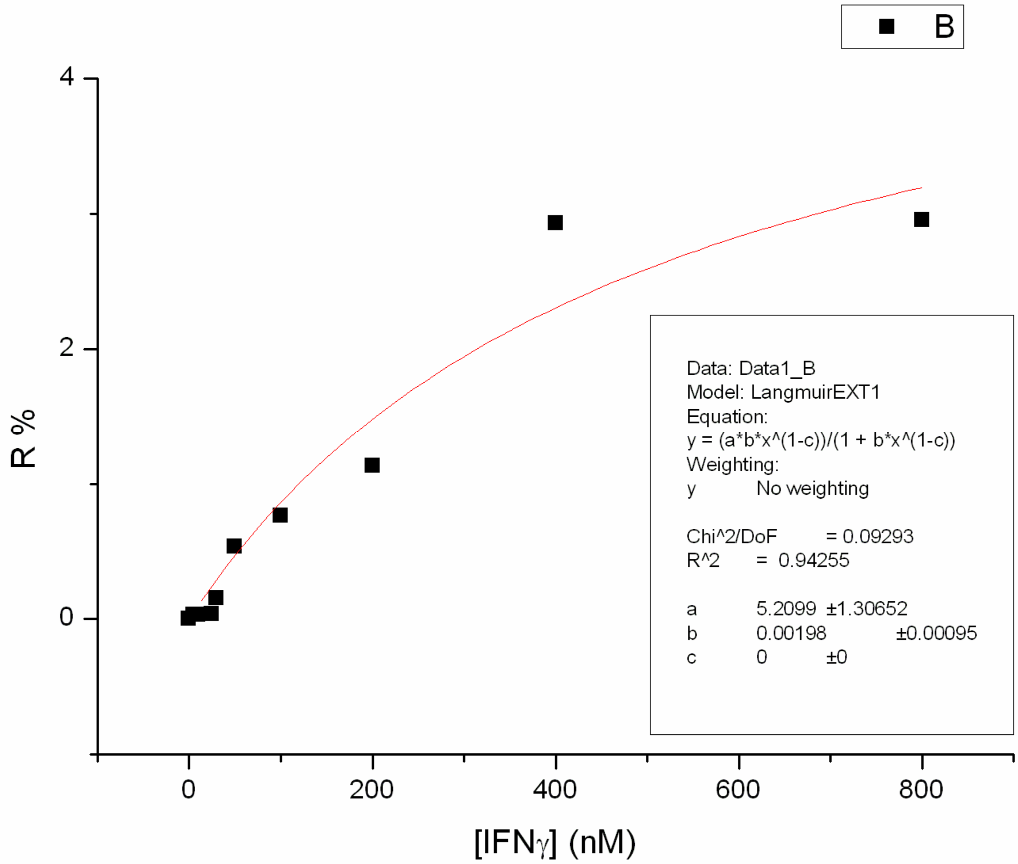

Figure 4.12. Data fitting by the Langmuir model. Each point corresponds to the mean reflectivity value obtained with all the eleven CoCRR spots for a given concentration.

A K_D value of **505 ± 242 nM** was extracted from this curve. Although this value is far from the extremely strong affinity measured for IFNγ-HS interaction (K_D = 1.5 nM) [147], we were positively surprised by the high affinity, in the nanomolar range, shown by the IFNγ towards the e-tongue.

In addition, in order to verify if the e-tongue showed less affinity to non HSbps, we tested three non-sugar binding proteins charged differently at pH 7.4: human Serum Albumin (HSA, pI = 5.2), Immunoglobulin G (IgG) from rabbit serum (pI = 7.5), and cytochrome C from horse heart (pI =

10.7). The concentration used was 500 nM for all of them and injections were made exactly in the same experimental conditions as those of IFNγ. In Figure 4.13 we present the results obtained with these proteins. It can be observed that for negatively charged HSA, there is almost no interaction with the CoCRR array. For neutral IgG, the maximal signal is comparable to that for IFNγ at only 50 nM, a concentration 10 times lower. For positively charged cytochrome C, as expected, there is more interaction with the CoCRR array and particularly with the CoCRR containing 100% sulfated lactose BB2. But still, the maximal signal is comparable to that for IFNγ at only 100 nM. Therefore, these results confirm that **the e-tongue shows an interesting capacity to detect HSbps with a special affinity not observed for non-HSbps**.

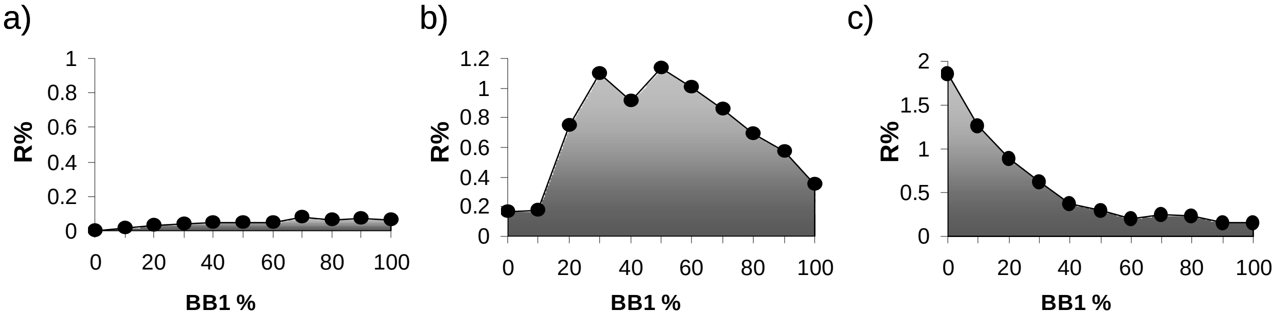

Figure 4.13. CEPs corresponding to three non-sugar binding proteins at the concentration of 500 nM. a) HSA b) IgG and c) Cytochrome C .

4.4.2. Electronic tongue/interferon γ interaction specificity

In order to verify if the e-tongue is still able to detect IFNγ even when it is present in a protein-rich media, in this study, we have performed analysis of the protein in diluted fetal bovine serum (FBS). FBS is the blood fraction remaining after the natural coagulation of blood, followed by centrifugation to remove any remaining red blood cells. Fetal bovine serum is the most widely used serum-supplement for the in vitro cell culture of eukaryotic cells. The experiment was made as follows: FBS was diluted to 1% in HEPES buffer (FBS+ HEPES) and injected on the CoCRR array following the usual protocol. 7-minute FBS injection and 7 minutes of buffer passage were made successively until the SPR signal upon FBS injection arrived to equilibrium where the signal loss after the injection was equivalent to the signal gain during the injection. This injection/rinse process was repeated five times until reaching the equilibrium. Then, IFNγ WT (50 nM) diluted in FBS+ HEPES was injected to see if the presence of the cytokine was detectable in such conditions. The second protein injection (100 nM) was made after two more FBS injection/rinse steps.

The obtained results are shown in Figure 4.14. In both cases (a and b) only the last two serum injections together with the subsequent injection of IFNγ in FBS+HEPES are presented. This is shown as a proof of the reached equilibrium, which ensures that the differences observed after the injection of IFNγ are entirely provoked by the presence of IFNγ in the injected solution.

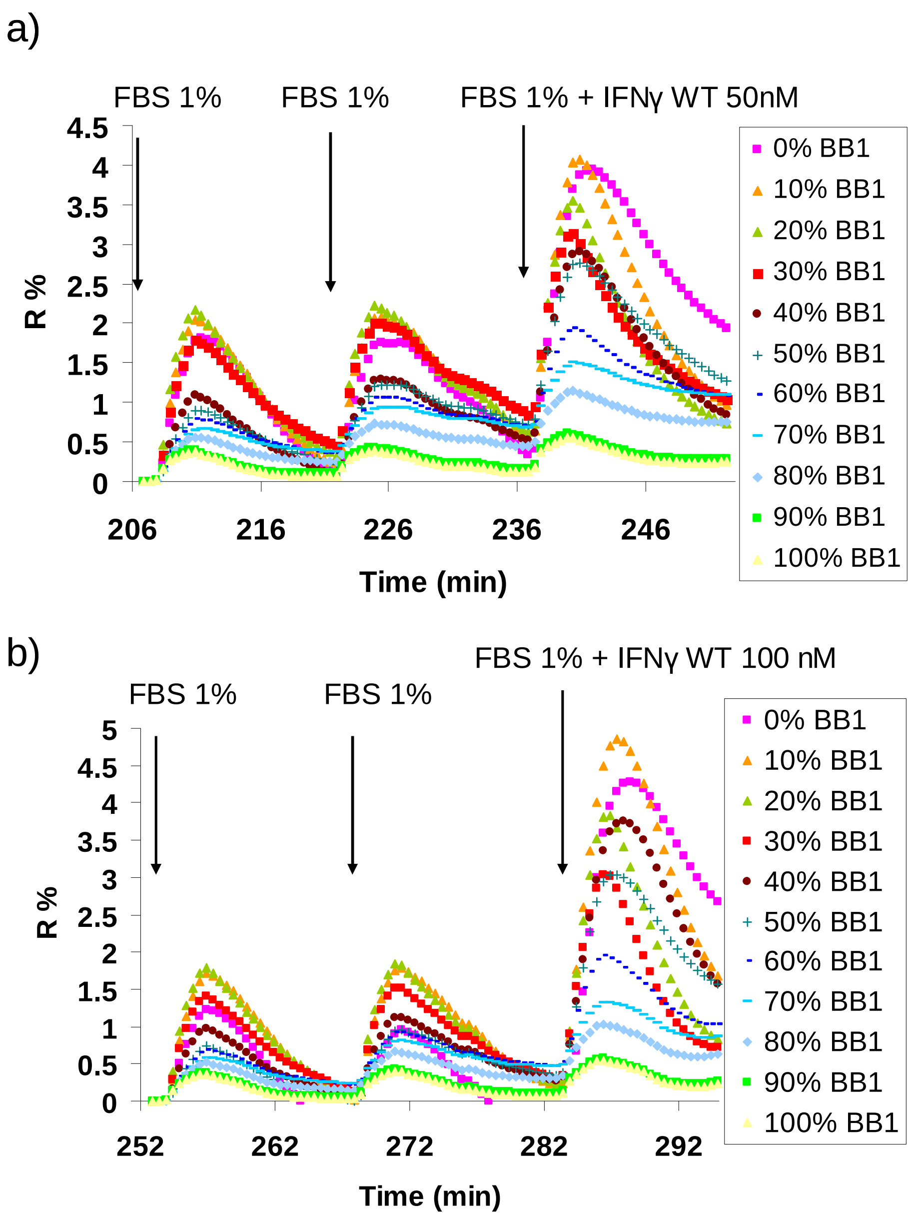

Figure 4.14. Detection of IFNγ WT in a protein-rich media by the e-tongue: a) IFNγ WT at 50 nM and b) IFNγ WT at 100 nM.

The results show that, when IFNγ is added to the injected solution, even if the protein content of FBS is important and varied, the presence of IFNγ is detected in form of a big increase of reflectivity in comparison to the increase induced by the injection of the serum. Very importantly, the increase of signal is related to the concentration of IFNγ. The higher the concentration of IFNγ in FBS + HEPES, the larger the increase of signal detected by the e-tongue.

Thanks to Biuret's method the total protein content of an FBS sample can be measured and it is estimated that the total protein content in this matrix can vary from 30 to 50 mg/mL [17]. After dilution to 1%, we obtained the total protein content of a standard sample between 0.3 and 0.5 mg/mL. The volume of the injected solution containing 50 nM IFNγ is 1 mL, which gives a total mass of $8.45 * 10^{-4}$ mg/mL for the protein. Thus, in the injected solution, IFNγ represents between

0.17% and 0.28% of the total protein present in the sample of 50 nM. In the case of the IFNγ at 100 nM it is between 0.34% and 0.56%.

These results confirm that, similarly to HS, the e-tongue has not only a good affinity to IFNγ, but also an impressive specificity.

4.5. Analysis of IFNγ mutants with the electronic tongue

In the SAGAG laboratory (IBS, France), Dr. Lortat-Jacob and colleagues have devoted important efforts in their research to the understanding of the role of the C-terminal region of IFNγ in the interaction with HS. The impressive results by this group about how basic amino acid clusters contribute to IFNγ -HS binding and the forces that drive such interactions obtained to date have been recently published [135]. To carry out their studies, they engineered and employed a collection of IFNγ mutants that they kindly shared with our team to permit the pursuit of our investigations.

The objective of this part of the work was to test if the e-tongue is capable of perceiving changes made in the C-terminal region amino acid sequence and making distinct recognition patterns for the different mutants. This could demonstrate its potential as a simple tool for better understanding HS-protein interaction mechanisms.

4.5.1. Presentation of the mutants

The structure of the wild type of IFNγ (IFNγ WT) and the C-terminal sequence of the studied mutants are presented in Figure 4.15. The expected and measured molecular masses are included too. Mutants can be classified in three groups: The first group was composed by 8 punctual mutants where a single basic arginine (R) amino acid was substituted by a neutral serine (S) one. The second group was composed of IFNγSD1 and IFNγSD2, where all the arginine units present in D1 and D2 were substituted by serine units, respectively. The third group of mutants, the deletion group, contained a mutant issue from the deletion of the D2 domain (IFNγΔ136) and another one issue from the complete deletion of both D1 and D2 domains (IFNγΔ124).

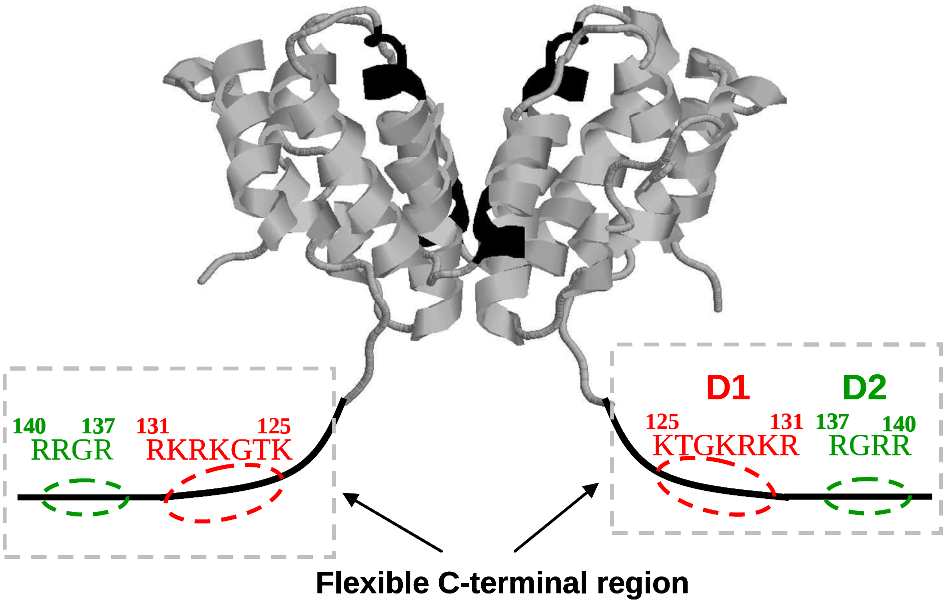

Name	IFNγ Carboxy-terminal sequence D1 D2	MM^{exp}	MM^{mea}
IFNγ$_{wt}$	AKTG**KRKR**SQMLF**RGRR**ASQ	16907.3	16907.7
IFNγ$_{\Delta124}$	A	14633.6	14634.2
IFNγ$_{\Delta 136}$	AKTG**KRKR**SQMLF	16095.4	16096.1
IFNγ$_{SD1}$	ASTGSSSSSQMLF**RGRR**ASQ	16645.8	16645.4
IFNγ$_{SD2}$	AKTG**KRKR**SQMLFSGSSASQ	16700.0	16700.8
IFNγ^{K125S}	ASTG**KRKR**SQMLF**RGRR**ASQ	16866.2	16866.7
IFNγ^{K128S}	AKTGS**RKR**SQMLF**RGRR**ASQ	16866.2	16866.6
IFNγ^{R129S}	AKTG**K**S**KR**SQMLF**RGRR**ASQ	16838.2	16838.7
IFNγ^{K130S}	AKTG**KR**S**R**SQMLF**RGRR**ASQ	16866.2	16866.6
IFNγ^{R131S}	AKTG**KRK**SSQMLF**RGRR**ASQ	16838.2	16838.4
IFNγ^{R137S}	AKTG**KRKR**SQMLFS**GRR**ASQ	16838.2	16838.6
IFNγ^{R139S}	AKTG**KRKR**SQMLF**RG**S**R**ASQ	16838.2	16838.7
IFNγ^{R140S}	AKTG**KRKR**SQMLF**RGR**SASQ	16838.2	16838.6

Figure 4.15. Presentation of the employed IFNγ mutants. On top, structure of IFNγ in its wild form with the amino acid sequence of the D1 and D2 domains of the C-terminal region included. On the table, the amino acid sequence of the two basic domains corresponding to IFNγ and each of the mutants and the expected and measured molecular masses. Replaced amino acids are shown in red color.

4.5.2. CEPs of IFNγ WT and mutants obtained by the electronic tongue

In this study, IFNγ WT and 12 mutants, all at the same concentration of 50 nM, were analyzed by the electronic tongue. Their CEPs obtained with the same CoCRR array are given below.

In Figure 4.16, the CEP of IFNγ WT is shown. It can be seen that IFNγ WT has higher affinity to CoCRRs rich in BB2 with a higher negative charge density. The maximal signal is obtained on the CoCRR containing 10% of BB1.

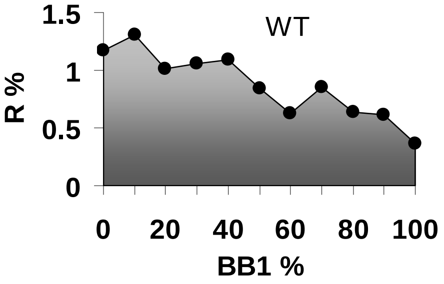

Figure 4.16. CEP of IFNγ WT (50 nM) obtained by the electronic tongue.

The obtained results for the punctual mutants of IFNγ are shown in Figure 4.17.

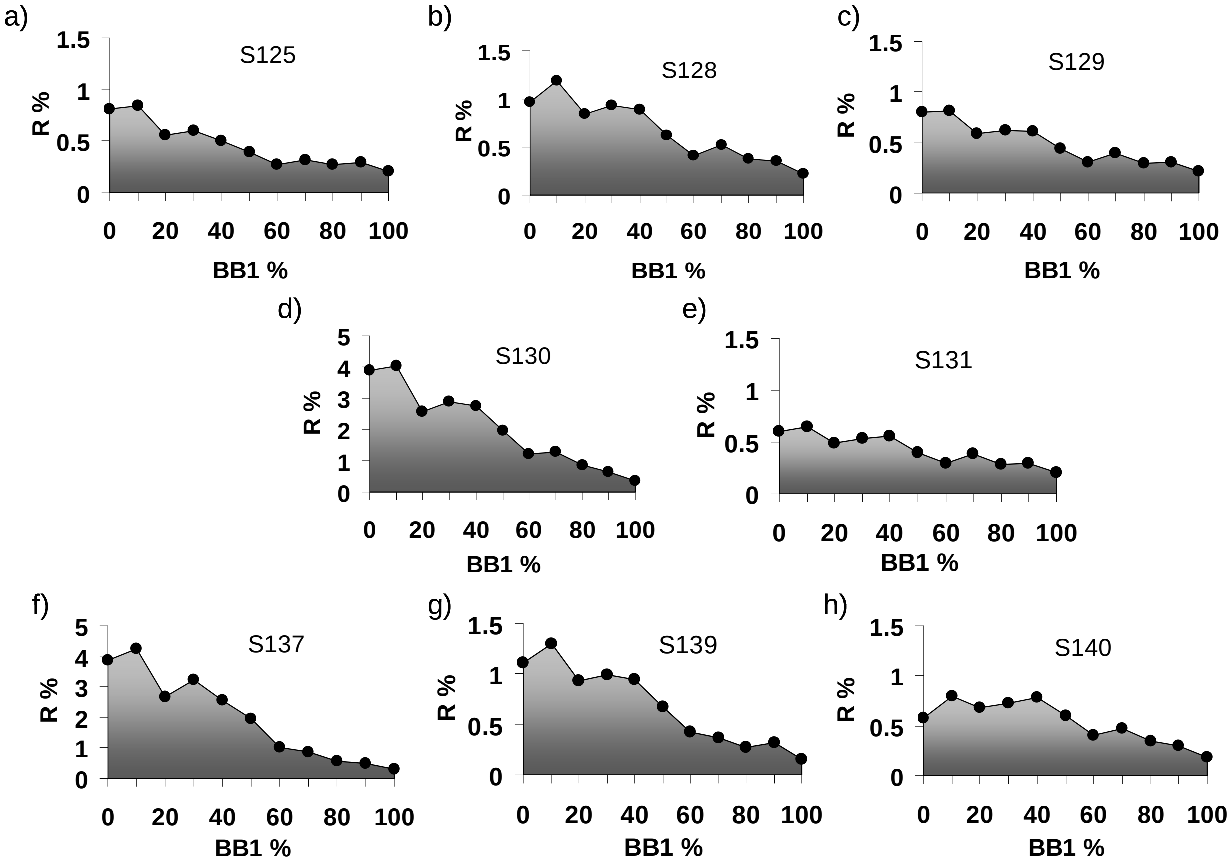

Figure 4.17. CEPs obtained for the punctual mutants of IFNγ, all at a concentration of 50 nM. In the first two rows, the CEPs corresponding to the mutations in D1 are given, including a) IFNγS125, b) IFNγS128, c) IFNγS129, d) IFNγS130, and e) IFNγS131. In the third row the CEPs corresponding to the mutations in D2 are given, including f) IFNγS137, g) IFNγS139, h) and IFNγS140.

Interestingly, the obtained CEPs for mutants in which a single amino acid has been substituted are not identical, but differ in terms of intensity of the whole profile. We can classify them into three groups. In the first group, two of the mutants, IFNγS130 and IFNγS137, though at the same concentration as all the others, attain much higher reflectivity values with a maximal signal of 4.5%, even higher than that of IFNγ WT. This indicates that there is an increase of affinity due to the mutation. In the second group, including IFNγS125, IFNγS129, IFNγS131, and IFNγS140, their

CEPs are quite flat, but the signal intensity of IFNγS131 and IFNγS140 are much lower than the two formers. In the last group, including IFNγS128 and IFNγS139, their CEPs are very similar to that of IFNγ WT, with a maximal signal at 10% of BB1. These results provide interesting information about the importance of each amino acid in the domain D1 and D2 for the HS-IFNγ recognition. Based on the CEPs of these mutants, it can be seen that some of the amino acids in the C-terminal region seem to be more implicated than others in the HS recognition, which is consistent with the findings obtained by Dr. Lortat-Jacob’s group.

Below we present together the CEPs for the mutants containing a whole muted domain (Figure 4.18) and for the deletion mutants IFNγΔ136 and IFNγΔ124 (Figure 4.19).

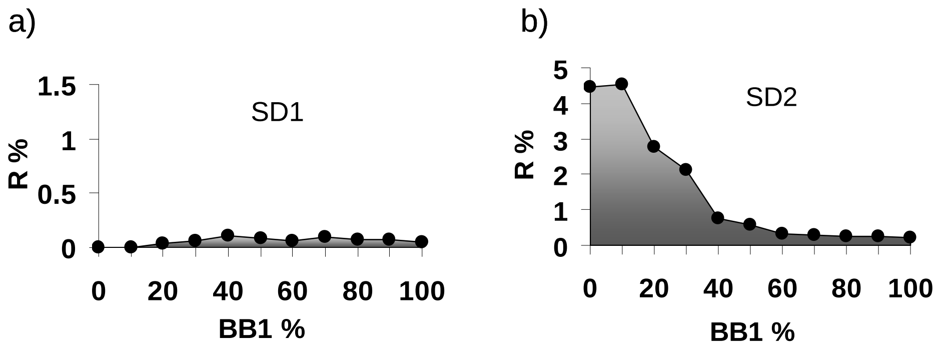

Figure 4.18. CEPs corresponding to the mutants in which all the basic amino acid residues a) in the domain D1 (for IFNγSD1) and b) in the domain D2 (for IFNγSD2) were substituted by serine, respectively.

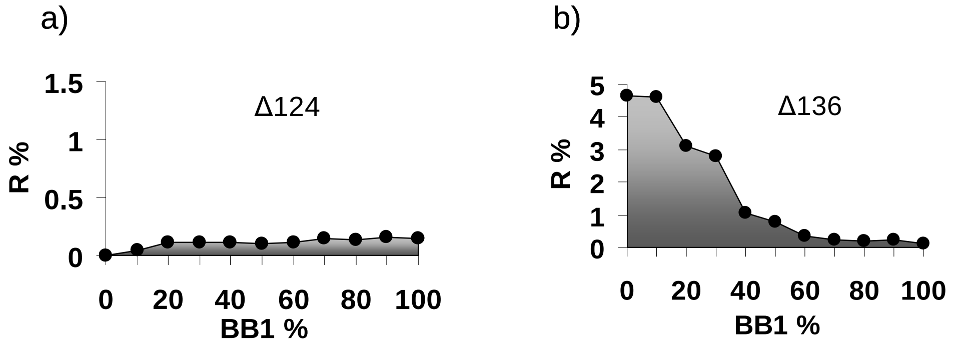

Figure 4.19. CEPs corresponding to the mutants a) IFNγΔ136 (deletion of amino acids 137 to 143) and b) IFNγΔ124 (deletion of amino acids 125 to 143)

The e-tongue was found to be extremely sensitive to major changes in the domain D1 and D2. On one hand, we observed that the complete mutation of the basic amino acid residues present in the domain D1 (IFNγSD1) or the complete deletion of these two domains (IFNγΔ124) gave as a result complete loss of the affinity between the array of CoCRRs and the protein. On the other hand, we observed that when the D2 domain is completely modified (IFNγSD2) or deleted (IFNγΔ136) the mutants had much higher affinity to the CoCRR array.

These results are in consistent with the biological findings reported by Dr. Hugues Lortat-Jacob. They have demonstrated that *in vivo*, unbound IFNγ is rapidly inactivated by the extensive carboxy-terminal proteolysis that cleaves both D1 and D2 domains [150]. However, HS bound to the IFNγ limits the proteolytic degradations to the D2 domain only, thus enhancing the cytokine activity, see

Figure 4.20. [150, 151] [139]. The D2 domain, in maximizing the association rate of IFNγ with HS, can thus be viewed as a motif enabling the cytokine to escape inactivation through D1 processing.

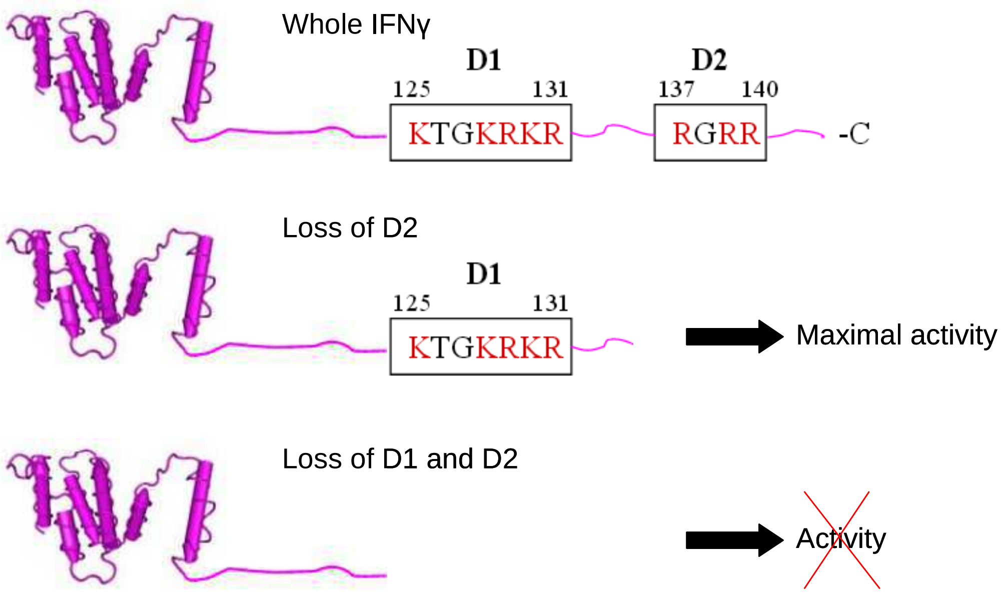

Figure 4.20. The D1 and D2 domains of IFNγ are important for the interaction with the HS [144]. The D1 domain seems to be involved in the interaction of the cytokine with its specific receptor [148]. For the activity of the cytokine, the loss of the domain 2 gives it a maximal activity, while the loss of both domains doesn't permit the transduction of its signal Adapted form reference [152].

Moreover, PCA was carried out based on these results. The data, containing 11-dimensions were previously normalized. Resulting score plot is presented in Figure 4.21 .

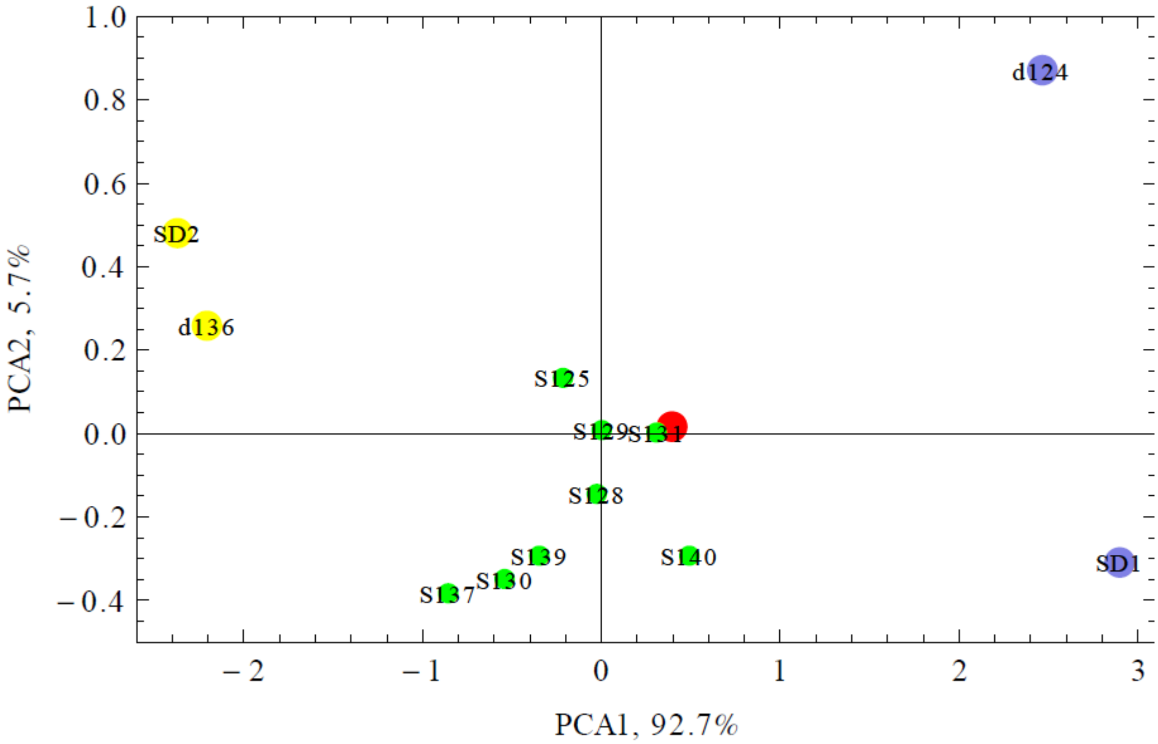

Figure 4.21. Two-dimensional PCA score plot for classification of IFNγ (red dot) and its mutants.

The obtained graphic shows that the mutants can be classified along the axis of the most important principal component PC1 into three clusters. The spot corresponding to IFNγ (in red) is at the centre of the graphic All around, in green, we find all the points corresponding to the punctual mutants. Unfortunately, no good discrimination between these punctual mutants could be observed. Global mutation or deletion of the D2 domain originated a new cluster (in yellow), which is located on the left hand and clearly separated from the others. Finally, the total mutation of the D1 domain and the total deletion of the C-terminal domain of the protein resulted in two spots which were also clearly apart from the central cluster; this time on the right hand of the graphic.

These results show that the e-tongue is able to perceive fine modifications made in the C-terminal region amino acid sequence of IFNγ and to differentiate its various mutants with very similar structures. This confirms that the e-tongue is able to mimic biological properties of HS and could be employed as a simple tool for better understanding of the nature of HS/protein interactions.

4.6. Study of the nature of the interactions between the electronic tongue and proteins

To better understand the nature of the interactions between the electronic tongue and HSbps, and more importantly, to understand the role of BB1 and BB2 in these interactions, we have carried out protein analysis by replacing lactose (BB1) and sulfated lactose (BB2) with other BBs. Meanwhile, this permits us to evaluate the importance of the first level of complexity for the e-tongue system as a HS mimetic.

In this study, BB1 was replaced by BB3, which is a non-sugar molecule, neutrally charged and which possess a comparable molecular length. BB2 was replaced by BB4, which is also a non-sugar molecule but negatively charged with almost the same molecular length as BB3, see Figure 4.21. Two proteins were chosen: IFNγSD2, with high affinity to BB2-rich CoCRRs, and ECL, with high affinity to BB1-rich CoCRRs. This work was done in collaboration with Benjamin Musnier during his internship (equivalent M2) in 2013.

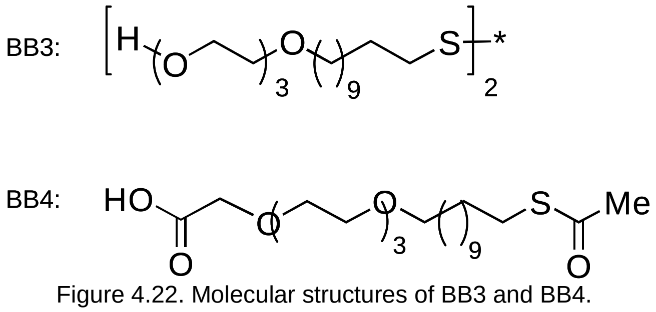

Figure 4.22. Molecular structures of BB3 and BB4.

For this study, all BB mixtures were deposited on the same prism, including 11 BB1/BB2 mixtures as described in Chapter 2 for reference, 11 BB1/BB4 mixtures with same ratios as BB1/BB2 mixtures only replacing BB2 with BB4, and 11 BB3/BB2 mixtures with same ratios only replacing BB1 with BB3. For each mixture, three replicates were used. Therefore, there were 99 spots deposited on the same prism in total. Here experimental preparation details are not given. The important point is that for protein analysis with this new array, the same procedures and same conditions were used for SPRi measurements.

In the following Figure 4.23, the CEPs of IFNγSD2 (50 nM) on the arrays composed of different BB mixtures are given.

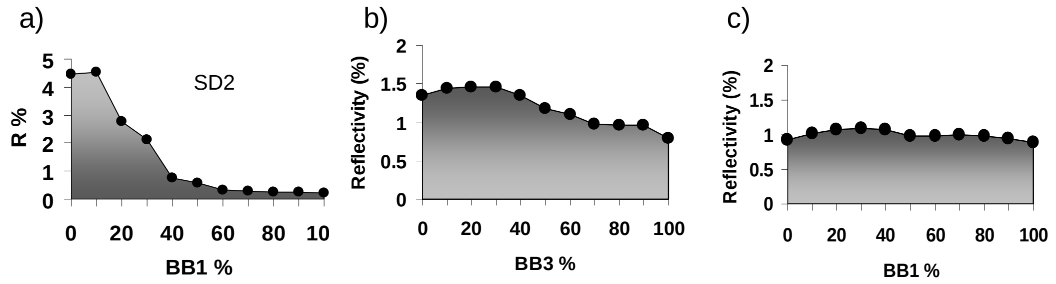

Figure 4.23. CEPs corresponding to IFNγSD2 (50 nM) obtained with the array a) containing 11 BB1/BB2 mixtures, b) containing 11 BB3/BB2 mixtures, and c) containing 11 BB1/BB4 mixtures.

Either when BB1 is replaced by BB3 (Figure 4.23b) or when BB2 is replaced by BB4 (Figure 4.23c), the protein recognition pattern undergoes strong modification. Replacement of BB1 by BB3 results in a flat profile with a little bit higher signal intensity for the CoCRRs rich in BB2 very probably due to electrostatic interactions, showing that the presence of BB1 is necessary for high affinity recognition. Replacement of BB2 by BB4 results in a flat profile, which proves that BB2 is also highly involved in the recognition related to not only its negative charge but also its structure.

In previous chapters it has been shown that combinatorial surfaces present more interesting properties than surfaces composed of pure BB1 or pure BB2. In Figure 4.24, CEPs obtained upon injection of ECL (200 nM) on the array composed of different BB mixtures are shown. The CEP of ECL (Figure 4.24a) obtained with the CoCRR array containing BB1/BB2 mixtures shows clearly the interest of mixing BBs. The protein has higher affinity to the CoCRRs containing 30% to 80% of lactose BB1 than to the CoCRR containing 100% of BB1, though it is known that ECL is specific to lactose.

The role of each of the BBs in ECL recognition was then studied. When BB1 was replaced by BB3 the signal on all BB3/BB2 mixtures is relatively low (Figure 4.24b). The maximal signal is obtained for the mixture containing 100% sulfated lactose BB2, which is very probably due to electrostatic interaction with the protein. For signal on the other mixtures, the higher the percentage of BB3 in the mixture, the lower the signal intensity. When BB2 was replaced by BB4 (Figure 4.24c), the intensity of signal is proportional to BB1% in the mixture with a maximal for 100% of lactose BB1. This illustrates that BB4 plays the role of a simple diluent while BB2 plays a more important role rather than a diluent.

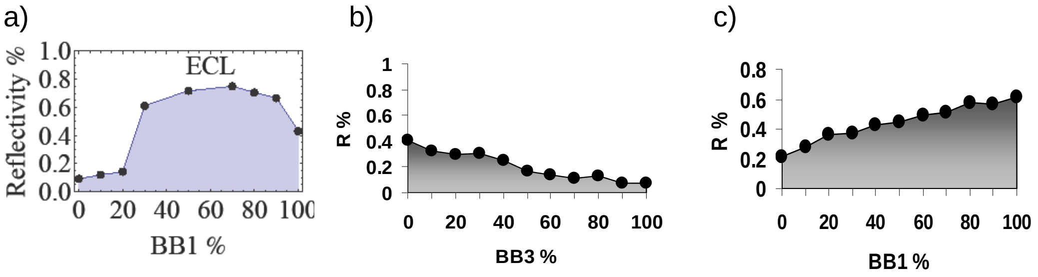

Figure 4.24. CEPs corresponding to ECL (200 nM) obtained with the array a) containing 11 BB1/BB2 mixtures, b) containing 11 BB3/BB2 mixtures, and c) containing 11 BB1/BB4 mixtures.

These results show that by combining lactose and sulfated lactose, combinatorial surfaces with surprising novel biological properties can be obtained. Their biological properties are dependent not only on charge of the used BBs but also on sugar structures of BBs, in an even more important way. **This affirmation is consistent with the comparison made between the first and second levels of diversity in HS structure and the e-tongue properties.**

4.7. Conclusions of the chapter

It has been demonstrated in this chapter that the e-tongue is very powerful for protein analysis, capable of differentiating even between mutants with very similar structures. But more interesting, our e-tongue system can mimic biological properties of heparan sulfate, useful as a simple tool for better understanding of HS/protein interaction and the elucidation of the role of different protein fragments involved in the recognition processes. In addition, it has been proven by combining lactose and sulfated lactose, combinatorial surfaces with surprising novel biological properties can be obtained and they are essential for the high affinity of the e-tongue to Hsbps, The biological properties of combinatorial surfaces are dependent not only on charge of the used BBs but also on sugar structures of BBs, in an even more important way. This is very promising in the design of new biomimetic nanovectors. In this regard, we proposed that the e-tongue could be used as a medium-throughput screening tool for the selection of BB mixtures with biologically interesting surface properties. This point will be addressed in the next chapter.

CHAPTER 5.

Preparation of 3D Biomimetic Nanovectors through Electronic Tongue Based Approach

Résumé en français du chapitre 5

Préparation de nanovecteurs biomimétiques 3D par une approche basée sur langue électronique

Depuis la commercialisation d'Arixtra®, un fragment de glycosaminoglycane (GAG) avec propriétés antithrombotiques, les interactions GAG-protéine sont au centre d'une recherche intense. La recherche de médicaments de type GAG nécessite l'étude structurale des fragments qui reconnaissent de façon spécifique la molécule thérapeutique visée. Cette approche peut vite devenir très compliquée à cause des problèmes associés à la synthèse de carbohydrates. Ce chapitre est donc dédié au développement d'une nouvelle approche qui consiste à mimer les propriétés biologiques des fragments de GAG pour la reconnaissance des protéines en utilisant des surfaces 3D exposant des disaccharides, assimilables à des nanovecteurs biomimetiques. Cette partie a pour origine le projet NanoGAG déposé avec l'équipe du Prof. Bonnaffé à Orsay.

Dans ce chapitre, du fait de sa capacité pour tester une grande quantité de mélanges de disaccharides de façon efficace, la langue électronique a été utilisée comme moyen de criblage de surfaces 2D bioactives. Le but était de transférer la surface bioactive 2D sélectionnée à une surface tridimensionnelle. Le support 3D choisi pour cette étude est celui des nanoparticules d'or. Comme il est présenté dans l'introduction de ce chapitre, les nanoparticules d'or ont déjà une riche histoire d'applications et de recherche dans le domaine du biomédical et du diagnostic. Cette grande expérience de ces objets, ainsi que le fait que l'or soit le matériau employé comme base pour le greffage des disaccharides durant l'élaboration des langues électroniques, nous ont encouragés à utiliser des nanoparticules d'or pour cette étude.

Une fois la surface 2D d'intérêt identifiée, la préparation des nanovecteurs est simple grâce à l'affinité entre les disaccharides thiolés et les nanoparticules d'or. La concentration de nanoparticules peut être calculée et suivie par spectrométrie UV-Visible grâce au pic d'absorption caractéristique des nanoparticules d'or d'environ 20 nm à 523 nm. La position du pic est dépendante du rayon des particules, ce qui permet de détecter l'attachement de molécules volumineuses sur les nanoparticules ainsi que l'agrégation des nanoparticules. Cette agrégation peut aussi être détectée par une perte d'intensité du pic d'absorption : le pic est proportionnel à la concentration de particules en suspension, et donc, sensible à la diminution de particules en solution provoquée par la formation d'agglomérats de particules.

La première difficulté rencontrée lors de la préparation de ces nanovecteurs fut leur instabilité en milieu salin. Une solution fut trouvée en modifiant les chaînes espaceurs des BBs par l'ajout d'une chaîne de polyéthylène glycol (PEG). Les nanoparticules fonctionnalisées avec les BBs contenant les chaines PEG sont beaucoup plus stables. Cela fut montré par des études en milieu salin, par spectroscopie UV-Visible, ainsi qu'à fortes concentrations, par SAXS.

La caractérisation des nanoparticules s'est terminée par une estimation théorique et experimentale de la densité de ligands attachés par nanoparticule.

Les propriétés biomimétiques des nanovecteurs furent testées au cours d'essais biologiques. Ces essais ont consisté à démontrer qu'il existait une certaine affinité entre les nanovecteurs et une protéine visée. Pour être spécifique, cette affinité ne doit pas exister dans le cas où le nanovecteur est fonctionnalisé avec une surface qui n'a pas montré d'activité préalable envers la protéine. Ces théories ont été confirmées par des tests SPRi et ELISA. Les résultats préliminaires montrent que les nanovecteurs synthétisés possèdent une affinité envers les protéines testées. Ces premiers résultats positifs encouragent à poursuivre la recherche dans cette direction.

Preparation of 3D Biomimetic Nanovectors through Electronic Tongue Based Approach

5.1. Nanotechnology in biomedical applications

Nanotechnology, a constantly expanding field, is nowadays able to provide the community with nanometric materials of controlled sizes (ranging from 1 nm to 100 nm), geometries (spheres, rods, shells...), core materials (organic, inorganic) and functionalities. Besides, as fabrication methods improve, new high technological characterization methods have progressively been developed giving rise to an era where the application of these materials becomes more challenging than their fabrication.

One of the greatest challenges in nanomaterials is their application in biomedicine. Nanomaterials find their place in this field thanks to their size scale which is comparable to that of biomolecules such as proteins, see Figure 5.1. Thus, when coupled to appropriate functionalities, nanoparticles (NPs) become excellent tools for many biological applications at the cellular and molecular level [153]. The new and vast scientific area born from the application of nanomaterials to biomedicine is called nanomedicine. [154]

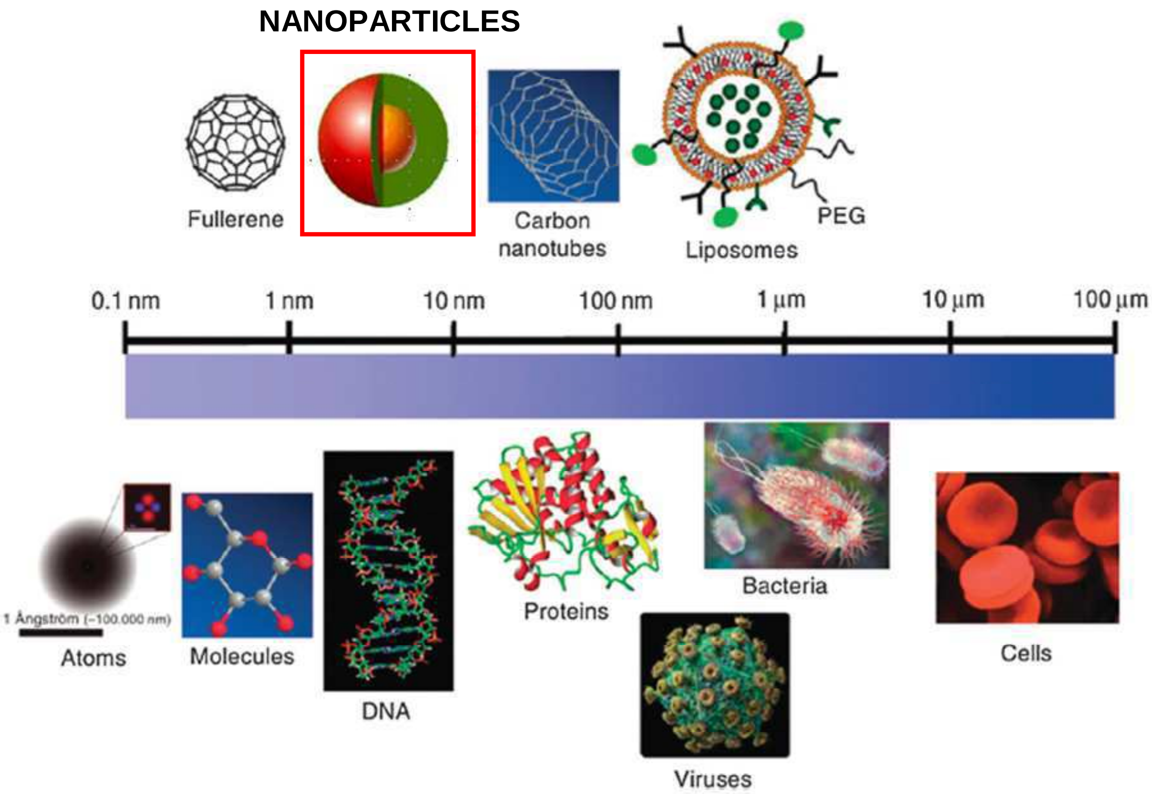

Figure 5.1. Illustration of the similar dimensions between nanoparticles (NPs) and biological entities, which favours the synergy of nanomaterials and biomedicine. Adapted from [155] and [153]

5.2. Gold nanoparticles and nanoconjugates

1.2.1 Gold nanoparticles

Among the diverse NPs containing organic, metallic and semiconductor materials as core materials (each of them showing characteristic physical, chemical and electronic properties) [156] [157-159] gold nanoparticles (Au NPs) are probably the most studied ones.

Au NPs have a rich history in chemistry, dating back to ancient roman times where they were used to stain glasses for decorative purposes. Characteristically, Au NPs exhibit a strong absorption band in the visible region which can be considered as small particle effect since it is absent in the individual atom as well as in the bulk metal. The physical origin of the light absorption by metallic NPs is the surface plasmon resonance, the collective oscillation of the conduction band electrons across the NP (diameter $d \ll \lambda$, where λ is the wavelength of the light) [160]. The resonance frequency of this SPR is strongly dependent upon the size, shape, dielectric properties and local environment of the NPs. In colloidal solutions, the color of Au NPs may range from red to purple depending on their size. The most popular example of the use of Au NPs with decorative purposes is the Lycurgus cup, a fourth-century Roman chalice which under ambient lighting appears green, but when illuminated from the inside, shines bright red due to nanometric gold and silver particles embedded in the glass, as shown in Figure 5.2.

Figure 5.2. The Lycurgus cup (British Museum, London, UK). Under ambient lighting, on the left, and illuminated from the inside, on the right.

The modern era of Au NPs began in 1857 with the work of Michael Faraday entitled *Experimental Relations of Gold (and Other Metals) to Light.* It was possibly the first work discussing that colloidal gold solutions have properties that differ from bulk gold. [161, 162] In the 20th century, and especially in the last decade, several methods for the preparation of gold colloids were reported. At present time, reliable and high-yielding methods for the synthesis of Au NPs have been already established [163].

Resulting NPs have unique properties such as size and shape dependent optical properties, a high surface area to volume ratio, and easily modifiable surfaces. This last property permits to introduce a wide range of functionalities on the surface of NPs, which is one of the key attractions for the use of these materials in biology and medicine.

Though barely applicable to real patients, some therapeutic effects have been observed for non-functionalized/bare Au NPs. It was found that 5 nm Au NPs exhibit anti-angiogenic properties in both *in vitro* and *in vivo* studies. This mechanism was explained by the ability of Au NPs to bind heparin-binding glycoproteins on the surface of endothelial cells and subsequent inhibition of their activity [164]. Non-functionalized Au NPs can also be applied to photothermal therapy. Photothermal therapy takes advantage of the ability of Au NPs to absorb light in the near infra-red region of the spectrum, where absorption of biological fluids and tissues is minimal, and convert it to heat to destroy cancer cells, bacteria and viruses. [165] [166] [167] The Au NPs can also be used together with other elements in composite materials to fabricate gold-containing devices such as thermo-sensitive microcapsules, films and hydrogels, to trigger drug release [168].

1.2.2. Gold nanoconjugates

More importantly, Au NPs can be easily conjugated with various molecules, including small inactive molecules, DNA, proteins, carbohydrates *etc*. The functionalized NPs are called nanoconjugates, as illustrated in Figure 5.3.

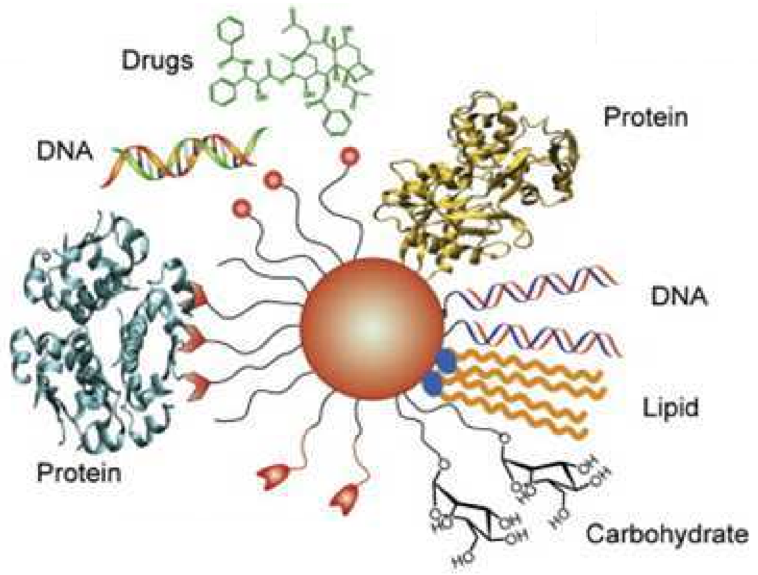

Figure 5.3. Illustration of the variety of ligands to which gold nanoparticles can be conjugated. Figure adapted from [169]

Gold nanoconjugates find many kinds of applications in the field of nanomedicine, including biodiagnostics for detecting target nucleic acids, proteins and other biologically relevant molecules, [170-176], therapeutics, where they are used as agents for killing cancer cells, bacteria and viruses, or as carriers for drug and gene delivery. [168] In addition, the versatility of gold nanoconjugates can be increased by incorporating multiple functional groups into one NP.

In the following part, some examples will be given for illustration.

a) Au NPs conjugated to small inactive molecules

Recently, it has been reported that Au NPs conjugated to small molecules with no therapeutic effects have potential for drug agents. This is very promising since it could greatly accelerate the discovery of effective new drug formulations [177]. A remarkable work was done by the group of Daniel L. Feldheim [177]. They demonstrated that by anchoring a biologically inactive small molecule onto Au NPs, the obtained nanoconjugates were able to effectively inhibit HIV-1 fusion to human T-cells. A similar example was provided by Baram-Pinto *et al*., who proposed to mimic the polysulfonated heparan sulfate simply by anchoring an inactive small molecule mercaptoethanesulfonate on a Au NP surface. This approach was shown to be efficient in the inhibition of Herpes virus type 1 infection [178].

Further work of Feldheim's group was dedicated to the creation of a library of thiol-monolayer-coated Au NPs. The employed thiols had simple structures, as shown in Figure 5.4, and were mixed at different proportions to obtain 119 nanoconjugates in total. This permitted the discovery of Au NPs with potent activity for *Escherichia Coli* growth inhibition and inhibitors of the gram-positive bacterium *Staphylococcus Aureus* [179] [180].

This inspiring work suggested that the display of ligand mixtures on Au NPs could present new opportunities in the rapid identification of nanomaterials with biological activity toward a range of microbes. However, in our opinion, this approach could be further improved if, instead of the preparation of a great number of nanoconjugates in a random way, a previous multiplexed step for the screening of active surface coverings using a microarray technique was added.

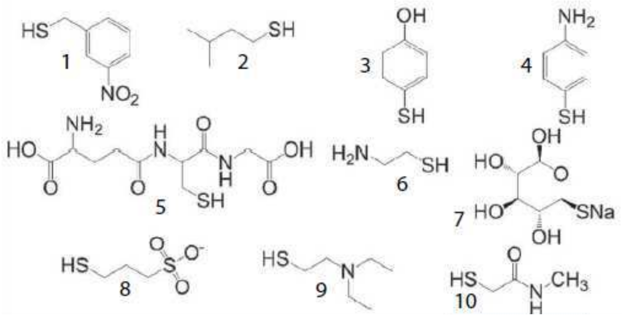

Figure 5.4. Chemical structures of thiols used for creation of a library of thiol-monolayer coated Au NPs. [180]

b) Au NPs conjugated to drug molecules

Au NPs have been conjugated to drug molecules to enhance their activity. Two types of drugs have been mainly tested: antibiotics and anticancer drugs. In the case of NPs conjugated to antibiotics including vancomycin [181] [182], ampicillin [183] or cefaclor [184], enhanced activity against bacteria was observed. This activity enhancement is mainly due to the high density of the drugs obtained upon conjugation to NPs, although some theories suggest that the antibiotic activity is also dependent on the particle structure [184].

Au NPs have also been explored to develop more efficient anticancer drugs. Cancer is a major target of new therapeutics because of the drawbacks associated with current treatment strategies which include large systematic side effects due to the non-specificity of many cancer drugs such as cisplatin, paclitaxel, tamoxifen or doxorubicin [185]. Attachment of anticancer drugs to Au NPs can lead to increased toxicity compared to free drug. However, this can be seen as an advantage if combined with increased specificity of the drug conjugate to cancer cells. In general, two approaches can be adopted for targeting therapeutics and avoid accumulation in healthy tissue: passive targeting and active targeting. Passive targeting takes advantage of the Enhanced Permeability and Retention (EPR) effect, illustrated in Figure 5.5, based on the fact that certain sizes of molecules (typically liposomes, NPs, and macromolecular drugs) tend to accumulate in tumour tissue much more than they do in normal tissues, due to the leaky and abnormal in form and architecture tumour vasculature [186, 187].

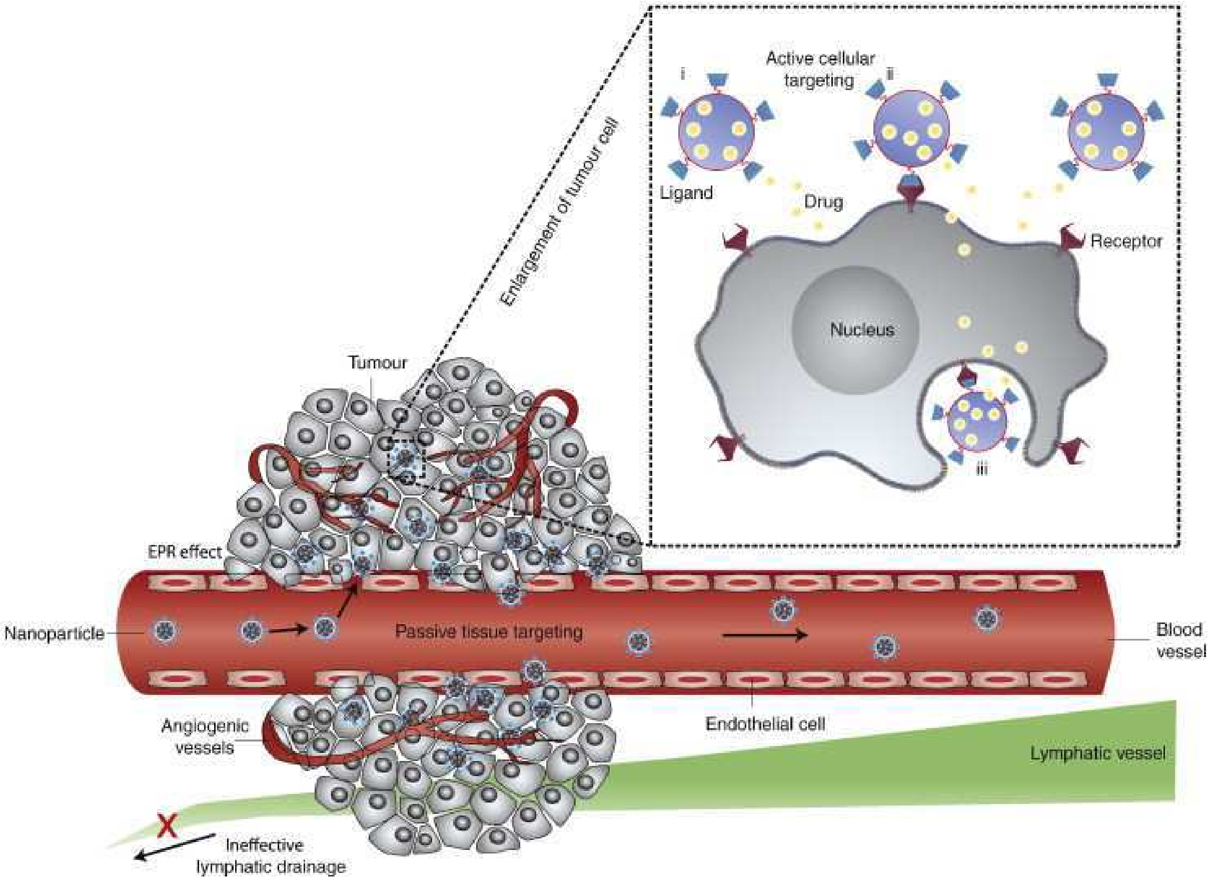

Figure 5.5. Illustration of the complex environment NP–drug conjugates experience upon intravenous delivery. Initially, particles flow through the vascular system (red), diffuse through the leaky endothelial walls associated with several diseases (dark gray), and finally reach the targeted cell (enlarged box). From reference [188].

Active targeting involves the attachment of antibodies or other targeting moieties (small molecules, biopolymers, peptides, oligonucleotides, fatty acids [185]) to the NPs often targeted to over-expressed binding domains on cancer cells compared to regular cells [189].

c) Au NPs conjugated to nucleic acids

Because of the extreme importance of nucleic acids in biological systems, learning to modulate the transcription and translation of DNA and RNA is expected to make gene therapy an important treatment methodology in the near future. Thus, being able to deliver inside cells a wide variety of oligonucleotides, such as plasmids, double stranded DNA, single stranded DNA, and single stranded RNA, could have large therapeutic benefits. However, due to their highly negative charge, these molecules cannot enter the cell without the help of some sort of delivery vehicle [185].

Au NPs are attractive platforms for DNA/RNA delivery thanks to their high surface-volume ratio that maximizes the payload-carrier ratio and enables efficient DNA/RNA compaction. DNA can be attached to NPs either by electrostatic interactions or by thiol modification of the DNA molecule, allowing direct anchorage of the DNA molecule on the Au NPs thanks to its strong affinity for gold surfaces. For the former, usually NP surfaces are charged positively by a monolayer containing substituents like cationic quaternary ammonium [190] [191] [192], primary amines [193{Kawano, 2006 #221]}, amino acids [194, 195], cyclodextrin-oligo(ethylenediamino) complexes [196] or polyethylenimine [197]. The positive charge of the nanoconjugate surface permits a non-covalent attachment of the DNA through electrostatic interaction and protects it from enzymatic digestion, see Figure 5.6. Interestingly, it has been reported that modified NPs show, in some cases, better transfection efficiency than the commercially available polyethylenimine or lipofectamine 2000, widely used transfecting agents.

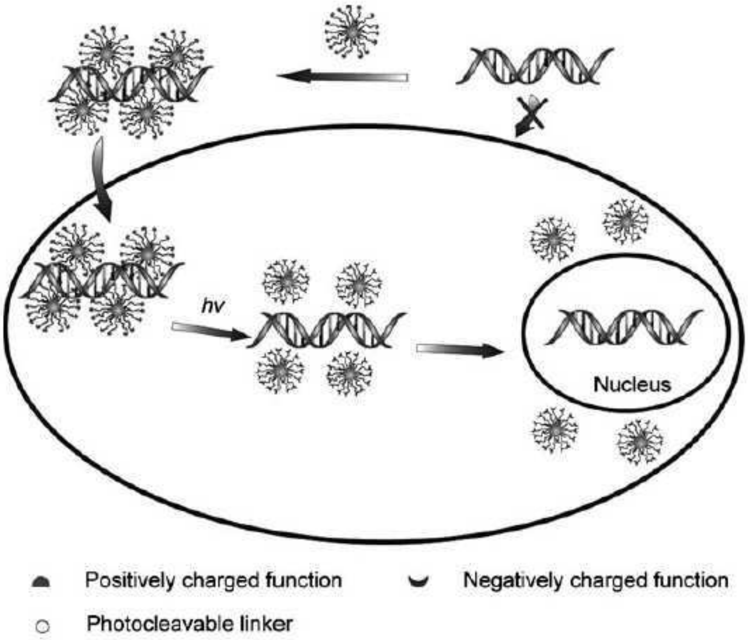

Figure 5.6. Example of the strategy for release of DNA from a photocleavable DNA-Au NP complex upon irradiation within the cell. From references [162, 191]

For the latter, DNA and RNA, generally modified with a thiol moiety, have also been successfully employed for gene silencing applications [198] [199]. It has been proven that this type of nanoconjugates can be digested by restriction enzymes and expressed as functional proteins inside mammalian cells [200]. Besides, it has been demonstrated that by covering the NPs with promoter DNA, DNA transcription could be inhibited [201].

In addition to intracellular applications, DNA-Au NPs have also been used for the development of colorimetric assays for detection of cancer cells [202]. In this case, Au NPs were functionalized with a monolayer of aptamers selected to have a high affinity for surface receptors expressed by a cancer cell line. The aptamer-functionalized nanoconjugates assemble on the cell surfaces, causing an interaction of their surface plasmon resonance and, thus, a red-shift in the extinction spectra. Detection could be made by the naked eye or using a spectrometer, making the assay potentially useful for cancer diagnosis or disease screening.

d) Au NPs conjugated to proteins

Antibodies are the most often used molecules to provide specificity and bioactivity to NPs, in particular, for active targeting purposes. It is possible to find antibodies that recognize an extraordinarily large number of antigens ranging from large pathogens (viruses, bacteria…) to small molecules (hormones, drugs, bacterial toxins…) with high specificity [189]. This property has also permitted the development of novel sensing methods based on antibody-Au NP conjugates. For instance, in Figure 5.7, we present the example of NanoDLSay^{TM} where the formation of a nanoconjugate cluster or the increase of the size of single nanoconjugate due to analyte attachment can be made by dynamic light scattering (DLS) particle size measurement.

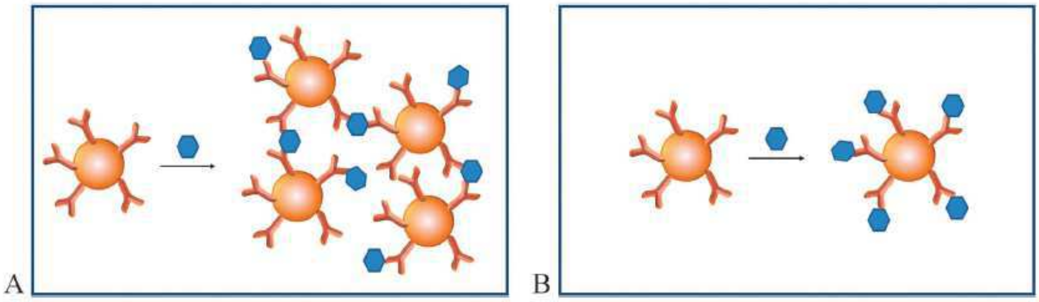

Figure 5.7. The principle of NanoDLSay^{TM}. Two assays are illustrated: A) Analyte binding induced NP cluster formation and B) Analyte binding induced individual NP size increase. In both cases, the particle size change of the assay solution is measured by dynamic light scattering. From [175]

Proteins of therapeutic interest can also be attached to NPs. This can be made non-covalently via electrostatic interactions or covalently without altering their biological activities. Many examples are found in the literature, including intracellular delivery of β-galactosidase [203], transmucosal delivery of insulin [204], or delivery of TNF-alpha, a cytokine with anti cancer efficacy, into mammary carcinomas grown in mice [205].

Moreover, NP-protein conjugates have been exploited as vaccine candidates. They are reviewed in the reference [155]. Herein, a very promising example is given. Recently, Stone and his colleagues have devoted to prepare a vaccine based on Au NPs against respiratory syncytial virus (RSV), a virus causing pneumonia in children [206]. To do so, they attached the major protective antigen of the virus, the fusion protein, on the surface of gold nanorods with the aim of mimicking the virus. To ensure high stability of the nanoconjugates in a physiological environment after inoculation *in vivo*, the covalent binding approach was chosen. It was shown that the nanoconjugates induced successfully human immune response.

e) Au NPs conjugated to carbohydrates

Carbohydrate-mediated interactions are central to many important biological phenomena. Characteristic features of most interactions involving carbohydrate are high specificity and low affinity. Nature overcomes this low affinity by simultaneously engaging multiple ligands for binding, leading to enhanced avidity through the multivalency effect. In this regard, carbohydrate-coated NPs, also called glyconanoparticles (glycoNPs), present a good bio-mimetic model of carbohydrate presentation on the cell surface [207]. The large surface areas of NPs permit the immobilization of multiple carbohydrate ligands, which can potentially enhance the weak affinities of individual ligands to their binding partners. Applications of these kind of nanoconjugates include the study of interactions where sugars are involved (carbohydrate-carbohydrate, carbohydrate-protein), biolabelling, bio-amplification strategies, as well as biomedicine [153, 208].

GlycoNPs as tools for carbohydrate-carbohydrate and carbohydrate-protein interaction study

GlycoNPs have been intensively used to investigate carbohydrate-carbohydrate interactions as well as carbohydrate-mediated cell-cell interactions by Penadés and co-workers [155]. They proved the requirement of Ca^{2+} ions for certain carbohydrate-carbohydrate interactions thanks to the aggregation of glycoNPs mediated by the mentioned cation, and they could study the kinetics of these interactions thanks to SPR measurements [209] [153].

These multivalent systems have been also used for the study of carbohydrate-protein interactions. In a similar way as for carbohydrate-carbohydrate interaction studies, carbohydrate-protein interactions can be detected by the aggregation of the glycoNPs in presence of the studied protein (see Figure 5.8) [210] or by competition experiments made using the glycoNPs (see Figure 5.9). [211].

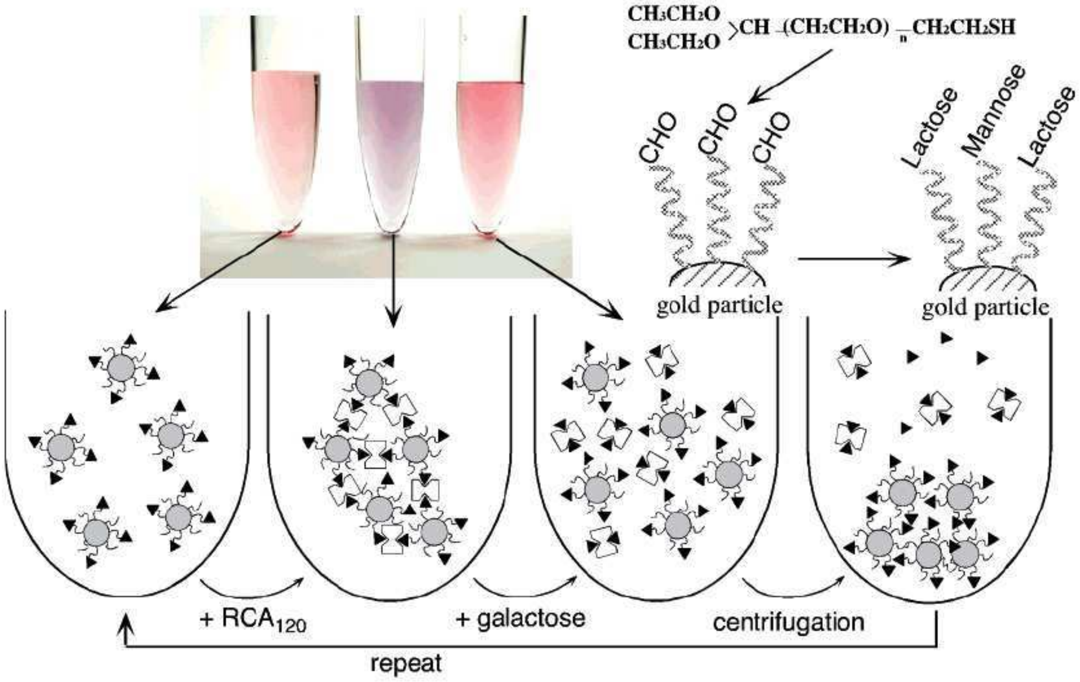

Figure 5.8. Schematic representation of the reversible aggregation-dispersion behavior of lactose-coated Au NPs by sequential addition of RCA120 lectin and galactose with the corresponding color changes of the solution. From reference [210].

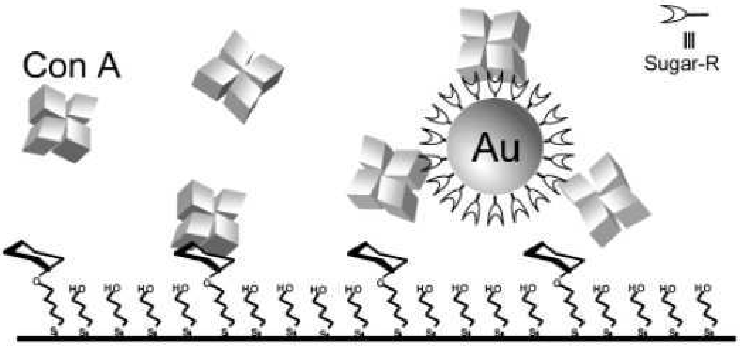

Figure 5.9. Schematic illustration of the interactions of glyconanoparticles and ConA on a biosensor chip during a competition assay. From reference [211].

GlycoNPs as biolabels

The strong affinity given by the multivalent ligand presentation by the glyconanoconjugates combined with the good visibility of Au NPs by transmission electron microscope makes these entities good candidates as biolabels. There is an interesting example of this application provided by the selective binding of mannose Au NPs to FimH adhesin of bacterial type I pili. The selective binding of the nanoconjugates to the bacterial type I pili observed by transmission electron microscope presented a novel method of labelling specific receptors for carbohydrates on the cell surface using glycoconjugates [212].

GlycoNPs for bio-amplification strategies

The easily observable aggregation of glycoNPs can be exploited for bio-amplification strategies. This was proved by Geddes *et al*., who developed a method to quantify glucose by monitoring the changes in the plasmon absorption of gold glycoNPs conjugated with a high-molecular-weight dextran. The method was based on the aggregation of Au NPs with ConA, which results in a significant shift and broadening of the gold plasmon absorption. The addition of glucose competitively binds to ConA, reducing Au NP aggregation and therefore decreasing the plasmon absorption [173].

GlycoNPs in biomedicine

GlycoNPs constitute a good biomimetic model to intervene in carbohydrate-mediated biological processes and, thus are promising for biomedical applications.

Several groups have proposed the conjugation of heparin to NPs with different purposes like inhibiting basic fibroblast growth factor-2 induced angiogenesis [213] or enhancing its anticoagulant activity [214]. However, the extreme complexity of polysaccharide design and synthesis has encouraged the research and development of more simple approaches to construct glycoNPs with biomedical interest.

Reynolds *et al*. have used small carbohydrate molecules galactose and fructose for preparing glycoNPs. They have shown that obtained glycoNPs were efficient inhibitors for two lectins (PA-IL and PA-IIL), responsible of the virulence and host invasion of *Pseudomonas aeruginosa*, an opportunistic bacteria responsible of numerous infections [215]. This was made via the so-called anti-adhesive approach, illustrated in Figure 5.10, which has been used not only for the prevention of pathogen invasion but also for anticancer applications. One of the critical steps of metastasis is the adhesion of tumour cells to vascular endothelium, which permits the growth of new tumour foci. Carbohydrate-carbohydrate interactions between glycosphingolipids expressed on the tumour and endothelial cell surfaces are involved in the adhesion step. Therefore, inhibition of this process by glycoNPs could provide effective anti-adhesion therapy and thus, avoid metastasis progression. [216]

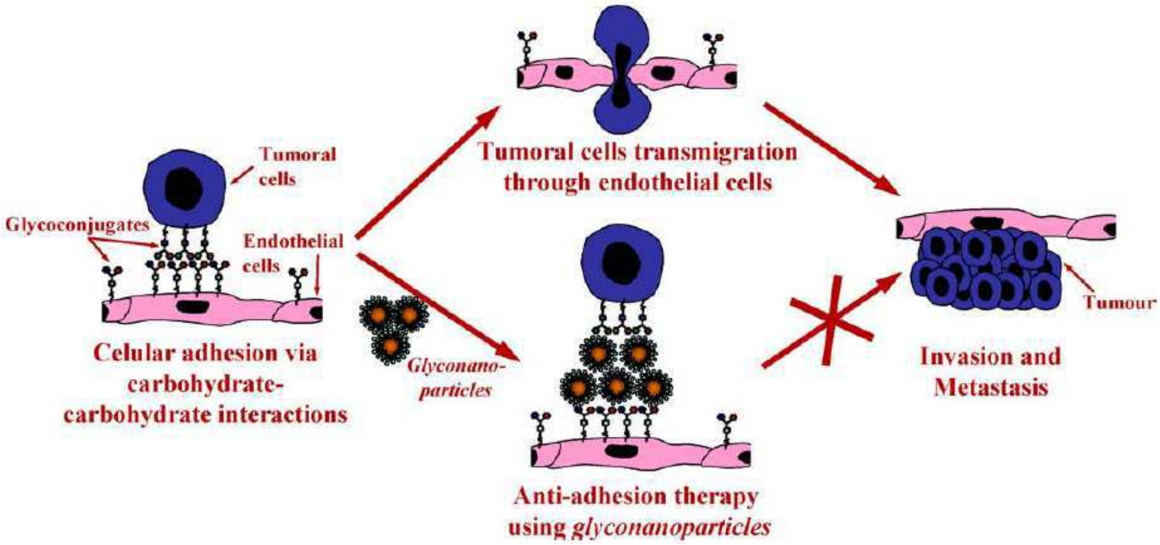

Figure 5.10. Possible action mechanism of glyconanoparticles in anti-adhesive therapy. From reference [209].

5.3. Objective of the chapter

Since the commercialization, in 2002, of Arixtra$^{(R)}$, a synthetic antithrombotic GAG fragment, GAG-protein interactions have been the centre of intense research. Search of new GAG type drugs rely on the elucidation of the structures of fragments binding specifically to the therapeutic target. However, this approach generally involves tremendous synthetic efforts in carbohydrate synthesis.

In this context, a project (ANR 06-NANO-045, 2006-2010) has been proposed by Prof. David Bonnaffé (University Paris-Sud, Orsay), Hugues Lortat-Jacob (IBS, Grenoble) and our lab. In this project, we have proposed to change drastically the approach. Instead of preparing GAG fragments or mimetics, we have decided to mimic directly the ability of GAG fragments to bind specifically a given protein by the multivalent display of more easily accessible synthetic disaccharides on a 3D surface, such as nanoparticles, for preparation of biomimetic nanovectors.

In this study, the developed electronic tongue is used as a medium throughput screening technique for bioactive 2D combinatorial surfaces since it permits to test the

maximum of disaccharide mixtures on a single array in a highly efficient way. Once the combinatorial surface of interest chosen, it will be then transferred to a 3D surface (NPs) for preparation of biomimetic nanovectors.

5.4. Preparation of 3D biomimetic nanovectors

As illustrated in Figure 5.11 for preparation of 3D biomimetic nanovectors, first, different building blocks are mixed with well-defined composition and ratio. The mixtures are spotted on the SPRi prism for screening of bioactive combinatorial surfaces. For this, the interaction between all the obtained combinatorial surfaces and the protein of interest are measured simultaneously by SPRi so as to determine the composition of the combinatorial surface which has the strongest affinity to the target protein. Once the combinatorial surface of interest chosen, the same composition is then transferred to a 3D surface (NPs) for preparation of biomimetic nanovectors.

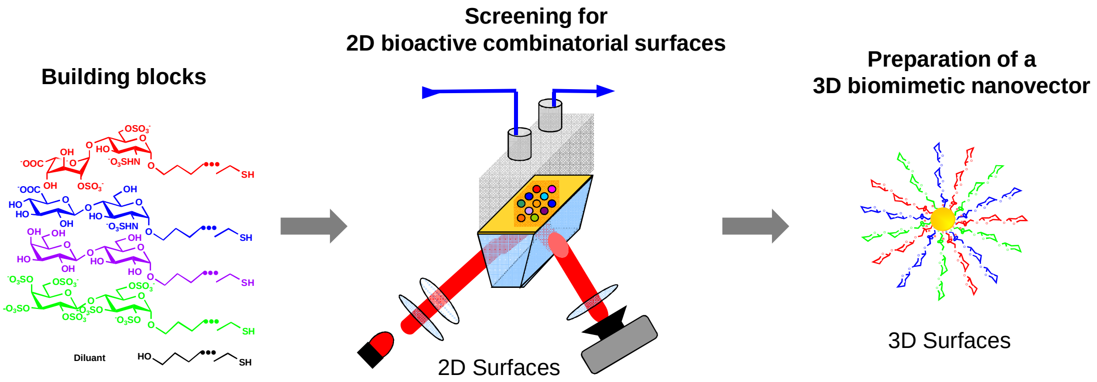

Figure 5.11. Schematic illustration for preparation of 3D biomimetic nanovectors through electronic tongue based screening of 2D bioactive combinatorial surfaces.

For proof of concept and as preliminary tests, we decided to prepare biomimetic nanovectors based on our previous results. That is to say, the two disaccharides lactose and sulphated lactose are used as BBs and the studied proteins, such as IFNγ, are used as protein of interest. For example, based on the CEP generated with the electronic tongue, we can easily determine that the combinatorial surface containing 10% BB1 and 90% BB2 is the most active one to IFNγ, as shown in Figure 5.12. Therefore, the mixture of BB1 and BB2 containing 10% of BB1 will be used for preparing the corresponding bioactive biomimetic nanovector.

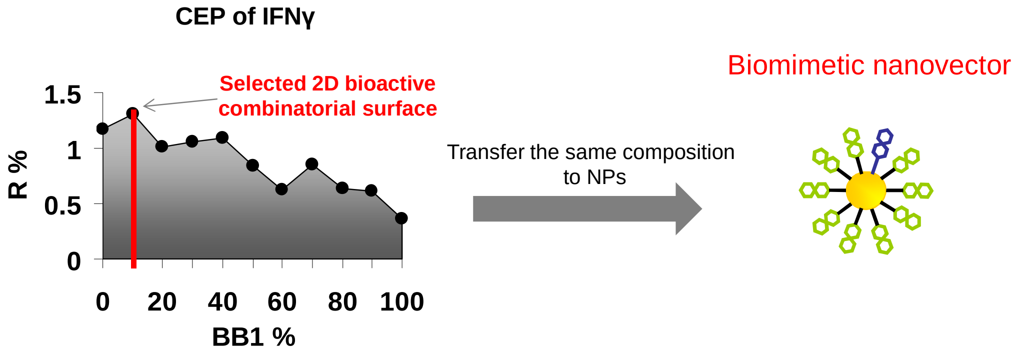

Figure 5.12. Screening of the 2D bioactive combinatory surface based on CEP generated by the electronic tongue in order to determine the composition of BB mixture for preparing the 3D biomimetic nanovector.

5.4.1. Choice of nanoparticles

In this study, gold nanoparticles were chosen as a multivalent 3D scaffolds, not only because they are widely studied in the literature but also because gold is the material used for the electronic tongue with SPRi detection system.

Although a variety of methods for synthesizing Au NPs have been reported [160], for this work we decided to use commercially available colloid solutions in order to avoid synthesis and characterization steps and ensure experimental reproducibility. The ones used during the experiments of this section were purchased from Sigma-Aldrich and BBInternational.

However, the exact molar concentration of Au NP suspension is often not given by the supplier. In our study, for preparation of the biomimetic nanovector by functionalizing Au NPs with the BB mixtures, this parameter is important to know. There are different ways to calculate the molar concentration of Au NPs.

If Au NPs are synthesized from a salt solution of $HAuCl_4$, the concentration can be calculated as follows [217]:

Assuming spherical shape and uniform face-centered cubic (fcc) structure, the average number of gold atoms (N) per nanosphere can be calculated by applying the following equation:

$$N = \frac{\pi}{6} \frac{\rho D^3}{M}$$

Equation 5.1. Average number of gold atoms per NP. ρ is the density of fcc gold (19.3g/cm^3), D is the diameter of the NP and M stands for the atomic weight of gold (197 g/mol).

Substituting the known data in the equation gives the number of gold atoms per particle as a function of the diameter:

$$N = 30.89602 D^3$$

Equation 5.2. Average number of gold atoms per NP as a function of the diameter (in nm) of the NP.

For example, for Au NPs of 20 nm, this leads to a number of 2,47x10^5 gold atoms per particle.

The molar concentration of a nanosphere solution is calculated by dividing the total number of gold atoms (N_{total}, equivalent to the initial amount of gold salt added to the reaction solution) over the average number of gold atoms per nanosphere (N) according to the following equation:

$$C = \frac{N_{Total}}{NVN_A}$$

Equation 5.3. Calculation of the molar concentration of Au NP solution. V is the volume of the reaction solution in liters and N_A is the Avogadro's constant. It is assumed that the reduction from gold (III) to gold atoms was 100% complete.

In our study, this calculation was used for the 20 nm Au NPs purchased from Sigma-Aldrich, in which the only concentration specified was 1% of gold. A concentration of 1.2 nM was obtained for this solution.

Another common method used for calculation of the molar concentration of Au NP is based on measurement of the characteristic absorbance peak of gold colloids (at 523 nm for Au NPs of 20 nm) using UV-spectroscopy. The intensity of the peak is proportional to NPs concentration. This method is very useful in certain cases, for instance, to control the concentration of NPs after a centrifugation cycle or to check if there is any loss of NPs due to aggregation after a long period of storage.

For the Au NPs of 20 nm purchased form BBInternational, the concentration was specified on the product notice: 1.16 nM. By plotting the solution absorbance at 523 nm versus different concentrations, we made a calibration curve, as shown in Figure 5.13. Based on it, we can determine concentration of Au NPs at any moment of our experiment for controlling the quantity of the particles simply by making an absorbance measurement. Calibration curve was also made for Au NPs of 5 nm and 10 nm.

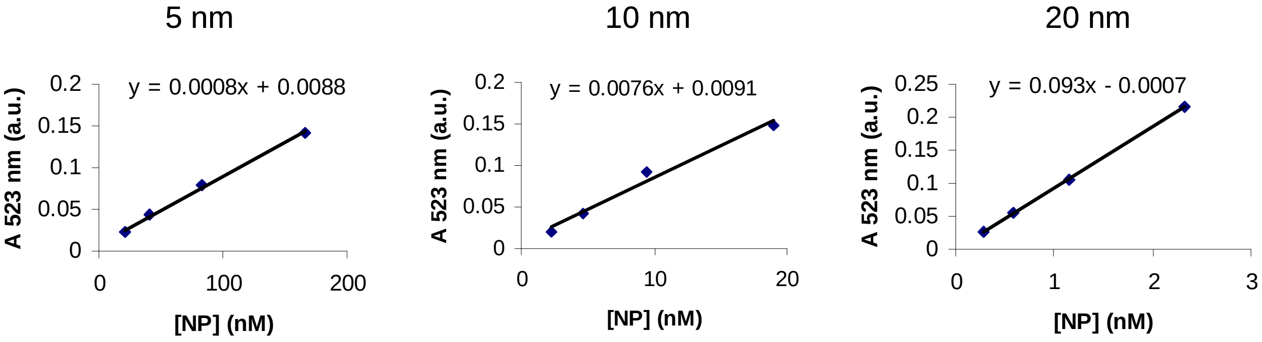

Figure 5.13. Calibration curves derived from the absorbance of colloidal solutions of controlled concentrations.

In addition, the correlation between the two calculation methods was checked using the solution of 20 nm Au NPs provided by Sigma-Aldrich. As shown previously, using the first calculation method, we obtained a concentration of 1.2 nM for this solution. After measuring by UV spectroscopy, the absorbance of this solution at 523 nm was 0.12 a.u., which corresponded to a concentration of 1.2 nM. As a consequence, the two calculation methods are consistent.

5.4.2. Choice of building blocks used for the functionalization of Au NPs

In this study, Au NPs were first functionalized with mixtures of BB1 and BB2 at various ratios by simply mixing the colloid solution and the BB mixtures at defined concentrations. After then, these functionalized NPs were re-dispersed in different media, including ultrapure water, HEPES buffer solution with and without NaCl, in order to study their stability under different conditions.

The stability of Au NPs can be simply evaluated by the color of the colloid solution. The characteristic red color caused by the surface plasmon absorption around 520 nm indicates good dispersion of Au NPs in the solutions. When aggregation occurs, solutions turn to blue since particle distance decreases and, thus, colloid solutions absorb at longer wavelengths. When total aggregation occurs, solutions become clear because the aggregates deposit at the bottom.

As seen in Figure 5.14, all functionalized NPs solutions were stable in ultrapure water. However, when they were re-dispersed in HEPES buffer containing NaCl, all the colloid solutions immediately turned to light blue except the BB2-coated NPs, which are strongly negatively charged. This is not surprising since it is known that the presence of charge on Au NP surface can give rise to columbic repulsion and thus favors dispersion of the NPs. Nevertheless, the coulombic repulsion can be diminished by the addition of a salt, leading to precipitation of the NPs or “salting out” [218]. Usually, physiological salt concentration (around 150 mM) is sufficient to cause precipitation of NPs lacking additional stabilization. In order to confirm that the instability of functionalized Au NPs is due to the presence of NaCl in the buffer, another set of experiments were performed by re-dispersing all functionalized Au NPs in the same HEPES buffer solution but without NaCl. As expected, all functionalized NPs stayed dispersed. These results revealed that the Au NPs functionalized with mixtures of BB1 and BB2 were not suitable to potential applications in nanomedicine due to their intrinsic instability in physiological conditions. Consequently, we decided to search for new BBs for preparation of biomimetic nanovectors.

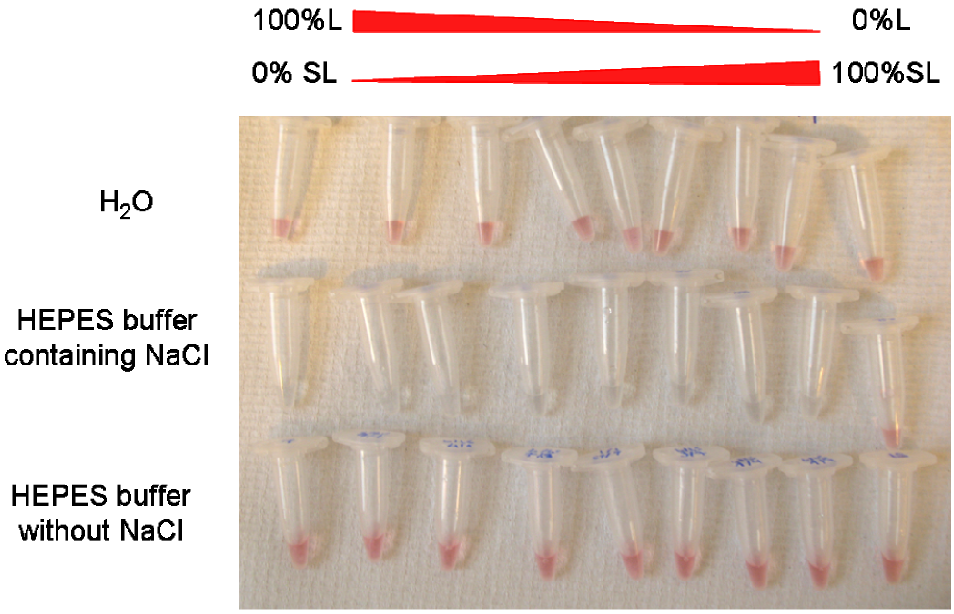

Figure 5.14. Photography of functionalized Au NPs with BB1 and BB2 mixtures at different ratios after re-dispersion in different media.

It was reported in the literature that hydrophilic polyethylene glycol (PEG) chains can be used as an effective coating materials for stabilizing NPs. On one hand, they could render functionalized NPs more hydrophilic and favour suspension of NPs; on the other hand, they could increase steric hindrance of functionalized NPs and thus avoid aggregation of NPs. [219, 220] [221] [222] [223] [224]. In addition, PEG has been extensively used as a biomaterial because of its low toxicity and low immunogenicity [225].

Therefore, we decided to integrate a PEG spacer in the BB1 and BB2. Two new building blocks were synthesized and provided by Prof. David Bonnaffé. Their structures are given in Figure 5.15. In this thesis, they are called BB1-PEG and BB2-PEG, respectively. Comparing to the structures of BB1 and BB2, the most important feature, the terminal functional group lactose and sulfated lactose, is conserved for BB1-PEG and BB2-PEG. Two major differences include the insertion of a PEG spacer and the addition of an acetyl group as protection for thiol head group for the new BBs.

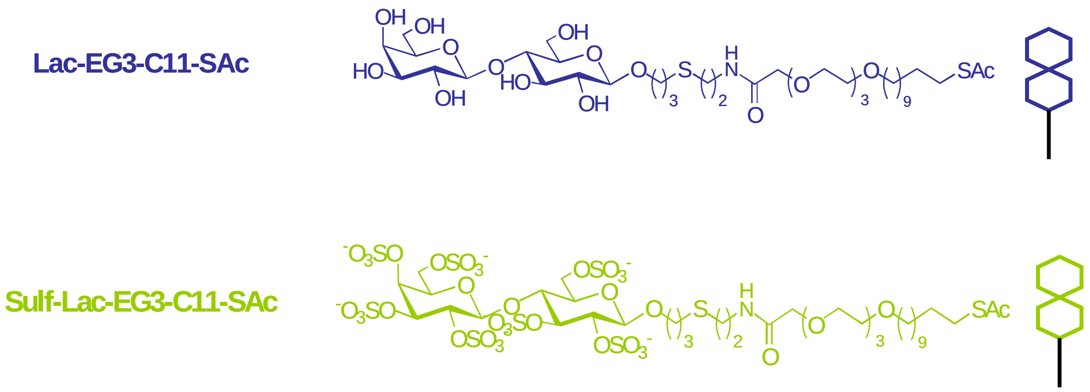

Figure 5.15. Chemical structures of BB1-PEG and BB2-PEG, which integrate a poly(ethylenglycol) spacer in BB1 and BB2, respectively.

Using BB1-PEG and BB2-PEG as building blocks, an electronic tongue was constructed based on 11-CoCRR array during internship of Laurie-Amandine Garçon in 2012. This electronic tongue was used for analysis of pure proteins ECL, CXCL12α and CXCL12γ. It was demonstrated that the CEPs obtained for these proteins are almost the same as the ones obtained with the electronic tongue constructed using BB1 and BB2. This means that mixtures of BB1/BB2 have similar properties to those of BB1-PEG/BB2-PEG.

5.4.3. Functionalization of Au NPs using new building blocks

The acetyl protection group of new BBs needed to be removed before use. The deprotection protocol was optimized using different basic solutions including NaOH (2.5 mM), NH_4OH (63 mM) and K_2CO_3 (2.5 mM). The quality of self-assembly of the two new BBs on gold surface (2D) was characterized by electrochemical impedance spectroscopy and cyclic voltammetry. The detailed experimental set-up and results are given in the Appendix D. In summary, the optimal conditions chosen were: treatment of the BBs with 2.5 mM sodium hydroxide (NaOH) for 1h before the spot deposition.

For functionalization of Au NPs using new BBs, a protocol was established. It is presented in detail in Table 5.1, and illustrated in Figure 5.16.

1- Add 50 µL of the desired BB mixture at a total concentration of 10 mM to an eppendorf.
2- Add 50 µL of NaOH at 5 mM to the BB mixture solution and wait for 1h. At this point, the BB concentration in solution is 5 mM and NaOH concentration is 2.5 mM.
3- Add 400 µL of Au NPs of 20 nm as received from BBInternational (concentration 1.16 nM). Final concentration for NPs is 0.93 nM, and for BBs, 1 mM.
4- Leave the mixed solution of step 3 overnight for self-assembly of BBs on Au NPs.
5- Rinse functionalized NPs and re-suspend in the desired solution (HEPES buffer or ultrapure water) by at least three centrifugation/supernatant removal/buffer addition cycles.

Table 5.1. Protocol employed for the functionalization Au NPs using the new BBs.

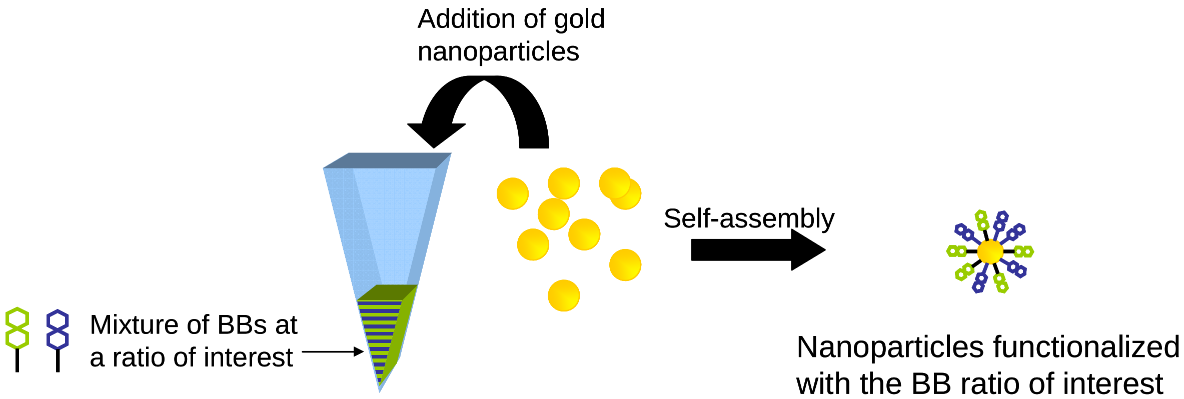

Figure 5.16. Schematic illustration of the protocol employed for particle functionalization

5.5. Characterization of functionalized NPs with new BBs

In this thesis, two important features of the nanoconjugates were studied: stability and ligand density. Stability in strong saline conditions was evaluated by UV-Visible spectroscopy measurements. Stability and monodispersity at high concentrations was measured by small angle x-ray scattering. Ligand density on NPs was theoretically estimated and colorimetrically quantified.

5.5.1. Direct visualization of the stability of functionalized Au NPs with new BBs

The Au NPs functionalized with BB1-PEG and BB2-PEG mixtures at different ratios were re-dispersed in HEPES buffer solution containing NaCl. Satisfyingly, this time, all the solutions containing functionalized NPs kept their bright red color, as shown in Figure 5.17. Only the eppendorf containing non-functionalized NPs lost its red color. This confirms that the introduction of PEG spacer in BBs increases greatly the stability of functionalized Au NPs. Therefore, the prepared nanoconjugates are stable under physiological conditions of pH and ionic strength. They are thus very promising for our further study on interaction between these functionalized NPs and proteins of therapeutic interest.

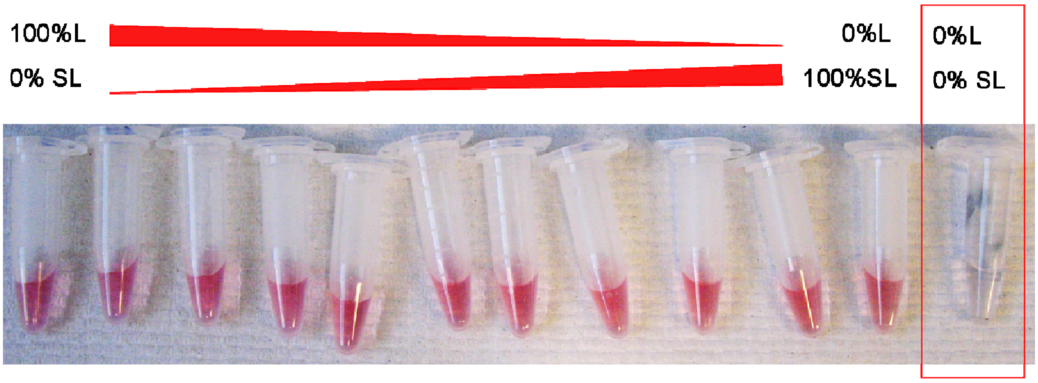

Figure 5.17. Photography of functionalized Au NPs with BB1-PEG and BB2-PEG mixtures at different ratios after re-dispersed in HEPES buffer containing NaCl. On the right, non-functionalized Au NPs after re-dispersed in HEPES buffer containing NaCl.

5.5.2. UV-Visible Spectroscopy

In addition, in this study, the stability of functionalized NPs in strong saline conditions was evaluated over time by UV-Visible spectroscopy measurements.

For this, NPs functionalized with mixed BB1-PEG/BB2-PEG at a ratio of 7/3 were used as an example and they were re-suspended in water. The measurements were performed with UV-Vis NanoDrop instrument before and after the addition of a NaCl solution (200 mM) during over time (1, 2, 3, 4, 5, 72 and 168 hours after storage). The mentioned apparatus permits to measure the absorbance of samples using a very small volume (~2 µL).

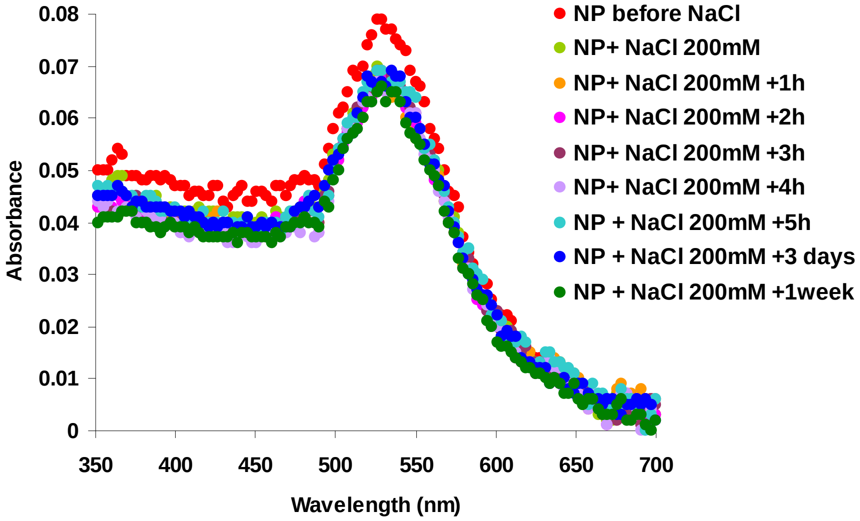

Figure 5.18. UV-Vis Spectra of the nanoconjugates (20 nm) before and after the addition of a NaCl solution over time.

From Figure 5.18 we can see that the absorbance intensity of NPs before NaCl addition is slightly higher than the ones of NPs after NaCl addition. This is very probably due to the dilution effect caused by the addition of the saline solution. Interestingly, for all the measurements made after NaCl addition there is neither shift for absorption peak position nor change for absorbance intensity, illustrating that no aggregation of NPs occurs under saline conditions during at least one week. These results confirm again that the introduction of PEG chain in BB1 and BB2 increases strongly the stability of nanoconjugates under saline conditions.

5.5.3. Small Angle X-Ray Scattering

Stability of nanoconjugates (especially those with a neutral surface charge) was also tested at very high concentrations in order to explore the limits of the steric stabilization provided by the PEG chains. This was made by Small Angle X-Ray Scattering (SAXS) technique, in collaboration with Arnaud de Geyer from the INAC/SGX laboratory.

A brief introduction to the SAXS technique, as well as technical details of the experiments done for this study, are included in the Appendix E. In brief, SAXS technique can give information about the individual nanoparticle and the presence of interferences between the nanoparticles in solution. These interferences are perceived in form of perturbation of the SAXS curve measured from individual (interaction-free) nanoparticles in the dilute regime. Indeed, the scattering from a colloidal suspension of isotropic spherical particles can be described by the combination of a first term which describes the scattering from individual nanoparticles (referred to as the form factor P(q)) and a second term which describes interactions between nanoparticles (referred to as the structure factor S(q)): $I(q)=P(q)S(q)$. In our case, two factors can induce inter-particle interferences: 1) the presence of charged particles 2) a small mean inter-particular distance (at high concentration of nanoparticles).

The samples used for the study were aqueous solutions of 10 nm Au NPs that were functionalized with pure neutrally charged molecules BB1-PEG or with pure negatively charged ones BB2-PEG at different concentrations. The objective was to see if increasing drastically the concentration of nanoparticles would affect their stability and induce aggregation.

The concentration of mother colloidal suspension purchased from BBInternational is 0.057 mg/ml. This concentration is 20 times lower than the concentration (1 mg/ml) normally required to measure within a reasonable acquisition time the scattering curves in the dilute regime. Thus we prepared functionalized NPs solutions with 10×, 20×, 35×, 60× and 160× higher concentrations comparing to the mother solution by centrifuging and re-suspending NPs in smaller volume, referred to as c10, c20, c35, c60 and c160, respectively. The information obtained by SAXS at different concentrations concerns the shape and size of the gold nanoparticles and their inter-particle interactions.

First, neutrally charged nanoparticles which were functionalized with BB1-PEG were analyzed. In Figure 5.19a, we show the SAXS curves obtained for c10, c20 and c35. The curves overlapped perfectly, indicating that there is no aggregation induced by high concentration of colloid solution.

The mean radius of the suspended nanoparticles can be calculated with measurements in the dilute regime both from the position of the first maximum of the curve Iq^4 *vs* q (Porod representation) or by a Guinier-type analysis of the scattering at very small angles (in range $qR<1$). As shown in Figures E3 and E4 included in the Appendix E, for the sample c35, both values are similar and fit well with the attended data for a stable monodisperse Au NP solution. From the first maximum around $q=0.065$ Å^{-1} in the Iq^4 curve we can deduce a value R_M = 43 Å and from the scattering intensity in the range 10^{-2} Å^{-1} – $2x10^{-2}$ Å^{-1} (satisfying condition $qR<1$) we can deduce a Guinier radius R_G =43 Å. Both values agree perfectly well confirming the spherical shape of the particles and the absence of inter-particle interactions at the measured concentration. It should be noticed that the radius 43 Å deduced from the SAXS analysis corresponds to the size of the metallic core of the nanoparticles and not to the whole size including the surrounding shell of organic ligands.

Besides, when we concentrated the nanoparticles up to c160, the monodispersity of the solution could still be proved (see Figure E5) since the slope of the Guinier representation of the SAXS data was the same to that of c35, meaning that the gyration radius was the same. We could strongly affirm, then, that the Au NPs studied were stable even at high concentrations.

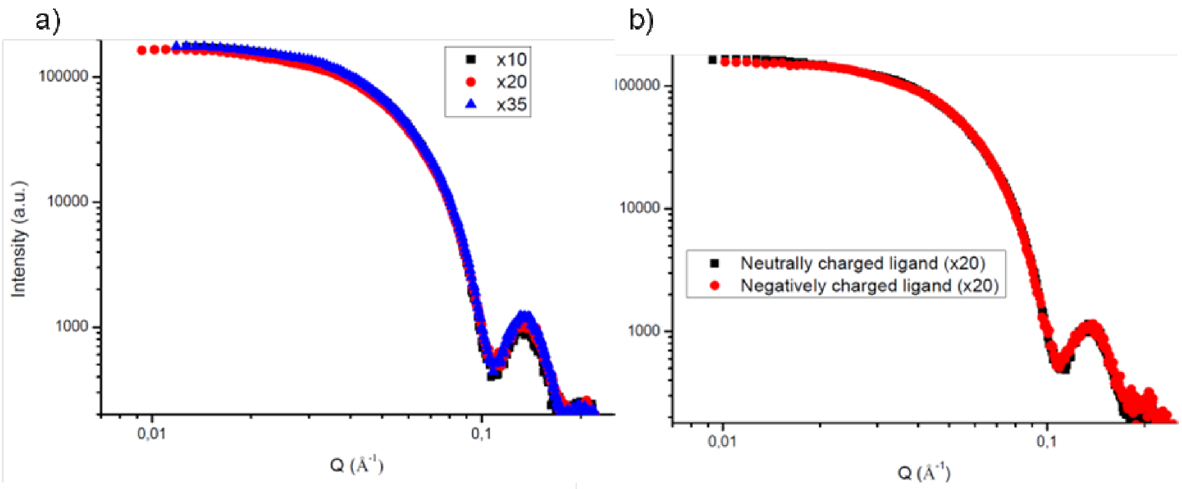

Figure 5.19. Scattering curves obtained for a) BB1-PEG nanoconjugates at x10, x20 and x35 concentrations and b) for BB1-PEG and BB2-PEG nanoconjugates at a x20 concentration (data represented as log(I) *vs* loq(q).)

Moreover, we were able to affirm that the functionalized nanoparticles, both negatively charged and non-charged, at a concentration of x20, stayed stable. There were no aggregates since both of the obtained curves showed a clear sharp first minimum, which suggests monodispersity of the nanoparticles (see Figure 5.19b).

However, for evaluation of the effect of charge repulsions, much more concentrated colloidal suspensions should be used. Taking into account of constraints like product-consumption, we finally did not perform experiment to study this point.

5.5.4. Determination of Ligand Density on Functionalized Nanoparticles

In this part, the ligand density on functionalized NPs was determined theoretically and experimentally, by a colorimetric technique.

a) Theoretical estimation of ligand density on functionalized NPs

Theoretical estimation of the quantity of ligands present on nanoparticles after functionalization was done by employing the data included in Table 5.2.

First, the surface of the nanoparticle was calculated in function of its diameter/radius ($S = 4\pi r^2$, in Å). Then, the number of ligand anchored on each NP was determined by assuming that S-S spacing is the same as the one obtained for self-assembled monolayers on a gold (1.1.1) planar surface (4.97 Å) and the area occupied per thiol molecule is 21.4 $Å^2$ [226]. For example, for the Au NPs of 20 nm, according to our calculation, there are 5872 ligands anchored on its surface after functionalization. In the fourth column, the number of ligand anchored on different size of NPs is listed. These data are consistent with those experimentally obtained in literature [227].

To functionalize Au NPs, we first centrifuged the colloid solution (as received from BBInternational) and removed all surnatant. Then, the same volume of solution containing the BBs was added to Au NPs. In practice, before functionalization, we calculated the concentration and quantity of BBs necessary for covering all NPs in solution in theory. The concentration of the commercially available nanoparticle solution (BBInternational) is known and included in the column five. This permitted to estimate the concentration of BBs necessary to cover all the NPs in solution. To make sure that all NPs are completely covered by BB molecules, we have used BBs with a concentration that is 100 times higher than the one determined in theory, as listed in last column.

D (nm)	**R (Å)**	**S ($Å^2$)**	**Number of ligands per particle***	**[NP] (nM)**	**[BBs] necessary for covering the NPs in theory (µM)**	**[BBs] used for functionalization of NPs (mM)**
2	10	1256	59	249	14.6*	1.4*
5	25	7854	367	83	30.5*	3*
10	50	31416	1468	7.5	10.9*	1*
20	100	125664	**5872**	1.2	6.8*	0.7*
40	200	502656	23489	0.15	3.5*	0.35*

Table 5.2. Parameters used for theoretical calculation of ligand density on Au NPs. D, R and S are the diameter, the radius (D/2), and the surface ($4\pi r^2$) of Au NPs. [NP] is the nanoparticle concentration as received commercially in our study; [BBs] is the building blocks concentration. *Estimation made under the assumption that the area occupied by each ligand (thiol) molecule is 21.4 $Å^2$. [226].

b) Colorimetric quantification of ligand density

In addition, the quantity of ligands present on nanoparticles after functionalization was also determined based on a colorimetric method using a protocol developed by our collaborators David Bonnaffé and Christine Le Narvor (University Paris-Sud, Orsay). This protocol used for the determination of oligosaccharide quantity attached to PolyEthylene Terephthalate (PET) surfaces was adapted to our needs.

Principle of the phenol/sulphuric acid technique

Mono-, oligo- and polysaccharides react with phenol and sulphuric acid to give as a result the formation of a colored molecule with an absorption maximum at 490 nm, as shown in Figure 5.20.

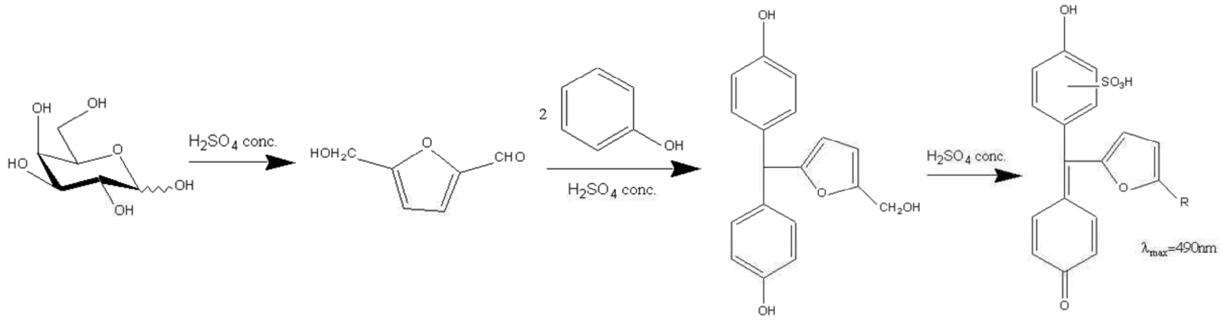

Figure 5.20. Reaction mechanism: in concentrated acid media, galactose is dehydrated and produces 5-hydroxymethylfurfural, which, in the presence of phenol, gives a colored substance showing a maximum of absorbance at λ = 490 nm.

Experimental method

The employed reagents were the following:

- 6% phenol solution in water
- Sulfuric acid solution 96%

First, a calibration curve was made using a 0.5 mg/mL solution of lactose monohydrate. Volumes of 0, 20, 40, 80, 100, 120, 140 and 160 µL of this solution were added to test tubes and then adjusted to 200 µL by adding ultrapure water. Afterwards, 200 µL of phenol solution (6%) were added to each tube followed by adding 1 mL of concentrated sulphuric acid solution.

Due to the presence of concentrated sulphuric acid in the media, the glycosidic bonds of lactose are hydrolyzed and the monosaccharides get free (see figure Figure 5.21).

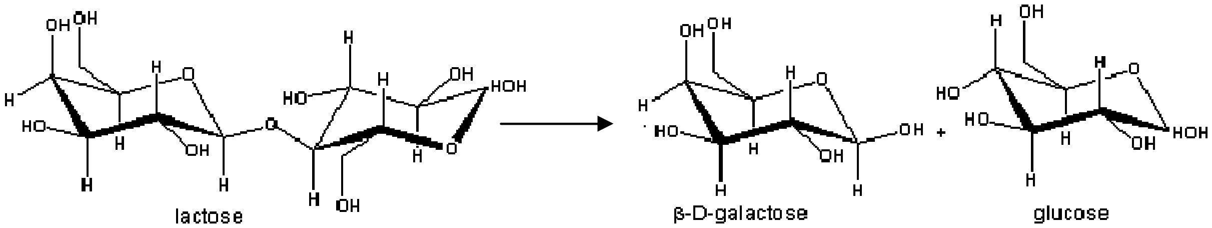

Figure 5.21. Hydrolysis of lactose to give β-D-galactose and glucose.

The monosaccharides in solution react with the sulphuric acid and the phenol by an exothermic reaction that leads to the formation of a yellow compound whose absorbance is measured with a UV-Vis spectrometer. The obtained calibration curve is shown in Figure 5.22.

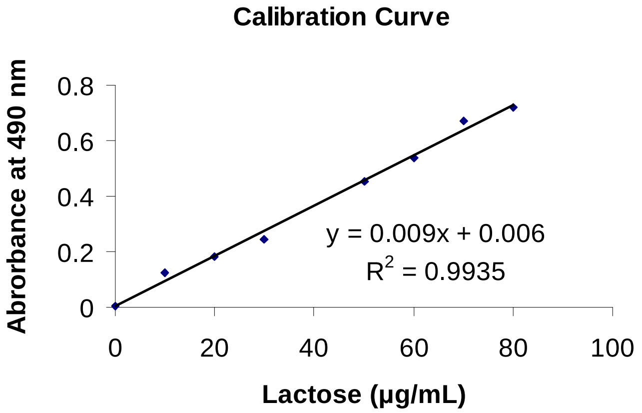

Figure 5.22. Calibration curve made by measuring the absorbance at 490 nm of the colored compound formed form the reaction of lactose with sulphuric acid and phenol.

The procedure to determine the quantity of disaccharides attached to the gold surfaces was very similar. 200 µL of functionalised NPs (20 nm) at the desired concentration (In this case the sample contained 5.6×10^{11} functionalized nanoparticles, which was calculated by absorbance measurement before the reaction) were put in a test tube. Then, phenol 6% (200 µL) and sulphuric acid (1mL) were added. As a consequence, the glycosidic bonds of the disaccharides were hydrolysed and the monosaccharides (both form BB1-PEG and BB2-PEG) got free in solution. They reacted as explained before to give a colored compound whose absorbance was then measured by UV-Vis spectroscopy. Before the measurement, an extra step of centrifugation was added in order to avoid the interference from absorbance peak of gold nanoparticles at about 520 nm. The obtained absorbance value for the sample was **A (490 nm) = 0.0176**

As a result, the quantity of disaccharides present in solution can be determined, which corresponds to the total number of ligand initially present on the nanoparticle surface. As nanoparticle concentration is known, it is possible to quantify the density of the ligands (each ligand contains one disaccharide moiety) that were initially attached per particle.

In this case, the absorbance value obtained corresponds to 4.012×10^{15} ligand molecules. Note: the calibration curve was made with monohydrated lactose. The nanoparticle quantity present in the sample can be calculated from the absorbance (A = 0.089) using the calibration curve for 20 nm NPs in Figure 5.13. This calculation gave a number of 5.67×10^{11} particles in the sample.

Thus, we can determine the ligand density per particle:

$$\frac{4.012\cdot10^{15}\,ligands}{5.67\cdot10^{11}\,nanoparticles}=7075\,ligands\ per\ particle$$

c) Comparison between theoretical and experimental results

As described above, ligand density on Au NPs (20 nm) were both determined by theoretical estimation and experimental quantification. The former gave 5872 ligands per nanoparticle; while the latter gave 7075 ligands per nanoparticle. Satisfyingly, they are in the same order of magnitude. Higher ligand density on Au NPs obtained by the second method could be explained by the fact that due to technical constraints there is always a remaining volume of BBs that were not anchored on Au NPs even after several cleaning circles by centrifugation. The quantity of BBs molecules in the remaining solution was unknown but it was included systematically in the calculation by this method.

Moreover, we have also performed some preliminary tests to determine the ratio of BB1-PEG/BB2-PEG on the functionalized Au NPs by measuring zeta potential, but due to time constraints that disallowed us to optimize the experimental set-up, the results were not very satisfying and they were not shown here.

5.6. Bioactivity of the 3D biomimetic nanovectors

After characterization, bioactivity of the 3D biomimetic nanovectors was evaluated by studying their interaction with proteins of interest by SPRi and ELISA. The proteins used as models were IFNγ and its mutants.

As described previously, the biomimetic nanovectors were prepared by functionalizing Au NPs with selected BB mixtures. The selection of the 2D bioactive combinatorial surfaces was made based on CEPs. In this study, the mixture BB1-PEG/BB2-PEG with a 10% of BB1-PEG was chosen. In addition, Au NPs were also functionalized with a BB mixture corresponding to a 2D less active combinatorial surface, based on CEP, for negative control, as illustrated in Figure 5.23.

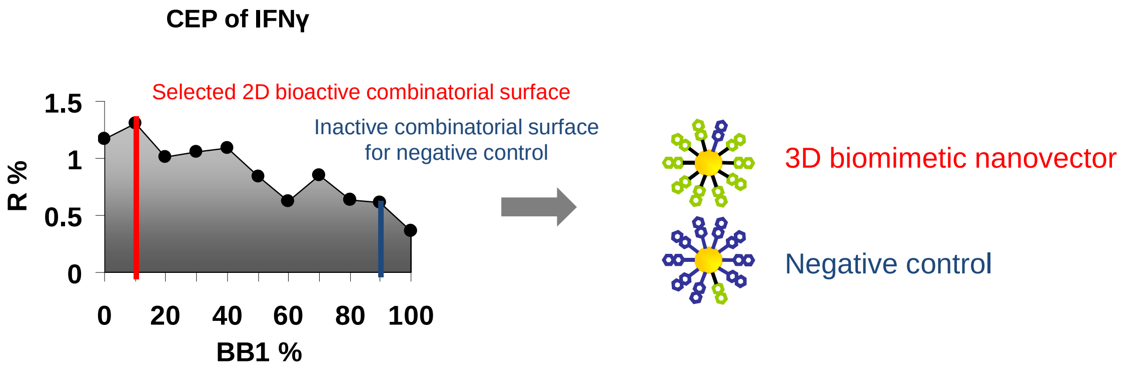

Figure 5.23. Schematic illustration for preparation of biomimetic nanovectors and inactive nanoconjugates based on CEP generated by electronic tongue.

5.6.1. Evaluation of the bioactivity of the 3D biomimetic nanovectors by SPRi

The principle of the competitive assay based on SPRi

To study the interaction between the protein and the biomimetic nanovectors by SPRi, a competitive assay was designed. The idea was to incubate the protein IFNγ Δ136 (50 nM) with the biomimetic nanovectors, and then to compare the signals obtained on the spot containing 10% of BB1 of the CoCRR array by injecting the protein IFNγ Δ136 (50 nM) with and without incubation with nanovectors. As illustrated in Figure 5.24:

- If the nanovector is inactive, there will be no interaction with the protein. Consequently, no signal change will be observed.

- If the nanovector is bioactive, there will be interaction with the protein, resulting in a decrease of concentration of free protein. Consequently, a decrease of signal will be induced by the 3D biomimetic nanovectors.

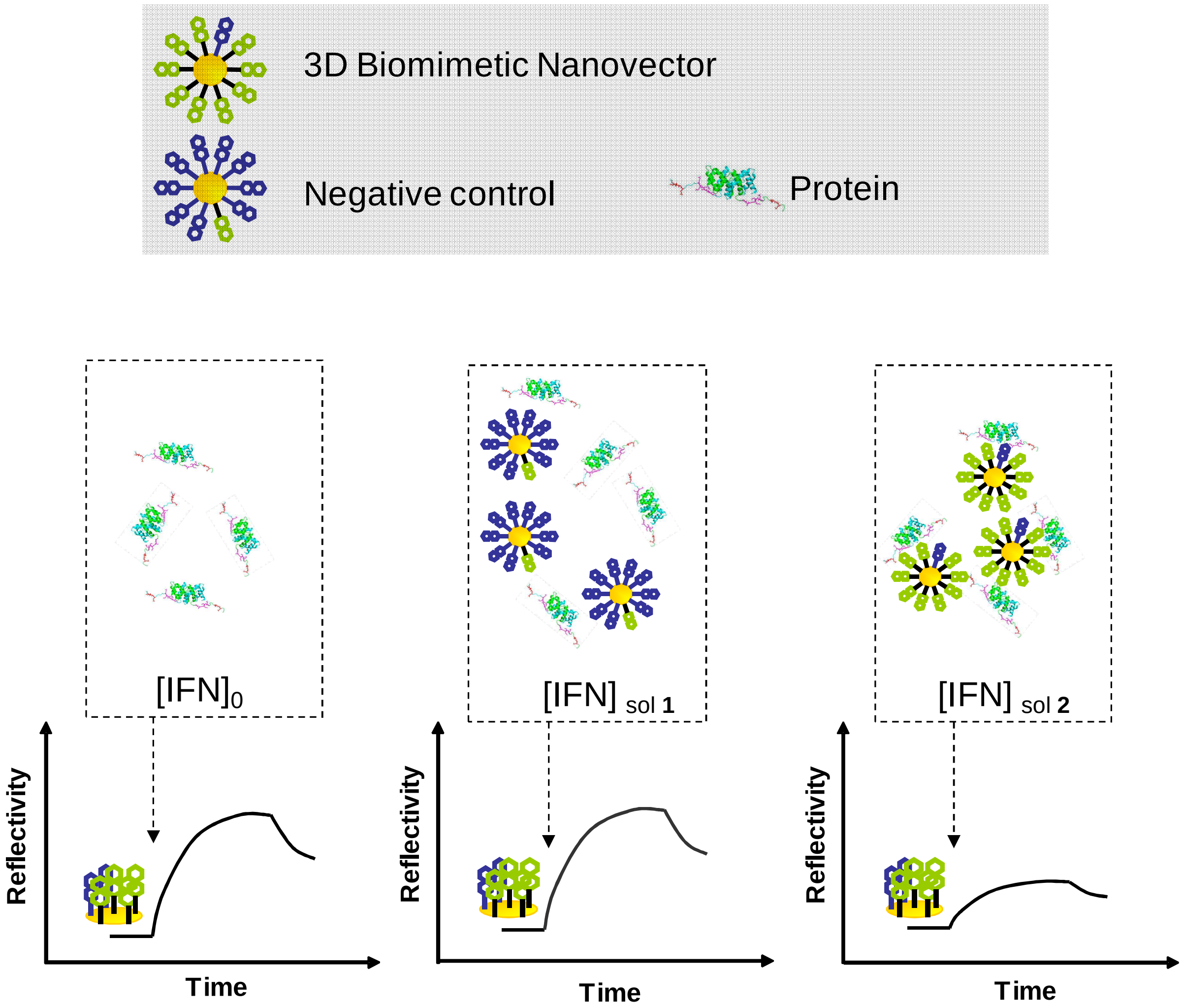

Figure 5.24. Schematic illustration of the principle of the competitive assay based on SPRi.

Experimental part and Results

In this study, IFNγ Δ136 (50 nM) was incubated with two sets of functionalized NPs for the same period of time, as illustrated in Figure 5.25. In the first set, the protein was incubated with inactive nanoconjugates at different concentrations: 0.005, 0.02, 0.08 and 0.2 nM. In the second set, the protein was incubated with active biomimetic nanovectors at different concentrations; 0.005, 0.01, 0.02, 0.04, 0.08, 0.1 and 0.2 nM. In practice, the functionalized nanoparticles at different concentrations were centrifuged and the supernatant removed. Then, 800 µL of IFNγ Δ136 (50 nM) were added to each eppendorf of NPs and they were mixed and left for incubation during at least 30 minutes before use.

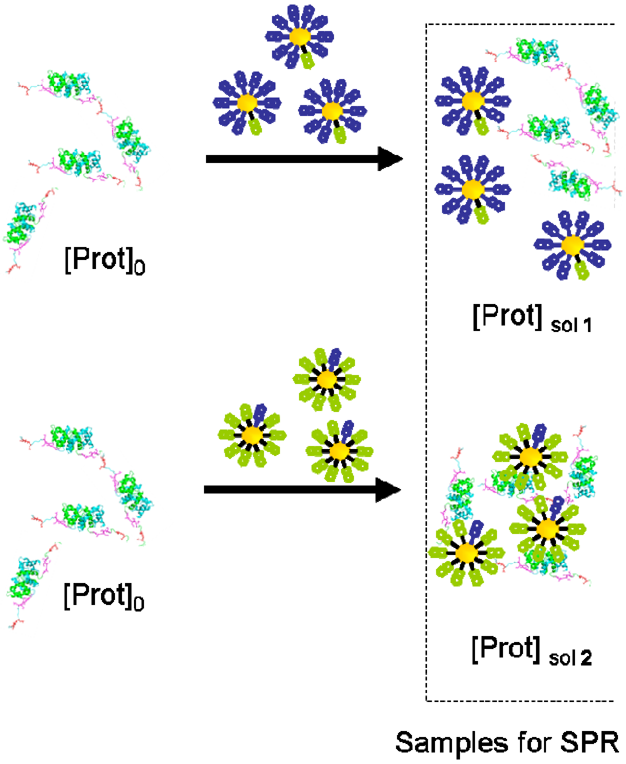

Figure 5.25. Preparation of the samples for injection on SPRi competition experiments.

The obtained results are shown in Figure 5.26. The maximal reflectivity on the spot containing 10% of BB1 was plotted against the nanoparticle concentration. As we can see, for the samples of the protein incubated with nanovectors functionalized with 10% BB1-PEG, the signal decreased significantly in a NP concentration-dependent manner. However, there was almost no signal decrease for the samples of the protein incubated with nanoconjugates functionalized with 90% of BB1-PEG. These preliminary results showed that the 3D biomimetic nanovectors we prepared are bioactive since they have affinity to the model protein. Thus, it is feasible to construct bioactive nanovectors which can mimic biological properties of GAG fragments simply by multivalent display of synthetic disaccharides onto nanoparticles.

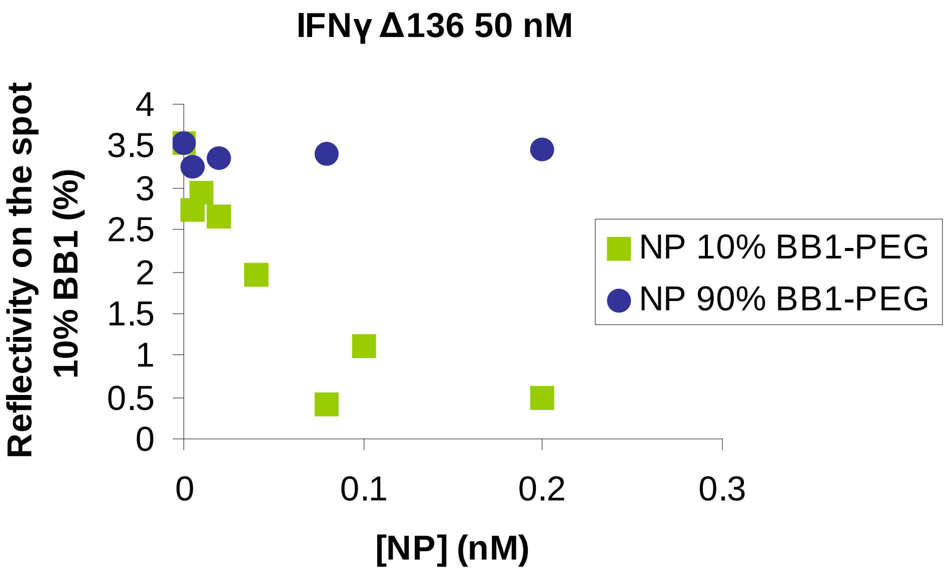

Figure 5.26. SPRi results obtained on the spot containing 10% of BB1 after injection of IFNγ Δ136 incubated both with biomimetic nanovectors at different concentrations (in green) and with inactive nanoconjugates at different concentrations (in blue).

5.6.2. Evaluation of the bioactivity of the 3D biomimetic nanovectors by ELISA

The interaction between the model protein and the biomimetic nanovectors was also evaluated with ELISA, which permits to accurately measure the concentration of IFNγ. In this study, the model protein IFNγ Δ136 and IFN Δ124 (for negative control) were incubated with different concentrations of 3D biomimetic nanovectors and inactive nanoconjugates. Afterwards, all these solutions were centrifuged, and their supernatants were used as samples for ELISA measurement to determine the concentration of free protein, as shown in Figure 5.27. Results will then be compared to a reference IFNγ solution, which would maintain a constant concentration of $[IFN]_0$ before and after the centrifugation step.

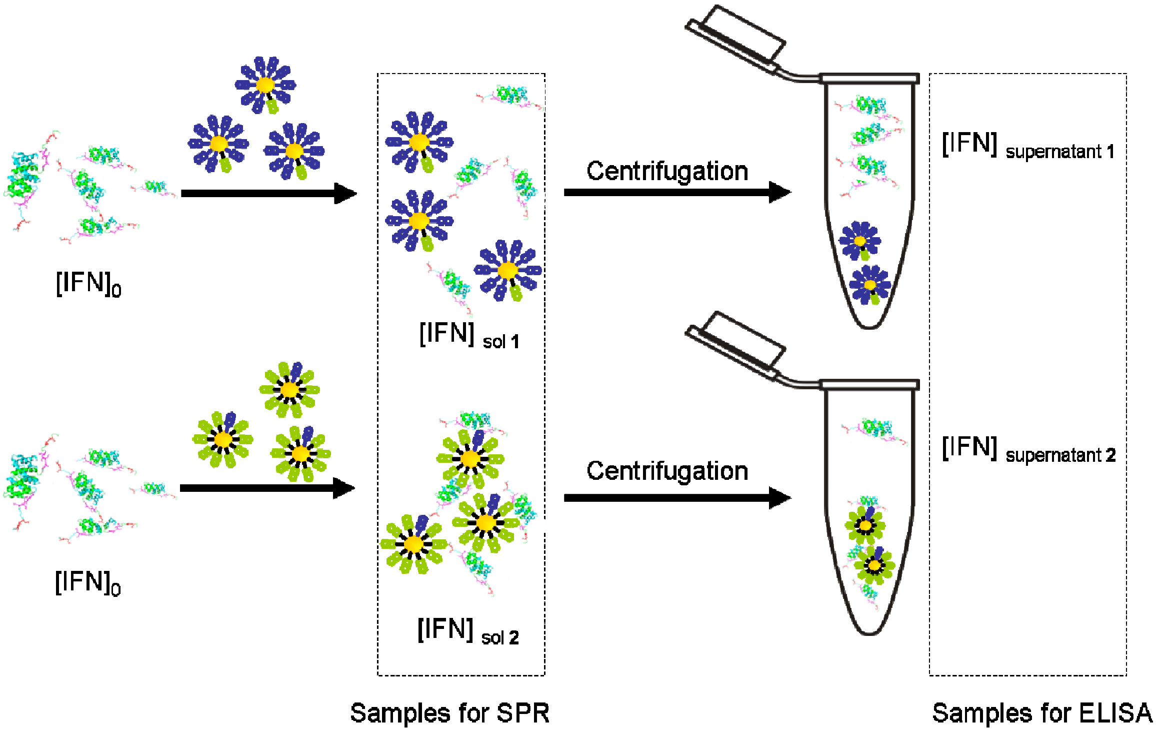

Figure 5.27. Comparison of sample preparation for studying the bioactivity of the 3D biomimetic nanovectors by SPRi and ELISA.

We anticipated that if the biomimetic nanovectors are active, the protein IFNγ Δ136 will be captured during incubation. Consequently, the concentration of the free protein in the supernatant will decrease comparing to the initial concentration. The higher the concentration of NPs used for incubation, the lower the concentration of free protein in the supernatant. When the model protein is incubated with inactive nanoconjugates, there is no affinity between the NPs and the protein. Consequently, the concentration of the protein in the supernatant should be the same as the initial concentration.

Determination of IFNγ concentration by ELISA

For IFNγ concentration determination, a commercial Quantikine® Human IFNγ Immunoassay was used. This assay employs the quantitative sandwich enzyme assay technique, illustrated in Figure 5.28. A polyclonal antibody specific for IFNγ is pre-coated onto a microplate. Standards and samples are pippeted into the wells and any IFNγ present is bound by the immobilized antibody. After washing away unbound substances, an enzyme-linked polyclonal antibody specific for IFNγ is added to the wells. Following a wash step to remove any unbound antibody-enzyme reagent, a substrate solution is added to the wells and color develops in proportion to the amount of IFNγ bound in the initial step. Finally, the color development is stopped and the intensity of the color is measured.

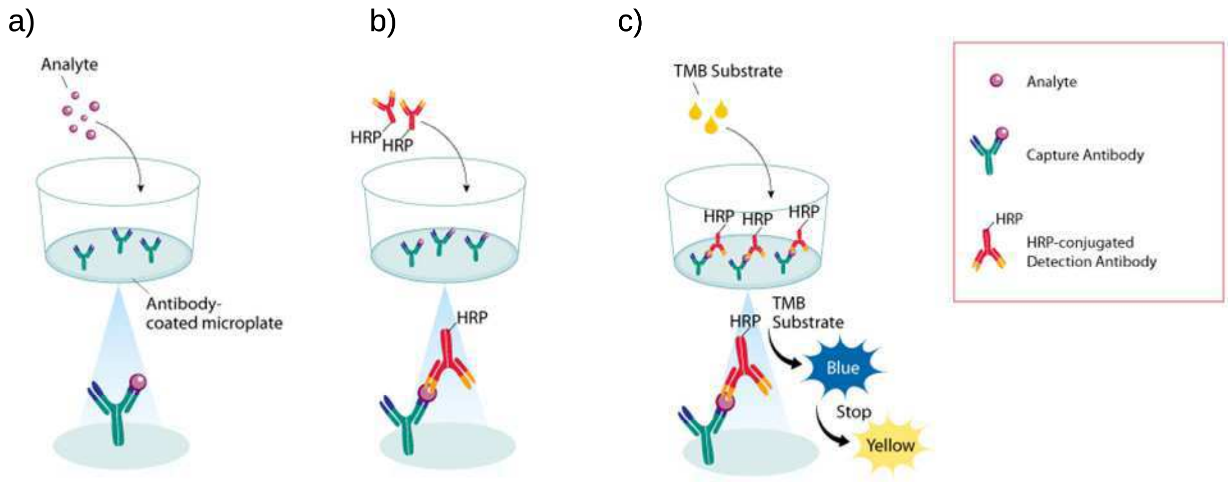

Figure 5.28. Illustration of the principle of ELISA based on a quantitative sandwich enzyme assay. a) A microplate pre-coated with capture antibody, on which samples or standard solutions are added; b) Addition of a second HRP-labelled antibody (detection antibody); c) Addition of tetramethylbenzidine (TMB) substrate solution to the wells, generating blue color. The color intensity is proportional to the amount of analyte present in the sample. Color development is stopped, turning the color in the wells to yellow. The absorbance of the color at 450 nm is measured.

Experimental part and Results

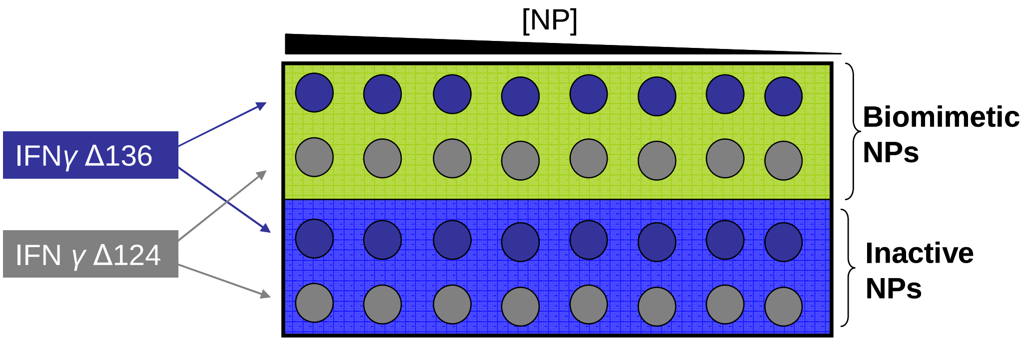

Figure 5.29. Illustration of the design used for the incubation of nanoparticles at different concentrations with the two proteins at a constant total concentration of 50 nM.

As illustrated in Figure 5.29, eight solutions of the biomimetic nanovectors (1.937, 0.717, 0.265, 0.098, 0.036, 0.013, 0.005 and 0 nM) were prepared in eppendorfs and they were divided into two sets, in the first set these solutions were put in contact with the protein IFNγΔ136 (50 nM) and in the second set with IFNγΔ124 (50 nM). The same procedure was used for the inactive nanoconjugates.

All these solutions were incubated 0.5 hour under agitation and 0.5 hour more without agitation. Afterwards, nanoparticles were centrifuged and the supernatants were diluted 1000 times (from a maximal concentration of 50 nM to 50 pM) in order to fit in with the concentration range of the calibration curve of the assay. All the diluted solutions were then used for ELISA analysis to determine the IFNγ concentration present in each well. The absorbance measurements at 450 nm (1.0 s) were made for each well at the IBS with a plate reader (Perkin Elmer, USA).

The results are shown in Figure 5.31. In the case where the protein IFNγ Δ136 was incubated with the biomimetic nanovectors at various concentrations (see Figure 5.30a, in green), the concentration of the free protein in the supernatant calculated by ELISA decreased significantly comparing to the initial concentration. Within the tested concentration range, the higher the concentration of NPs used for incubation, the lower the concentration of free protein in the supernatant. In the case where IFNγ Δ136 was incubated with the inactive nanoconjugates, see Figure 5.31a, in blue, decrease of the concentrations of the free protein in the supernatant was also observed for [NP] at 0.8 and 2 nM, but was much less important.

The protein IFNγ Δ124 was used for negative control due to its completely lost biological activity (as discussed in Chapter 4). For this protein, after incubation with either biomimetic nanovectors or inactive nanoconjugates, the concentrations of free protein in the supernatant were almost the same as the initial concentration, see Figure 5.30b. There was no concentration decrease, illustrating that this protein has neither affinity to biomimetic nanovectors nor with inactive nanoconjugates. This proves that the 3D biomimetic nanovector is not only active but also selective to the target protein.

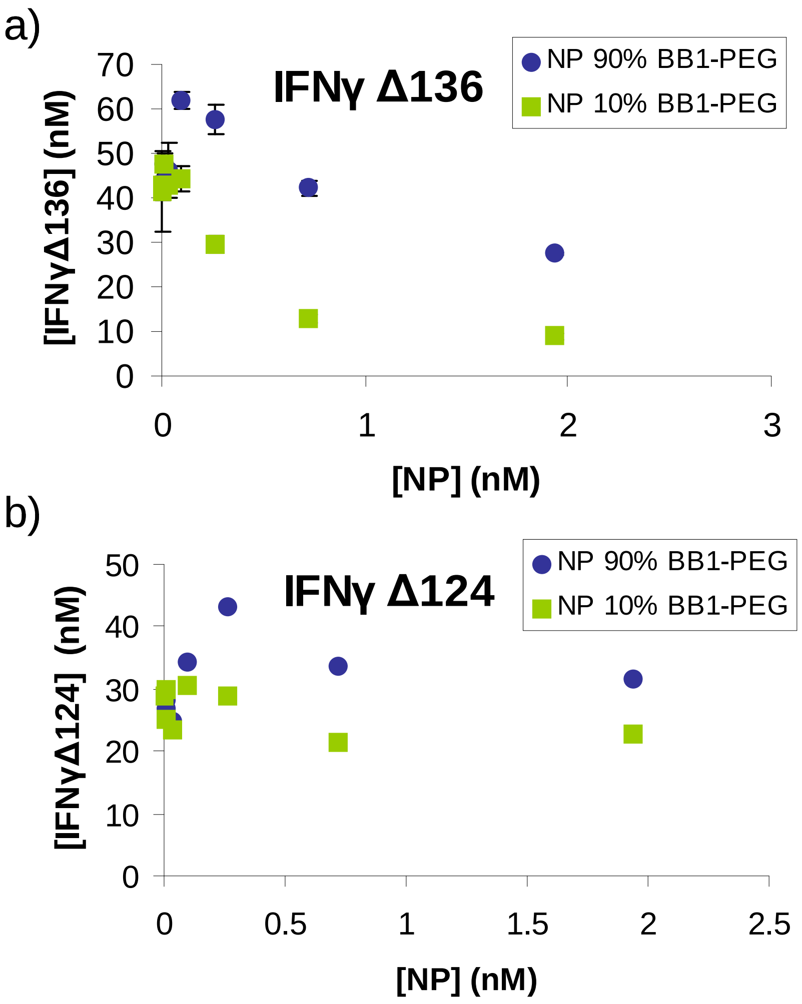

Figure 5.30. ELISA results obtained with two proteins IFNγ Δ136 and IFNγ Δ124 after incubation with the active nanovectors at different concentrations (in green) and with the inactive nanoconjugates at different concentrations (in blue).

5.7. Main conclusions of the chapter

In this chapter, it has been demonstrated that the developed electronic tongue is very efficient as a medium throughput screening technique for bioactive 2D combinatorial surfaces. Based on the generated CEPs, the most active combinatorial surface can be easily selected and then transferred to 3D Au NPs for preparation of biomimetic nanovectors.

However, the obtained biomimetic nanovectors are not stable in the buffer solution containing salt. To obtain stable ones new building blocking (BB1-PEG and BB2-PEG) were prepared by integrating a PEG spacer in the BB1 and BB2. The biomimetic nanovectors functionalized with BB1-PEG/BB2-PEG mixtures are very stable under physiological conditions of pH and ionic strength as well as at very high concentrations, as proven by UV-spectroscopy and SAXS.

The bioactivity of the 3D biomimetic nanovectors was evaluated by studying their interaction with proteins of interest (IFNγΔ136 as a model) by SPRi and ELISA. Results obtained by SPRi and ELISA showed that biomimetic nanovectors containing 10% BB1-PEG are active since they have affinity to the model protein IFNγΔ136. In contrast, nanoconjugates containing 90% of BB1-PEG have no affinity to the model protein. In addition, the 3D biomimetic nanovectors have no affinity to the protein IFNγΔ124 who has no affinity to heparin sulfate and was used for negative control. Thus, the 3D biomimetic nanovector is not only active but also selective to the target protein.

These preliminary results confirmed that it is feasible to prepare biomimetic nanovectors that mimic directly the biological properties of GAG fragments by the multivalent display of inactive and easily accessible synthetic disaccharides on gold nanoparticles. More importantly, our approach is not limited to the domain of glycobiology. It could be extremely useful for other therapeutic domains in which the multivalent presentation of a (bio)molecule is a key factor for its bioactivity.

Conclusions and Perspectives

The last two decades witnessed a rapidly growing interest in e-noses/tongues due to their potential in a wide range of domains, including controlling the quality of foods and beverages, monitoring pollutants and explosives in the environment and diagnosing diseases. However, generally, the preparation of e-noses/tongues sensing arrays requires designing and synthesizing from 5 to 50 cross-reactive receptors whose structures are sometimes very complex, requiring laborious synthesis. The development and more widespread use of this kind of devices should be greatly facilitated if the design and production of sensing elements was simplified.

In this context, the objective of this thesis is to develop a novel approach that greatly simplifies the design and production of sensing materials for the construction of e-tongues. For this, we have proposed a novel strategy. Instead of synthesizing a great number of complex molecules, cross-reactive receptors have been prepared by mixing and self-assembly of a restricted set of building blocks, ideally small and easily accessible molecules displaying different physicochemical properties. Upon combination of such BBs in varying and controlled proportions, a collection of combinatorial cross-reactive receptors with evolutive properties have been obtained. A major advantage of this approach is to allow a very quick growth of the diversity: eleven CoCRRs can be prepared by mixing only two BBs with concentration varying from 0 to 100% in 10 % increment, while 66 can theoretically be accessed by adding a third BB. Such growth can be generalized to n BBs and i % concentration increment, leading to an impressive number of $[(100/i)+n-1]!/(n-1)!(100/i)!$ potential different CoCRRs. Moreover, the composition of each CoCRR is linked and close to that of its neighbors and each CoCRR provides a signal that is related to that of its neighbor. Thus, the series of signals generated upon interaction between CoCRRs and analytes can be considered as continuous. As a consequence, abnormal signals can be easily identified, paving the way to analysis with unprecedented reliability.

In this thesis, a model e-tongue has been successfully constructed for proof of concept based on a CoCRR array combined with an optical detection system surface plasmon resonance imaging. The CoCRR array was inspired by the way cell surface heparan sulfates recognize HS binding proteins and it was prepared by using only two small disaccharides, lactose and sulfated lactose, as BBs.

To evaluate discrimination and identification capacities of our system as an electronic tongue, samples of varying complexities have been analyzed, including single-component samples, such as pure proteins of both HSbps and non-HSbps, dual-component samples by mixing two pure proteins, as well as real-world complex samples, such as beer, wine and milk. We have demonstrated that the e-tongue system is able to generate distinct 3D continuous evolution landscapes and 2D continuous evolution profiles behaving as “fingerprints” for differentiation and identification of these samples. The e-tongue is very powerful for protein analysis, capable of differentiating even proteins of the same family, such as CXCL12α and CXCL12γ. The analysis of dual-component protein samples has revealed that the CEP of the protein mixtures indicates additive behavior with respect to the signals obtained from the pure proteins, showing the potential of the system for identification of components in this kind of relatively simple mixtures. Furthermore, the e-tongue is also very efficient for differentiation and identification of complex mixtures. Besides, it allows monitoring the deterioration of UHT milk, a very promising illustration for future applications in quality control of food and beverages.

For any e-nose and e-tongue system, there are two important features, repeatability and stability. In this thesis, they have been addressed. The results show that e-tongue exhibits very good repeatability, both from measurement to measurement and from batch to batch, and good stability upon prolonged storage period up to 5 months. Therefore, we believe that this new methodology will contribute to the design of cheaper and more reliable e-noses/tongues and facilitate their implementation in even broader domains of application.

The extraordinary capacity of e-tongue for differentiation of CXCL12α and CXCL12γ of the same family has suggested that the e-tongue has biological properties of heparan sulfate somehow. Very interestingly, as we have demonstrated, both e-tongue and heparan sulfate have two complexity levels that determine their recognition capacity: local microheterogeneities and overall charge topologies. In nature, for HS, the combination of these two levels of polymer complexity gives it the specificity in the recognition of the targeted protein.

We have thus performed a complete study to check this point by using a protein of therapeutic interest, IFNγ and its mutants. It has been successfully demonstrated that the e-tongue has very good affinity to IFNγ in the nanomolar range, but very low affinity to non-sugar binding proteins, such as HSA, IgG, or cytochrome C. Even when IFNγ is diluted in a protein-rich media containing fetal bovine serum, the e-tongue is still able to detect the protein in a concentration-dependent way. This illustrated well the specificity of interaction between the protein and the e-tongue system. In addition, by analyzing various mutants of IFNγ, we have demonstrated that the e-tongue is able to perceive fine modifications made in the C-terminal region amino acid sequence of IFNγ and to differentiate its various mutants with very similar structures. This confirms further that the e-tongue is able to mimic biological properties of HS and thus could be employed as a simple tool for better understanding of the nature of HS/protein interactions interaction. In glycobiochemistry, the idea that many protein-HS interactions depend more on the overall organization of the HS domains (charge density and distribution along the chain) than on the fine structure (specific sulfation and epimerization sequences) is still a matter of debate so far, the approach of e-tongue we developed in this thesis offers an unprecedented and simple tool to investigate this point.

To better understand the nature of the interactions between the e-tongue and HSbps, and more importantly, to understand the role of lactose BB1 and sulfated lactose BB2 in these interactions, we have carried out protein analysis by replacing lactose (BB1) and sulfated lactose (BB2) with other BBs having similar physicochemical properties but without disaccharide unit. The obtained results have proven that both BB1 and BB2 play very important role in this interaction. In fact, by combining lactose and sulfated lactose, combinatorial surfaces with surprising novel biological properties can be obtained and they are essential for the high affinity of the e-tongue to HSbps, The biological properties of combinatorial surfaces are dependent not only on charge of the used BBs but also on sugar structures of BBs, in an even more important way. This is very promising in the design of new biomimetic nanovectors.

In the last part of this thesis, we have proposed to use the developed e-tongue as a medium throughput screening technique for bioactive 2D combinatorial surfaces since it permits to test the maximum of disaccharide mixtures on a single array in a highly efficient way. Once the combinatorial surface of interest chosen, it was then transferred to a 3D surface (NPs) for preparation of biomimetic nanovectors that mimic directly the biological properties of GAG fragments.

It has been demonstrated that the developed e-tongue is very efficient for screening bioactive 2D combinatorial surfaces. Based on the generated CEPs, the most active combinatorial surface can be easily selected and then transferred to 3D Au NPs for preparation of biomimetic nanovectors. Herein, the biomimetic nanovectors functionalized with BB1-PEG/BB2-PEG mixtures are very stable under physiological conditions of pH and ionic strength as well as at very high concentrations, as proven by UV-spectroscopy and SAXS. Based on results obtained by SPRi and ELISA, the biomimetic nanovectors containing 10% of BB1-PEG are active with good affinity to the model protein IFNγΔ136. In contrast, nanoconjugates containing 90% of BB1-PEG have no affinity to this protein. In addition, the 3D biomimetic nanovectors have no affinity to the protein IFNγΔ124 as negative control since it has no any affinity to heparan sulfate. Thus, the 3D biomimetic nanovector is not only active but also selective to the target protein.

These preliminary results confirmed that it is feasible to prepare biomimetic nanovectors that mimic directly the biological properties of GAG fragments by the multivalent display of inactive and easily accessible synthetic disaccharides on gold nanoparticles. More importantly, our approach is not limited to the domain of glycobiology. It could be extremely useful for other therapeutic domains in which the multivalent presentation of a (bio)molecule is a key factor for its bioactivity.

In conclusion, in this thesis we have developed a novel approach that greatly simplifies the design and production of sensing materials for the construction of e-tongues. The model e-tongue constructed based on the CoCRR array and SPRi is very efficient for differentiation and identification of samples of varying complexities, from pure proteins to complex mixtures. Moreover, this system is a very useful tool for conception of 2D and 3D biomimetic surfaces, with promising applications either for better understanding of the nature of HS/protein interactions or for preparation of biomimetic nanovectors to target specifically proteins of therapeutic interest.

Appendices

Appendix A: The composition of buffer solutions used in this thesis

HEPES:

The HEPES buffer solution employed in this thesis consists of 10 mM HEPES, 150 mM NaCl, and 0.005%Tween®. The pH was adjusted to 7.4 with a NaOH solution. Before storage at -20 °C, the buffer was filtered through a 0.8 µm Acrodisc® filter.

TRIS-Mannitol:

TRIS-Mannitol buffer solution contains 25 mg/mL mannitol and 10 mM Tris. The pH was adjusted to 6.8.

This buffer solution was used for dilution of protein samples received from IBS. The protein samples were then aliquoted and conserved at -80°C until use.

Appendix B: RMN of BB1 and BB2 building blocks

The ^{1}H-NMR and ^{13}C-NMR spectra of BB1 and BB2, as well as their peak assignation are given here. These data were provided by Prof. Bonnaffé.

NMR spectra were recorded in D_2O at room temperature with Bruker Avance 400 spectrometer using standard pulse programs. Chemical shifts are given in part per millions (ppm) relative to acetone (1H d = 2.225 ppm and 13C d = 30.5 ppm). The aglycon carbons are numbered a, b, c, d, e, f and g, starting from the one linked to the lactosyl moiety.

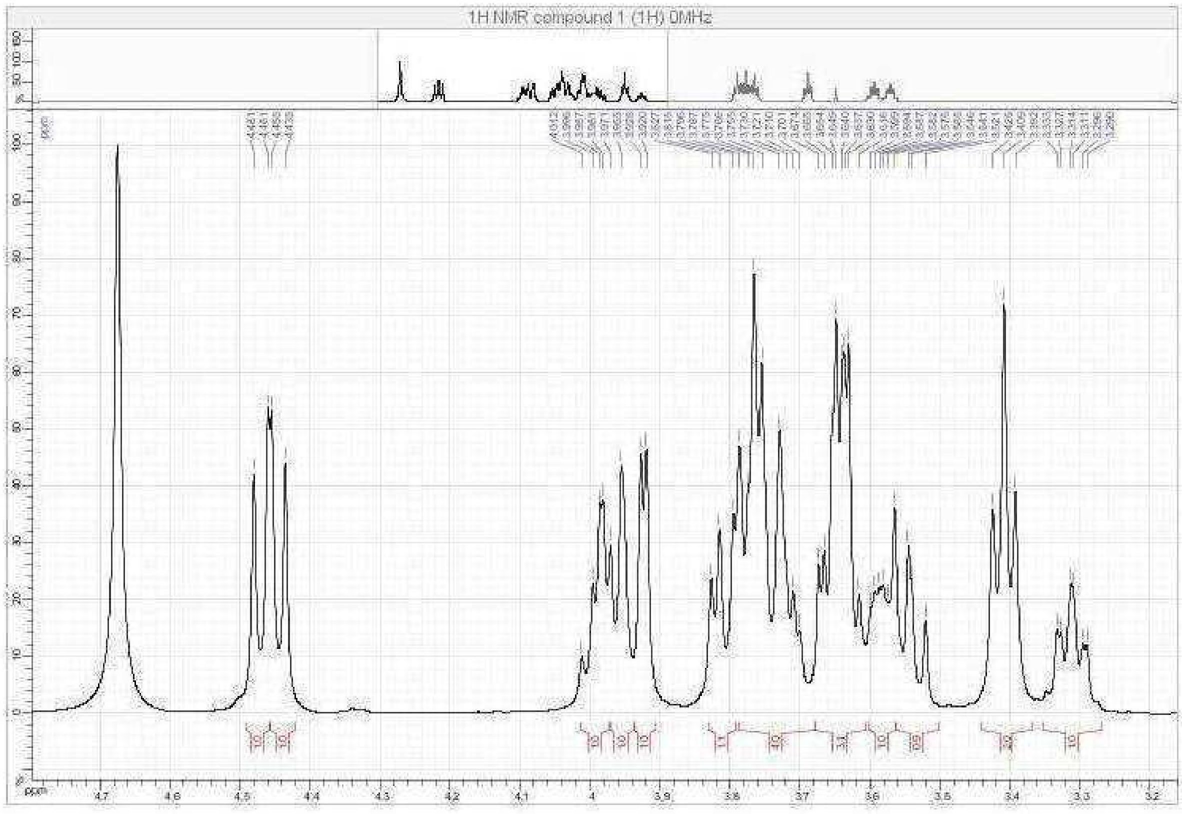

Figure B.1. ^{1}H NMR of BB1 molecule (400 MHz, D2O, ref Acetone): δ = 4.47 (d, *J1, 2*= 8.0 Hz, 1H, H-1), 4.45 (d, *J1’, 2’*= 7.5 Hz, 1H, H-1’), 3.99 (dd, *Ja, a’*= 10.0 Hz, *Ja, b*=6.5 Hz, 1H, H-a), 3.97 (dd, *J6a, 6b*= 12,5 Hz, *J6a, 5*= 2.0 Hz, 1H, H-6a), 3.92 (d, *J4’, 3’*= 3.5 Hz, 1H, H-4’), 3.81 (dd, *J6b, 6a*= 12,5 Hz, *J6b, 5* = 4 .5 Hz, 1H, H-6b), 3.80-3.69 (m, 4H, H-a’, H-5’, H-6'a, H-6'b), 3.66 (dd, *J3’, 2’*= 10.0 Hz, *J3’, 4’*= 3.5 Hz, 1H, H-3’), 3.65-3.60 (m, 2 H, H-3 and H-4), 3.58 (ddd, *J5, 4* = 10.0 Hz, *J5,6b* = 4,5 Hz, *J5,6a’*= 2,0 Hz, 1H, H-5), 3.55 (dd, *J2’, 3’*= 10.0 Hz, *J2’,1’*= 7.5 Hz, 1H, H-2’), 3.41 (t, *Je, d*= 6.5 Hz, 2H, H-e), 3.35-3.27 (m, 1H, H-2), 2.77 (t, *Jf, e*= *Jf, g*= 6.5 Hz, 2H, H-f), 2.0 (quint, *Jg, h*= *Jg, f*= 6.5 Hz, 2H, H-g), 1.91 (m, 2H, H-b)

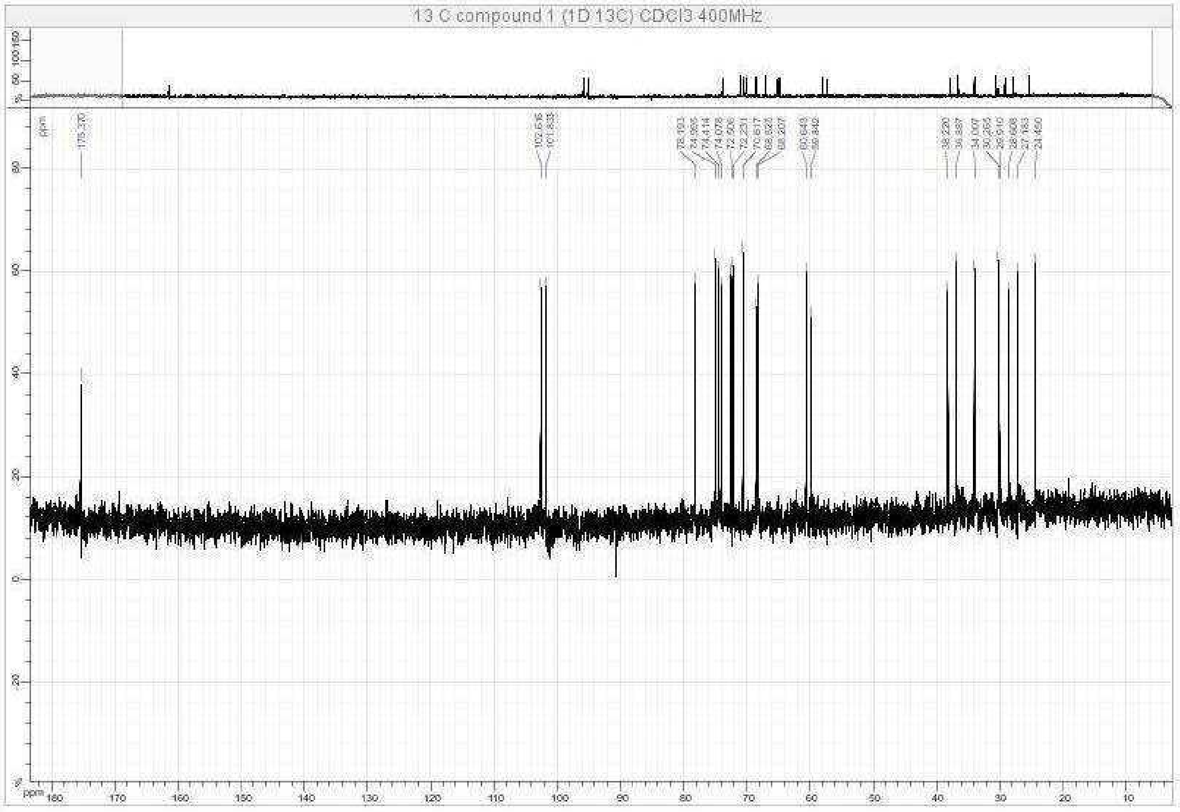

Figure B.2. ^{13}C NMR of BB1 (400 MHz, D2O, ref Acetone): δ = 175.37 (CO), 102.62 (C-1'), 101.84 (C-1), 78.20 (C-4), 75.00 (C-5'), 74.42 (C-5), 74.42 (C-3'), 72.51 (C-2), 72.24 (C-3), 70.62 (C-2'), 68.53 (C-a), 68.21 (C-4'), 60.65 (C-6), 59.85 (C-6'), 38.23 (C-e), 36.90 (C-h), 34.02 (C-f), 30.27 (Cd), 28.62 (C-b), 27.19 (C-c), 24.46 (C-g).

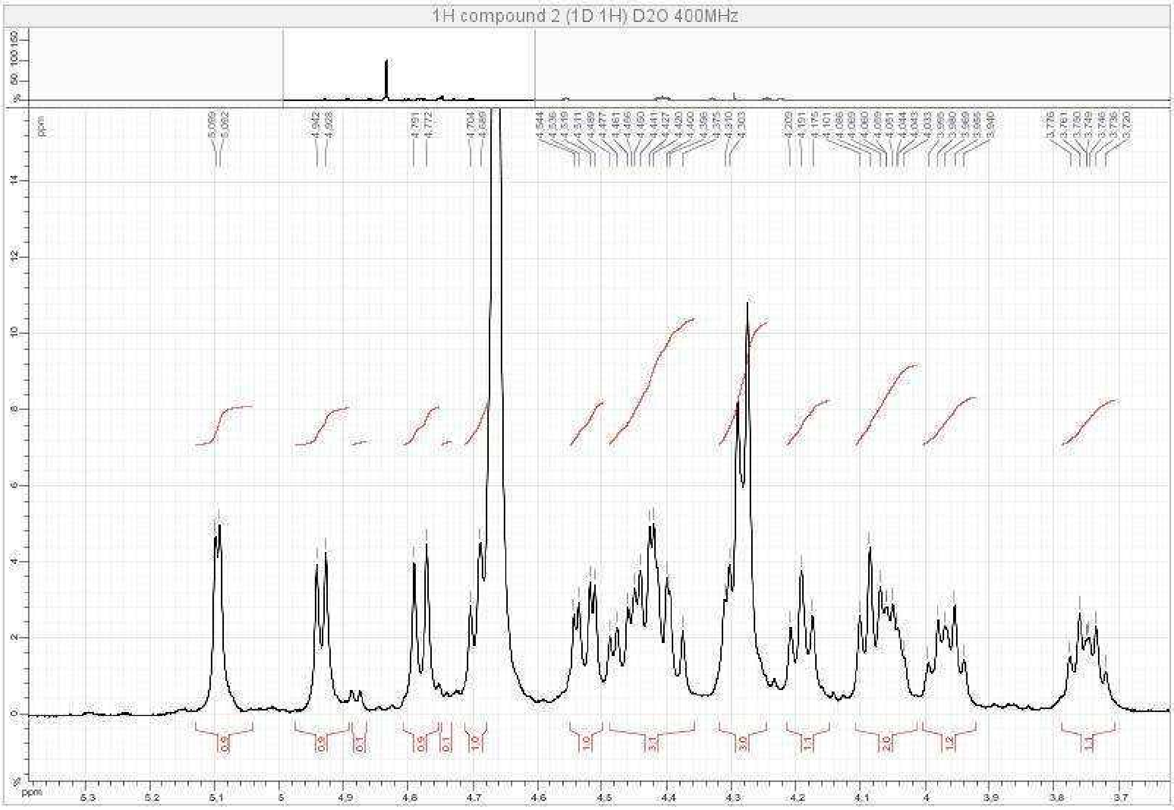

Figure B.3. ^{1}H NMR of BB2 (400 MHz, D2O, ref Acetone): δ= 5.10 (d, *J4’, 3’*= 3.0 Hz, 1H, H-4’), 4.94 (d, *J1, 2*= 6.0 Hz, 1H, H-1), 4.78 (d, *J1’, 2’*= 7.5 Hz, 1H, H-1’), 4.69 (dd, *J3, 4*= 7.0 Hz, *J3, 2*= 5.0 Hz, 1H, H-3), 4.53 (dd, *J3’, 2’*= 10.0 Hz, *J3’, 4’*= 3.0 Hz, 1H, H-3’), 4.47 (dd, *J6a, 6b*= 10.5 Hz, *J6a, 5*= 5.5 Hz, 1H, H-6a), 4.44 (dd, *J2, 1*= 6.0 Hz, *J2, 3*= 5.0 Hz, 1H, H-2), 4.39 (dd, *J2’, 3’*= 10.0 Hz, *J2’, 1’*= 7.5 Hz, 1H, H-2’), 4.29 (dd, *J6b, 6a*= 10.5 Hz, *J6b, 5*= 3.5 Hz, 1H, H-6b), 4.28 (d, *J6’, 5’*= 6.0 Hz, 2H, H-6’a= H-6’b), 4.19 (t, *J4, 5*= *J4, 3*= 7.0 Hz, 1H, H-4), 4.08 (t, *J5’, 6’*= 6.0 Hz, 1H, H-5’), 4.05 (dd, *J5, 4* = 7.0 Hz, *J5, 6a*= 5.5 Hz, *J5, 6b*= 3.5 Hz, 1H, H-5), 3.97 (dt, *Ja, a’*= 10.0 Hz, *Ja, b*= 6.0 Hz, 1H, H-a), 3.95 (dt, *Ja, a’*= 10.0 Hz, *Ja, b*= 6.0 Hz, 1H, H-a’), 3.45 (t, *Je, d*= 6.5 Hz, 2H, H-e), 2.76 (t, *Jh, g*= 7.0 Hz, 2H, H-h), 2.72 (t, *Jd, e*= 6.5 Hz, 2H, H-d), 2.69 (t, *Jc, b*= 7.5 Hz, 2H, H-c), 2.37 (t, *Jf, g*= 7.0 Hz, 2H, H-f), 1.99 (quint, *Jg, h*= *Jg, f*= 7.0 Hz, 2H, H-g), 1.93-1.86 (m, 2H, H-b).

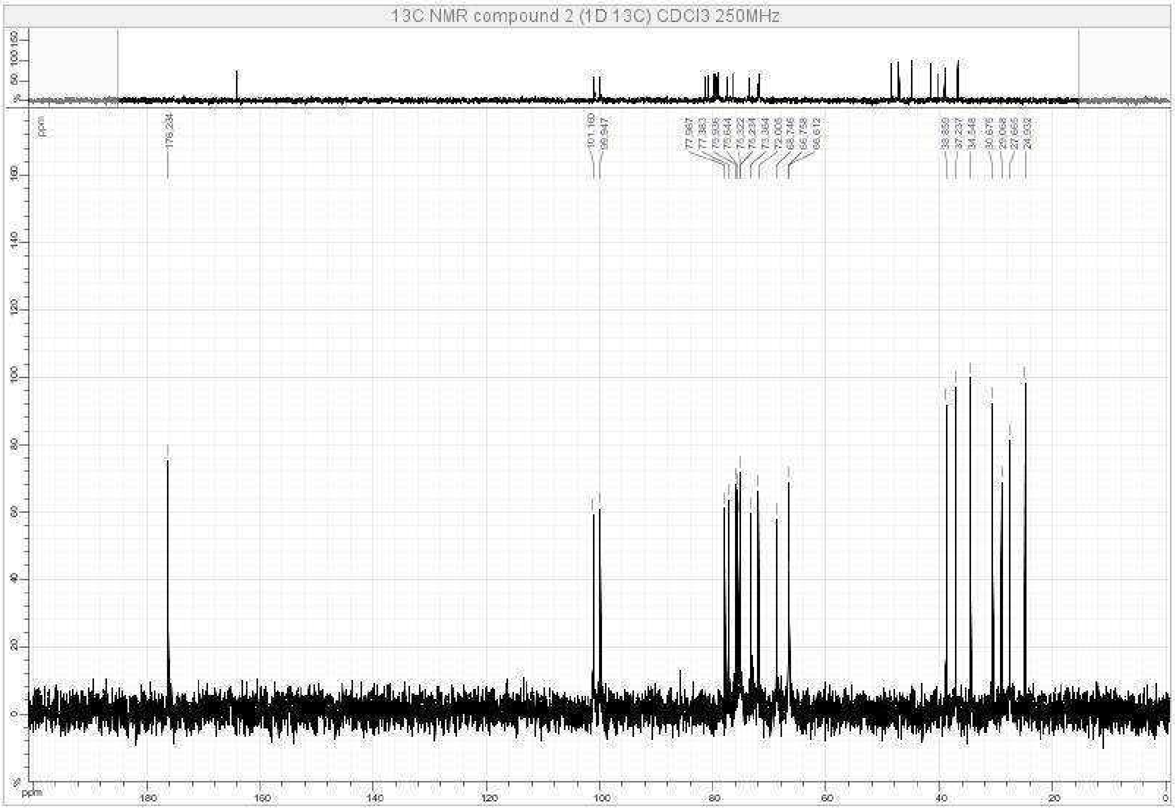

Figure B.4. ^{13}C NMRof BB2 (250 MHz, D2O, ref Acetone): δ= 176.2 (CO), 101.2 (C-1'), 99.9 (C-1), 77.9 (C-3), 77.4 (C-2), 75.9 (C-3'), 75.6 (C-2'), 75.3 (C- 4'), 75.2 (C-4), 73.3 (C-5), 72.0 (C-5') 68.7 (C-a), 66.7 (C-6), 66.6 (C-6'), 38.9 (C-e), 37.2 (C-h), 34.6 (C-f), 30.7 (C-d), 29.1 (C-b), 27.7 (Cc), 25.0 (C-g).

Appendix C: Spotting design used for preparation of the 11- CoCRR array

To prepare the CoCRR array, eleven BB1/BB2 mixed solutions were deposited on the prism with four replicates for each ratio using a non-contact piezoelectric spotter. A spotting map (see Figure C1) was designed and used for preparation of almost all CoCRR arrays in this thesis in order to obtain more reproducible measurements from batch to batch. Taking into account fluidic effect in the flow cell, the four replicates of each ratio were placed randomly in different zones on the prism, for example, in the center, at the edge, close to flow input/output of the flow cell.

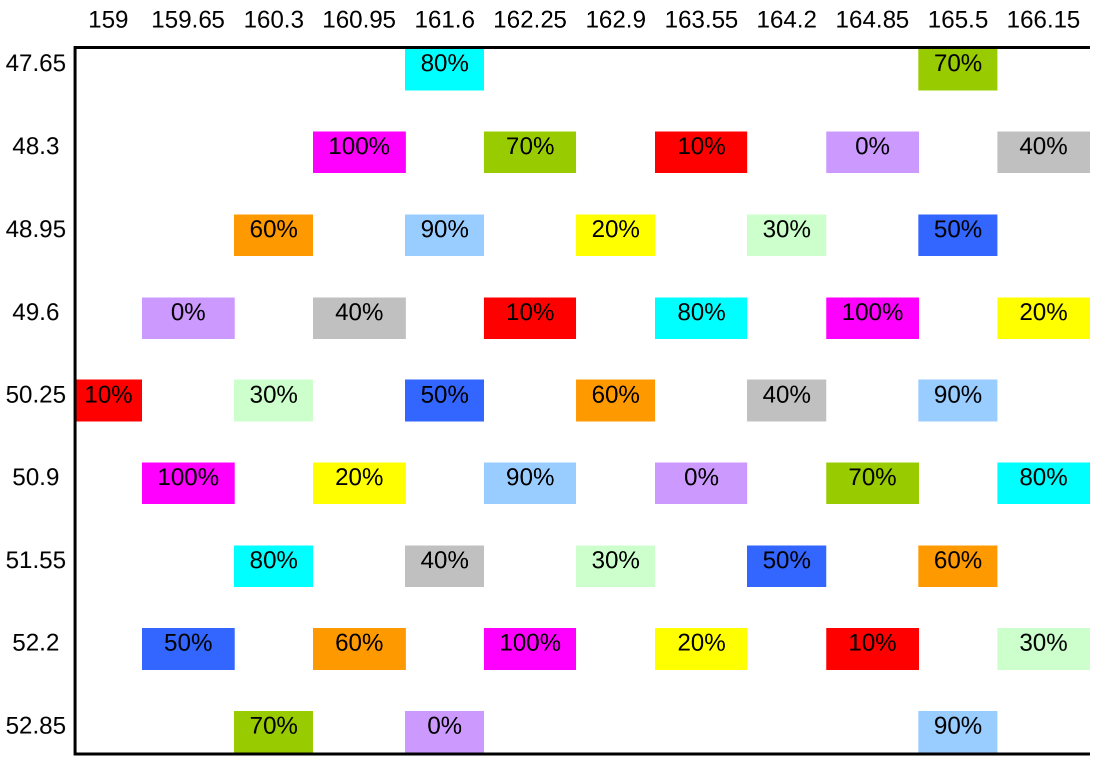

	159	159.65	160.3	160.95	161.6	162.25	162.9	163.55	164.2	164.85	165.5	166.15
47.65					80%						70%	
48.3				100%		70%		10%		0%		40%
48.95			60%		90%		20%		30%		50%	
49.6		0%		40%		10%		80%		100%		20%
50.25	10%		30%		50%		60%		40%		90%	
50.9		100%		20%		90%		0%		70%		80%
51.55			80%		40%		30%		50%		60%	
52.2		50%		60%		100%		20%		10%		30%
52.85			70%		0%						90%	

Figure C1. Representation of the spotting design used for preparing 11-CoCRR array.

Appendix D: Optimisation of protocol for the deprotection of BB-PEG head groups

The acetyl protection group of BB-PEG needed to be removed before use to deprotect the thiol head group. The deprotection could be done using a basic solution. In this study, the deprotection protocol was optimized by testing three basic solutions, including, from strong to weak base NaOH (2.5 mM), NH_4OH (63 mM) and K_2CO_3 (2.5 mM). For this study, BB1-PEG was used. After deprotected, it was used to functionalize a gold electrode by formation of SAMs, whose quality was characterized by electrochemical impedance spectroscopy and cyclic voltammetry.

In practice, first, a gold-covered glass sheet was cut in five pieces and cleaned by 5 min immersion in acetone, 2 min in piranha solution (H_2SO_4: H_2O_2 7:3 v:v) and immediate rinse with ethanol. The five pieces were then dried under a flow of Argon and put inside four small Petri dishes. Afterwards, one piece was kept for reference (Electrode 1), one another was functionalized with BB1-PEG without deprotection (Electrode 2), and the three others were functionalized by the BB1-PEG (50 µM) after deprotection using K_2CO_3 (2.5 mM) (Electrode 3), NH_4OH (63 mM) (Electrode 4) and NaOH (2.5 mM) (Electrode 5), and, respectively. The samples were left overnight and the day after they were cleaned with ultrapure water.

Electrochemical measurements were performed using a three-electrode system: the gold sheet as working electrode, a 150µm Pt wire as counter electrode and an Ag/AgCl reference electrode. The gold electrode was set-up on a support for electrical contact, as shown in Figure D1a. The other side of the electrode was inserted inside a screwing electrochemical cell containing a 5.7 mm diameter joint, shown in Figure D1b.

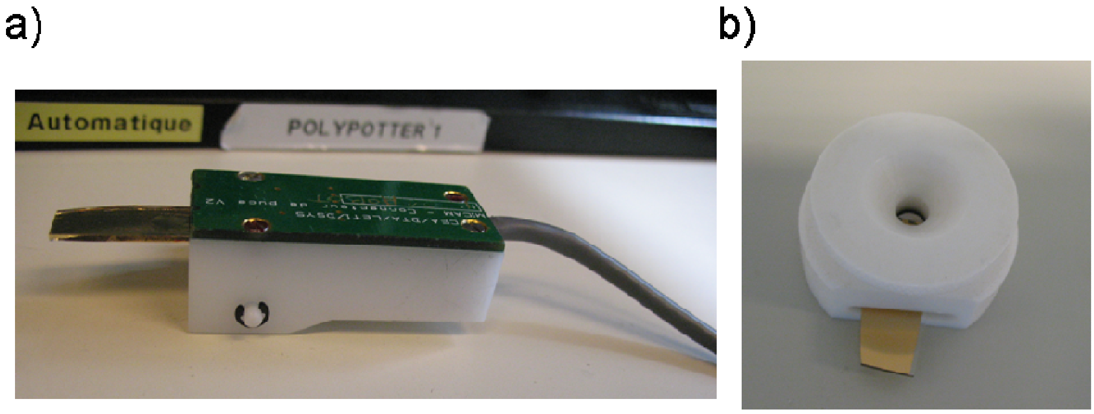

Figure D1. Positioning of the gold electrode a) One side of the gold electrode was put on a support and b) the other side is inserted in the electrochemical cell.

The aqueous solution used for the electrochemical measurements contained:

- Lithium Perchlorate ($LiClO_4$) 100 mM
- Potassium ferrocyanide ($K_4Fe(CN)_6 \cdot 3H_2O$) 5 mM
- Potassium ferricyanide ($K_3Fe(CN)_6$) 5 mM

The whole electrochemical set-up is shown in Figure D2.

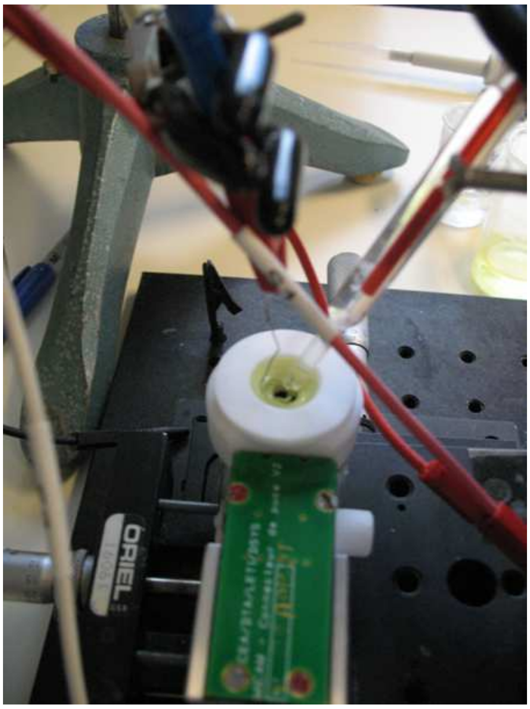

Figure D2. Experimental electrochemical set-up.

The results obtained by cyclic voltammetry (Figure D3)(-0.2-0.6V; scan rate 10mV/s), show that except for the bare gold electrode, electron transfer on the other electrodes was blocked due to the formation of SAMs of BB1-PEG on their surfaces.

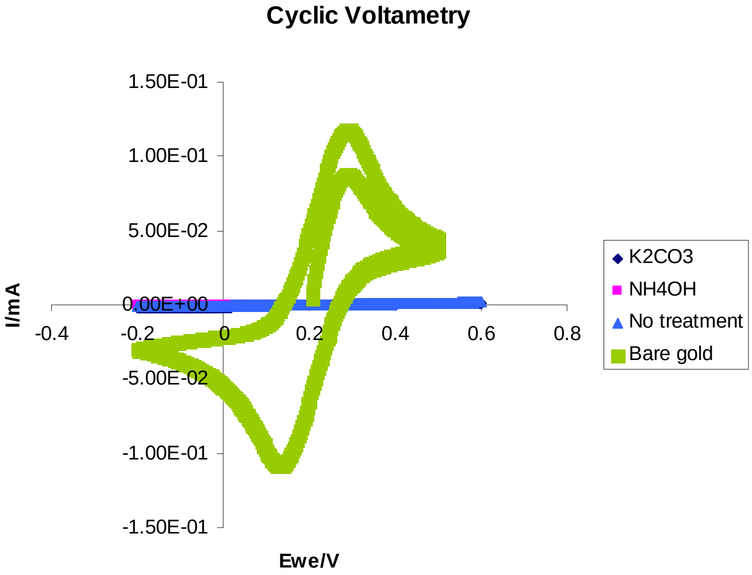

.

Figure D3. Cyclic voltammetry curves for a bare gold electrode (green), and three others functionalized by the BB1-PEG without deprotection (blue), after deprotection with K_2CO_3 (dark blue), and NH_4OH (pink)

Unfortunately, the cyclic voltammetry data corresponding to NaOH were lost.

Moreover, electrochemical impedance measurements were also performed (200kHz-10mHz; amplitude = 10mV).

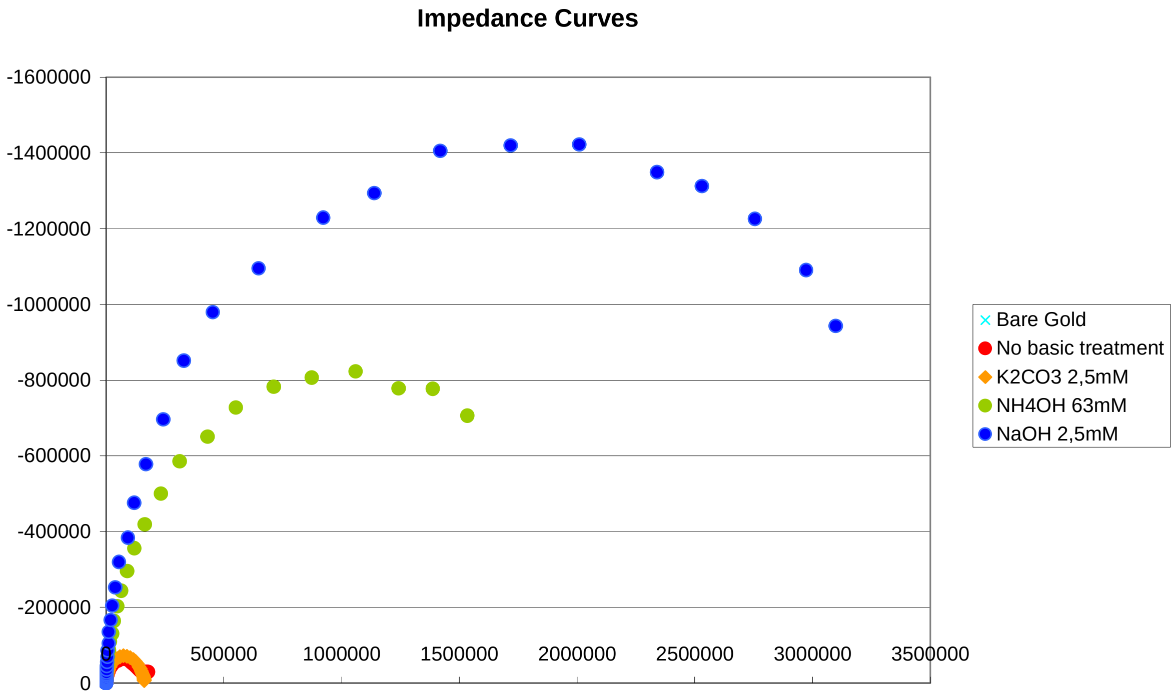

Figure D X. Impedance curves obtained on a bare gold electrode(light blue), and on the four other electrodes, functionalized by BB1-PEG without deprotection (red), after deprotection with K_2CO_3 (orange), NH_4OH (green) and NaOH (blue).

From the impedance data, we obtained the electron transfer resistance for each sample, listed in Table D1. The higher the resistance, the better quality of SAMs formed on the electrode surface. and, thus, the better the deprotection treatment. Consequently, due to its higher resistance, NaOH 2.5mM was considered the best solution to give more compact and probably more stable layers.

	Electrode 1	Electrode 2	Electrode 3	Electrode 4	Electrode 5
Electron transfer resistance	36 Ω	125 000 Ω	146 000 Ω	1 550 000 Ω	2 800 000 Ω

Table D1.- Electron transfer resistance values for the five electrodes.

Appendix E: Small-angle X-ray scattering

Small-angle X-ray scattering (SAXS) is an experimental technique widely used to study the structural properties of matter. The elastic scattering of radiation in the sample leads to interference effects,resulting in a scattering pattern, which can be analysed to provide information about size and shape of the component of the sample.

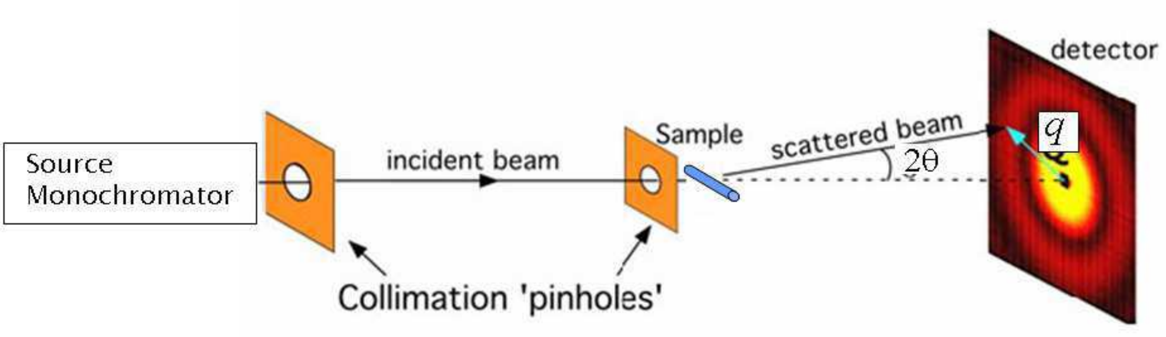

Figure E1. Schematic setup of SAXS experiments.

The principle of a SAXS experiment is the following: X-rays are generated in an X-ray source and passed through a collimator. The beam direction is defined by a set of pinholes and the sample is placed after the last one. When the x-rays traverse the sample, some of them are scattered and can be detected on a position-sensitive detector. A beamstop is placed in front of the detector to absorb the strong direct unscattered beam.

For most samples, the main SAXS intensity is present close to the beamstop and decreases as a function of the scattering angle. Instead of displaying the logarithm of the intensity I(q) as a function of the scattering angle 2θ, it is usual to display it as a function of length of the scattering vector $q = 4\pi \sin(\theta)/\lambda$ where λ is the x-ray wavelength. This q parameter allows an easier comparison of data recorded with different wavelengths.

Measurements used a laboratory point collimation SAXS camera equipped with a rotating anode generator (FR591 Nonius) operating with a copper target at 45 kV and 66 mA and a point focus source of 200 µm size. The X-ray beam was Kα/Kβ filtered (λ=1.5418 Å) by total reflection from two curved Ni-coated Franks mirrors and by transmission through a thin 10 µm Ni foil. A multi-wire gas filled proportional counter with a large 17x17 cm^2 active area was used, enabling measurements covering a large q range. The distance between the sample and the detector was 180 cm which leads to a range of scattering vector q between 10^{-2} $Å^{-1}$ and 0.3 $Å^{-1}$. The calibration in the reciprocal q-space was performed using the scattering from the silver behenate as reference sample with a first diffraction peak occurring at q = 0.10763 $Å^{-1}$. The scattering curves I(q) of the colloidal objects were obtained by reduction of the data by radial integration of intensities from the centre of the two-dimensional SAXS isotropic patterns after correction for the background scattering from the solvent. The colloidal suspensions were studied in 1 mm thin-walled glass capillaries.

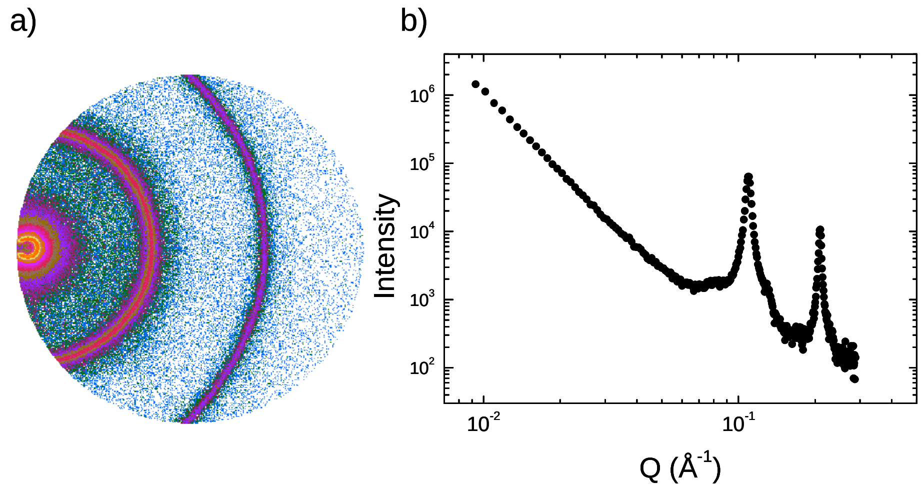

Figure E2. SAXS data collected from a Silver Behenate. a) SAXS data collected from a silver behenate powder capillary as reference sample for q calibration (first diffraction ring occurring for q = 0.10763 Å^{-1}). b) I(q) curve from a silver behenate powder sample obtained by data reduction of the two-dimensional SAXS isotropic pattern (data represented as log(I) *vs* loq(q).

Resulting Graphs:

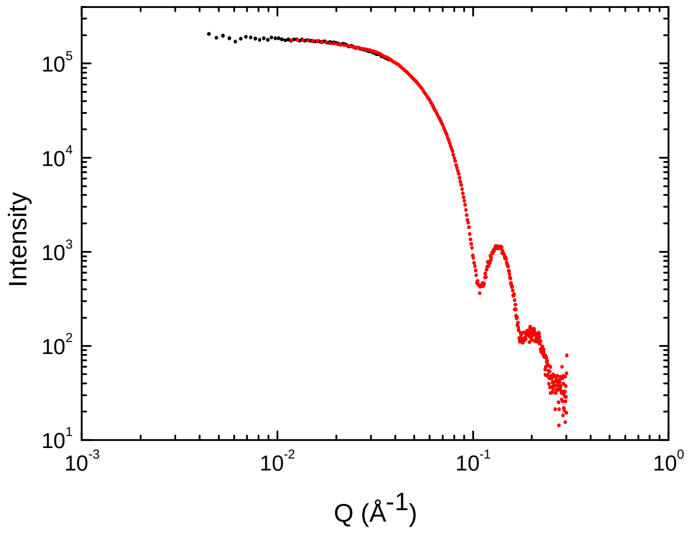

Figure E3. SAXS curve of sample c35 showing the Guinier region at smallest q (qR<1) and a series of very well defined oscillations at higher q characteristic for monodisperse particles.

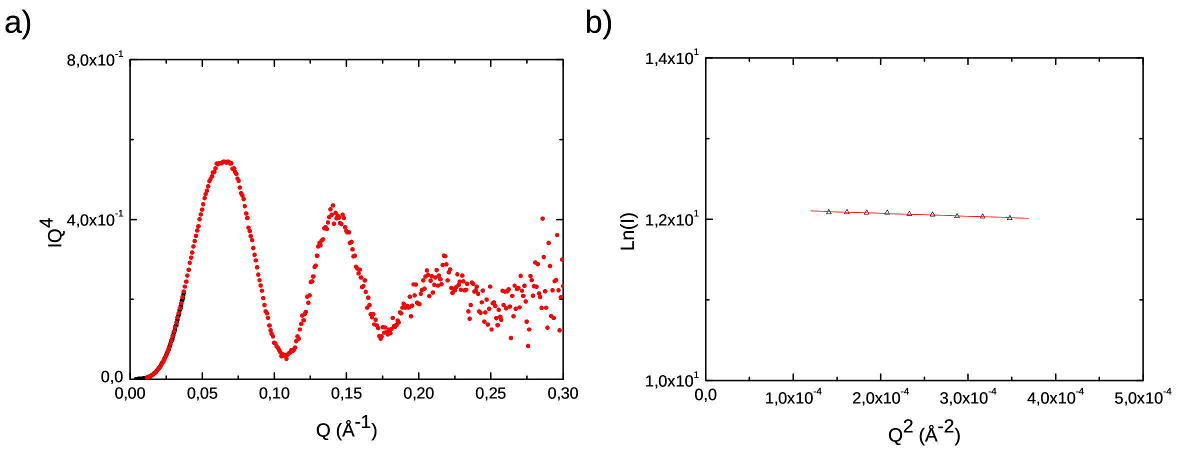

Figure E4 . a) Porod representation of SAXS curve for sample c35. From the position of the first maximum at q_M=0.065 Å^{-1} we can deduce a radius R_M= 43 Å ($q_M R_M$= 2.78 for spherical objects).b) Guinier representation of SAXS curve for sample c35 at lowest angles (in q range qR<1). From the slope of the curve ln(I) *vs* q^2 we can deduce a radius of gyration R_g = 33 Å which combined with the relation $R_G=\sqrt{5}/\sqrt{3}\, R_g$ valid for spherical objects leads to a Guinier radius R_G=43 Å in perfect agreement with the radius deduced from the Porod representation.

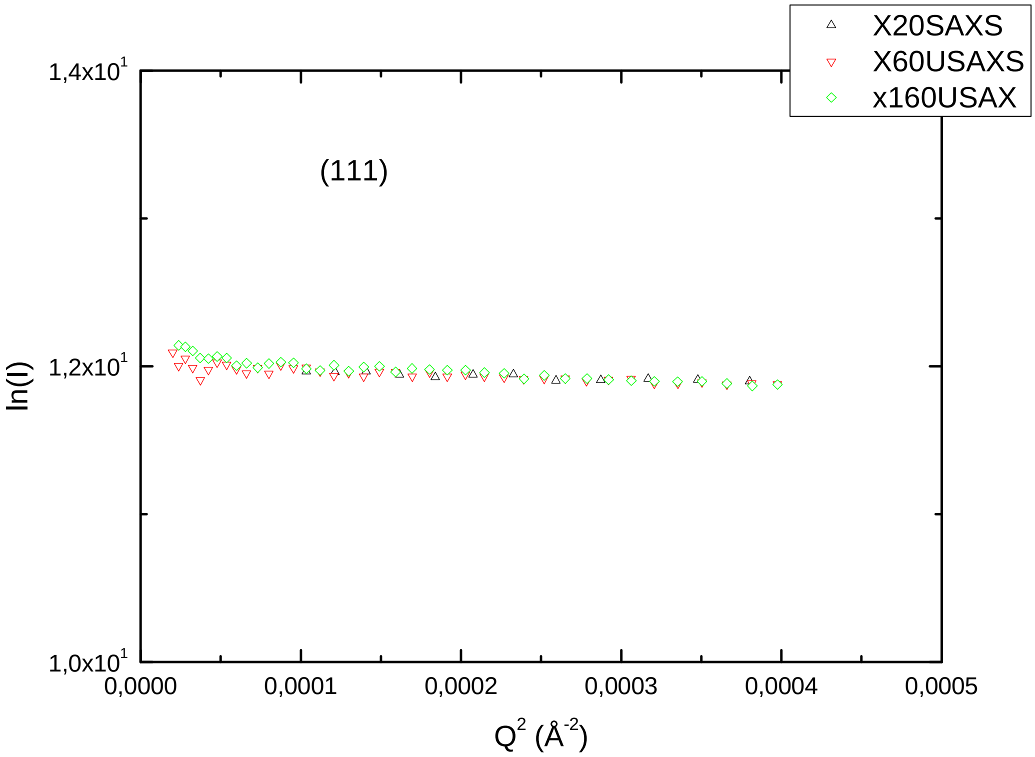

Figure E5. Guinier representation of SAXS curve for samples x20, x60 and x160. The parallel lines indicate that the radius of gyration for the three samples is the same, suggesting that even at high concentrations (x160) nanoparticles stay monodisperse.

References

1. Buck L, Axel R. A Novel Multigene Family May Encode Odorant Receptors. Journal of General Physiology. 1991 Dec;98(6):A3-A.
2. Savage N. TECHNOLOGY The taste of things to come. Nature. 2012 Jun 21;486(7403):S18-S9.
3. Chandrashekar J, Hoon MA, Ryba NJP, Zuker CS. The receptors and cells for mammalian taste. Nature. 2006 Nov 16;444(7117):288-94.
4. Bakalar N. SENSORY SCIENCE Partners in flavour. Nature. 2012 Jun 21;486(7403):S4-S5.
5. Buck LB. Unraveling the sense of smell (Nobel lecture). Angewandte Chemie-International Edition. 2005;44(38):6128-40.
6. Menini A, Lagostena L, Boccaccio A. Olfaction: From odorant molecules to the olfactory cortex. News in Physiological Sciences. 2004 Jun;19:101-4.
7. Breer H. Olfactory receptors: molecular basis for recognition and discrimination of odors. Analytical and Bioanalytical Chemistry. 2003 Oct;377(3):427-33.
8. Spehr M, Munger SD. Olfactory receptors: G protein-coupled receptors and beyond. Journal of Neurochemistry. 2009 Jun;109(6):1570-83.
9. Su CY, Menuz K, Carlson JR. Olfactory Perception: Receptors, Cells, and Circuits. Cell. 2009 Oct 2;139(1):45-59.
10. Malnic B, Hirono J, Sato T, Buck LB. Combinatorial receptor codes for odors. Cell. 1999 Mar 5;96(5):713-23.
11. Vlasov YG, Ermolenko YE, Legin AV, Rudnitskaya AM, Kolodnikov VV. Chemical sensors and their systems. Journal of Analytical Chemistry. 2010 Sep;65(9):880-98.
12. Umali AP, Anslyn EV. A general approach to differential sensing using synthetic molecular receptors. Current Opinion in Chemical Biology. 2010 Dec;14(6):685-92.
13. Lavigne JJ, Anslyn EV. Sensing a paradigm shift in the field of molecular recognition: From selective to differential receptors. Angewandte Chemie-International Edition. 2001;40(17):3119-30.
14. Vlasov YG, Legin AV, Rudnitskaya AM. Electronic tongue: Chemical sensor systems for analysis of aquatic media. Russian Journal of General Chemistry. 2008 Dec;78(12):2532-44.
15. Gardner JW, Bartlett PN. A Brief-History of Electronic Noses. Sensors and Actuators B-Chemical. 1994 Mar;18(1-3):211-20.
16. Kobayashi Y, Habara M, Ikezazki H, Chen R, Naito Y, Toko K. Advanced taste sensors based on artificial lipids with global selectivity to basic taste qualities and high correlation to sensory scores. Sensors (Basel, Switzerland).10(4):3411-43.

17. ; [cited]; Available from: http://blog.odotech.com/.

18. Tahara Y, Toko K. Electronic Tongues-A Review. Ieee Sensors Journal. 2013 Aug;13(8):3001-11.

19. Gutes A, Cespedes F, del Valle M, Louthander D, Krantz-Rulcker C, Winquist F. A flow injection voltammetric electronic tongue applied to paper mill industrial waters. Sensors and Actuators B-Chemical. 2006 May 23;115(1):390-5.

20. Krantz-Rulcker C, Stenberg M, Winquist F, Lundstrom I. Electronic tongues for environmental monitoring based on sensor arrays and pattern recognition: a review. Analytica Chimica Acta. 2001 Jan 12;426(2):217-26.

21. Di Natale C, Macagnano A, Davide F, D'Amico A, Legin A, Vlasov Y, et al. Multicomponent analysis on polluted waters by means of an electronic tongue. Sensors and Actuators B-Chemical. 1997 Oct;44(1-3):423-8.

22. Young RC, Buttner WJ, Linnell BR, Ramesham R. Electronic nose for space program applications. Sensors and Actuators B-Chemical. 2003 Aug 1;93(1-3):7-16.

23. ; [cited 24 06 2013]; Available from: http://enose.jpl.nasa.gov/intro.html.

24. Fend R, Bessant C, Williams AJ, Woodman AC. Monitoring haemodialysis using electronic nose and chemometrics. Biosensors & Bioelectronics. 2004 Jul 15;19(12):1581-90.

25. Rudnitskaya A, Legin A. Sensor systems, electronic tongues and electronic noses, for the monitoring of biotechnological processes. Journal of Industrial Microbiology & Biotechnology. 2008 May;35(5):443-51.

26. Bonifacio LD, Ozin GA, Arsenault AC. Photonic Nose-Sensor Platform for Water and Food Quality Control. Small. 2011 Nov 18;7(22):3153-7.

27. Escuder-Gilabert L, Peris M. Review: Highlights in recent applications of electronic tongues in food analysis. Analytica Chimica Acta. 2010 Apr 14;665(1):15-25.

28. Baldwin EA, Bai JH, Plotto A, Dea S. Electronic Noses and Tongues: Applications for the Food and Pharmaceutical Industries. Sensors. 2011 May;11(5):4744-66.

29. El Barbri N, Llobet E, El Bari N, Correig X, Bouchikhi B. Application of a portable electronic nose system to assess the freshness of Moroccan sardines. Materials Science & Engineering C-Biomimetic and Supramolecular Systems. 2008 Jul 1;28(5-6):666-70.

30. Woodka MD, Schnee VP, Polcha MP. Fluorescent Polymer Sensor Array for Detection and Discrimination of Explosives in Water. Analytical Chemistry. 2010 Dec 1;82(23):9917-24.

31. Oh EH, Song HS, Park TH. Recent advances in electronic and bioelectronic noses and their biomedical applications. Enzyme and microbial technology. May 6;48(6-7):427-37.

32. Wilson AD, Baietto M. Advances in Electronic-Nose Technologies Developed for Biomedical Applications. Sensors. 2011 Jan;11(1):1105-76.

33. Peng G, Tisch U, Adams O, Hakim M, Shehada N, Broza YY, et al. Diagnosing lung cancer in exhaled breath using gold nanoparticles. Nature Nanotechnology. 2009 Oct;4(10):669-73.

34. The 5 in 5. [cited 24-06-2013]; Available from: http://www.ibm.com/smarterplanet/us/en/ibm_predictions_for_future/ideas/index.html.

35. Arshak KM, E.; Lyons, G.M.; Harris, J.; Clifford, S. A review of gas sensors employed in electronic nose applications. Sensor Review. [Review]. 2004;24(2):181-98.

36. Stussi E, Stella R, De Rossi D. Chemoresistive conducting polymer-based odour sensors: influence of thickness changes on their sensing properties. Sensors and Actuators B-Chemical. 1997 Sep;43(1-3):180-5.

37. Wilson AD, Lester DG, Oberle CS. Application of conductive polymer analysis for wood and woody plant identifications. Forest Ecology and Management. 2005 May 2;209(3):207-24.

38. Otto M, Thomas JDR. Model Studies on Multiple Channel Analysis of Free Magnesium, Calcium, Sodium, and Potassium at Physiological Concentration Levels with Ion-Selective Electrodes. Analytical Chemistry. 1985;57(13):2647-51.

39. Ciosek P, Wroblewski W. Sensor arrays for liquid sensing - electronic tongue systems. Analyst. 2007;132(10):963-78.

40. Del Valle M. Sensor Arrays and Electronic Tongue Systems. International journal of electrochemistry. [Review Article]. 2012;2012:11.

41. Toko K. Taste sensor with global selectivity. Materials Science & Engineering C-Biomimetic Materials Sensors and Systems. 1996 Jun;4(2):69-82.

42. Vlasov Y, Legin A, Rudnitskaya A. Cross-sensitivity evaluation of chemical sensors for electronic tongue: determination of heavy metal ions. Sensors and Actuators B-Chemical. 1997 Oct;44(1-3):532-7.

43. Legin AV, Rudnitskaya AM, Vlasov YG. Application of electronic tongue for qualitative and quantitative analysis of complex liquid media. Technical Digest of the Seventh International Meeting on Chemical Sensors. 1998:232-4.

44. Legin A, Rudnitskaya A, Lvova L, Vlasov Y, Di Natale C, D'Amico A. Evaluation of Italian wine by the electronic tongue: recognition, quantitative analysis and correlation with human sensory perception. Analytica Chimica Acta. 2003 May 7;484(1):33-44.

45. Vlasov YG, Legin AV, Rudnitskaya AM, D'Amico A, Di Natale C. "Electronic tongue" - new analytical tool for liquid analysis on the basis of non-specific sensors and methods of pattern recognition. Sensors and Actuators B-Chemical. 2000 Jun 30;65(1-3):235-6.

46. Winquist F, Wide P, Lundstrom I. An electronic tongue based on voltammetry. Analytica Chimica Acta. 1997 Dec 30;357(1-2):21-31.

47. Winquist F. Voltammetric electronic tongues - basic principles and applications. Microchimica Acta. 2008 Sep;163(1-2):3-10.

48. Goldsmith BR, Mitala JJ, Josue J, Castro A, Lerner MB, Bayburt TH, et al. Biomimetic Chemical Sensors Using Nanoelectronic Readout of Olfactory Receptor Proteins. Acs Nano. 2011 Jul;5(7):5408-16.

49. Akimov V, Alfinito E, Bausells J, Benilova I, Paramo IC, Errachid A, et al. Nanobiosensors based on individual olfactory receptors. Analog Integrated Circuits and Signal Processing. 2008 Dec;57(3):197-203.

50. Gomila G, Casuso I, Errachid A, Ruiz O, Pajot E, Minic J, et al. Advances in the production, immobilization, and electrical characterization of olfactory receptors for olfactory nanobiosensor development. Sensors and Actuators B-Chemical. 2006 Jul 28;116(1-2):66-71.

51. Minic J, Persuy MA, Godel E, Aioun J, Connerton I, Salesse R, et al. Functional expression of olfactory receptors in yeast and development of a bioassay for odorant screening. Febs Journal. 2005 Jan;272(2):524-37.

52. Pajot-Augy E, Crowe M, Levasseur G, Salesse R, Connerton I. Engineered Yeasts as reporter systems for odorant detection. Journal of Receptors and Signal Transduction. 2003;23(2-3):155-71.

53. Lee SH, Kwon OS, Song HS, Park SJ, Sung JH, Jang J, et al. Mimicking the human smell sensing mechanism with an artificial nose platform. Biomaterials. 2012 Feb;33(6):1722-9.

54. Song HS, Kwon OS, Lee SH, Park SJ, Kim UK, Jang J, et al. Human Taste Receptor-Functionalized Field Effect Transistor as a Human-Like Nanobioelectronic Tongue. Nano Letters. 2013 Jan;13(1):172-8.

55. Hauptmann P, Borngraeber R, Schroeder J, Auge J. Application of novel sensor electronics for quartz resonators in artificial tongue. Proceedings of the 2000 Ieee/Eia International Frequency Control Symposium & Exhibition. 2000:100-5.

56. Di Natale C, Paolesse R, D'Arcangelo G, Comandini P, Pennazza G, Martinelli E, et al. Identification of schizophrenic patients by examination of body odor using gas chromatography-mass spectrometry and a cross-selective gas sensor array. Medical Science Monitor. 2005 Aug;11(8):Cr366-Cr75.

57. Jacesko S, Abraham JK, Ji T, Varadan VK, Cole M, Gardner JW. Investigations on an electronic tongue with polymer microfluidic cell for liquid sensing and identification. Smart Materials & Structures. 2005 Oct;14(5):1010-6.

58. Vivancos JL, Racz Z, Cole M, Gardner JW. Surface acoustic wave based analytical system for the detection of liquid detergents. Sensors and Actuators B-Chemical. 2012 Aug-Sep;171:469-77.

59. Lang HP, Baller MK, Berger R, Gerber C, Gimzewski JK, Battiston FM, et al. An artificial nose based on a micromechanical cantilever array. Analytica Chimica Acta. 1999 Jun 30;393(1-3):59-65.

60. Karabacak DM, Sieben-Xu L, Vandecasteele M, van Andel Y, Wouters D, Calama MC, et al. Toward a Miniaturized Low-Power Micromechanical Electronic Nose. Ieee Sensors Journal. 2012 Nov;12(11):3184-8.

61. Crego-Calama M, Brongersma S, Karabacak D, Van Bavel M. A low-power integrated electronic nose system. Sensor Review. 2012;32(1):72-6.

62. Abraham JK, Karjathkar S, Jacesko S, Varadan VK, Gardner JW. Identification of soft drinks using MEMS-IDT microsensors. Smart Structures and Materials 2005: Smart Electronics, Mems, Biomems, and Nanotechnology. 2005;5763:414-24.

63. Boisen A, Dohn S, Keller SS, Schmid S, Tenje M. Cantilever-like micromechanical sensors. Reports on Progress in Physics. 2011 Mar;74(3).

64. Rochat S, Gao J, Qian XH, Zaubitzer F, Severin K. Cross-Reactive Sensor Arrays for the Detection of Peptides in Aqueous Solution by Fluorescence Spectroscopy. Chemistry-a European Journal. 2010;16(1):104-13.

65. Lavigne JJ, Savoy S, Clevenger MB, Ritchie JE, McDoniel B, Yoo SJ, et al. Solution-based analysis of multiple analytes by a sensor array: Toward the development of an "electronic tongue". Journal of the American Chemical Society. 1998 Jul 1;120(25):6429-30.

66. Goodey A, Lavigne JJ, Savoy SM, Rodriguez MD, Curey T, Tsao A, et al. Development of multianalyte sensor arrays composed of chemically derivatized polymeric microspheres localized in micromachined cavities. Journal of the American Chemical Society. 2001 Mar 21;123(11):2559-70.

67. Goodey AP, McDevitt JT. Multishell microspheres with integrated chromatographic and detection layers for use in array sensors. Journal of the American Chemical Society. 2003 Mar 12;125(10):2870-1.

68. Mayr T, Igel C, Liebsch G, Klimant I, Wolfbeis OS. Cross-reactive metal ion sensor array in a micro titer plate format. Analytical Chemistry. 2003 Sep 1;75(17):4389-96.

69. Basabe-Desmonts L, van der Baan F, Zimmerman RS, Reinhoudt DN, Crego-Calama M. Cross-reactive sensor array for metal ion sensing based on fluorescent SAMs. Sensors. 2007 Sep;7(9):1731-46.

70. Greene NT, Morgan SL, Shimizu KD. Molecularly imprinted polymer sensor arrays. Chemical Communications. 2004 May 21(10):1172-3.

71. Greene NT, Shimizu KD. Colorimetric molecularly imprinted polymer sensor array using dye displacement. Journal of the American Chemical Society. 2005 Apr 20;127(15):5695-700.

72. Zhang C, Suslick KS. A colorimetric sensor array for organics in water. Journal of the American Chemical Society. 2005 Aug 24;127(33):11548-9.

73. Zhang C, Suslick KS. Colorimetric sensor array for soft drink analysis. Journal of Agricultural and Food Chemistry. 2007 Jan 24;55(2):237-42.

74. Zhang C, Bailey DP, Suslick KS. Colorimetric sensor arrays for the analysis of beers: A feasibility study. Journal of Agricultural and Food Chemistry. 2006 Jul 12;54(14):4925-31.

75. Zhou HC, Baldini L, Hong J, Wilson AJ, Hamilton AD. Pattern recognition of proteins based on an array of functionalized porphyrins. Journal of the American Chemical Society. 2006 Feb 22;128(7):2421-5.

76. Baldini L, Wilson AJ, Hong J, Hamilton AD. Pattern-based detection of different proteins using an array of fluorescent protein surface receptors. Journal of the American Chemical Society. 2004 May 12;126(18):5656-7.

77. Stojanovic MN, Green EG, Semova S, Nikic DB, Landry DW. Cross-reactive arrays based on three-way junctions. Journal of the American Chemical Society. 2003 May 21;125(20):6085-9.

78. Bunz UHF, Rotello VM. Gold Nanoparticle-Fluorophore Complexes: Sensitive and Discerning "Noses" for Biosystems Sensing. Angewandte Chemie-International Edition. 2010;49(19):3268-79.

79. Stewart S, Syrett A, Pothukuchy A, Bhadra S, Ellington A, Anslyn E. Identifying Protein Variants with Cross-Reactive Aptamer Arrays. Chembiochem. 2011 Sep 5;12(13):2021-4.

80. Kirby R, Cho EJ, Gehrke B, Bayer T, Park YS, Neikirk DP, et al. Aptamer-based sensor arrays for the detection and quantitation of proteins. Analytical Chemistry. 2004 Jul 15;76(14):4066-75.

81. Buryak A, Severin K. A chemosensor array for the colorimetric identification of 20 natural amino acids. Journal of the American Chemical Society. 2005 Mar 23;127(11):3700-1.

82. Severin K. Pattern-based sensing with simple metal-dye complexes. Current Opinion in Chemical Biology. 2010 Dec;14(6):737-42.

83. Thete AR, Henkel T, Gockeritz R, Endlich M, Kohler JM, Gross GA. A hydrogel based fluorescent micro array used for the characterization of liquid analytes. Analytica Chimica Acta. 2009 Feb 2;633(1):81-9.

84. Margulies D, Hamilton AD. Combinatorial protein recognition as an alternative approach to antibody-mimetics. Current Opinion in Chemical Biology. 2010 Dec;14(6):705-12.

85. Wright AT, Griffin MJ, McDevitt JT, Anslyn EV. Differential receptors create patterns that distinguish various proteins. Abstracts of Papers of the American Chemical Society. 2005 Mar 13;229:U578-U.

86. Collins BE, Anslyn EV. Pattern-based peptide recognition. Chemistry-a European Journal. 2007;13(17):4700-8.

87. Reddy MM, Kodadek T. Protein "fingerprinting" in complex mixtures with peptoid microarrays. Proceedings of the National Academy of Sciences of the United States of America. 2005 Sep 6;102(36):12672-7.

88. Savariar EN, Ghosh S, Gonzalez DC, Thayumanavan S. Disassembly of noncovalent amphiphilic polymers with proteins and utility in pattern sensing. Journal of the American Chemical Society. 2008 Apr 23;130(16):5416-+.

89. Gonzalez DC, Savariar EN, Thayumanavan S. Fluorescence Patterns from Supramolecular Polymer Assembly and Disassembly for Sensing Metallo- and Nonmetalloproteins. Journal of the American Chemical Society. 2009 Jun 10;131(22):7708-16.

90. Miranda OR, You CC, Phillips R, Kim IB, Ghosh PS, Bunz UHF, et al. Array-based sensing of proteins using conjugated polymers. Journal of the American Chemical Society. 2007 Aug 15;129(32):9856-+.

91. You CC, Miranda OR, Gider B, Ghosh PS, Kim IB, Erdogan B, et al. Detection and identification of proteins using nanoparticle-fluorescent polymer 'chemical nose' sensors. Nature Nanotechnology. 2007 May;2(5):318-23.

92. Bajaj A, Miranda OR, Kim IB, Phillips RL, Jerry DJ, Bunz UHF, et al. Detection and differentiation of normal, cancerous, and metastatic cells using nanoparticle-polymer sensor arrays. Proceedings of the National Academy of Sciences of the United States of America. 2009 Jul 7;106(27):10912-6.

93. Phillips RL, Miranda OR, You CC, Rotello VM, Bunz UHF. Rapid and efficient identification of bacteria using gold-nanoparticle - Poly(para-phenyleneethynylene) constructs. Angewandte Chemie-International Edition. 2008;47(14):2590-4.

94. De M, Rana S, Akpinar H, Miranda OR, Arvizo RR, Bunz UHF, et al. Sensing of proteins in human serum using conjugates of nanoparticles and green fluorescent protein. Nature Chemistry. 2009 Sep;1(6):461-5.

95. Miranda OR, Chen HT, You CC, Mortenson DE, Yang XC, Bunz UHF, et al. Enzyme-Amplified Array Sensing of Proteins in Solution and in Biofluids. Journal of the American Chemical Society. 2010 Apr 14;132(14):5285-9.

96. Miranda OR, Creran B, Rotello VM. Array-based sensing with nanoparticles: 'Chemical noses' for sensing biomolecules and cell surfaces. Current Opinion in Chemical Biology. 2010 Dec;14(6):728-36.

97. Stranick SJ, Atre SV, Parikh AN, Wood MC, Allara DL, Winograd N, et al. Nanometer-scale phase separation in mixed composition self-assembled monolayers. Nanotechnology. 1996 Dec;7(4):438-42.

98. Campbell CT, Kim G. SPR microscopy and its applications to high-throughput analyses of biomolecular binding events and their kinetics. Biomaterials. 2007 May;28(15):2380-92.

99. Steiner G. Surface plasmon resonance imaging. Analytical and Bioanalytical Chemistry. 2004 Jun;379(3):328-31.

100. Grosjean L, Cherif B, Mercey E, Roget A, Levy Y, Marche PN, et al. A polypyrrole protein microarray for antibody-antigen interaction studies using a label-free detection process. Analytical Biochemistry. 2005 Dec 15;347(2):193-200.

101. Villiers MB, Cortes S, Brakha C, Lavergne JP, Marquette CA, Deny P, et al. Peptide-protein microarrays and surface plasmon resonance detection: Biosensors for versatile biomolecular interaction analysis. Biosensors & Bioelectronics. 2010 Dec 15;26(4):1554-9.

102. Mercey E, Sadir R, Maillart E, Roget A, Baleux F, Lortat-Jacob H, et al. Polypyrrole oligosaccharide array and surface plasmon resonance imaging for the measurement of glycosaminoglycan binding interaction. Analytical Chemistry. 2008 May 1;80(9):3476-82.

103. Karamanska R, Clarke J, Blixt O, MacRae JI, Zhang JQQ, Crocker PR, et al. Surface plasmon resonance imaging for real-time, label-free analysis of protein interactions with carbohydrate microarrays. Glycoconjugate Journal. 2008 Jan;25(1):69-74.

104. Guedon P, Livache T, Martin F, Lesbre F, Roget A, Bidan G, et al. Characterization and optimization of a real-time, parallel, label-free, polypyrrole-based DNA sensor by surface plasmon resonance imaging. Analytical Chemistry. 2000 Dec 15;72(24):6003-9.

105. Naka MH, Hattori K, Ohashi T, Ikeuchi K. Evaluation of the effect of collagen network degradation on the frictional characteristics of articular cartilage using a simultaneous analysis of the contact condition. Clinical Biomechanics. 2005 Dec;20(10):1111-8.

106. Elodie LY-MORIN SB, Géraldine MÉLIZZI,Chiraz FRYDMAN. Biomarker Discovery using Surface Plasmon Resonance Imaging. [cited 24-06-2013]; Available from: http://www.horiba.com/uploads/media/R39e_12_082_Biomarker_Discovery_05.pdf.

107. Smith EA, Corn RM. Surface plasmon resonance imaging as a tool to monitor biomolecular interactions in an array based format. Applied Spectroscopy. 2003 Nov;57(11):320a-32a.

108. Biacore. [cited 24-06-2013]; Available from: https://www.biacore.com/lifesciences/index.html.

109. Gutierrez-Osuna R. Pattern Analysis for Machine Olfaction: A Review. Ieee Sensors Journal. 2002 Jun;2(3):189-202.

110. Eriksson L, Andersson PL, Johansson E, Tysklind M. Megavariate analysis of environmental QSAR data. Part I - A basic framework founded on principal component analysis (PCA), partial least squares (PLS), and statistical molecular design (SMD). Molecular Diversity. 2006 May;10(2):169-86.

111. Iglesias JL, Lis H, Sharon N. Purification and Properties of a D-Galactose-N-Acetyl-D-Galactosamine-Specific Lectin from Erythrina-Cristagalli. European Journal of Biochemistry. 1982;123(2):247-52.

112. Hou YX, Genua M, Batista DT, Calemczuk R, Buhot A, Fornarelli P, et al. Continuous Evolution Profiles for Electronic-Tongue-Based Analysis. Angewandte Chemie-International Edition. 2012;51(41):10394-8.

113. Laguri C, Arenzana-Seisdedos F, Lortat-Jacob H. Relationships between glycosaminoglycan and receptor binding sites in chemokines - the CXCL12 example. Carbohydrate Research. 2008 Aug 11;343(12):2018-23.

114. Lortat-Jacob H. The molecular basis and functional implications of chemokine interactions with heparan sulphate. Current Opinion in Structural Biology. 2009 Oct;19(5):543-8.

115. Lortat-Jacob H, Grosdidier A, Imberty A. Structural diversity of heparan sulfate binding domains in chemokines. Proceedings of the National Academy of Sciences of the United States of America. 2002 Feb 5;99(3):1229-34.

116. Murphy JW, Cho Y, Sachpatzidis A, Fan CP, Hodsdon ME, Lolis E. Structural and functional basis of CXCL12 (strornal cell-derived factor-1 alpha) binding to heparin. Journal of Biological Chemistry. 2007 Mar 30;282(13):10018-27.

117. Sadir R, Baleux F, Grosdidier A, Imberty A, Lortat-Jacob H. Characterization of the stromal cell-derived factor-l alpha-heparin complex. Journal of Biological Chemistry. 2001 Mar 16;276(11):8288-96.

118. Yu L, Cecil J, Peng SB, Schrementi J, Kovacevic S, Paul D, et al. Identification and expression of novel isoforms of human stromal cell-derived factor 1. Gene. 2006 Jun 7;374:174-9.

119. Turton K, Natesh R, Thiyagarajan N, Chaddock JA, Acharya KR. Crystal structures of Erythrina cristagalli lectin with bound N-linked oligosaccharide and lactose. Glycobiology. 2004 Oct;14(10):923-9.

120. Svensson C, Teneberg S, Nilsson CL, Kjellberg A, Schwarz FP, Sharon N, et al. High-resolution crystal structures of Erythrina cristagalli lectin in complex with lactose and 2 '-alpha-L-fucosyllactose and correlation with thermodynamic binding data. Journal of Molecular Biology. 2002 Aug 2;321(1):69-83.

121. Lortat-Jacob H, Turnbull JE, Grimaud JA. Molecular-Organization of the Interferon Gamma-Binding Domain in Heparan-Sulfate. Biochemical Journal. 1995 Sep 1;310:497-505.

122. Bonnaffe D. Bioactive synthetic heparan sulfate and heparin derivatives: From long fragments mimetics to chimeras. Comptes Rendus Chimie. 2011 Jan;14(1):59-73.

123. Suslick BA, Feng L, Suslick KS. Discrimination of Complex Mixtures by a Colorimetric Sensor Array: Coffee Aromas. Analytical Chemistry. 2010 Mar 1;82(5):2067-73.

124. Sim MYM, Shya TJ, Ahmad MN, Shakaff AYM, Othman AR, Hitam MS. Monitoring of milk quality with disposable taste sensor. Sensors. 2003 Sep;3(9):340-9.

125. Bernfield M, Kokenyesi R, Kato M, Hinkes MT, Spring J, Gallo RL, et al. Biology of the Syndecans - a Family of Transmembrane Heparan-Sulfate Proteoglycans. Annual Review of Cell Biology. 1992;8:365-93.

126. Kreuger J, Spillmann D, Li JP, Lindahl U. Interactions between heparan sulfate and proteins: the concept of specificity. Journal of Cell Biology. 2006 Jul 31;174(3):323-7.

127. Oyelaran O, Gildersleeve JC. Glycan arrays: recent advances and future challenges. Current Opinion in Chemical Biology. 2009 Oct;13(4):406-13.

128. de Paz JL, Seeberger PH. Deciphering the glycosaminoglycan code with the help of microarrays. Molecular Biosystems. 2008;4(7):707-11.

129. Gandhi NS, Mancera RL. The Structure of Glycosaminoglycans and their Interactions with Proteins. Chemical Biology & Drug Design. 2008 Dec;72(6):455-82.

130. Imberty A, Lortat-Jacob H, Perez S. Structural view of glycosaminoglycan-protein interactions. Carbohydrate Research. 2007 Feb 26;342(3-4):430-9.

131. Rudd TR, Skidmore MA, Guerrini M, Hricovini M, Powell AK, Siligardi G, et al. The conformation and structure of GAGs: recent progress and perspectives. Current Opinion in Structural Biology. 2010 Oct;20(5):567-74.

132. Bishop JR, Schuksz M, Esko JD. Heparan sulphate proteoglycans fine-tune mammalian physiology. Nature. 2007 Apr 26;446(7139):1030-7.

133. Lindahl U, Backstrom G, Thunberg L, Leder IG. Evidence for a 3-O-Sulfated D-Glucosamine Residue in the Antithrombin-Binding Sequence of Heparin. Proceedings of the National Academy of Sciences of the United States of America-Biological Sciences. 1980;77(11):6551-5.

134. Petitou M, van Boeckel CAA. A synthetic antithrombin III binding pentasaccharide is now a drug! What comes next? Angewandte Chemie-International Edition. 2004;43(24):3118-33.

135. Saesen E, Sarrazin S, Laguri C, Sadir R, Maurin D, Thomas A, et al. Insights into the Mechanism by Which Interferon-gamma Basic Amino Acid Clusters Mediate Protein Binding to Heparan Sulfate. J Am Chem Soc. 2013 Jun 26;135(25):9384-90.

136. Skurkovich B, Skurkovich S. Anti-interferon-gamma antibodies in the treatment of autoimmune diseases. Current Opinion in Molecular Therapeutics. 2003 Feb;5(1):52-7.

137. Bouma G, Strober W. The immunological and genetic basis of inflammatory bowel disease. Nature Reviews Immunology. 2003 Jul;3(7):521-33.

138. Sarrazin S, Bonnaffe D, Lubineau A, Lortat-Jacob H. Heparan sulfate mimicry: a synthetic glycoconjugate that recognizes the heparin binding domain of interferon-gamma inhibits the cytokine activity. The Journal of biological chemistry. 2005 Nov 11;280(45):37558-64.

139. Farrar MA, Schreiber RD. The molecular cell biology of interferon-gamma and its receptor. Annual review of immunology. 1993;11:571-611.

140. Walter MR, Windsor W, Nagabhushan TL, Lundell DJ, Lunn CA, Zauodny PJ, et al. Crystal-Structure of a Complex between Interferon-Gamma and Its Soluble High-Affinity Receptor. Nature. 1995 Jul 20;376(6537):230-5.

141. Randal M, Kossiakoff AA. The structure and activity of a monomeric interferon-gamma:alpha-chain receptor signaling complex. Structure. 2001 Feb 7;9(2):155-63.

142. Randal M, Kossiakoff AA. Crystallization and preliminary X-ray analysis of a 1:1 complex between a designed monomeric interferon-gamma and its soluble receptor. Protein Sci. 1998 Apr;7(4):1057-60.

143. Lortat-Jacob H, Grimaud JA. Interferon-gamma binds to heparan sulfate by a cluster of amino acids located in the C-terminal part of the molecule. FEBS letters. 1991 Mar 11;280(1):152-4.

144. Lortat-Jacob H, Grimaud JA. Binding of interferon-gamma to heparan sulfate is restricted to the heparin-like domains and involves carboxylic--but not N-sulfated--groups. Biochimica et biophysica acta. 1992 Sep 15;1117(2):126-30.

145. VanHaverbeke C, Simorre JP, Sadir R, Gans P, Lortat-Jacob H. NMR characterization of the interaction between the C-terminal domain of interferon-gamma and heparin-derived oligosaccharides. Biochemical Journal. 2004 Nov 15;384:93-9.

146. Saesen E. Bases Sructurales de la regulation de cytokines par les héparanes sulfates: Caractreisation de l'IFNg avec les héparanes sulfates. Grenoble: Université de Grenoble; 2013.

147. Lortat-Jacob H, Kleinman H, Grimaud JA. [Connective matrix and localization of a biological signal: demonstration of a matrix receptor for interferon-gamma in basement membranes]. Comptes rendus de l'Academie des sciences. 1990;311(4):143-7.

148. Sadir R, Forest E, Lortat-Jacob H. The heparan sulfate binding sequence of interferon-gamma increased the on rate of the interferon-gamma-interferon-gamma receptor complex formation. The Journal of biological chemistry. 1998 May 1;273(18):10919-25.

149. Lortat-Jacob H, Kleinman HK, Grimaud JA. High-affinity binding of interferon-gamma to a basement membrane complex (matrigel). The Journal of clinical investigation. 1991 Mar;87(3):878-83.

150. Lortat-Jacob H, Baltzer F, Grimaud JA. Heparin decreases the blood clearance of interferon-gamma and increases its activity by limiting the processing of its carboxyl-terminal sequence. Journal of Biological Chemistry. 1996 Jul 5;271(27):16139-43.

151. Dobeli H, Gentz R, Jucker W, Garotta G, Hartmann DW, Hochuli E. Role of the Carboxy-Terminal Sequence on the Biological-Activity of Human Immune Interferon (Ifn-Gamma). Journal of Biotechnology. 1988 Mar;7(3):199-216.

152. Sarrazin S. Caractérisation des interactions glycosaminoglycannes/potéines dans le but de développer des molécules d'interêt therapeutique: Exemples de l'Endocan et de l'IFNg: Université de Grenoble; 2007.

153. De la Fuente JM, Penades S. Glyconanoparticles: Types, synthesis and applications in glycoscience, biomedicine and material science. Biochimica Et Biophysica Acta-General Subjects. 2006 Apr;1760(4):636-51.

154. Wei A, Mehtala JG, Patri AK. Challenges and opportunities in the advancement of nanomedicines. Journal of Controlled Release. 2012 Dec 10;164(2):236-46.

155. Reichardt NC, Martin-Lomas M, Penades S. Glyconanotechnology. Chemical Society Reviews. 2013;42(10):4358-76.

156. Huang XH, Neretina S, El-Sayed MA. Gold Nanorods: From Synthesis and Properties to Biological and Biomedical Applications. Advanced Materials. 2009 Dec 28;21(48):4880-910.

157. Jain PK, Huang XH, El-Sayed IH, El-Sayed MA. Noble Metals on the Nanoscale: Optical and Photothermal Properties and Some Applications in Imaging, Sensing, Biology, and Medicine. Accounts of Chemical Research. 2008 Dec;41(12):1578-86.

158. Probst CE, Zrazhevskiy P, Bagalkot V, Gao X. Quantum dots as a platform for nanoparticle drug delivery vehicle design. Adv Drug Deliv Rev. 2013 May;65(5):703-18.

159. Qiao RR, Yang CH, Gao MY. Superparamagnetic iron oxide nanoparticles: from preparations to in vivo MRI applications. Journal of Materials Chemistry. 2009;19(35):6274-93.

160. Saha K, Bajaj A, Duncan B, Rotello VM. Beauty is Skin Deep: A Surface Monolayer Perspective on Nanoparticle Interactions with Cells and Biomacromolecules. Small. 2011 Jul 18;7(14):1903-18.

161. Faraday M. The Bakerian Lecture: Experimental Relations of Gold (and Other Metals) to Light. The Royal Society. 1857;147(1857): 145-81

162. Giljohann DA, Seferos DS, Daniel WL, Massich MD, Patel PC, Mirkin CA. Gold Nanoparticles for Biology and Medicine. Angewandte Chemie-International Edition. 2010;49(19):3280-94.

163. Daniel MC, Astruc D. Gold nanoparticles: Assembly, supramolecular chemistry, quantum-size-related properties, and applications toward biology, catalysis, and nanotechnology. Chemical Reviews. 2004 Jan;104(1):293-346.

164. Mukherjee P, Bhattacharya R, Wang P, Wang L, Basu S, Nagy JA, et al. Antiangiogenic properties of gold nanoparticles. Clinical Cancer Research. 2005 May 1;11(9):3530-4.

165. Dreaden EC, Mackey MA, Huang XH, Kang B, El-Sayed MA. Beating cancer in multiple ways using nanogold. Chemical Society Reviews. 2011;40(7):3391-404.

166. Dickerson EB, Dreaden EC, Huang XH, El-Sayed IH, Chu HH, Pushpanketh S, et al. Gold nanorod assisted near-infrared plasmonic photothermal therapy (PPTT) of squamous cell carcinoma in mice. Cancer Letters. 2008 Sep 28;269(1):57-66.

167. Cobley CM, Au L, Chen JY, Xia YN. Targeting gold nanocages to cancer cells for photothermal destruction and drug delivery. Expert Opinion on Drug Delivery. 2010 May;7(5):577-87.

168. Dreaden EC, Alkilany AM, Huang XH, Murphy CJ, El-Sayed MA. The golden age: gold nanoparticles for biomedicine. Chemical Society Reviews. 2012;41(7):2740-79.

169. Rana S, Bajaj A, Mout R, Rotello VM. Monolayer coated gold nanoparticles for delivery applications. Advanced Drug Delivery Reviews. 2012 Feb;64(2):200-16.

170. Rosi NL, Mirkin CA. Nanostructures in biodiagnostics. Chemical Reviews. 2005 Apr;105(4):1547-62.

171. Saha K, Agasti SS, Kim C, Li XN, Rotello VM. Gold Nanoparticles in Chemical and Biological Sensing. Chemical Reviews. 2012 May;112(5):2739-79.

172. Liu YZ, Wu ZT, Zhou GH, He ZK, Zhou XD, Shen AG, et al. Simple, rapid, homogeneous oligonucleotides colorimetric detection based on non-aggregated gold nanoparticles. Chemical Communications. 2012;48(26):3164-6.

173. Aslan K, Lakowicz JR, Geddes CD. Nanogold-plasmon-resonance-based glucose sensing. Analytical Biochemistry. 2004 Jul 1;330(1):145-55.

174. Penn SG, He L, Natan MJ. Nanoparticles for bioanalysis. Current Opinion in Chemical Biology. 2003 Oct;7(5):609-15.

175. Jans H, Huo Q. Gold nanoparticle-enabled biological and chemical detection and analysis. Chemical Society Reviews. 2012;41(7):2849-66.

176. Hirsch LR, Jackson JB, Lee A, Halas NJ, West J. A whole blood immunoassay using gold nanoshells. Analytical Chemistry. 2003 May 15;75(10):2377-81.

177. Bowman MC, Ballard TE, Ackerson CJ, Feldheim DL, Margolis DM, Melander C. Inhibition of HIV fusion with multivalent gold nanoparticles. Journal of the American Chemical Society. 2008 Jun 4;130(22):6896-+.

178. Baram-Pinto D, Shukla S, Gedanken A, Sarid R. Inhibition of HSV-1 Attachment, Entry, and Cell-to-Cell Spread by Functionalized Multivalent Gold Nanoparticles. Small. 2010 May 7;6(9):1044-50.

179. Bresee J, Maier KE, Melander C, Feldheim DL. Identification of antibiotics using small molecule variable ligand display on gold nanoparticles. Chemical Communications. 2010;46(40):7516-8.

180. Bresee J, Maier KE, Boncella AE, Melander C, Feldheim DL. Growth Inhibition of Staphylococcus aureus by Mixed Monolayer Gold Nanoparticles. Small. 2011 Jul 18;7(14):2027-31.

181. Gu HW, Ho PL, Tong E, Wang L, Xu B. Presenting vancomycin on nanoparticles to enhance antimicrobial activities. Nano Letters. 2003 Sep;3(9):1261-3.

182. Huang WC, Tsai PJ, Chen YC. Functional gold nanoparticles as photothermal agents for selective-killing of pathogenic bacteria. Nanomedicine. 2007 Dec;2(6):777-87.

183. Saha B, Bhattacharya J, Mukherjee A, Ghosh AK, Santra CR, Dasgupta AK, et al. In vitro structural and functional evaluation of gold nanoparticles conjugated antibiotics. Nanoscale Research Letters. 2007 Dec;2(12):614-22.

184. Rai A, Prabhune A, Perry CC. Antibiotic mediated synthesis of gold nanoparticles with potent antimicrobial activity and their application in antimicrobial coatings. Journal of Materials Chemistry. 2010;20(32):6789-98.

185. Vigderman L, Zubarev ER. Therapeutic platforms based on gold nanoparticles and their covalent conjugates with drug molecules. Adv Drug Deliv Rev. 2013 May;65(5):663-76.

186. Iyer AK, Khaled G, Fang J, Maeda H. Exploiting the enhanced permeability and retention effect for tumor targeting. Drug Discovery Today. 2006 Sep;11(17-18):812-8.

187. Cho KJ, Wang X, Nie SM, Chen Z, Shin DM. Therapeutic nanoparticles for drug delivery in cancer. Clinical Cancer Research. 2008 Mar 1;14(5):1310-6.

188. Doane T, Burda C. Nanoparticle mediated non-covalent drug delivery. Adv Drug Deliv Rev. 2013 May;65(5):607-21.

189. Montenegro JM, Grazu V, Sukhanova A, Agarwal S, de la Fuente JM, Nabiev I, et al. Controlled antibody/(bio-) conjugation of inorganic nanoparticles for targeted delivery. Adv Drug Deliv Rev. 2013 May;65(5):677-88.

190. McIntosh CM, Esposito EA, Boal AK, Simard JM, Martin CT, Rotello VM. Inhibition of DNA transcription using cationic mixed monolayer protected gold clusters. Journal of the American Chemical Society. 2001 Aug 8;123(31):7626-9.

191. Han G, Martin CT, Rotello VM. Stability of gold nanoparticle-bound DNA toward biological, physical, and chemical agents. Chemical Biology & Drug Design. 2006 Jan;67(1):78-82.

192. Sandhu KK, McIntosh CM, Simard JM, Smith SW, Rotello VM. Gold nanoparticle-mediated Transfection of mammalian cells. Bioconjugate Chemistry. 2002 Jan-Feb;13(1):3-6.

193. Noh SM, Kim WK, Kim SJ, Kim JM, Baek KH, Oh YK. Enhanced cellular delivery and transfection efficiency of plasmid DNA using positively charged biocompatible colloidal gold nanoparticles. Biochimica Et Biophysica Acta-General Subjects. 2007 May;1770(5):747-52.

194. Ghosh PS, Han G, Erdogan B, Rosado O, Krovi SA, Rotello VM. Nanoparticles featuring amino acid-functionalized side chains as DNA receptors. Chemical Biology & Drug Design. 2007 Jul;70(1):13-8.

195. Ghosh PS, Kim CK, Han G, Forbes NS, Rotello VM. Efficient Gene Delivery Vectors by Tuning the Surface Charge Density of Amino Acid-Functionalized Gold Nanoparticles. Acs Nano. 2008 Nov;2(11):2213-8.

196. Wang H, Chen Y, Li XY, Liu Y. Synthesis of oligo(ethylenediamino)-beta-cyclodextrin modified gold nanoparticle as a DNA concentrator. Molecular Pharmaceutics. 2007 Mar-Apr;4(2):189-98.

197. Thomas M, Klibanov AM. Conjugation to gold nanoparticles enhances polyethylenimine's transfer of plasmid DNA into mammalian cells. Proceedings of the National Academy of Sciences of the United States of America. 2003 Aug 5;100(16):9138-43.

198. Rosi NL, Giljohann DA, Thaxton CS, Lytton-Jean AK, Han MS, Mirkin CA. Oligonucleotide-modified gold nanoparticles for intracellular gene regulation. Science (New York, NY. 2006 May 19;312(5776):1027-30.

199. Seferos DS, Giljohann DA, Rosi NL, Mirkin CA. Locked nucleic acid-nanoparticle conjugates. Chembiochem. 2007 Jul 23;8(11):1230-2.

200. Tsai CY, Shiau AL, Cheng PC, Shieh DB, Chen DH, Chou CH, et al. A biological strategy for fabrication of Au/EGFP nanoparticle conjugates retaining bioactivity. Nano Letters. 2004 Jul;4(7):1209-12.

201. Agbasi-Porter C, Ryman-Rasmussen J, Franzen S, Feldheim D. Transcription inhibition using oligonucleotide-modified gold nanoparticles. Bioconjugate Chemistry. 2006 Sep 20;17(5):1178-83.

202. Medley CD, Smith JE, Tang Z, Wu Y, Bamrungsap S, Tan WH. Gold nanoparticle-based colorimetric assay for the direct detection of cancerous cells. Analytical Chemistry. 2008 Feb 15;80(4):1067-72.

203. Ghosh P, Yang XC, Arvizo R, Zhu ZJ, Agasti SS, Mo ZH, et al. Intracellular Delivery of a Membrane-Impermeable Enzyme in Active Form Using Functionalized Gold Nanoparticles. Journal of the American Chemical Society. 2010 Mar 3;132(8):2642-5.

204. Bhumkar DR, Joshi HM, Sastry M, Pokharkar VB. Chitosan reduced gold nanoparticles as novel carriers for transmucosal delivery of insulin. Pharmaceutical Research. 2007 Aug;24(8):1415-26.

205. Visaria RK, Griffin RJ, Williams BW, Ebbini ES, Paciotti GF, Song CW, et al. Enhancement of tumor thermal therapy using gold nanoparticle-assisted tumor necrosis factor-alpha delivery. Molecular Cancer Therapeutics. 2006 Apr;5(4):1014-20.

206. Stone JW, Thornburg NJ, Blum DL, Kuhn SJ, Wright DW, Crowe JE, Jr. Gold nanorod vaccine for respiratory syncytial virus. Nanotechnology. 2013 Jul 26;24(29):295102.

207. Wang X, Ramstrom O, Yan MD. Glyconanomaterials: Synthesis, Characterization, and Ligand Presentation. Advanced Materials. 2010 May 4;22(17):1946-53.

208. El-Boubbou K, Huang XF. Glyco-Nanomaterials: Translating Insights from the "Sugar-Code" to Biomedical Applications. Current Medicinal Chemistry. 2011 May;18(14):2060-78.

209. de la Fuente JM, Penades S. Understanding carbohydrate-carbohydrate interactions by means of glyconanotechnology. Glycoconjugate Journal. 2004;21(3-4):149-63.

210. Otsuka H, Akiyama Y, Nagasaki Y, Kataoka K. Quantitative and reversible lectin-induced association of gold nanoparticles modified with alpha-lactosyl-omega-mercapto-poly(ethylene glycol). Journal of the American Chemical Society. 2001 Aug 29;123(34):8226-30.

211. Lin CC, Yeh YC, Yang CY, Chen GF, Chen YC, Wu YC, et al. Quantitative analysis of multivalent interactions of carbohydrate-encapsulated gold nanoparticles with concanavalin A. Chemical Communications. 2003(23):2920-1.

212. Lin CC, Yeh YC, Yang CY, Chen CL, Chen GF, Chen CC, et al. Selective binding of mannose-encapsulated gold nanoparticles to type 1 pili in Escherichia coli. Journal of the American Chemical Society. 2002 Apr 10;124(14):3508-9.

213. Kemp MM, Kumar A, Mousa S, Dyskin E, Yalcin M, Ajayan P, et al. Gold and silver nanoparticles conjugated with heparin derivative possess anti-angiogenesis properties. Nanotechnology. 2009 Nov 11;20(45).

214. Kim HS, Jun SH, Koo YK, Cho S, Park Y. Green synthesis and nanotopography of heparin-reduced gold nanoparticles with enhanced anticoagulant activity. Journal of nanoscience and nanotechnology. 2013 Mar;13(3):2068-76.

215. Reynolds M, Marradi M, Imberty A, Penades S, Perez S. Multivalent Gold Glycoclusters: High Affinity Molecular Recognition by Bacterial Lectin PA-IL. Chemistry-a European Journal. 2012 Apr;18(14):4264-73.

216. Rojo J, Diaz V, de la Fuente JM, Segura I, Barrientos AG, Riese HH, et al. Gold glyconanoparticles as new tools in antiadhesive therapy. Chembiochem. 2004 Mar 5;5(3):291-7.

217. Liu XO, Atwater M, Wang JH, Huo Q. Extinction coefficient of gold nanoparticles with different sizes and different capping ligands. Colloids and Surfaces B-Biointerfaces. 2007 Jul 1;58(1):3-7.

218. Thanh NTK, Green LAW. Functionalisation of nanoparticles for biomedical applications. Nano Today. 2010 Jun;5(3):213-30.

219. Fang C, Bhattarai N, Sun C, Zhang MQ. Functionalized Nanoparticles with Long-Term Stability in Biological Media. Small. 2009 Jul 17;5(14):1637-41.

220. Takae S, Akiyama Y, Otsuka H, Nakamura T, Nagasaki Y, Kataoka K. Ligand density effect on biorecognition by PEGylated gold nanoparticles: Regulated interaction of RCA(120) lectin with lactose installed to the distal end of tethered PEG strands on gold surface. Biomacromolecules. 2005 Mar-Apr;6(2):818-24.

221. Zhang Y, Kohler N, Zhang MQ. Surface modification of superparamagnetic magnetite nanoparticles and their intracellular uptake. Biomaterials. 2002 Apr;23(7):1553-61.

222. Sun C, Veiseh O, Gunn J, Fang C, Hansen S, Lee D, et al. In vivo MRI detection of gliomas by chlorotoxin-conjugated superparamagnetic nanoprobes. Small. 2008 Mar;4(3):372-9.

223. Kohler N, Fryxell GE, Zhang MQ. A bifunctional poly(ethylene glycol) silane immobilized on metallic oxide-based nanoparticles for conjugation with cell targeting agents. Journal of the American Chemical Society. 2004 Jun 16;126(23):7206-11.

224. Zhang Y, Sun C, Kohler N, Zhang MQ. Self-assembled coatings on individual monodisperse magnetite nanoparticles for efficient intracellular uptake. Biomedical Microdevices. 2004 Mar;6(1):33-40.

225. Zhu B, Eurell T, Gunawan R, Leckband D. Chain-length dependence of the protein and cell resistance of oligo(ethylene glycol)-terminated self-assembled monolayers on gold. Journal of Biomedical Materials Research. 2001 Sep 5;56(3):406-16.

226. Ulman A. Wetting studies of molecularly engineered surfaces. Thin Solid Films. 1996 Feb;273(1-2):48-53.

227. Hostetler MJ, Wingate JE, Zhong CJ, Harris JE, Vachet RW, Clark MR, et al. Alkanethiolate gold cluster molecules with core diameters from 1.5 to 5.2 nm: Core and monolayer properties as a function of core size. Langmuir. 1998 Jan 6;14(1):17-30.